

ABSTRACT

MANTZ, ROBERT ALLEN. Investigations of Ambient-Temperature Chloroaluminate Molten Salts. (Under the Direction of Robert A. Osteryoung.)

The objective of this project was to further characterize ambient-temperature chloroaluminate ionic liquids (melts) composed of aluminum chloride and 1-ethyl-3-methylimidazolium chloride (EMIC). These studies can be broken down into three broad areas: properties of neutral buffered and binary melts, investigation of structure present in $\text{AlCl}_3\cdot\text{EMIC}$ melts, and high frequency square wave voltammetry of solutes in the melts.

Within the area of melt properties of the buffered and binary melts three studies were conducted. In the first, the stoichiometry of a "latent acidity" observed in melts buffered with alkali metal chloride salts is found to be unity with respect to the alkali metal cation concentration.

The second study dealing with properties of alkali metal chloride neutral buffered and binary melts dealt with the determination of the Gutmann acceptor numbers for a series of binary and neutral buffered melts. The neutral buffered melts do not achieve the same Lewis acidity as the binary melts. The LiCl neutral buffered melt is the most Lewis acidic followed by the NaCl and finally the KCl neutral buffered melts.

The third study dealing with properties of buffered melts involved the generation of buffered melts through the addition of water. The buffering agent

is an aluminum hydroxide species formed in the melt through the addition of water.

The investigation of a structure making interaction present in certain melts was conducted using rotating frame nuclear Overhauser effect spectroscopy (ROESY). The presence of structure making interactions due to hydrogen bonding which can be present in melts is confirmed.

Two studies involving the use of square wave voltammetry of the Cu(I)/Cu(II) couple in a melt using microdisk electrodes were conducted. In the first study the electron transfer parameters are determined using normal pulse and square wave voltammetry.

The second study also used the Cu(I)/Cu(II) couple in a melt as a model system to investigate the difficulties in attempting square wave voltammetry at square wave frequencies up to 200 kHz. Potential difficulties are identified and limitations imposed by each interference are estimated.

**INVESTIGATIONS OF AMBIENT-TEMPERATURE
CHLOROALUMINATE MOLTEN SALTS**

by

Robert Allen Mantz

A dissertation submitted to the Graduate Faculty of
North Carolina State University
in Partial fulfillment of the
requirements for the Degree of
Doctor of Philosophy

CHEMISTRY

Raleigh

1997

APPROVED BY:

Chair of Advisory Committee

DEDICATION

I would like to dedicate this disseration to the people that have supported me throughout my education thus far. My Babes who has been unbelievably supportive and helpful. My parents who have stood behind me during each phase of my life and who passed on to me the value of a quality education. Paul Trulove who has given me many ideas as well as allowed me to bounce ideas off of him during this research. Robert Osteryoung, who kept my nose to the grindstone and who has allowed me the freedom to pursue these varied research projects.

BIOGRAPHY

I was born in 1967 in Oxnard, California, to Robert L. Mantz and Sandra S. Mantz. After attending a variety of grade schools in Colorado Springs, Colorado; Karmasel, Turkey; and Raton, New Mexico, I attended high school in Raton New Mexico. After graduation from high school in 1985 I attended the United States Air Force Academy in Colorado Springs, Colorado, and graduated in 1989 with a B. S. in Chemistry. I was commissioned as a second Lieutenant in the Air Force 31 May 1989 and was stationed to Edwards Air Force Base, California. While working at Edwards I attended night school and earned a M. S. in Chemistry from California State University, Northridge. I was sponsored by the Air Force to obtain a PhD in Chemistry and moved to Raleigh, North Carolina, to attend graduate school at NCSU.

ACKNOWLEDGEMENTS

I would like to give special thanks to John O'Dea without whose help most electrochemical experiments would be next to impossible to collect and analyze. I would also like to thank Dr. Charles Cornman who allowed me to use the Hewlett Packard Spectrophotometer in his laboratory.

I would also like to acknowledge Dr. Paul Trulove whose constant ideas and discussions have been invaluable for almost the last ten years and who laid the trail for me to follow in obtaining his PhD.

I would also like to thank the many people at North Carolina State University who have been very supportive and helpful throughout my time here. Michelle Clark, Konnie McCauley, and Cynthia Martin have all been very helpful and made my day to day life here bearable. Dan Knauss who graciously proofed this document for grammatical errors. Curtis Harris has made it possible to get items shipped in and out of here in a timely fashion but who is also always there when you need him. Eddie Barefoot and Bill Patrick who have always gone out of their way to help build and repair various pieces of equipment. The personnel in the machine shop and the glass blower who have built the specialized equipment necessary to conduct research in the laboratory.

TABLE OF CONTENTS

	Page
LIST OF TABLES	x
LIST OF FIGURES	xiv
Chapter 1: Introduction to Ambient-Temperature Chloroaluminate Molten Salts	1
1.1 Introduction	1
1.2 History of Ambient-Temperature Molten Salts	1
1.3 Chemical Properties of AlCl_3 :EMIC Molten Salts	3
1.4 Neutral Buffered Chloroaluminate Ionic Liquids	10
Chapter 1 References	12
Chapter 2: General Experimental	19
2.1 Materials	19
2.1.1 Synthesis of 1-Ethyl-3-Methylimidazolium Chloride (EMIC)	19
2.1.1.1 Purification of 1-Methylimidazole	19
2.1.1.2 Distillation of Acetonitrile	24
2.1.1.3 Purification of Ethyl Chloride	26
2.1.1.4 Synthesis of EMIC	30
2.1.1.5 Purification of Crude EMIC	31
2.1.2 Purification of Aluminum Chloride	38
2.1.3 Preparation of AlCl_3 :EMIC Melts	43
2.1.4 Purification of Alkali Metal Chlorides	44
2.1.5 Preparation of Neutral Buffered Melts	45
2.2 Equipment and Procedures	45
2.2.1 Dry box	45
2.2.2 Proton and Oxide Removal from AlCl_3 :EMIC Melts	46
2.2.3 NMR Measurements	51

2.2.4 Electrochemical Measurements	52
2.2.4.1 RDE Measurements/Electrode Holder	54
2.2.4.2 Fabrication of Reference Electrodes	54
Chapter 2 References	59
 Chapter 3: Quantification of Latent Acidity	 62
3.1 Introduction	62
3.2 Specialized Experimental Procedures	64
3.2.1 Materials	64
3.2.2 Equipment and Procedures	64
3.2.2.1 UV-vis Measurements	64
3.3 Results and Discussion	64
3.3.1 Acetylferrocene	64
3.3.2 Dimethylaniline (DMA)	76
3.4 Conclusions	81
Chapter 3 References	87
 Chapter 4: Gutmann Acceptor Numbers	 90
4.1 Introduction	90
4.2 Specialized Equipmental Procedures	93
4.2.1 Materials	93
4.2.2 Equipment and Procedures	94
4.2.2.1 NMR Preparation	94
4.2.2.2 Triethylphosphine Oxide Concentration Effect on Chemical Shift	94
4.2.2.3 Change in ³¹ P Chemical Shift of TEPO vs. Melt Composition	95
4.2.2.4 Identification of Small Downfield Peak	98
4.2.2.5 Determination of Volume Magnetic Susceptibilities	98
4.2.2.6 Determination of Alkali Metal Concentration in Neutral Buffered Melts	104
4.3 Results and Discussion	106
4.3.1 NMR Data	106
4.3.2 ICP Data	115
4.3.3 Gutmann Acceptor Numbers of Binary AlCl ₃ /EMIC Melts	117

4.3.4	Gutmann Acceptor Numbers of Alkali Metal Neutral Buffered Melt	120
4.3.4.1	Weighted Average Model to Describe Neutral Buffered Acceptor Numbers	123
4.3.4.2	Equilibrium Model to Describe Neutral Buffered Acceptor Numbers	124
4.3.5	Effect of Oxide/Hydroxide on Acceptor Number	126
4.4	Conclusions	127
	Chapter 4 References	130
 Chapter 5: ROESY NMR of Basic Ambient-Temperature Chloroaluminate Ionic Liquids		 132
5.1	Introduction	132
5.1.1	Physical and Structural Properties of the Chloroaluminate Ionic Liquids	132
5.1.2	Nuclear Overhauser Effect Spectroscopy.	143
5.1.3	Rotating Frame Nuclear Overhauser Enhancement Spectroscopy (ROESY)	149
5.2	Specialized Experimental Procedures	156
5.2.1	Materials	156
5.2.1.1	Synthesis of <i>d</i> 11-1-Ethyl-3-Methylimidazolium Chloride	156
5.2.2	Equipment and Procedures	156
5.2.2.1	NMR Preparation	156
5.2.2.2	NMR Experiments	158
5.2.2.3	NMR Data Treatment	159
5.3	Results and Discussion	159
5.3.1	Relaxation Studies	159
5.3.1.1	T1 Relaxation	159
5.3.1.2	T2 Relaxation	164
5.3.1.3	T1ρ Relaxation	169
5.3.1.4	Molecular Correlation Time.	171
5.3.2	ROESY Studies	177
5.4	Conclusions	195
	Chapter 5 References	197

Chapter 6: Characterization of the Cu(I/II) Couple in Ambient-Temperature Chloroaluminate Molten Salts	204
6.1 Introduction	204
6.2 Specialized Experimental Procedures	207
6.2.1 Materials	207
6.2.2 Equipment and Procedures for Electrochemical Experiments	207
6.3 Results and Discussion	212
6.3.1 Normal Pulse Voltammetry Results	212
6.3.2 Square Wave Voltammetry Results	213
6.4 Conclusions	245
Chapter 6 References	249
 Chapter 7: Behavior of Oxide Containing Melts	 253
7.1 Introduction	253
7.2 Specialized Experimental Procedures	261
7.2.1 Materials	261
7.2.2 Equipment and Procedures	261
7.2.2.1 Electrochemical Measurements	261
7.2.2.2 ^{17}O NMR Experiments	265
7.2.2.3 Sample Preparation	266
7.3 Results and Discussion	271
7.3.1 Electrochemical Results	271
7.3.2 ^{17}O NMR Results	282
7.4 Conclusions	306
Chapter 7 References	308
 Chapter 8: Fast Square Wave Voltammetry of Cu(I/II) in Chloroaluminate Molten Salts	 312
8.1 Introduction	312
8.1.1 Electrochemistry of the Cu(I)/(II) Couple	312
8.1.2 Square Wave Voltammetry	313

8.2 Specialized Experimental Procedures	315
8.2.1 Materials	315
8.2.2 Equipment and Procedures	316
8.2.2.1 Potentiostat Frequency Response	316
8.2.2.2 RC Time Constants	316
8.2.2.3 Square Wave Voltammetry	320
8.3 Results and Discussion	324
8.3.1 Potentiostat Frequency Response	324
8.3.2 RC Time Constants	333
8.3.3 Square Wave Voltammetry	337
8.4 Conclusions	351
Chapter 8 References	361
 Appendix I: Aluminum Temperature Control Blocks	 363
 Appendix II: Phosgenation and Proton Removal Procedure	 375

LIST OF TABLES

	Page
Table 2.1 The NMR frequencies of the nuclei studied . . .	53
Table 3.1 Concentrations of free and bound acetylferrocene as the concentration of acetyl ferrocene is increased . . .	72
Table 3.2 Molar absorptivity of acetylferrocene in AlCl ₃ :EMIC and alkali metal chloride neutral buffered melts . . .	77
Table 3.3 UV-vis data for absorbance at 580 nm vs. acetylferrocene concentration	80
Table 3.4 ¹ H NMR chemical shift (ppm) of the DMA methyl hydrogen vs. DMA concentration divided by the initial sodium cation concentration	82
Table 3.5 ¹ H NMR chemical shift (ppm) of the DMA methyl hydrogen vs. ([DMA] _t -[Na ⁺])/[DMA] _t	85
Table 4.1 Typical Gutmann acceptor numbers	91
Table 4.2 Dependence of the ³¹ P chemical shift of TEPO on TEPO concentration	96
Table 4.3 ³¹ P chemical shift of TEPO vs. melt composition	97
Table 4.4 ¹³ C chemical shift differences of benzene-d ₆ between inner and annular regions of coaxial pair	102
Table 4.5 Volume magnetic susceptibility of melts	105
Table 4.6 Alkali metal concentrations determined from ICP data for a series of alkali metal chloride neutral buffered melts	107
Table 4.7 ³¹ P NMR chemical shift dependence on TEPO concentration	110
Table 4.8 Volume bulk magnetic susceptibility of the binary and alkali chloride buffered melts	112
Table 4.9 Gutmann acceptor numbers of binary AlCl ₃ :EMIC melts	113
Table 4.10 Gutmann acceptor numbers for each of the alkali metal	

	chloride neutral buffered melts	114
Table 4.11	Least squared fit values of the Gutmann acceptor numbers of alkali metal chloride neutral buffered melts to a linear equation	122
Table 5.1	Results of ^1H T1 inversion recovery experiment for each position on the EMIC molecule	165
Table 5.2	Results of ^1H T2 spin refocusing experiment for each position on the EMIC molecule	168
Table 5.3	Results of ^1H T1 ρ spin locking experiment for each position on the EMIC molecule	170
Table 5.4	Results of ^1H T1 ρ spin refocusing experiment for each position on the EMIC molecule for a 0.5:1.0 melt at 25 °C	172
Table 5.5	Results of ^1H T1 ρ spin locking experiment for each position on the EMIC molecule for a 0.5:1.0 melt at 40 °C	173
Table 5.6	Results of ^1H T1 ρ spin locking experiment for each position on the EMIC molecule for a 0.99:1.0 melt at 25 °C	174
Table 5.7	Molecular correlation time for each molecular position on EMIC molecule	176
Table 5.8	Intramolecular distances for the EMIC molecule	192
Table 6.1	Common electrochemical experimental parameters used Cu(I)/Cu(II) electron transfer parameter experiments	211
Table 6.2	Electron transfer parameters for Cu(I)/Cu(II) determined using square wave voltammetric data obtained in a 1.5:1.0 melt. Fit between 1.7 and 2.2 V. Using a 9 μm diameter tungsten electrode	237
Table 6.3	Electron transfer parameters for Cu(I)/Cu(II) determined using square wave voltammetric data obtained in a 1.5:1.0 melt. Fit between 1.8 and 2.1 V. Using a 9 μm diameter tungsten electrode	238
Table 6.4	Electron transfer parameters for Cu(I)/Cu(II) determined using square wave voltammetric data obtained in a 1.5:1.0 melt. Fit between 1.7 and 2.2 V. Using a 25 μm diameter tungsten electrode	239

Table 6.5	Electron transfer parameters for Cu(I)/Cu(II) determined using square wave voltammetric data obtained in a 1.5:1.0 melt. Fit between 1.8 and 2.1 V. Using a 25 μm diameter tungsten electrode	240
Table 6.6	Diffusion coefficient of Cu(I) determined using square wave voltammetric data obtained in a 1.5:1.0 melt	242
Table 6.7	κ and k_a° of Cu(I)/Cu(II) determined using square wave voltammetric data obtained in a 1.5:1.0 melt using the slope of $\kappa \times \sqrt{t_p}$ vs. $\sqrt{t_p}$	243
Table 6.8	κ and k_a° of Cu(I)/Cu(II) determined using square wave voltammetric data obtained in a 1.5:1.0 melt using the mean of the κ values	244
Table 6.9	The net square wave currents from the 9 μm and 25 μm diameter tungsten electrodes. Currents have been normalized to the 25 μm diameter electrode	247
Table 7.1	Normal pulse voltammetry parameters for the detection of oxidation of chloride and deposition of aluminum	263
Table 7.2	Square wave voltammetry parameters used during the Nb(V)Cl titration with oxide containing melt	264
Table 7.3	Titration of initial melt using AlCl_3	265
Table 7.4	Actual stock solution weights used to generate a series of samples with 75 mM oxide	273
Table 7.5	Actual stock solution weights used to generate a series of samples with 50 mM oxide	274
Table 7.6	Actual stock solution weights used to generate a series of samples with 25 mM oxide	275
Table 7.7	Actual stock solution weights used to generate a series of samples with 0 mM oxide	276
Table 7.8	Displacement of Al_2Cl_7^- concentration	284
Table 7.9	Observed current obtained using normal pulse voltammetry and a 250 μm diameter tungsten electrode in a series of	

	melts with 75 mM oxide concentration	289
Table 7.10	Observed current obtained using normal pulse voltammetry and a 250 μm diameter tungsten electrode in a series of melts with 50 mM oxide concentration	290
Table 7.11	Observed current obtained using normal pulse voltammetry and a 250 μm diameter tungsten electrode in a series of melts with 25 mM oxide concentration	291
Table 7.12	Observed current obtained using normal pulse voltammetry and a 250 μm diameter tungsten electrode in a series of melts with 0 mM oxide concentration	292
Table 7.13	Melt oxide concentration and melt buffering capacity	294
Table 8.1	Experimental parameters used in square wave voltammetry study	322
Table 8.2	EG&G PAT 283 test-bed 283 potentiostat frequency response using 1 $\text{k}\Omega$ resistor and a current range of 1 nA	325
Table 8.3	EG&G PAT 283 test-bed 283 potentiostat frequency response using 1 $\text{k}\Omega$ resistor and a current range of 10 nA	326
Table 8.4	EG&G PAT 283 test-bed 283 potentiostat frequency response using 1 $\text{k}\Omega$ resistor and a current range of 100 nA	327
Table 8.5	EG&G PAT 283 test-bed 283 potentiostat frequency response using 1 $\text{k}\Omega$ resistor and a current range of 1 μA	328
Table 8.6	EG&G PAT 283 test-bed 283 potentiostat frequency response using 1 $\text{k}\Omega$ resistor and a current range of 10 μA	329
Table 8.7	Table of the RC time constants for a series of tungsten microdisk electrodes	336
Table 8.8	Square wave data from voltammograms of Cu(I)/Cu(II) using a 9 μm diameter tungsten electrode	349
Table 8.9	Square wave data from voltammograms of Cu(I)/Cu(II) using a 21 μm diameter tungsten electrode	350

LIST OF FIGURES

	Page
Figure 1.1 Distribution of anionic species in AlCl_3 :EMIC melts as a function of mole ratio of AlCl_3 to EMIC	5
Figure 1.2 Melt electrochemical windows vs. Al(III)/Al(0)	7
Figure 1.3 The effect of the AlCl_3 :EMIC melt composition on pCl at 30 °C	8
Figure 2.1 Distillation apparatus for 1-methylimidazole	21
Figure 2.2 Pressure bottle used for the EMIC synthesis	22
Figure 2.3 Stainless steel valve and transfer line assembly used for the EMIC synthesis	23
Figure 2.4 Apparatus for the purification of ethyl chloride	27
Figure 2.5 Modified Stetser-Norton gas drying bottles for dry absorbents	28
Figure 2.6 FEP tubing to glass or steel tubing connections	29
Figure 2.7 Apparatus for the removal of excess ethyl chloride	32
Figure 2.8 2 L pressure bottles for solvents	34
Figure 2.9 Apparatus for removal of organic solvents from EMIC	37
Figure 2.10 Heavy walled bomb tube used to purify AlCl_3	40
Figure 2.11 High vacuum stopcock used for AlCl_3 purification	41
Figure 2.12 Schematic of the apparatus used for proton and oxide removal	48
Figure 2.13 Custom rotating disk electrode holder	55
Figure 2.14 Reference electrode	56
Figure 3.1 Sealed UV-vis cell used for acetylferrocene measurements	65
Figure 3.2 Cyclic staircase voltammogram of acetylferrocene in a sodium chloride neutral buffered melt	69

Figure 3.3 RDE voltammograms of acetylferrocene in a NaCl neutral neutral buffered melt $[\text{Na}^+] = 80 \text{ mM}$. Rotation rate 2000 rpm	70
Figure 3.4 Limiting currents of each species against $\omega^{1/2}$ for melt containing 120 mM acetylferrocene	71
Figure 3.5 Plot of RDE I_{lim} at 2000 rpm against total acetylferrocene concentration	73
Figure 3.6 Scheme for chemical and electrochemical reactions of acetylferrocene in the melts	75
Figure 3.7 UV-vis spectra of acetylferrocene in a sodium chloride buffered melt. The Na^+ concentration equals 80 mM	78
Figure 3.8 Plot of absorbance at 580 nm vs. acetylferrocene concentration in a 0.05 cm path length cell	79
Figure 3.9 ^1H NMR chemical shift (ppm) of the DMA methyl hydrogen vs. DMA concentration divided by initial sodium cation	82
Figure 3.10 ^1H NMR shift (ppm) of dimethylaniline (DMA) methyl methyl hydrogen vs. $([\text{DMA}]_t - [\text{Na}^+])/[\text{DMA}]_t$	84
Figure 4.1 ^{31}P chemical shift of TEPO dissolved in N-butylpyridinium chloride and 1-ethyl-3-methylimidazolium chloride based chloroaluminate ionic liquids	92
Figure 4.2 Typical ^{31}P NMR spectrum. This spectrum is of TEPO dissolved in a LiCl neutral buffered melt	99
Figure 4.3 Coaxial tube configuration for volume magnetic susceptibility (χ_v) measurements	100
Figure 4.4 ^{31}P NMR chemical shift dependence of triethylphosphine oxide upon the concentration of triethylphosphine oxide in the melt	109
Figure 4.5 Volume magnetic susceptibility (χ_v) of LiCl neutral buffered $\text{AlCl}_3/\text{EMIC}$ ionic liquid	111
Figure 4.6 Alkali metal cation concentration determined using ICP vs. the mole ratio of AlCl_3 to EMIC prior to buffering	116
Figure 4.7 Dependence of the Gutmann acceptor number for binary melts upon the mole ratio of AlCl_3 to EMIC	119

Figure 4.8 Dependence of the Gutmann acceptor number for alkali metal chloride neutral buffered melts upon the mole ratio of AlCl_3 to EMIC	121
Figure 4.9 Dependence of the Gutmann acceptor number upon the mole fraction of alkali metal tetrachloroaluminate present in the ionic liquid	125
Figure 4.10 ^{31}P NMR spectrum of melt containing oxide and hydroxide. Sample was prepared by adding water to a melt containing TEPO	128
Figure 5.1 Absolute viscosity (cP) vs. the mole ratio of AlCl_3 to EMIC at 25 °C.	133
Figure 5.2 Structure and numbering of the positions of 1-ethyl-3-methylimidazolium chloride (EMIC)	134
Figure 5.3 ^1H NMR chemical shift (δ) dependence of H-2 hydrogen upon mole ratio of AlCl_3 :EMIC in the melts	136
Figure 5.4 Wilkes proposed model of alternating oligomeric chains in the melts proposed to explain the ^1H NMR data	137
Figure 5.5 Stacks of EMI^+ ions in the crystalline EMIC obtained using X-ray crystallography	139
Figure 5.6 Chloride hydrogen bonding to three EMI^+ cations in EMIC crystal	141
Figure 5.7 EMI^+ cation hydrogen bonding to three chloride anions in crystalline EMIC	142
Figure 5.8 Depiction of a steady-state NOE difference measurement	144
Figure 5.9 Energy level diagram to describe NOE	146
Figure 5.10 Maximum observable steady-state NOE vs. the molecular correlation time and spectrometer frequency	148
Figure 5.11 NOESY and ROESY pulse sequences	150
Figure 5.12 Maximum observable transient NOE vs. the molecular correlation time and spectrometer frequency	152

Figure 5.13 Maximum observable transient NOE using a spin locking experiment vs the molecular correlation time and the spectrometer frequency	153
Figure 5.14 Ratio of the cross relaxation rates of the NOESY and ROESY pulse sequences	154
Figure 5.15 Wilmad coaxial NMR tubes which were utilized to acquire ROESY spectra	157
Figure 5.16 ^1H NMR spectrum of 0.5:1.0 EMIC/ AlCl_3 melt	160
Figure 5.17 ^1H NMR inversion recovery experiment for H-6.	162
Figure 5.18 ^1H NMR inversion recovery experiment for H-6. Data is plotted according to Equation 5.6	163
Figure 5.19 ^1H NMR spin refocusing experiment for H-7	166
Figure 5.20 ^1H NMR spin refocusing experiment for H-7. Data is plotted according to Equation 5.8	167
Figure 5.21 Plot of T_1 and T_2 vs. $\omega_0 \tau_c$	175
Figure 5.22 500 MHz ^1H NMR ROESY (spin locking time 50 msec) spectrum of 0.5:1.0 melt at 25 °C.	178
Figure 5.23 500 MHz ^1H NMR ROESY (spin locking time 100 msec) spectrum of 0.5:1.0 melt at 25 °C.	179
Figure 5.24 500 MHz ^1H NMR ROESY (spin locking time 150 msec) spectrum of 0.5:1.0 melt at 25 °C.	180
Figure 5.25 500 MHz ^1H NMR ROESY (spin locking time 200 msec) spectrum of 0.5:1.0 melt at 25 °C.	181
Figure 5.26 500 MHz ^1H NMR ROESY (spin locking time 250 msec) spectrum of 0.5:1.0 melt at 25 °C.	182
Figure 5.27 500 MHz ^1H NMR ROESY (spin locking time 300 msec) spectrum of 0.5:1.0 melt at 25 °C.	183
Figure 5.28 500 MHz ^1H NMR ROESY (spin locking time 350 msec) spectrum of 0.5:1.0 melt at 25 °C.	184
Figure 5.29 500 MHz ^1H NMR ROESY (spin locking time 400 msec) spectrum of 0.5:1.0 melt at 25 °C.	185

Figure 5.30 500 MHz ^1H NMR ROESY (spin locking time 500 msec) spectrum of 0.5:1.0 melt at 25 °C.	186
Figure 5.31 500 MHz ^1H NMR ROESY (spin locking time 50 msec) spectrum of a 95% perdeuterated 0.5:1.0 melt at 25 °C.	187
Figure 5.32 500 MHz ^1H NMR ROESY (spin locking time 200 msec) spectrum of 0.5:1.0 melt at 40 °C.	188
Figure 5.33 500 MHz ^1H NMR ROESY (spin locking time 300 msec) spectrum of 0.5:1.0 melt at 40 °C.	189
Figure 5.34 500 MHz ^1H NMR ROESY (spin locking time 200 msec) spectrum of 0.99:1.0 melt at 25 °C.	190
Figure 5.35 500 MHz ^1H NMR ROESY (spin locking time 400 msec) spectrum of 0.99:1.0 melt at 25 °C.	191
Figure 6.1 Sealed electrochemical cell used for Cu(I)/Cu(II) electron transfer parameter measurements	208
Figure 6.2 Normal pulse voltammograms of Cu(I)/Cu(II) in a 1.5:1.0 melt using a 9 μm diameter tungsten electrode	214
Figure 6.3 Normal pulse voltammograms of Cu(I)/Cu(II) in a 1.5:1.0 melt using a 25 μm diameter tungsten electrode	215
Figure 6.4 Normal pulse voltammograms of Cu(I)/Cu(II) in a 1.5:1.0 melt using a 9 μm diameter tungsten electrode	216
Figure 6.5 Limiting current of normal pulse voltammograms vs. $1/\sqrt{t_p}$ for Cu(I)/Cu(II) in a 1.5:1.0 melt using a 25 μm diameter tungsten electrode	217
Figure 6.6 Square wave voltammograms of Cu(I)/Cu(II) in a 1.5:1.0 melt using a 9 μm diameter tungsten electrode	219
Figure 6.7 Square wave voltammograms of Cu(I)/Cu(II) in a 1.5:1.0 melt using a 25 μm diameter tungsten electrode	220
Figure 6.8 $E_{1/2}$ vs. square wave frequency from voltammograms of Cu(I)/Cu(II) in a 1.5:1.0 melt using a 9 μm diameter tungsten electrode. Data obtained using quasi-reversible fits of the experimental data, between 1.7 and 2.2 V, from the COOL algorithm	221

Figure 6.9 $E_{1/2}$ vs. square wave frequency from voltammograms of Cu(I)/Cu(II) in a 1.5:1.0 melt using a 9 μm diameter tungsten electrode. Data obtained using quasi-reversible fits of the experimental data, between 1.8 and 2.1 V, from the COOL algorithm	222
Figure 6.10 $E_{1/2}$ vs. square wave frequency from voltammograms of Cu(I)/Cu(II) in a 1.5:1.0 melt using a 25 μm diameter tungsten electrode. Data obtained using quasi-reversible fits of the experimental data, between 1.7 and 2.2 V, from the COOL algorithm	223
Figure 6.11 $E_{1/2}$ vs. square wave frequency from voltammograms of Cu(I)/Cu(II) in a 1.5:1.0 melt using a 25 μm diameter tungsten electrode. Data obtained using quasi-reversible fits of the experimental data, between 1.8 and 2.1 V, from the COOL algorithm	224
Figure 6.12 β vs. square wave frequency from voltammograms of Cu(I)/Cu(II) in a 1.5:1.0 melt using a 9 μm diameter tungsten electrode. Data obtained using quasi-reversible fits of the experimental data, between 1.7 and 2.2 V, from the COOL algorithm	225
Figure 6.13 β vs. square wave frequency from voltammograms of Cu(I)/Cu(II) in a 1.5:1.0 melt using a 9 μm diameter tungsten electrode. Data obtained using quasi-reversible fits of the experimental data, between 1.8 and 2.1 V, from the COOL algorithm	226
Figure 6.14 β vs. square wave frequency from voltammograms of Cu(I)/Cu(II) in a 1.5:1.0 melt using a 25 μm diameter tungsten electrode. Data obtained using quasi-reversible fits of the experimental data, between 1.7 and 2.2 V, from the COOL algorithm	227
Figure 6.15 β vs. square wave frequency from voltammograms of Cu(I)/Cu(II) in a 1.5:1.0 melt using a 25 μm diameter tungsten electrode. Data obtained using quasi-reversible fits of the experimental data, between 1.8 and 2.1 V, from the COOL algorithm	228

Figure 6.16 Slope vs $1/\sqrt{t_p}$ vs. square wave frequency from voltammograms of Cu(I)/Cu(II) in a 1.5:1.0 melt using a 9 μm diameter tungsten electrode. Data obtained using quasi-reversible fits of the experimental data, between 1.7 and 2.2 V, from the COOL algorithm	229
Figure 6.17 Slope vs $1/\sqrt{t_p}$ vs. square wave frequency from voltammograms of Cu(I)/Cu(II) in a 1.5:1.0 melt using a 9 μm diameter tungsten electrode. Data obtained using quasi-reversible fits of the experimental data, between 1.8 and 2.1 V, from the COOL algorithm	230
Figure 6.18 Slope vs $1/\sqrt{t_p}$ vs. square wave frequency from voltammograms of Cu(I)/Cu(II) in a 1.5:1.0 melt using a 25 μm diameter tungsten electrode. Data obtained using quasi-reversible fits of the experimental data, between 1.7 and 2.2 V, from the COOL algorithm	231
Figure 6.19 Slope vs $1/\sqrt{t_p}$ vs. square wave frequency from voltammograms of Cu(I)/Cu(II) in a 1.5:1.0 melt using a 25 μm diameter tungsten electrode. Data obtained using quasi-reversible fits of the experimental data, between 1.8 and 2.1 V, from the COOL algorithm	232
Figure 6.20 $\kappa \times \sqrt{t_p}$ vs $\sqrt{t_p}$ vs. square wave frequency from voltammograms of Cu(I)/Cu(II) in a 1.5:1.0 melt using a 9 μm diameter tungsten electrode. Data obtained using quasi-reversible fits of the experimental data, between 1.7 and 2.2 V, from the COOL algorithm	233
Figure 6.21 $\kappa \times \sqrt{t_p}$ vs $\sqrt{t_p}$ vs. square wave frequency from voltammograms of Cu(I)/Cu(II) in a 1.5:1.0 melt using a 9 μm diameter tungsten electrode. Data obtained using quasi-reversible fits of the experimental data, between 1.8 and 2.1 V, from the COOL algorithm	234
Figure 6.22 $\kappa \times \sqrt{t_p}$ vs $\sqrt{t_p}$ vs. square wave frequency from voltammograms of Cu(I)/Cu(II) in a 1.5:1.0 melt using a 25 μm diameter tungsten electrode. Data obtained using quasi-reversible fits of the experimental data, between 1.7 and 2.2 V, from the COOL algorithm	235

Figure 6.23 $\kappa \times \sqrt{tp}$ vs \sqrt{tp} vs. square wave frequency from voltammograms of Cu(I)/Cu(II) in a 1.5:1.0 melt using a 25 μm diameter tungsten electrode. Data obtained using quasi-reversible fits of the experimental data, between 1.8 and 2.1 V, from the COOL algorithm	236
Figure 6.24 Comparison of the net square wave currents from the 9 μm and 25 μm diameter tungsten electrodes for 19.6 mM Cu(I) in a 1.5:1.0 melt. The net current from the 9 μm diameter electrode has been multiplied by 6.25 to correct for the difference in area between the two electrodes	246
Figure 7.1 Plot of the integrated intensities of the ^{17}O NMR peaks present in acidic melts in the absence of proton vs. melt composition	258
Figure 7.2 Structures of species with the stoichiometry indicated by the models proposed by Zawodzinski	260
Figure 7.3 Experimental flow chart for the generation of proton free melts with known composition and oxide concentration	267
Figure 7.4 Titration of initial melt using AlCl_3 . AlCl_3 is added and either the Cl^- oxidation or the aluminum deposition is monitored	268
Figure 7.5 Electrochemical window present in oxide buffered melts	272
Figure 7.6 Observed current obtained using normal pulse voltammograms and a 250 μm diameter tungsten electrode vs. Al_2Cl_7^- concentration in a series of melts with 75 mM oxide concentration	278
Figure 7.7 Observed current obtained using normal pulse voltammograms and a 250 μm diameter tungsten electrode vs. Al_2Cl_7^- concentration in a series of melts with 50 mM oxide concentration	279
Figure 7.8 Observed current obtained using normal pulse voltammograms and a 250 μm diameter tungsten electrode vs. Al_2Cl_7^- concentration in a series of melts with 25 mM oxide concentration	280

Figure 7.9 Observed current obtained using normal pulse voltammograms and a 250 μm diameter tungsten electrode vs. Al_2Cl_7^- concentration in a series of melts with no oxide	281
Figure 7.10 Plot of displacement of Al_2Cl_7^- concentration for Figures 7.6 to 7.9 against oxide concentration	283
Figure 7.11 Observed current obtained using normal pulse voltammograms and a 250 μm diameter tungsten electrode vs. Al_2Cl_7^- concentration in a series of melts with 75 mM oxide concentration. Al_2Cl_7^- concentration has been adjusted to remove X axis offset	285
Figure 7.12 Observed current obtained using normal pulse voltammograms and a 250 μm diameter tungsten electrode vs. Al_2Cl_7^- concentration in a series of melts with 50 mM oxide concentration. Al_2Cl_7^- concentration has been adjusted to remove X axis offset	286
Figure 7.13 Observed current obtained using normal pulse voltammograms and a 250 μm diameter tungsten electrode vs. Al_2Cl_7^- concentration in a series of melts with 25 mM oxide concentration. Al_2Cl_7^- concentration has been adjusted to remove X axis offset	287
Figure 7.14 Observed current obtained using normal pulse voltammograms and a 250 μm diameter tungsten electrode vs. Al_2Cl_7^- concentration in a series of melts with no oxide. Al_2Cl_7^- concentration has been adjusted to remove X axis offset	288
Figure 7.15 Melt buffering capacity against the oxide concentration determined from Figures 7.11 to 7.14	293
Figure 7.16 ^{17}O NMR spectrum of melt containing 75 mM oxide at 85 $^\circ\text{C}$. This sample contains 75 mM Al_2Cl_7^- using the original stock solution compositions and 93 mM Al_2Cl_7^- using the modified stock solution compositions	296

Figure 7.17 ^{17}O NMR spectrum of melt containing 75 mM oxide at 85 °C. This sample contains 55 mM Al_2Cl_7^- using the original stock solution compositions and 74 mM Al_2Cl_7^- using the modified stock solution compositions	297
Figure 7.18 ^{17}O NMR spectrum of melt containing 75 mM oxide at 85 °C. This sample contains 45 mM Al_2Cl_7^- using the original stock solution compositions and 64 mM Al_2Cl_7^- using the modified stock solution compositions	298
Figure 7.19 ^{17}O NMR spectrum of melt containing 75 mM oxide at 85 °C. This sample contains 25 mM Al_2Cl_7^- using the original stock solution compositions and 44 mM Al_2Cl_7^- using the modified stock solution compositions	299
Figure 7.20 ^{17}O NMR spectrum of melt containing 75 mM oxide at 85 °C. This sample contains 15 mM Al_2Cl_7^- using the original stock solution compositions and 34 mM Al_2Cl_7^- using the modified stock solution compositions	300
Figure 7.21 ^{17}O NMR spectrum of melt containing 75 mM oxide at 85 °C. This sample contains 0 mM Al_2Cl_7^- using the original stock solution compositions and 19 mM Al_2Cl_7^- using the modified stock solution compositions	301
Figure 7.22 ^{17}O NMR spectrum of melt containing 75 mM oxide at 85 °C. This sample contains 5 mM Cl^- using the original stock solution compositions and 14 mM Al_2Cl_7^- using the modified stock solution compositions	302
Figure 7.23 ^{17}O NMR spectrum of melt containing 75 mM oxide at 85 °C. This sample contains 15 mM Cl^- using the original stock solution compositions and 4 mM Al_2Cl_7^- using the modified stock solution compositions	303
Figure 7.24 ^{17}O NMR spectrum of melt containing 75 mM oxide at 85 °C. This sample contains 25 mM Cl^- using the original stock solution compositions and 5 mM Cl^- using the modified stock solution compositions	304

Figure 7.25 ^{17}O NMR spectrum of melt containing 75 mM oxide at 85 °C. This sample contains 44 mM Cl^- using the original stock solution compositions and 24 mM Cl^- using the modified stock solution compositions	305
Figure 8.1 Experimental setup to determine the frequency response of the EG&G PAR 283 test-bed potentiostat	317
Figure 8.2 Experimental setup to determine the RC time constant of the tungsten microdisk electrodes	319
Figure 8.3 Sealed electrochemical cell used for the Cu(I)/Cu(II) square wave measurements in a 1.5:1.0 melt	321
Figure 8.4 Bode plot generated from the data in Tables 8.2 to 8.6	330
Figure 8.5 Plot of the 3 dB attenuation of a sinusoidal signal at each current range as a function of the signal frequency	332
Figure 8.6 Depiction of a typical RC time constant experiment	334
Figure 8.7 Plot of the RC time constant of a series of tungsten microdisk electrodes vs. the electrode diameter	335
Figure 8.8 $E_{1/2}$ vs. square wave frequency from voltammograms of Cu(I)/Cu(II) in a 1.5:1.0 melt using a 9 μm diameter tungsten electrode	341
Figure 8.9 β vs. square wave frequency from voltammograms of Cu(I)/Cu(II) in a 1.5:1.0 melt using a 9 μm diameter tungsten electrode	342
Figure 8.10 Slope vs $1/\sqrt{t_p}$ from voltammograms of Cu(I)/Cu(II) in a 1.5:1.0 melt using a 9 μm diameter tungsten electrode	343
Figure 8.11 κ vs. square wave frequency from voltammograms of Cu(I)/Cu(II) in a 1.5:1.0 melt using a 9 μm diameter tungsten electrode	344
Figure 8.12 $E_{1/2}$ vs. square wave frequency from voltammograms of Cu(I)/Cu(II) in a 1.5:1.0 melt using a 21 μm diameter tungsten electrode	345

Figure 8.13 β vs. square wave frequency from voltammograms of Cu(I)/Cu(II) in a 1.5:1.0 melt using a 21 μm diameter tungsten electrode	346
Figure 8.14 Slope vs $1/\text{sqrt}(t_p)$ from voltammograms of Cu(I)/Cu(II) in a 1.5:1.0 melt using a 21 μm diameter tungsten electrode	347
Figure 8.15 κ vs. square wave frequency from voltammograms of Cu(I)/Cu(II) in a 1.5:1.0 melt using a 21 μm diameter tungsten electrode	348
Figure 8.16 $E_{1/2}$ vs. square wave frequency from voltammograms of Cu(I)/Cu(II) in a 1.5:1.0 melt using a 9 μm diameter tungsten electrode. Data retained using signal to noise and Figures 8.10 and 8.14	352
Figure 8.17 β vs. square wave frequency from voltammograms of Cu(I)/Cu(II) in a 1.5:1.0 melt using a 9 μm diameter tungsten electrode. Data retained using signal to noise and Figures 8.10 and 8.14	353
Figure 8.18 Slope vs $1/\text{sqrt}(t_p)$ from voltammograms of Cu(I)/Cu(II) in a 1.5:1.0 melt using a 9 μm diameter tungsten electrode. Data retained using signal to noise and Figures 8.10 and 8.14	354
Figure 8.19 κ vs. square wave frequency from voltammograms of Cu(I)/Cu(II) in a 1.5:1.0 melt using a 9 μm diameter tungsten electrode. Data retained using signal to noise and Figures 8.10 and 8.14	355
Figure 8.20 $E_{1/2}$ vs. square wave frequency from voltammograms of Cu(I)/Cu(II) in a 1.5:1.0 melt using a 21 μm diameter tungsten electrode. Data retained using signal to noise and Figures 8.10 and 8.14	356
Figure 8.21 β vs. square wave frequency from voltammograms of Cu(I)/Cu(II) in a 1.5:1.0 melt using a 21 μm diameter tungsten electrode. Data retained using signal to noise and Figures 8.10 and 8.14	357
Figure 8.22 Slope vs $1/\text{sqrt}(t_p)$ from voltammograms of Cu(I)/Cu(II) in a 1.5:1.0 melt using a 21 μm diameter tungsten electrode. Data retained using signal to noise and Figures 8.10 and 8.14	358

Figure 8.23 κ vs. square wave frequency from voltammograms of Cu(I)/Cu(II) in a 1.5:1.0 melt using a 21 μm diameter tungsten electrode. Data retained using signal to noise and Figures 8.10 and 8.14	359
Figure AI.1 Heating block	364
Figure AI.2 Heating block insert for use with EG&G PARC 303A cell	365
Figure AI.3 Heating block insert cover for use with EG&G PARC 303A cell	366
Figure AI.4 Heating block insert for use with 2 ounce Qorpak bottle	367
Figure AI.5 Heating block insert for use with 8 ounce Qorpak bottle	368
Figure AI.6 Heating block insert for use with 1.5 ounce Qorpak bottle	369
Figure AI.7 Heating block inser for use with 7 Dram vial	370
Figure AI.8 Faraday cage left side view	371
Figure AI.9 Faraday cage front view	372
Figure AI.10 Faraday cage right side view	373
Figure AI.11 Faraday cage back view	374
Figure AII.1 Diagram of the oxide and proton removal apparatus	376

Chapter 1

Introduction to Ambient-Temperature Chloroaluminate Molten Salts

1.1 Introduction

The work presented in this thesis deals with investigations into the properties of aluminum chloride / 1-ethyl-3-methylimidazolium chloride ambient temperature chloroaluminate molten salts and their alkali metal chloride neutral buffered counterparts. Ambient-temperature chloroaluminate molten salts are an important class of non-aqueous solvents that have been used for a wide variety of chemical and electrochemical studies.¹⁻⁷ This chapter was written to provide the reader with general background information about the physical and chemical properties of these unique solvent systems. For more detailed information on the chemistry and properties of chloroaluminate molten salts the reader is referred to several reviews on this subject.¹⁻⁷

1.2 History of Ambient-Temperature Molten Salts

A variety of ambient-temperature molten salt systems exist. In recent years interest has centered on molten salts consisting of a mixture of an aluminum halide and an organic halide salt. In 1951 Hurley and Wier

demonstrated that a mixture of aluminum chloride (AlCl_3) and N-ethylpyridinium bromide (EtPyBr) was a liquid at room temperature.⁸ The eutectic mixture is composed of a 2.0:1.0 mole ratio of AlCl_3 to EtPyBr.

NOTE: Throughout this thesis, melt compositions will be referred to as mole ratios of aluminum chloride to the organic halide. For example: a 2.0:1.0 melt is a melt composed of 2 moles of (AlCl_3) to 1 mole of (EtPyBr).

The AlCl_3 :EtPyBr melts were investigated by Hurley and Wier due to their ability to electrodeposit aluminum at room temperature.⁹ A few years later Chum used the molten salt system as solvent for electrochemical studies.¹⁰ Although several investigations were conducted in AlCl_3 :EtPyBr melts, the use of these ionic liquids was very limited. The system is only liquid at room temperature at a 2:1 mole ratio and the potential window is restricted due to the ease of oxidation of the bromide ion.

In 1978 Osteryoung and coworkers found that replacing the EtPyBr with N-butylpyridinium chloride (BuPyCl) significantly improved the properties of the resulting ionic liquid.^{11,12} These systems were found to be liquid at room temperature over a composition range $\text{N}(\text{AlCl}_3) : \text{N}(\text{BuPyCl})$ of 0.75:1.00 to 2.00:1.00. In addition these melts had an improved anodic limit due to the replacement of the bromide ion with the chloride ion. AlCl_3 :BuPyCl ionic liquids were investigated as components of high energy-density batteries¹³ and also for numerous chemical and electrochemical studies.¹⁻⁴ A disadvantage of the AlCl_3 :BuPyCl melts was the relative ease of reduction of the BuPy^+ cation.¹⁴

In 1982 Wilkes and coworkers performed MNDO (Modified Neglect of Diatomic Overlap) calculations which indicated that N,N'-disubstituted imidazolium cations would be more difficult to reduce than the BuPy⁺ cation due to its higher electron affinity.¹⁵ The resulting melts were even lower melting than the BuPyCl based system. The best combination of physical properties and cation stability to reduction was found to be 1-ethyl-3-methylimidazolium chloride (EMIC).¹⁶ The AlCl₃:EMIC melts are liquid at room temperature over a composition range N(AlCl₃) : N(EMIC) of 0.40:1.00 to 2.00:1.00. In addition to being liquid at room temperature over a larger composition range than the AlCl₃:BuPyCl melts, the imidazolium cation is harder to reduce than the butylpyridinium cation. Because of these advantages, AlCl₃:EMIC melts have largely replaced AlCl₃:BuPyCl melts as the chloroaluminate ionic liquid most often studied.

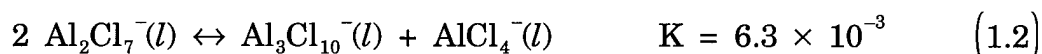
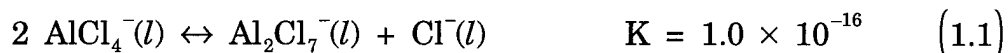
Although initial studies with room temperature molten salts centered on electrodepositing aluminum from the melts,^{8,9,17-19} these unique solvents have been investigated for use in high energy-density batteries²⁰ as well as a wide variety of both chemical and electrochemical studies.⁴⁻⁷

1.3 Chemical Properties of AlCl₃:EMIC Molten Salts

The chloroaluminate ionic liquids discussed in this thesis are mixtures of aluminum chloride (AlCl₃) and 1-ethyl-3-methylimidazolium chloride (EMIC). These two solids react over a wide range of stoichiometries to yield imidazolium

cations (EMI^+) and one or more of the following anions: Cl^- , AlCl_4^- , Al_2Cl_7^- , and $\text{Al}_3\text{Cl}_{10}^-$. The distribution of anions is dependent upon the stoichiometry of the AlCl_3 and EMIC used to prepare the room-temperature molten salt.

Melt anion composition is controlled by two equilibria, the first of which is analogous to the auto-protolysis of water.^{21,22}



In basic melts, added aluminum chloride is neutralized by reaction with the chloride anion to form the AlCl_4^- anion. As the mole ratio of the two components approaches 1.0:1.0, the Cl^- concentration drops until the melt contains only the AlCl_4^- anion. In melts containing mole ratios greater than unity, the anions AlCl_4^- , Al_2Cl_7^- , and possibly $\text{Al}_3\text{Cl}_{10}^-$ are present (Figure 1.1). At mole ratios greater than 1.0:1.0, the Al_2Cl_7^- mole fraction increases and the AlCl_4^- mole fraction decreases. However, if the mole ratio is increased to 1.6:1.0 or higher, the AlCl_4^- mole fraction continues to drop and the Al_2Cl_7^- mole fraction peaks and then declines as the $\text{Al}_3\text{Cl}_{10}^-$ mole fraction grows.²²

The melts are defined as acidic, basic, or neutral if the mole ratio of AlCl_3 to EMIC is greater than, less than, or equal to unity. In melts with mole ratios less than 1.0:1.0, the Cl^- anion is present and is a Lewis base. In melts with mole ratios greater than 1.0:1.0, the Lewis acidic anions Al_2Cl_7^- , $\text{Al}_3\text{Cl}_{10}^-$ are present. The concentrations of melt components are such that:

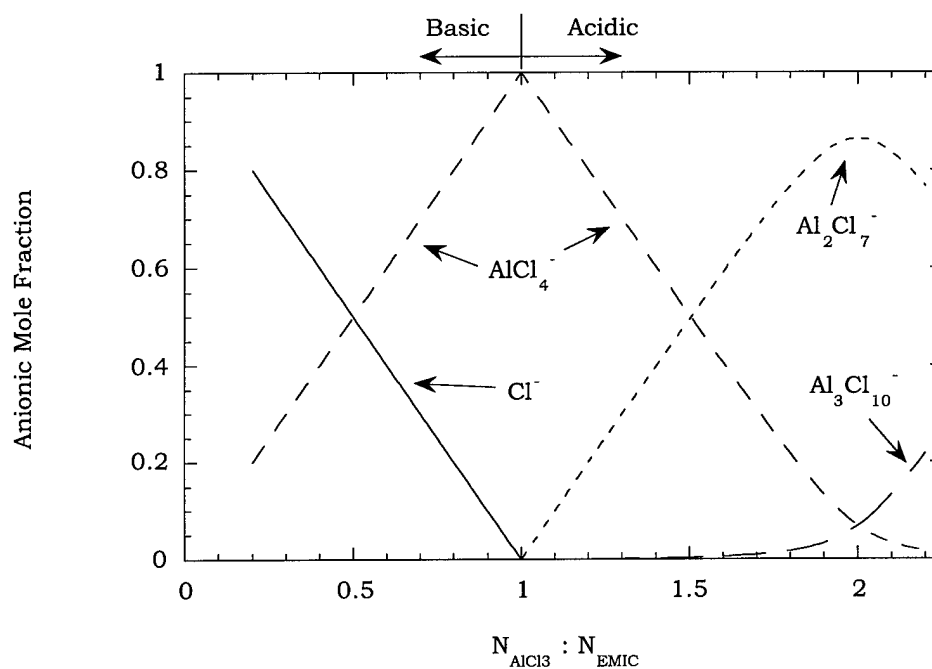


Figure 1.1 Distribution of anionic species in $\text{AlCl}_3:\text{EMIC}$ melts as a function of mole ratio of AlCl_3 to EMIC. Chloride is a Lewis base. Al_2Cl_7^- and $\text{Al}_3\text{Cl}_{10}^-$ are Lewis acids. AlCl_4^- is considered to be Lewis neutral.

$$[\text{EMI}^+] = [\text{Cl}^-] + [\text{AlCl}_4^-] + [\text{Al}_2\text{Cl}_7^-] + [\text{Al}_3\text{Cl}_{10}^-] \quad (1.3)$$

In the special case when the AlCl_3 :EMIC mole ratio equals 1.0:1.0, the only anion present is AlCl_4^- . Such a melt is termed "neutral" and is difficult to prepare. The difficulty arises due to the necessity that $N(\text{AlCl}_3) = N(\text{EMIC})$. Weighing errors or the presence of any impurities will shift the neutral melt to become acidic or basic. In a neutral melt the concentrations of the melt components are:

$$[\text{EMI}^+] = [\text{AlCl}_4^-] \quad (1.4)$$

The neutral melts have an electrochemical window over 4 V wide while the basic and acidic melts have truncated windows (Figure 1.2).

The chemistry of solutes observed in the melts is strongly affected by melt composition. This change in chemistry is due to the change in anionic speciation of the melt with composition. In most cases a base in the AlCl_3 :EMIC melts can be thought of as a chloride donor while an acid is a chloride acceptor. The dependence of the acid-base characteristics of the melts can be seen in terms of pCl, where pCl is defined as $-\log[\text{Cl}^-]$ (Figure 1.3). The dependence of pCl upon melt composition is easily seen. Melts prepared with mole ratios less than 1.0 have a small, relatively constant pCl. For melts with mole ratios approaching 1.0, the melts are not buffered and pCl changes rapidly. In melts with mole ratios greater than 1.0, pCl is large and relatively constant.

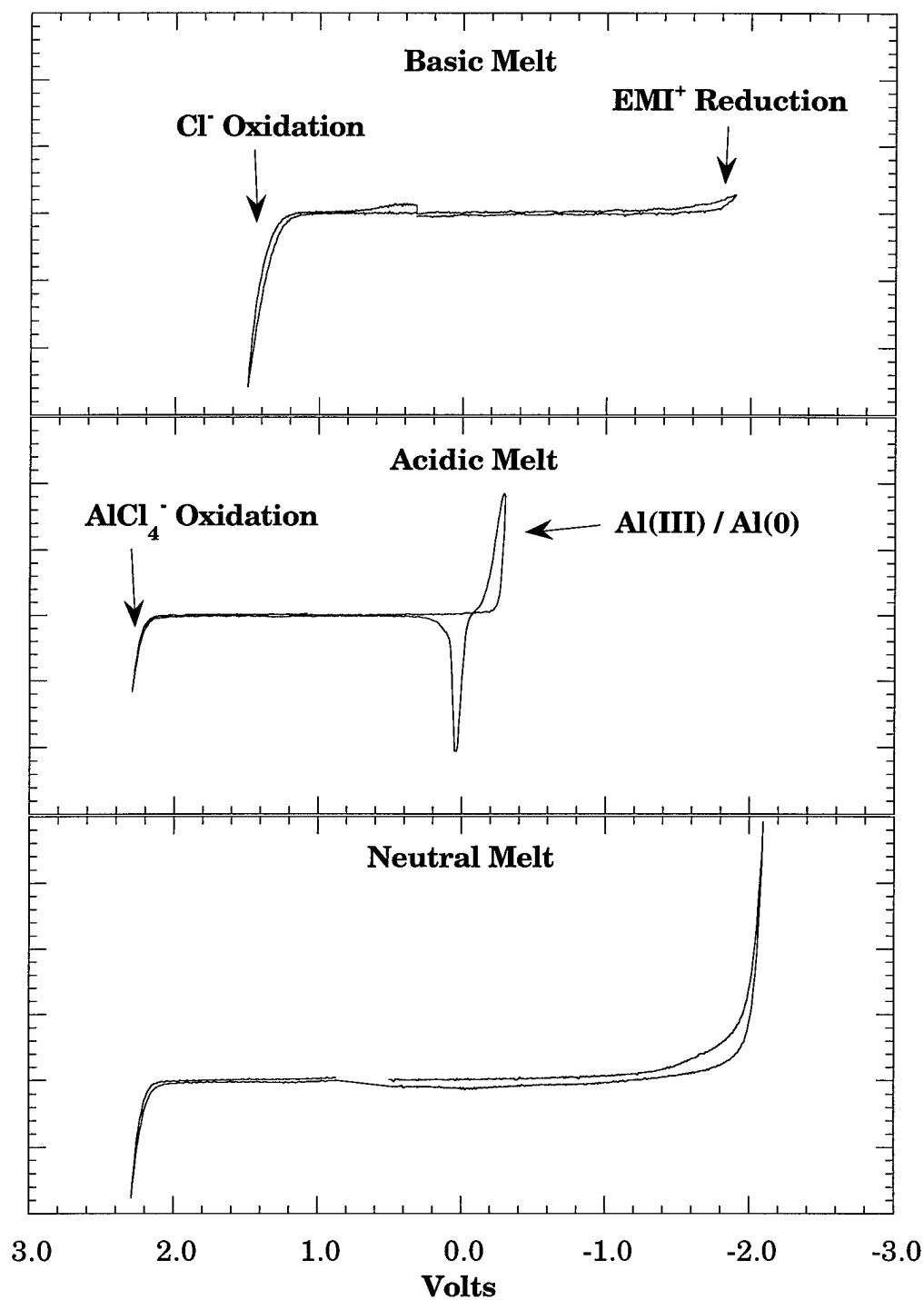


Figure 1.2 Melt electrochemical windows vs. $\text{Al(III)} / \text{Al(0)}$ (0.0V) with a glassy carbon electrode.

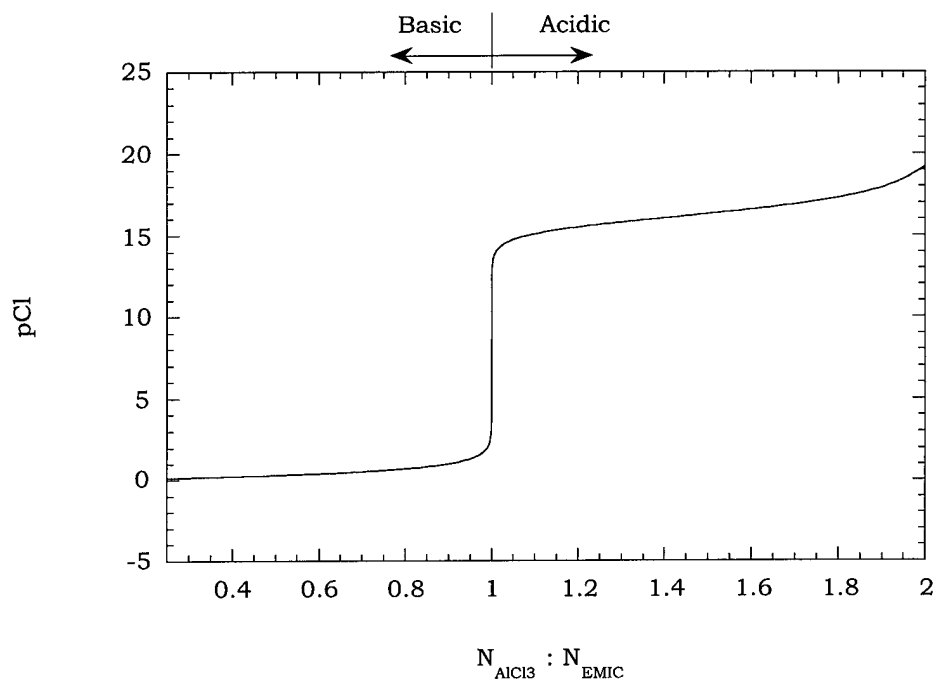


Figure 1.3 The effect of the AlCl_3 :EMIC melt composition on pCl at 30 °C.

Many studies have been conducted on the melts themselves to determine their physical properties. Several studies warrant comment; these include mass spectrometry, raman spectroscopy, and determination of the transport numbers of the melts themselves.

Mass spectrometry studies conducted in the melts have been limited due to the low vapor pressure of basic melts. In order to obtain mass spectra the samples have been subjected to fast ion bombardment (FAB). FAB mass spectrometry has been used to show the existence of $\text{Al}_3\text{Cl}_{10}^-$ in acidic melts.²³⁻²⁶ In addition, FAB mass spectrometry has been utilized to study solute species in acidic melts. $\text{M}(\text{AlCl}_4^-)_3^-$ species were detected, where M is cobalt or nickel.²⁷

Raman spectroscopy conducted with room temperature melts is the extension of work conducted in higher temperature melts.^{28,29} Al_2Cl_7^- was detected in both $\text{NaCl} / \text{AlCl}_3$ and $\text{KCl} / \text{AlCl}_3$ melts.^{28,29} Raman spectra of aluminum species present in ambient temperature melts determined that the ions AlCl_4^- and Al_2Cl_7^- were present in these melts as well.³⁰

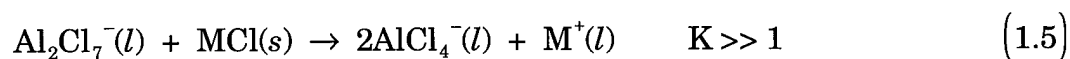
Øye and Hussey determined the transport numbers in the ambient temperature chloroaluminate ionic liquids.³¹ Knowledge of the transport number for a solvent is important because it has a significant impact upon the liquid junction potentials. There are actually two types of transport numbers, external and internal. The external transport number is a description of how current is carried relative to a porous membrane while the internal transport number is relative to chloride ion. Only the internal transport number needs to

be known in order to calculate liquid junction potentials. The transport numbers were experimentally determined to be 1.00 for the imidazolium cation internal transport number and 0.71 for the imidazolium cation external transport number.³¹ Because the internal transport number is unity for the imidazolium cation, liquid junction potentials between melts of different compositions should be negligible.

1.4 Neutral Buffered Chloroaluminate Ionic Liquids

Neutral melts, in which the principal ionic species are EMI^+ and AlCl_4^- ($[\text{EMI}^+] = [\text{AlCl}_4^-]$), may be prepared by adding exactly stoichiometric amounts of AlCl_3 to the organic chloride. The concentrations of Lewis acidic species Al_2Cl_7^- and Lewis basic species Cl^- are equal and virtually nonexistent.

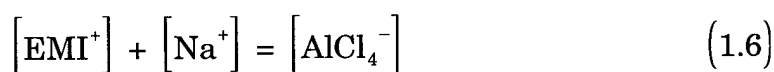
In 1990 Wilkes and coworkers first reported the preparation of neutral buffered chloroaluminate salts.²² This result is important because it simplifies the preparation of neutral melts. Neutral-buffered chloroaluminate melts are prepared by the addition of an alkali metal chloride (MCl) to an acidic melt.^{22,32,33} The following reaction takes place when MCl is added to an acidic melt:



The melt that results does not contain Al_2Cl_7^- , so it is no longer described as acidic; instead it contains only the AlCl_4^- anion making the melt neutral. The

electrochemical window of these neutral buffered melts is essentially the same as that of the neutral unbuffered melts.³⁴ The melts are considered buffered because if a strongly acidic species is added, MCl, which is virtually insoluble in a neutral melt, dissolves and reacts to bring the melt back to neutrality. If a strong basic species is added to the melt, the dissolved M^+ reacts to form MCl which is insoluble in a neutral melt and precipitates out of the solution.

The buffering mechanism alters the composition of the melt such that:



This subtle change in the cationic species in neutral buffered melts has a large effect on the chemical properties of the melt. Quarmby and Osteryoung observed that neutral buffered melts exhibit a "latent acidity," generating $AlCl_3$ adducts when a weak Lewis base is added to the melt.³⁵ In unbuffered neutral melts no adduct formation occurs. Semi-quantitative results from cyclic voltammetric experiments suggested that speciation of weak Lewis bases in the buffered melts was controlled by the equilibrium:



where B: is a weak Lewis base.

It should be noted the buffered melts actually are a ternary $AlCl_3$:EMIC:MCl molten salt system which increases the complexity with respect to the binary melts.

Chapter 1 References

- (1) Chum, H. L.; Osteryoung, R. A. In *Ionic Liquids*; Inman, D; Lovering, D. G., Ed.; Plenum Press: New York, 1981; pp 407-423.
- (2) Gale, R. J.; Osteryoung, R. A. In *Molten Salt Techniques*; Lovering, D. G.; Gale R. J.; Eds.; Plenum Press: New York, 1983; Vol. 1, pp 55-78.
- (3) Hussey C. L. In *Advances in Molten Salt Chemistry*; Mamantov, G.; Eds.; Elsevier: New York, 1983, Vol. 5, pp. 185-230.
- (4) Osteryoung, R. A. In *Molten Salt Chemistry*; Mamantov, G.; Marassi, R., Eds.; D. Reidel Publishing: New York, 1987; pp 329-364.
- (5) Wilkes J. S. In *Molten Salt Chemistry*; Mamantov, G.; Marassi, R., Eds.; D. Reidel Publishing: New York, 1987; pp 217-236.
- (6) Hussey, C. L. "Room Temperature Haloaluminate Ionic Liquids. Novel Solvents for Transition Metal Solution Chemistry." *Pure Appl. Chem.* **1988**, *60*, 1763-1772.
- (7) Mamantov, G.; Hussey, C. L.; Marassi, R. In *Techniques for Characterization of Electrodes and Electrochemical Processes*; Varma, R.; Selman, J. R., Eds.; Wiley: New York, 1991; pp 471-513.

- (8) Hurley, F. H.; Wier, T. P. "Electrodeposition of Metals from Fused Quaternary Ammonium Salts." *J. Electrochem. Soc.* **1951**, *98*, 203-206.
- (9) Hurley F. H.; Wier, T. P. "The Electrodeposition of Aluminum from Nonaqueous Solutions at Room Temperature." *J. Electrochem. Soc.* **1951**, *98*, 207-212.
- (10) Chum, H. L.; Koch, V. R.; Miller, L. L.; Osteryoung, R. A. "An Electrochemical Scrutiny of Organometallic Iron Complexes and Hexamethylbenzene in a Room Temperature Molten Salt." *J. Am. Chem. Soc.* **1975**, *97*, 3264-3265.
- (11) Gale, R. J.; Gilbert, B.; Osteryoung, R. A. "Raman Spectra of Molten Aluminum Chloride: 1-Butylpyridinium Chloride Systems at Ambient Temperatures." *Inorg. Chem.* **1978**, *17*, 2728-2729.
- (12) Robinson, J.; Osteryoung, R. A. "An Electrochemical and Spectroscopic Study of Some Aromatic Hydrocarbons in the Room Temperature Molten Salt System Aluminum Chloride-n-Butylpyridinium Chloride." *J. Am. Chem. Soc.* **1979**, *101*, 323-327.
- (13) Carpio, R. A.; King, L. A.; Lindstrom, R. E.; Nardi, C. L.; Hussey, C. L. "Density, Electric Conductivity, and Viscosity of Several N-Alkylpyridinium

Halides and Their Mixtures with Aluminum Chloride." *J. Electrochem. Soc.* **1979**, *126*, 1644-1650.

(14) Gale, R. J.; Osteryoung, R. A. "Potentiometric Investigation of Dialuminum Heptachloride Formation in Aluminum Chloride-1-Butylpyridinium Chloride Mixtures." *Inorg. Chem.* **1979**, *18*, 1603-1605.

(15) Wilkes, J. S.; Levisky, J. A.; Wilson, R. A.; Hussey, C. L. "Dialkylimidazolium Chloroaluminate Melts: A New Class of Room-Temperature Ionic Liquids for Electrochemistry, Spectroscopy, and Synthesis." *Inorg. Chem.* **1982**, *21*, 1263-1264.

(16) Fannin, A. A.; Floreani, D. A.; King, L. A.; Landers, J. S.; Piersma, B. J.; Stech, D. J.; Vaughn, R. L.; Williams, J. L. "Properties of 1,3-Dialkylimidazolium Chloride-Aluminum Chloride Ionic Liquids. 2. Phase Transitions, Densities, Electrical Conductivities, and Viscosities." *J. Phys. Chem.* **1984**, *88*, 2614-2621.

(17) Robinson, J.; Osteryoung, R. A. "The Electrochemical Behavior of Aluminum in the Low Temperature Molten Salt System n-Butyl Pyridinium Chloride: Aluminum Chloride and Mixtures of This Molten Salt with Benzene." *J. Electrochem. Soc.* **1980**, *127*, 122-128.

- (18) Qin, Q-X.; Skyllas-Kazacos, M. "Electrodeposition and Dissolution of Aluminium in Ambient Temperature Molten Salt System Aluminum Chloride N-Butylpyridinium Chloride." *J Electroanal. Chem.* **1984**, 168, 193-206.
- (19) Auburn, J. J.; Barberio, Y. L. "An Ambient Temperature Secondary Aluminum Electrode: Its Cycling Rates and Its Cycling Efficiencies." *J. Electrochem. Soc.* **1985**, 132, 598-601.
- (20) Vaughn, L. R. *Evaluation of Room-Temperature Chloroaluminate Molten Salts as Electrolytes for High Energy Density Batteries*; FJSRL-TR-90-0001, April 1990.
- (21) Hussey, C. L.; Scheffler, T. B.; Wilkes, J. S.; Fannin, A. A. "Chloroaluminate Equilibria in the Aluminum Chloride 1-Methyl-3-ethylimidazolium Chloride Ionic Liquid." *J. Electrochem. Soc.* **1986**, 133, 1389-1391.
- (22) Melton, T. J.; Joyce, J.; Maloy, J. T.; Boon, J. A.; Wilkes, J. S. "Electrochemical Studies of Sodium Chloride as a Lewis Buffer for Room Temperature Chloroaluminate Molten Salts." *J. Electrochem. Soc.* **1990**, 137, 3865-3869.

- (23) Frazen, G.; Gilbert, B. P.; Pelzer, G.; DePauw, E. "The Anionic Structure of Room-Temperature Organic Chloroaluminate Melts from Secondary Ion Mass Spectrometry." *Org. Mass Spectrom.* **1986**, *21*, 443-444.
- (24) Wicelinski, S. P.; Gale, R. J.; Pamidimukkala, K. M.; Laine, R. A. "Fast Atom Bombardment Mass Spectrometry of Low Temperature Chloroaluminate and Chlorogallate Melts." *Anal .Chem.* **1988**, *60*, 2228-32.
- (25) Abdul-Sada, A. K.; Greenway, A. M.; Seddon, K. R.; Welton, T. "Upon the Existence of $[\text{Al}_3\text{Cl}_{10}]^-$ in Room Temperature Chloroaluminate Ionic Liquids." *Org. Mass Spectrom.* **1989**, *24*, 917-918.
- (26) Abdul-Sada, A. K.; Greenway, A. M.; Seddon, K. R.; Welton, T. "A Fast Atom Bombardment Mass Spectrometric Study of Room-Temperature 1-Ethyl-3-methylimidazolium Chloroaluminate(III) Ionic Liquids. Evidence for the Existence of the Decachlorotrialuminate(III) Anion." *Org. Mass Spectrom.* **1993**, *28*, 759-765.
- (27) Abdul-Sada, A. K.; Greenway, A. M.; Seddon, K. R.; Welton, T. "Fast Atom Bombardment Mass Spectrometric Evidence for the Formation of Tris(tetrachloroaluminate(III)metallate(II) Anions, $[\text{M}(\text{AlCl}_4)_3]^-$, in Ambient-Temperature Ionic Liquids." *Org. Mass Spectrom.* **1992**, *27*, 648-649.

- (28) Torsi, G.; Mamantov, G.; Begun, G. M. "Raman Spectra of the AlCl_3 -NaCl System." *Inorg. Nucl. Chem. Letters* **1970**, 6, 553-560.
- (29) Øye, H. A.; Rytter, E.; Klæboe, P.; Cyvin, S. "Raman Spectra of KCl- AlCl_3 Melts and Normal Coordinate Analysis of Al_2Cl_7^- ." *J. Acta Chem. Scand.* **1971**, 25, 559-576.
- (30) Gale, R. J.; Gilbert, B.; Osteryoung, R. A. "Raman Spectra of Molten Aluminum Chloride: 1-Butylpyridinium Chloride Systems at Ambient Temperatures." *Inorg. Chem.* **1978**, 17, 2728-2729.
- (31) Hussey, C. H.; Øye, H. A. "Transport Numbers in Molten Acidic Aluminum Chloride - 1 - Methyl -3- Ethylimidazolium Chloride." *J. Electrochem. Soc.* **1984**, 131, 1621-1625.
- (32) Scordilis-Kelley, C.; Fuller, J.; Carlin, R. T.; Wilkes, J. S. "Alkali Metal Reduction Potentials Measured in Chloroaluminate Ambient-Temperature Molten Salts." *J. Electrochem. Soc.* **1992**, 139, 694-699.
- (33) Riechel, T. L.; Wilkes, J. S. "The Lewis Acidity of Room Temperature Chloroaluminate Molten Salts Buffered with Sodium Chloride." *J. Electrochem. Soc.* **1993**, 140, 3104-3107.

(34) Lipsztajn, M.; Osteryoung, R. A. "Increased Electrochemical Window in Ambient Temperature Neutral Ionic Liquids." *J. Electrochem. Soc.* **1983**, *130*, 1968-1969.

(35) Quarmby, I. C.; Osteryoung, R. A. "Latent Acidity in Buffered Chloroaluminate Ionic Liquids." *J. Am. Chem. Soc.* **1994**, *116*, 2649-2650.

Chapter 2

General Experimental

This chapter describes the materials, equipment, and procedures that are generally used for all melts throughout this thesis. Experimental procedures which are utilized in a single chapter will be described in detail within that chapter.

2.1 Materials

2.1.1 Synthesis of 1-Ethyl-3-Methylimidazolium Chloride (EMIC)

The following is a detailed description of the procedures involved in synthesizing 1-ethyl-3-methylimidazolium chloride (EMIC) from 1-methylimidazole and ethyl chloride. The following procedures are modified versions of published procedures.¹⁻³ Prior to the actual synthesis of the EMIC each of the reagents must be purified.

2.1.1.1 Purification of 1-Methylimidazole

1-Methylimidazole was purified using the procedure described below. A 2 L single neck round bottom flask was loaded with approximately 10 g of CaH_2 and an egg shaped Teflon coated stir bar. A customized still head was then

attached to the single 24/40 T joint (Figure 2.1). A heating mantle was placed under the round bottom flask, and then both the flask and heating mantle were placed on top of a magnetic stirrer. The entire apparatus was evacuated and then refilled with dry nitrogen gas a minimum of three times. While purging with dry nitrogen, the still head was detached from the round bottom flask, a funnel was inserted, and approximately 1 L of 1-methylimidazole was added to the round bottom flask while stirring. The apparatus was reassembled. Once reassembled, the entire apparatus was evacuated and refilled with dry nitrogen gas at least three times. The apparatus was slowly evacuated to ≈ 30 mtorr. Once full vacuum was reached, the round bottom flask was slowly heated to approximately 90 °C. At this temperature the 1-methylimidazole began to reflux, and was allowed to reflux for 3 hours.

A 250 mL single necked round bottom flask with a 14/20 T joint was attached to the outlet of the still, evacuated, and refilled with dry nitrogen gas at least 4 times. The recirculation valve on the still head was closed and ≈ 100 mL of 1-methylimidazole collected in the solvent reservoir. The 250 mL round bottom flask was placed under vacuum. Then the outlet valve of the still was opened, and the initial distillate was drained into the round bottom flask. The outlet valve of the still was then closed, and the 250 mL round bottom flask was refilled with dry nitrogen gas. The 250 mL round bottom flask was removed and the distillate discarded.

Next a custom-made pressure reaction bottle containing a Teflon stir bar, a stainless steel valve, and a transfer line assembly was attached to the still outlet (Figures 2.2 and 2.3). The pressure bottle was evacuated and refilled

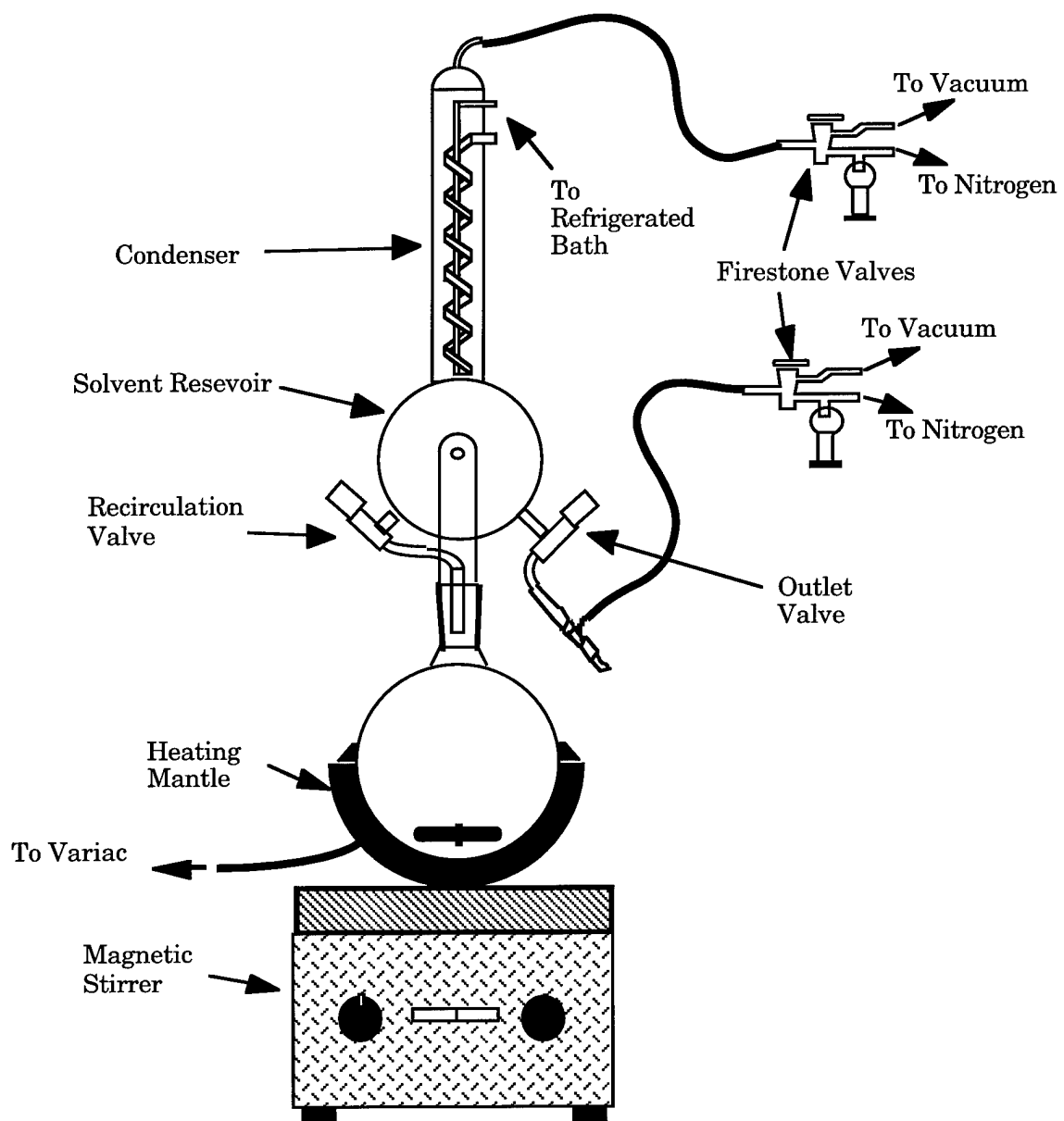


Figure 2.1 Distillation apparatus for 1-methylimidazole

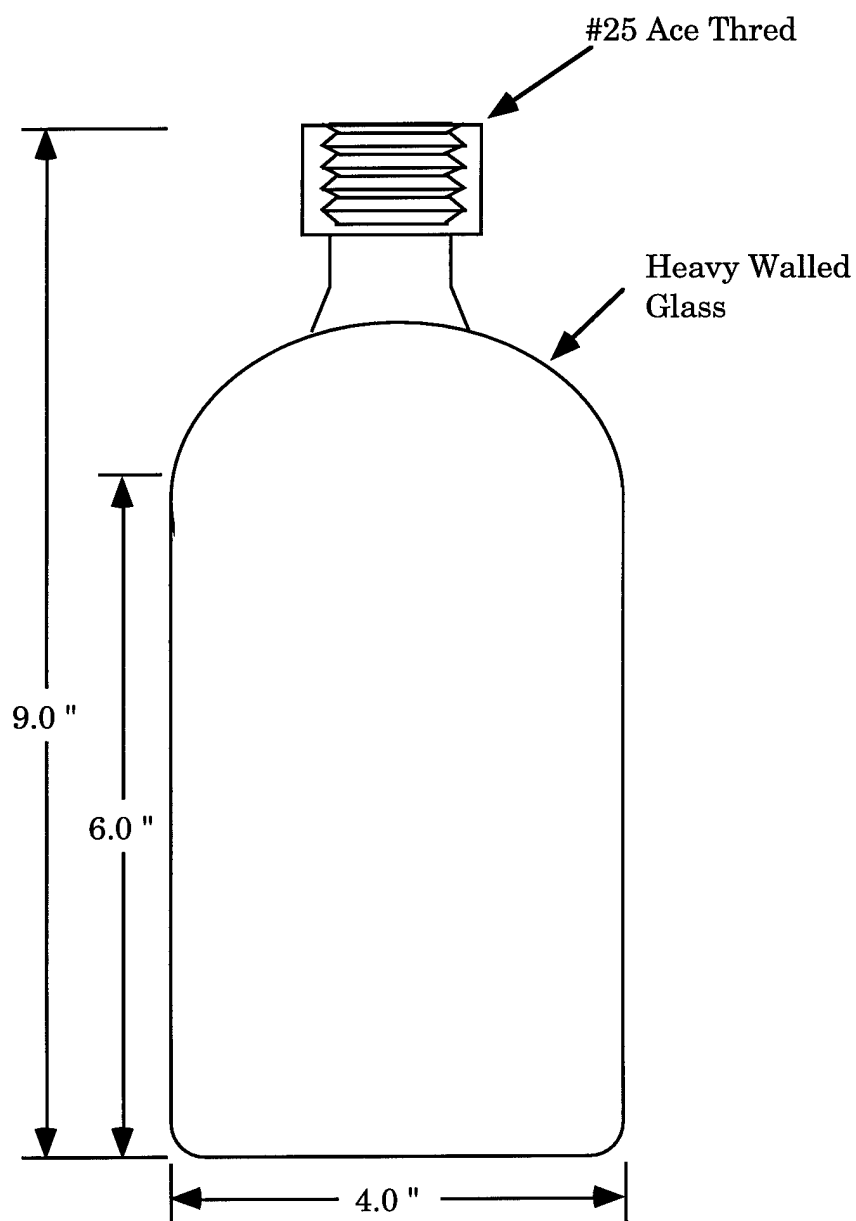


Figure 2.2 Pressure bottle used for the EMIC synthesis.

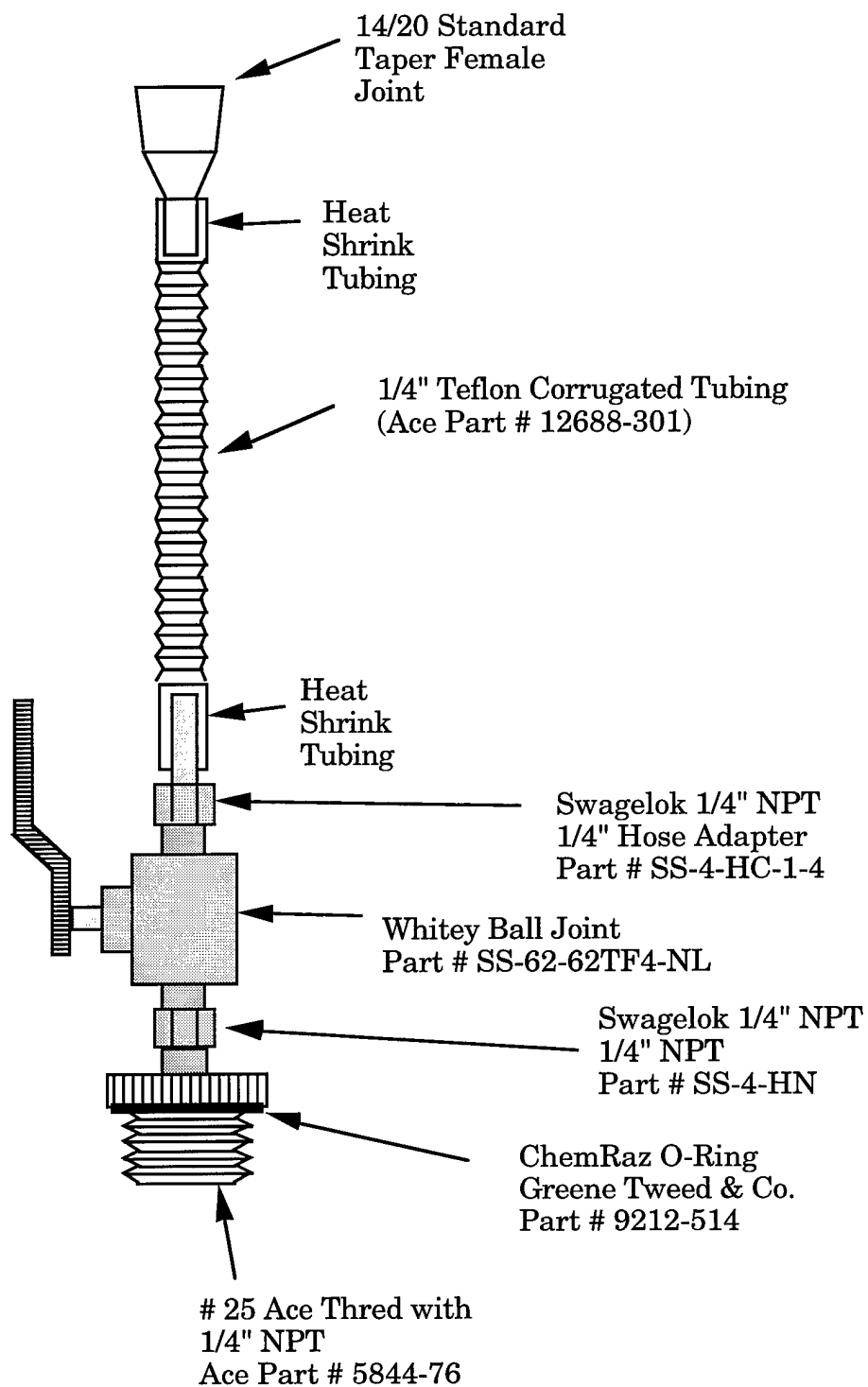


Figure 2.3 Stainless steel valve and transfer line assembly used for the EMIC synthesis.

with dry nitrogen gas at least 4 times. When 300 mL of 1-methylimidazole had distilled into the solvent reservoir, the pressure bottle was evacuated. Next the outlet valve of the still was opened, and the distillate was drained into the pressure bottle. Then the outlet valve of the still was closed. The transfer line and valve of the pressure bottle were briefly purged with dry nitrogen gas and re-evacuated. The stainless steel valve was then closed, and the pressure bottle transfer line was disconnected from the still.

In the next step, acetonitrile was distilled into the pressure bottle containing 1-methylimidazole. The acetonitrile helps solubilize the EMIC, thus allowing the reaction to approach completion before precipitation occurs.

2.1.1.2 Distillation of Acetonitrile

Acetonitrile was added to the pressure bottle which already contained purified 1-methylimidazole, so that as EMIC was formed, acetonitrile would solubilize it in the pressure bottle. This allows the reaction to go to completion. Otherwise the EMIC precipitates before all the 1-methylimidazole can react with the 1-chloroethane. Once precipitation occurs the reaction stops. The distillation of the acetonitrile is described below.

A 2 L single neck round bottom flask was loaded with approximately 10 g of CaH_2 and an egg shaped Teflon coated stir bar. A customized still head was then attached to the single 24/40 T joint (Figure 2.1). A heating mantle was placed under the round bottom flask, and then both the flask and heating mantle were placed on top of a magnetic stirrer. The entire apparatus was

evacuated and then refilled with dry nitrogen gas a minimum of three times. While purging with dry nitrogen, the still head was detached from the round bottom flask, a funnel was inserted, and approximately 1.5 L acetonitrile was added to the round bottom flask while stirring. The apparatus was reassembled. Once reassembled the apparatus was maintained under a slow purge of dry nitrogen gas. The round bottom flask was slowly heated to reflux the acetonitrile. The mixture was allowed to reflux for at least 12 hours. The recirculation valve on the still head was closed, and the solvent reservoir was allowed to fill.

The pressure bottle and valve assembly, which already contained 1-methylimidazole, was connected to the still outlet valve. The pressure bottle assembly was evacuated, the stainless steel valve was closed, and the transfer line assembly was refilled with dry nitrogen. The entire pressure bottle assembly was again placed under vacuum. This procedure was repeated at least four times. The pressure bottle assembly was left under vacuum but closed to the vacuum pump. The drain valve on the still was opened slightly, and 100 mL of acetonitrile was transferred into the pressure bottle assembly. The drain valve was closed and the transfer line and valve of the pressure bottle were briefly purged with dry nitrogen gas and re-evacuated. The stainless steel valve was then closed, and the pressure bottle transfer line was disconnected from the still.

2.1.1.3 Purification of Ethyl Chloride

Ethyl chloride was dried and condensed into the EMIC pressure reaction bottle in one step. This procedure is designed to remove water and to filter out any fine iron particulate generated by the bottle, valves, and fittings.

The apparatus used to purify the ethyl chloride is shown in Figure 2.4. It consists of two modified Stetser-Norton gas drying bottles for dry absorbents (Figure 2.5), a Drierite gas purifier containing Drierite and 5A molecular sieves (Fisher), a Dewar type condenser, and a Firestone valve. The gas washing bottles were filled with potassium hydroxide and phosphorous pentaoxide desiccant on an inert support (Fluka). The components of the apparatus were attached using 5/16" ID .030" wall FEP tubing (Nalgene 890 Teflon). The tubing was secured by first heating the glass or steel portion of the connection and then pushing the tubing onto the connection. Next, heat shrink tubing 3/8" SST (super shrink Teflon) was placed over the connection and heated. Over this layer of shrink tubing was placed another length of 1/2" SST (SPC Technology, Voltrex Brand) that was heated (Figure 2.6).

The EMIC pressure reaction assembly that had been filled with 1-methylimidazole and acetonitrile was attached to the apparatus with the stainless steel valve closed. The entire apparatus was evacuated and refilled with dry nitrogen gas at least five times using the Firestone valve. Ethyl chloride (99% Matheson) was allowed to slowly pass through the gas washing bottles and the drying cartridge. The Dewar type condenser was filled with dry ice / acetone. At this time the stainless steel valve was opened to the reaction

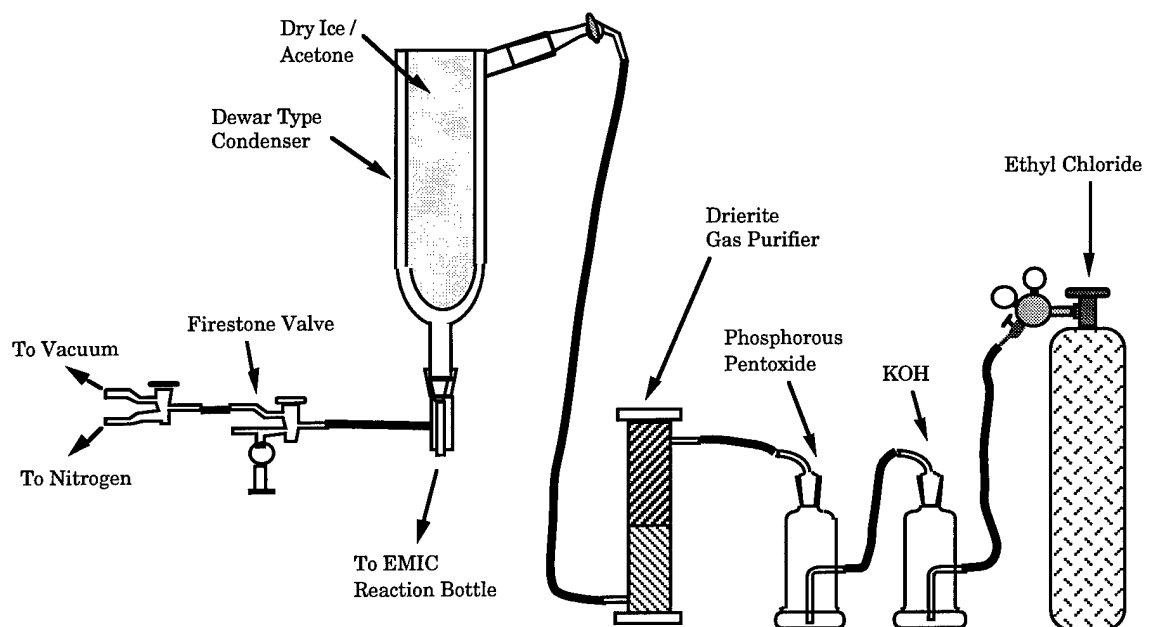


Figure 2.4 Apparatus for the purification of ethyl chloride.

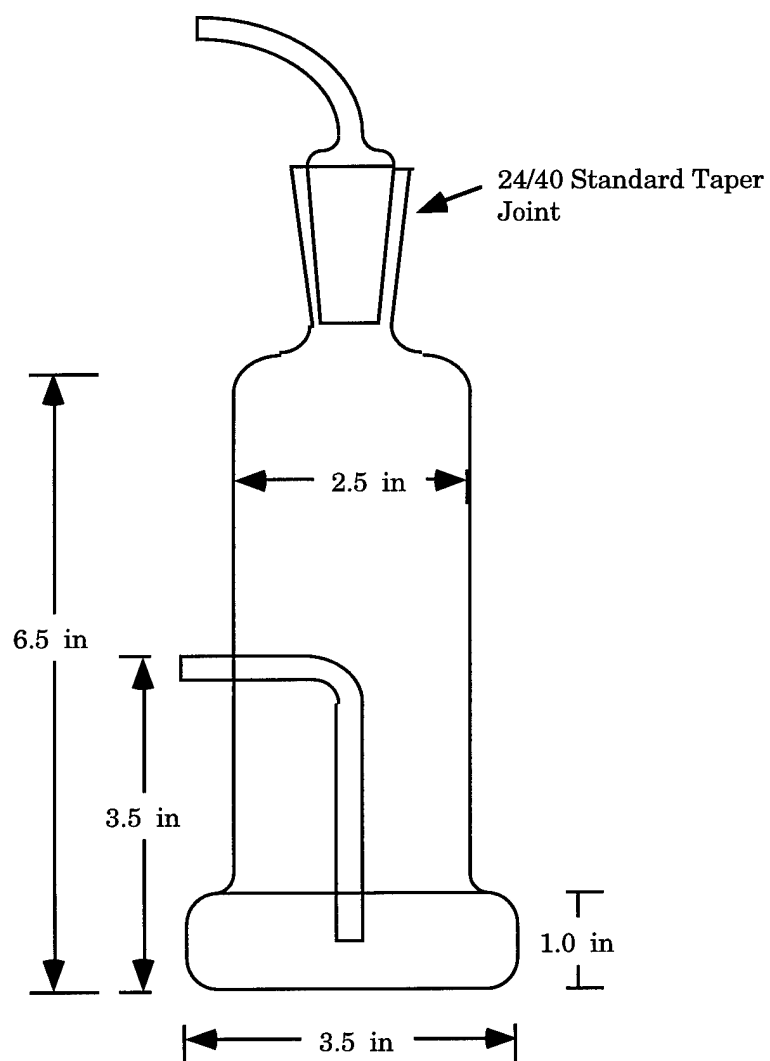


Figure 2.5 Modified Stetser-Norton gas drying bottles for dry absorbents.

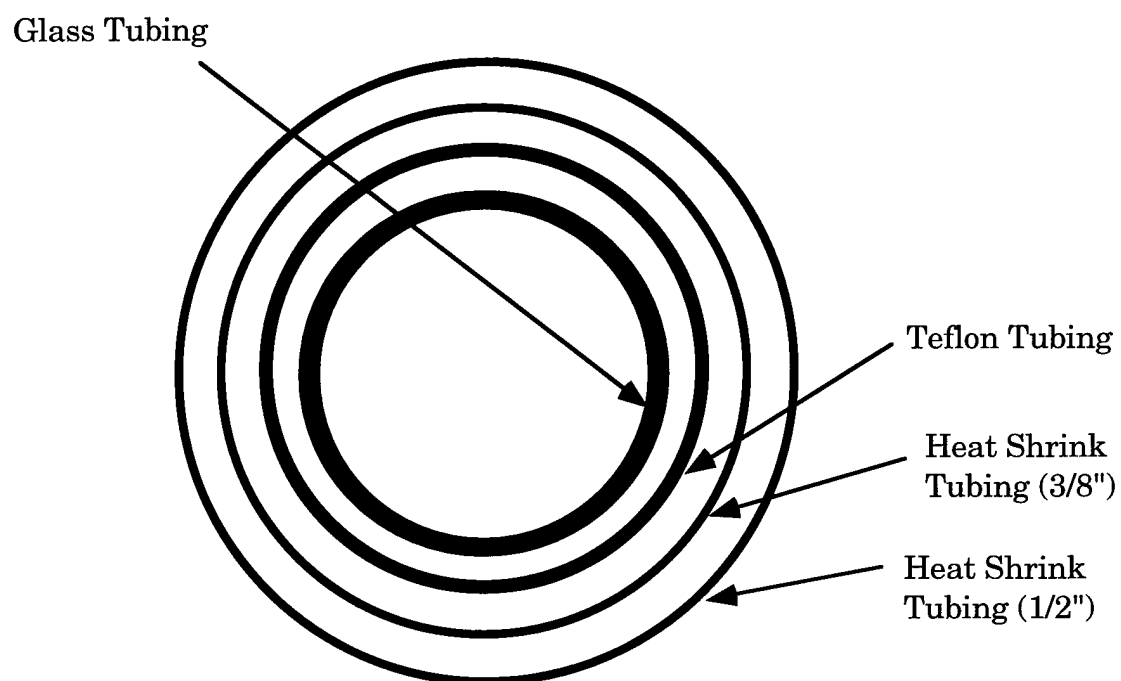


Figure 2.6 FEP tubing to glass or steel tubing connections.

bottle. As the condensed ethyl chloride dripped from the condenser it entered the reaction flask.

The flow of ethyl chloride was controlled using the valve on the ethyl chloride cylinder. The flow was maintained so that there was always a slight positive pressure of ethyl chloride on the system as indicated by the Firestone valve oil bubbler. As the ethyl chloride flowed from the gas cylinder, the cylinder cooled, and the pressure inside the cylinder decreased. In order to maintain a reasonable flow of ethyl chloride, the tank may require slight heating. If necessary, this was accomplished using a heat gun.

This process was allowed to continue until ≈ 450 mL of ethyl chloride had been transferred into the pressure bottle. About 150 mL of extra space was left in the reaction bottle when the transfer was complete in order to allow for the expansion of ethyl chloride upon warming. When the transfer was complete, the stainless steel valve was closed, and the pressure bottle was removed.

2.1.1.4 Synthesis of EMIC

The synthesis of EMIC consisted of placing the pressure bottle containing the purified 1-methylimidazole, acetonitrile, and ethyl chloride in a stainless steel bucket on top of a magnetic stirrer and stirring rapidly at room temperature. The bucket was present to minimize the safety hazard due to the pressurized glass reaction bottle. The reaction takes from 10 to 20 days. The reaction proceeded from a clear colorless two phase mixture until the EMIC

precipitated. This signifies that the reaction was complete. The reaction mixture may be purified immediately, or the reaction flask may be stored in a refrigerator until purification is performed.

2.1.1.5 Purification of Crude EMIC

The quality of the purified EMIC is largely determined by how carefully it is purified. Patience and care are required to obtain a high purity product. The crude EMIC is contaminated primarily with excess ethyl chloride and unreacted 1-methylimidazole. The purification process is broken into three steps. The first step is the removal of bulk excess ethyl chloride. The second step is precipitation of the EMIC to remove unreacted 1-methylimidazole. The third and final step is melting the EMIC under a vacuum to remove any organic solvent.

The removal of bulk excess ethyl chloride was performed outside the dry box. The pressure bottle was cooled using ice water or by refrigeration. The cooling was necessary to relieve pressure (≈ 2 atm) caused by the excess ethyl chloride. Next the pressure bottle was placed in a stainless steel bucket filled with water on a hot plate / magnetic stirrer and attached to a one-way bubbler in a laboratory hood (Figure 2.7). After the bubbler had been attached, the stainless steel valve was slowly opened. The ethyl chloride escaped through the bubbler and was vented into the hood. As the ethyl chloride escaped, the temperature of the pressure bottle dropped and the boil off rate decreased. In order to maintain a reasonable boil off rate, the hot plate was turned to its

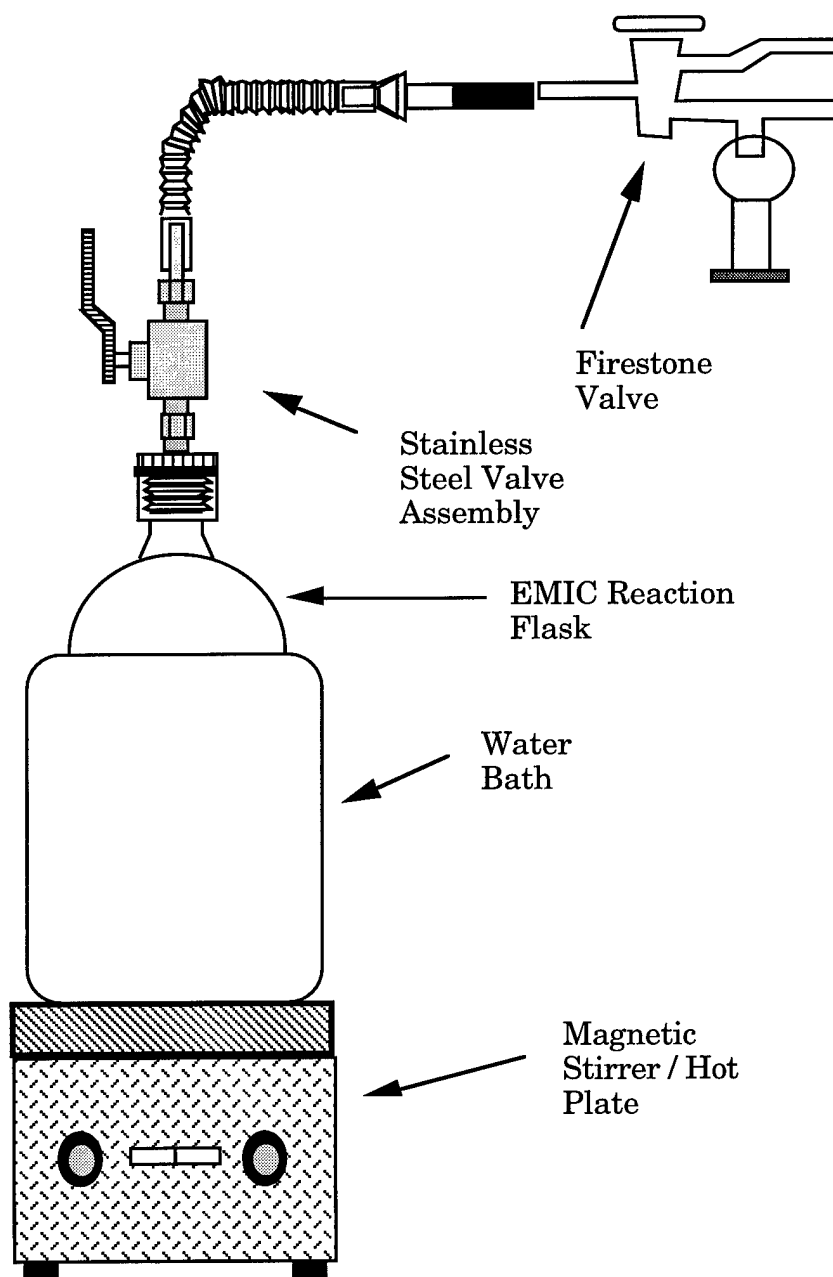


Figure 2.7. Apparatus for removal of excess ethyl chloride.

lowest setting to warm the water bath. In addition, as the ethyl chloride escaped, the EMIC redissolved so the solution was stirred. When the bubbling stopped, the stainless steel valve was closed, and the reaction bottle was dried and transferred into a dry box.

This portion of the purification procedure was performed under an inert atmosphere (nitrogen) in a dry box. The oxygen and water levels were maintained at less than 5 ppm. The purification procedure involves large amounts of organic solvents, namely ethyl acetate and acetonitrile. These solvents generate vapors inside the dry box, and to lengthen catalyst life the dry trains were isolated from the dry box during this procedure. It is also advisable to trap out vapors before they reach the vacuum pumps. Several other precautions can be followed which will help prevent contamination of the EMIC as well as maintain dry box cleanliness. Powder free examination gloves (Fisher) should be worn over the dry box gloves to prevent contaminants on the gloves from being introduced into the EMIC as well as to lengthen the lives of the gloves. Aluminum foil should be placed over all open flasks to prevent particulate contamination, and aluminum foil should be placed on the floor of the dry box in the work area to catch spills and to make clean up easier.

Ethyl acetate and acetonitrile were dried and distilled from calcium hydride using the procedures outlined in Section 2.1.1.2 into 2 L pressure bottles of the same design as the reaction bottle (Figure 2.8).

After all reagents were transferred into the dry box and the catalyst beds isolated, purification proceeded. The stainless steel valve was removed from the EMIC reaction bottle and acetonitrile was added to make the total

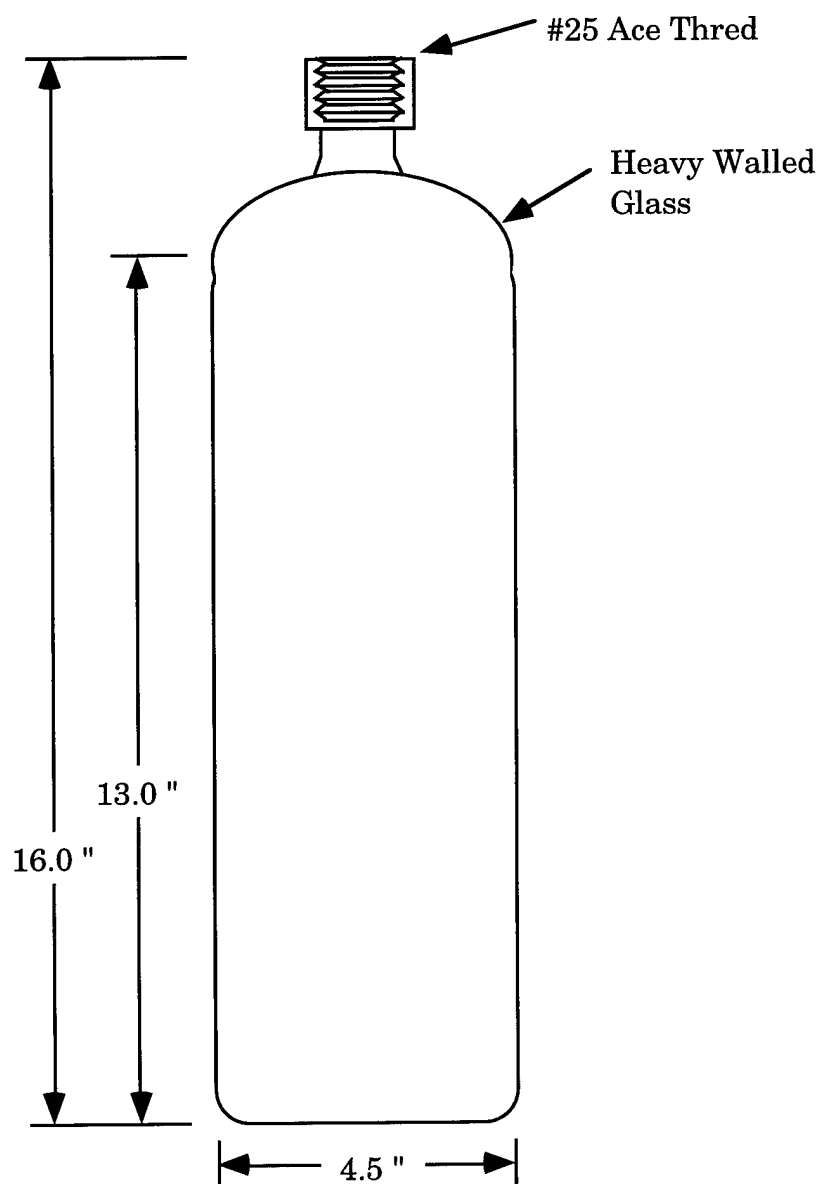


Figure 2.8. 2 L pressure bottles for solvents.

volume \approx 500 mL. This solution was then gravity filtered into a 500 mL separation funnel. 500 to 600 mL of ethyl acetate was added to each of five clean, dry 1000 mL Erlenmeyer flasks. Each flask contained a Teflon coated stir bar. With vigorous stirring, one fifth of the acetonitrile / EMIC solution was slowly dripped into each Erlenmeyer flask (about 1 drop per second). As the acetonitrile / EMIC solution fell into the stirred ethyl acetate, the EMIC precipitated out as a white to off-white solid. Rapid addition of the acetonitrile / EMIC solution to the ethyl acetate resulted in oil formation and generally results in unsatisfactory EMIC. If the precipitated EMIC started to collect on the walls of the Erlenmeyer flask, the addition was stopped, and the EMIC was removed from the walls using a glass rod. After the precipitate was removed from the walls, the dropwise addition of the acetonitrile / EMIC solution was resumed.

After all the acetonitrile / EMIC solution had been added to the five Erlenmeyer flasks, the precipitate was vacuum filtered using a Buchner funnel and medium grade qualitative filter paper. The combined precipitates were washed several times with \approx 300 mL of ethyl acetate. The precipitate was allowed to dry for several minutes and was then carefully scooped into a 1000 mL beaker containing a Teflon coated stir bar. Approximately 500 mL of acetonitrile was added, and the EMIC was allowed to dissolve. The acetonitrile / EMIC solution was poured into a 500 mL addition funnel, and the precipitation procedure was again followed. The EMIC was precipitated and filtered three times to ensure purity. After all three precipitations were complete, the

removal of organic solvents which is the final portion of the purification, was performed.

The precipitation procedure exposed the EMIC to ethyl acetate and acetonitrile. It is necessary to remove these organic contaminants before the EMIC can be used to make melts. The apparatus used for the removal of the organic solvents is shown in Figure 2.9. The EMIC was scooped into a 1 L single neck round bottom flask containing an egg shaped Teflon coated stir bar. A high vacuum stopcock with a hose adapter head was then attached to the single 24/40 Tjoint.

The round bottom flask was removed from the dry box and placed in a heating mantle on top of a magnetic stirrer. The heating mantle was connected to a temperature controller and variac, and the thermocouple from the temperature controller was inserted between the heating mantle and the round bottom flask. The round bottom flask was evacuated (< 1 torr), and the EMIC was slowly heated to 100°C . As the EMIC melted, stirring was initiated and the resulting liquid bubbled, releasing the organic solvents. A heat gun may be necessary to gently warm the round bottom flask above the heating mantle to melt all the EMIC. After all the EMIC was liquefied and the bubbling had ceased, the round bottom flask was maintained under vacuum for at least 2 additional hours.

After the additional 2 hours had elapsed, the temperature controller and the magnetic stirrer were turned off. The EMIC was allowed to solidify in the round-bottom flask under vacuum. When all the EMIC was solid, the high vacuum stopcock was closed, and the round bottom flask was transferred into

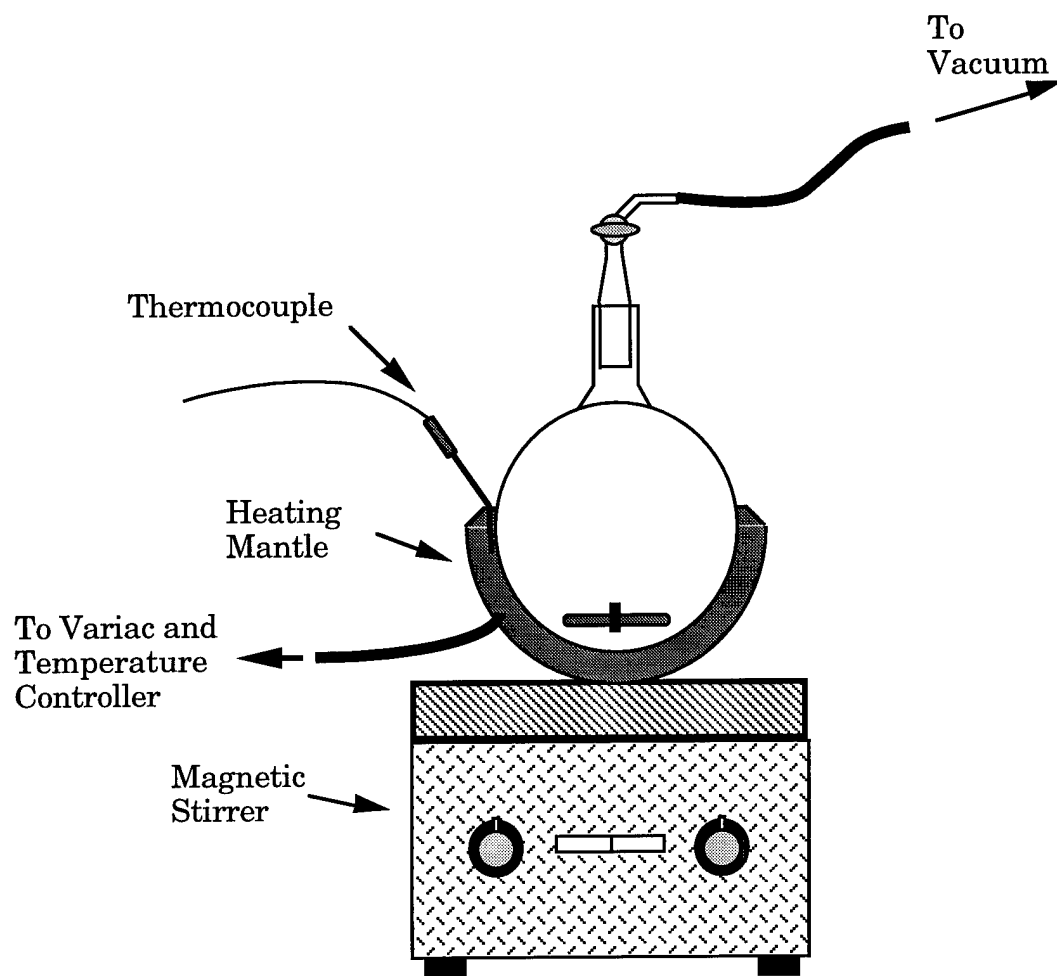


Figure 2.9 Apparatus for removal of organic solvents from EMIC.

a dry box with an inert atmosphere. The dry box in which part two of the purification is conducted must be purged and/or the solvents trapped out so the catalyst beds may be brought on-line and an inert atmosphere attained prior to the purified EMIC being exposed to the box atmosphere. The high vacuum stopcock was removed and the round bottom flask wrapped in tin foil. The round bottom flask was then broken and the EMIC placed in Qorpak bottles. Normally 400 to 500 g of white product was obtained from the above procedure.

2.1.2 Purification of Aluminum Chloride

The AlCl_3 , used in the room-temperature chloroaluminate molten salts, is purified by sublimation in a sealed glass tube containing aluminum wire and sodium chloride.^{1,4} The major impurities contained in commercially available AlCl_3 are miscellaneous organics, FeCl_3 and aluminum oxides. Using this procedure, the residual organic contaminants are removed by the application of a vacuum while the AlCl_3 is heated. The FeCl_3 is reduced to iron by the aluminum wire, and the aluminum oxide impurities remain in the AlCl_3 / NaCl eutectic mixture present in the bottom of the glass tube during the sublimation.

It is imperative to begin with high quality AlCl_3 . The AlCl_3 used exclusively in this laboratory is Fluka purissimo. Although other manufacturers (Aldrich) claim higher purity, we have found the AlCl_3 to

contain unacceptable levels of contaminants, evidenced by the AlCl_3 having a yellow color.

A heavy walled glass bomb tube which had been annealed several times to relieve stress was cleaned and soaked in a nitric acid bath (Figure 2.10). The heavy walled glass tube was then dried in an oven at 180°C and transferred into a dry box. Approximately 5 to 10 g of dry NaCl was added to the bomb tube (Aldrich, 99.999%) followed by 10 to 20, 1 cm pieces of aluminum wire (Alpha Inorganics, 99.999%) that had been acid cleaned and oven dried. Next the AlCl_3 was poured into a glass or plastic tray. Using forceps, the discolored chunks of AlCl_3 were removed and discarded. The white AlCl_3 crystals were added to the bomb tube until it was $2/3$ to $3/4$ full. A high vacuum stopcock with 24/40 Tjoints and glass wool inserted into the male Tjoint was attached to the glass tube (Figure 2.11).

The assembly was removed from the dry box and attached to a vacuum line while suspended in a tube furnace. The assembly was evacuated to < 1 torr and heated to 90°C overnight. This procedure removed volatile organics from the AlCl_3 . It is very important that this step is followed. Excess organics can increase pressure in the bomb tube as well as degrade the purity of the resulting AlCl_3 .

The bomb tube was flame sealed under vacuum and suspended vertically in a tube furnace using copper wire. Glass wool was placed on either end of the tube furnace.

Caution: The bomb tube is subjected to significant pressure during the

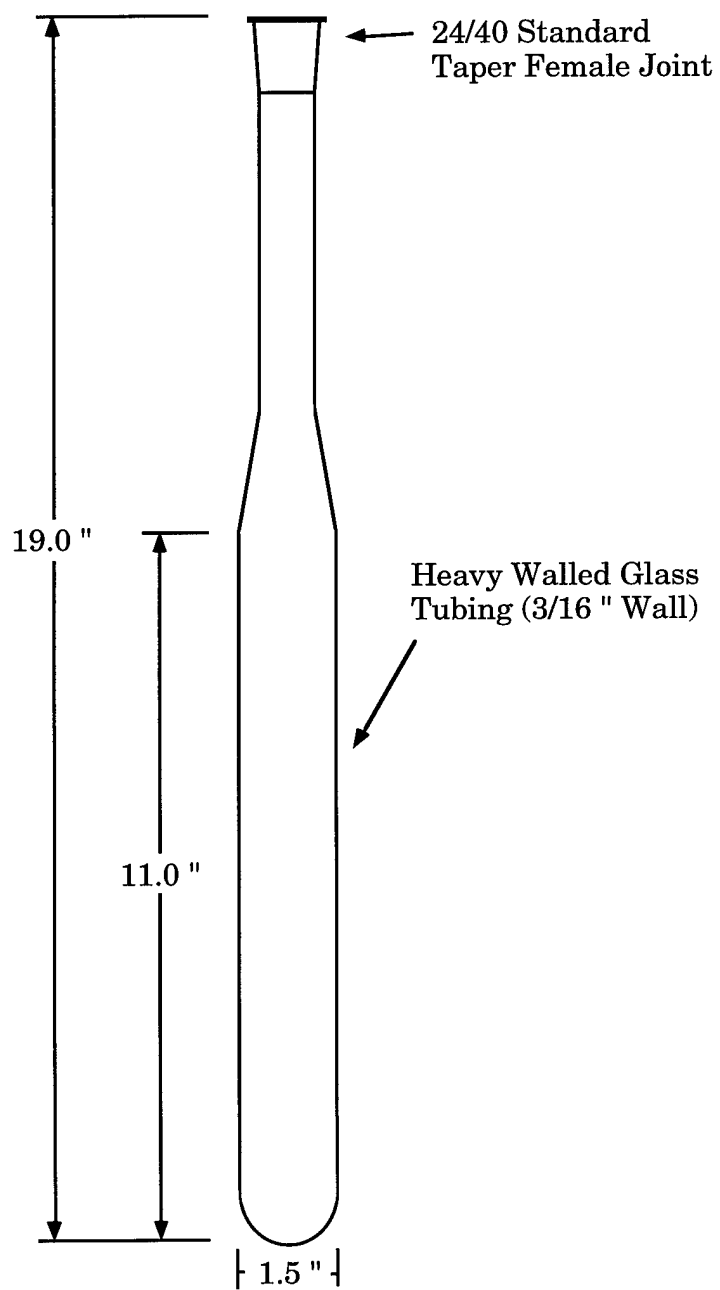


Figure 2.10. Heavy walled bomb tube used to purify AlCl_3 .

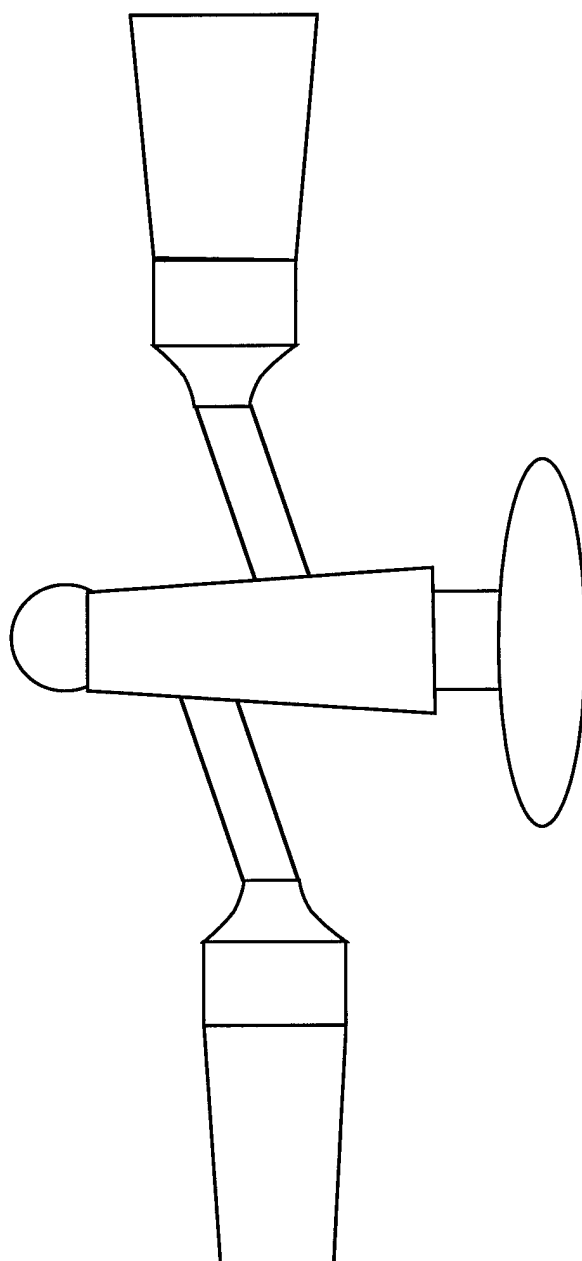


Figure 2.11 High vacuum stopcock used for AlCl_3 purification.

sublimation of AlCl_3 . The tube furnace should be placed behind a safety shield in a well ventilated fume hood due to the explosion hazard.

The tube furnace was connected to a temperature controller and industrial light dimmer. The light dimmer limits the output of the temperature controller. The furnace temperature was slowly raised to $\approx 180 - 210^\circ\text{C}$. The entire contents of the tube were molten before the sublimation was allowed to proceed. There should be two liquid phases present in the bomb tube. The lower liquid phase consists of the NaAl_2Cl_7 , $\text{NaCl} / 2\text{AlCl}_3$, melt. This ionic phase is generally discolored due to the presence of impurities. The upper layer should be clear and contains AlCl_3 (actually Al_2Cl_6). Once the entire contents of the tube were molten, the tube was left for several hours and then gently raised in 3 cm increments every 30 minutes. As the bomb tube was raised, AlCl_3 sublimed and collected at the cooler top of the bomb tube. When ≈ 0.5 cm of the AlCl_3 layer remained on top of the NaAl_2Cl_7 layer, the furnace was turned off, and the bomb tube and furnace were allowed to cool.

Once the bomb tube cooled to room temperature, it was removed from the furnace. The circumference of the bomb tube was scored completely with a glass-cutting knife at the bottom of the purified AlCl_3 . After the scoring was complete, the bomb tube was transferred into a dry box where it was wrapped in several layers of heavy duty aluminum foil. A hammer was then used to break the tube at the score. The transparent AlCl_3 was separated from the glass shards and placed in bottles. Under normal circumstances 100 g of pure AlCl_3 were obtained using the above procedure.

2.1.3 Preparation of AlCl_3 :EMIC Melts

Melts were prepared by mixing weighed amounts of AlCl_3 and EMIC in Qorpak bottles to produce a basic melt. The reaction between AlCl_3 and EMIC is very exothermic. If the components are allowed to heat excessively during the melt preparation, discolored melts often result. In addition, acidic melts are generally more colored than their basic counterparts.

To avoid melt coloration, the AlCl_3 and EMIC chunks that were mixed were at least 0.5 cm in diameter. The use of large chunks reduces the surface area which in turn limits the rate the two substances react. In addition, the EMIC was always added to the glass bottle first so it was on the bottom. This avoids the preparation of a melt that is even transiently acidic. After the melt components are in the Qorpak bottle, the reaction between AlCl_3 and EMIC was allowed to occur without stirring to prevent excessive heating. After most of the reaction had occurred, the melt was stirred to dissolve any remaining components.

After a basic melt has been prepared, the melt should be clear and colorless if the starting materials are reasonably pure. All melts were treated with phosgene and evacuated to remove oxide and proton impurities (See Section 2.22). After the oxide and proton impurities were removed, if an acidic melt was desired, weighed AlCl_3 was added to achieve the desired melt composition.

In the special case that a neutral melt was desired or the melt composition had to be known exactly, then cyclic staircase voltammetry was

used to monitor the melt electrochemical limits as small weighed amounts of AlCl_3 were added. The melt is neutral when neither the chloride oxidation wave nor the Al_2Cl_7^- reduction wave is observed. After the melt was neutral it could either be left at the composition, additional weighed AlCl_3 could be added, or additional EMIC could be added, depending upon the melt composition desired.

2.1.4 Purification of Alkali Metal Chlorides

LiCl (Aldrich, 99.994%), NaCl (Aldrich, 99.999%), and KCl (Aldrich, 99.999%) were dried at 400 °C under vacuum (25×10^{-3} torr) for at least 3 days to ensure dryness. The major impurity in the alkali metal salts is water. Using this procedure, the water contamination is reduced using a combination of heat and vacuum. The alkali metal salt was first transferred into a dry box and then loaded into the same heavy walled glass tube as described above in Section 2.1.2 (Figure 2.10). The white alkali metal salt crystals were added to the heavy walled glass tube until it was $\approx 1/2$ full. A high vacuum stopcock with 24/40 T joints and glass wool inserted into the male T joint was attached to the glass tube (Figure 2.11).

The assembly was removed from the dry box and attached to a vacuum line while suspended in a tube furnace. Glass wool was placed on either end of the tube furnace. The assembly was evacuated (1×10^{-3} torr) and the tube furnace temperature raised to 400 °C. The assembly was maintained under these conditions for at least 3 days, after which the furnace was turned off and

the assembly allowed to slowly cool to room temperature. After the bomb tube had cooled to room temperature, the vacuum stopcock was closed and the apparatus transferred into a dry box. Once inside the dry box, the now dry alkali metal chloride was stored in glass bottles until needed.

2.1.5 Preparation of Neutral Buffered Melts

The preparation of neutral buffered melts from acidic melts has been described.^{5,6} This procedure simply involves adding alkali metal chloride to an acidic melt. The acidic melts were prepared as described above in section 2.1.3 while the alkali metal chlorides were prepared as described above in section 2.1.4. The neutral buffered melts were prepared by the addition of 150 weight percent of the metal chloride required to neutralize the acidic melt. The weight percent of metal chloride required to buffer the melt was determined from the Al_2Cl_7^- concentration in the unbuffered melt.

2.2 EQUIPMENT AND PROCEDURES

2.2.1 Dry box

All melt preparation and handling was carried out in a Vacuum Atmospheres dry box. The dry box atmosphere which consisted of either helium (99.99%) or nitrogen (99.99%) was circulated through a Vacuum

Atmospheres MO-40 Inert Gas Purifier or equivalent. The quality of the atmosphere was evaluated with a light bulb with the tungsten filament exposed. These bulbs were prepared by gently poking a hole in the top of the bulb with an electric engraving tool and immediately transferring the bulb into the dry box. If the oxygen and water levels are below 5 ppm then the bulb will stay lit for at least 14 days.⁷

Aluminum block heaters were used to regulate sample temperature in the dry box when necessary.⁸ These heaters consisted of aluminum blocks containing two 1/2" X 5 1/2" cartridge heaters. Bottles were set into holes drilled into the aluminum blocks. The exposed portion of the bottles were surrounded by additional blocks of aluminum cut to fit the bottle contour. (Drawings of the aluminum heating blocks and the additional blocks are contained in appendix A.) The temperature of the aluminum heating blocks was controlled using a J or K type thermocouple and a Thermo Electric temperature controller hooked to a variac. The variac was used to limit the output from the Thermo Electric temperature controller. Sample temperatures could be regulated to ± 1 °C using these systems.

2.2.2 Proton and Oxide Removal from AlCl_3 :EMIC Melts

The removal of oxide impurities from room temperature molten salts using phosgene has been reported.^{9,10} Proton impurities can be removed using vacuum.¹¹ An apparatus has been developed and procedures written so that both oxide and proton impurities can be removed from room temperature

molten salts.³ The apparatus and procedures have been improved and amended to allow the safe manipulation of phosgene and allow evacuation to pressures as low as 1×10^{-7} torr.

Safety Note. Phosgene is an extremely toxic gas which should be used with caution. At room temperature and pressure it is a colorless gas with an odor resembling that of moldy hay.¹² The odor detection limit is considered to be 0.5 ppm while the time-weighted average Threshold Limit Value (TLV) is 0.1 ppm.^{13,14} A phosgene detector, Matheson Toxic Gas Detector Model 8014LA, was used to test for leaks in the apparatus employed. In addition, the phosgene procedure was conducted in a well ventilated laboratory hood.¹¹

The following is a brief description of the procedure used to remove both the proton and oxide impurities from the room temperature molten salts. For the detailed drawings and a step by step procedure refer to appendix B.

A schematic of the apparatus used for oxide and proton removal is shown in Figure 2.12. The apparatus was constructed primarily from glass and Teflon with minimal lengths of reinforced Nalgene tubing due to the solubility of phosgene in both silicon and petroleum based greases, as well as its permeability through most types of elastomeric tubing (Tygon, neoprene, latex, etc.).^{13,15} The system used an oil diffusion pump coupled to a rotary mechanical pump to achieve pressures down to 1×10^{-7} torr. The system had a neutralizing system to eliminate excess phosgene. The neutralizing system

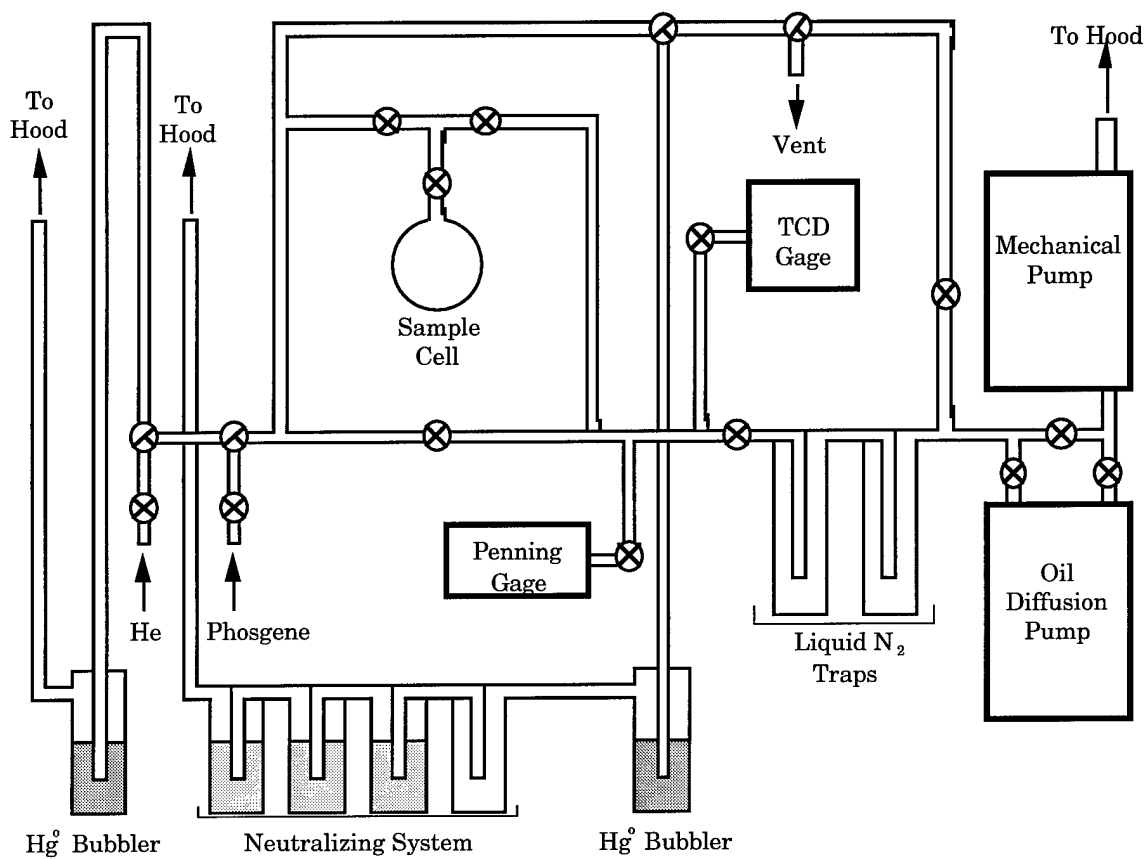


Figure 2.12 Schematic of the apparatus used for proton and oxide removal.

was composed of an overflow trap and three gas washing bottles filled with 10 % aqueous NaOH. The aqueous NaOH solutions decompose the phosgene to sodium chloride and carbon dioxide.

The generic procedure started with 25 - 100 mL of melt being loaded into a single necked round bottom flask with a female 24/40 T joint. Next a high vacuum stopcock was attached. The round bottom flask and stopcock were then removed from the dry box and attached to vacuum / gas line (Figure 2.12). Initially the melt was evacuated to 1×10^{-3} torr using the rotary mechanical pump and refilled with helium at least three times. This establishes an inert atmosphere over the melt.

Note. Phosgene, as well as nitrogen and helium, are very soluble in melts. When vacuum is applied it should only be done very gradually to prevent foaming and splattering of the melt.

After an inert atmosphere had been established over the melt, the melt was evacuated again and the oil diffusion pump was started. The melt was then heated to 70 °C using a thermocouple and temperature control unit with the output limited through a variac. This evacuation removed protons from the melt. The presence of protons is suspected to interfere with the oxide removal process.¹⁶ The melt was subjected to these conditions until the equilibrium pressure was $< 5 \times 10^{-6}$ torr. Normally about 24 hours were necessary to achieve this pressure.

To remove oxide from the melt, the diffusion pump was disengaged and the melt temperature lowered to 30 °C. The melt was exposed to a phosgene atmosphere under a positive pressure for 5 minutes. The melt was then sealed and allowed to react with dissolved phosgene for an additional five minutes. Next the melt was evacuated using the rotary mechanical pump for at least 10 minutes. To ensure complete oxide removal, the exposure to phosgene, the reaction with phosgene, and the evacuation of the melt was completed two more times.

After the phosgenation was complete, the melt was left under vacuum for \approx 1 hour and then isolated. The vacuum pump was isolated and the vacuum and gas lines purged with helium so that residual phosgene was swept from the system and into the gas washing bottles where it was neutralized. The liquid nitrogen traps were then slowly removed. Carbon dioxide (formed by the reaction of phosgene with oxide) and unreacted phosgene were purged into the gas washing bottles using helium.

At this point the initial protons present in the melt as well as the oxides have been removed. Unfortunately, the phosgenation procedure introduces some proton impurity and the proton removal procedure was repeated after the phosgenation procedure was complete. This consisted of using the oil diffusion pump and mechanical pump to remove any residual phosgene and proton from the melt. During this second vacuum procedure it was very important initially to allow the melt to stay at 30 °C for about 30 minutes to an hour before slowly raising the melt temperature to 70 °C. The delay before

heating is necessary to remove any residual phosgene that may be present in the melt as this can cause the phosgene to attack the melt and discolor it.

The procedure for proton removal without oxide removal was identical to the vacuum procedure described above and no phosgene gas was used.

2.2.3 NMR Measurements

NMR samples were prepared in a dry box and if necessary filtered through PTFE, Glass Fiber, or PVDF syringe filters (Gelman) into a precision NMR tube (Wilmad Glass Co., or New Era), which were either capped and sealed with Parafilm or removed from the box and flame sealed. Those samples which had to be flame sealed were constricted 1 inch below the top by our glassblower prior to use. Prior to removal of these samples from the dry box, an adapter (Wilmad, Part# 552-5 and 552-10) was attached to the end of the NMR tube. This adapter prevented atmospheric contamination of the NMR sample and allowed the sample to be evacuated prior to flame sealing.

^1H spectra were externally referenced to either 0.1 % TMS in CDCl_3 , 0 ppm, (Aldrich) or to d_3 -acetonitrile (Aldrich), 1.94 ppm. ^{17}O spectra were externally referenced to natural abundance H_2^{17}O in water, 0 ppm. ^{31}P were externally referenced to 85 weight% phosphoric acid in water (Aldrich), 0 ppm.

NMR spectra were acquired using a GE Omega 300 NMR spectrometer, a GE Omega 500 NMR spectrometer, and a Bruker ARX 500 NMR spectrometer. The 300 MHz spectrometers operate at a field of 7.0 Tesla,

while the 500 MHz spectrometers operate at a field of 11.7 Tesla. The nuclei studied in this thesis and their resonance frequencies are listed in Table 2.1.

2.2.4 Electrochemical Measurements

Electrochemical experiments were performed using a three electrode system consisting of a working, a counter, and a reference electrode. Working electrodes used included: BAS platinum disk (area = 0.020 cm²), BAS glassy carbon (GC) disk (area = 0.071 cm²), and several tungsten microdisk electrodes. Working electrodes were polished using Metadi II diamond polishing compound in Metadi fluid extender on polishing cloth (Buehler). The Metadi II diamond polishing compound was initially large particle size to remove gross defects and then gradually stepped to smaller particle sizes. In situ cleaning of the working electrodes was accomplished by sweeping anodically three times from 0.3 to 3.0 V with a sweep rate of 500 mV/sec.¹⁷ The counter electrode was a coiled platinum wire (99.998 %, puratronic, Alfa Aesar). The platinum wire was treated by soaking in concentrated nitric acid to remove contaminants. The reference electrode was an aluminum wire suspended in a 1.5:1.0 melt. The fabrication of the reference electrode is discussed below in section 2.2.4.1.

Voltammetric studies were performed using a EG&G PARC Model 273 Potentiostat / Galvanostat. The potentiostat was controlled and the data recorded using an IBM personal computer (PC).¹⁸ The software used to control the Model 273 and collect the data was Wotan, an in-house PC program.¹⁹ Data was analyzed using FSQPLT, another in-house PC program.

Nucleus	300 MHz	500 MHz
^1H	300.13 MHz	500.13 MHz
^{13}C	75.47 MHz	125.77 MHz
^{17}O	–	67.80 MHz
^{31}P	121.50 MHz	–

Table 2.1 The NMR frequencies of the nuclei studied.

2.2.4.1 RDE Measurements / Electrode Holder

Rotating disk electrode experiments were conducted using the same computer and potentiostat as described above with the addition of a Pine MSR electrode rotator. The working electrode was either a Platinum disk (area = 0.020 cm^2 , Bioanalytical Systems) or a glassy Carbon disk (area = 0.071 cm^2 , Bioanalytical Systems) attached to a Pine MSR electrode rotator with a custom electrode adapter that allows Bioanalytical Systems electrodes to be used as the working electrodes (Figure 2.13). The Pine MSR Speed Control was used to control the rotation rate of the disk.

2.2.4.2 Fabrication of Reference Electrodes

The reference electrode is depicted in Figure 2.14. Reference electrodes were fabricated using a 4 cm length of 1 mm diameter aluminum wire (99.999%, Alpha Aesar) that had been soaked in concentrated nitric acid to remove contaminants. A glass tube 7 cm in length with an outside diameter of 6 mm that was tapered on one end to an outside diameter of 3 mm with a 4.5 mm lip was custom made by our glassblower based on the BAS design (Part# MF-2042) The glass tubes were also cleaned using concentrated nitric acid. Both the aluminum wire and glass tube were rinsed using deionized water and dried in an oven at $180\text{ }^{\circ}\text{C}$. Next a 1/2 inch length of 3/8 inch diameter Teflon heat shrink tubing was placed on the small end of the glass tube over the lip, and a 1/8 inch length of 3 mm diameter Vycor rod was inserted into it. The

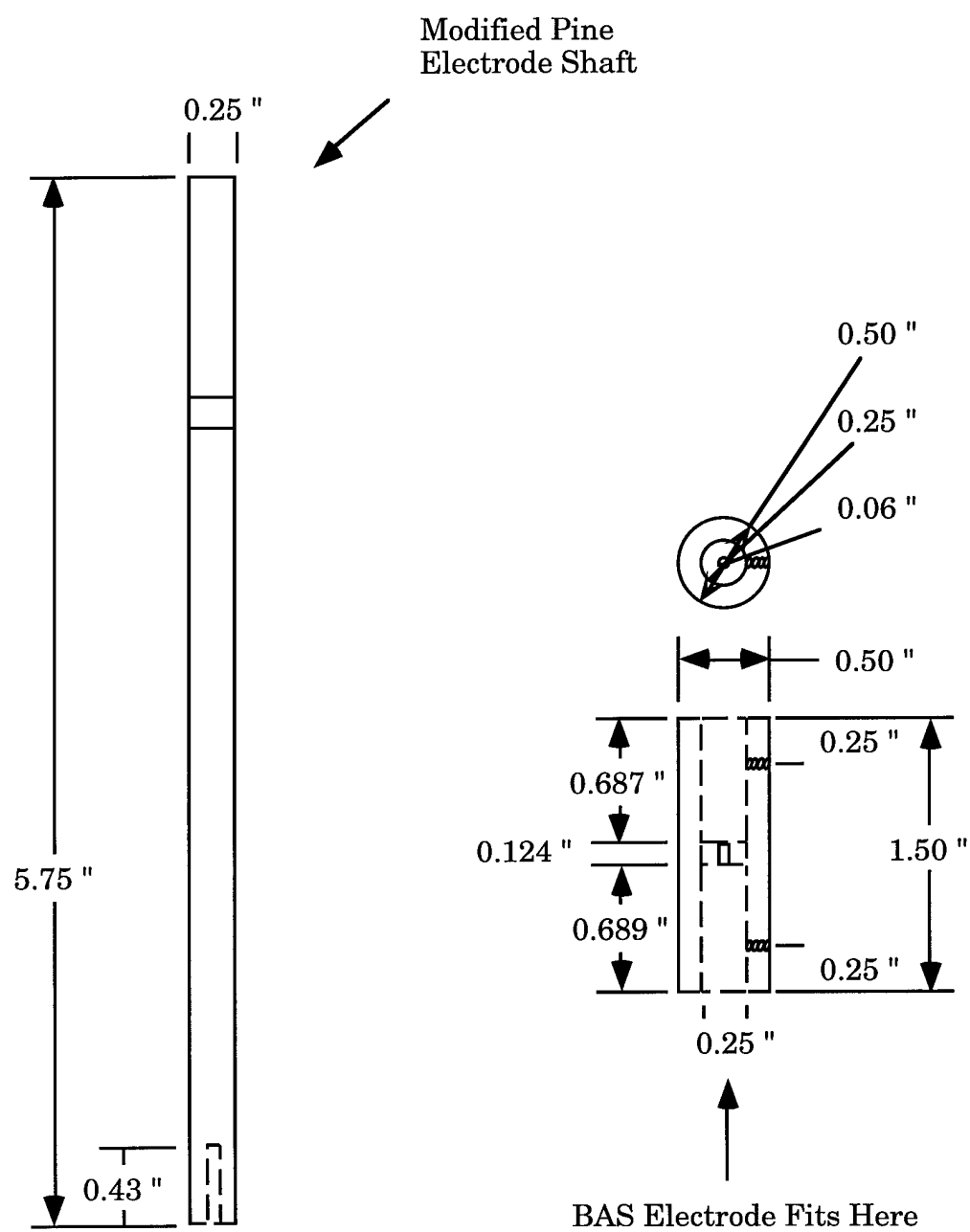


Figure 2.13 Custom rotating disk electrode holder.

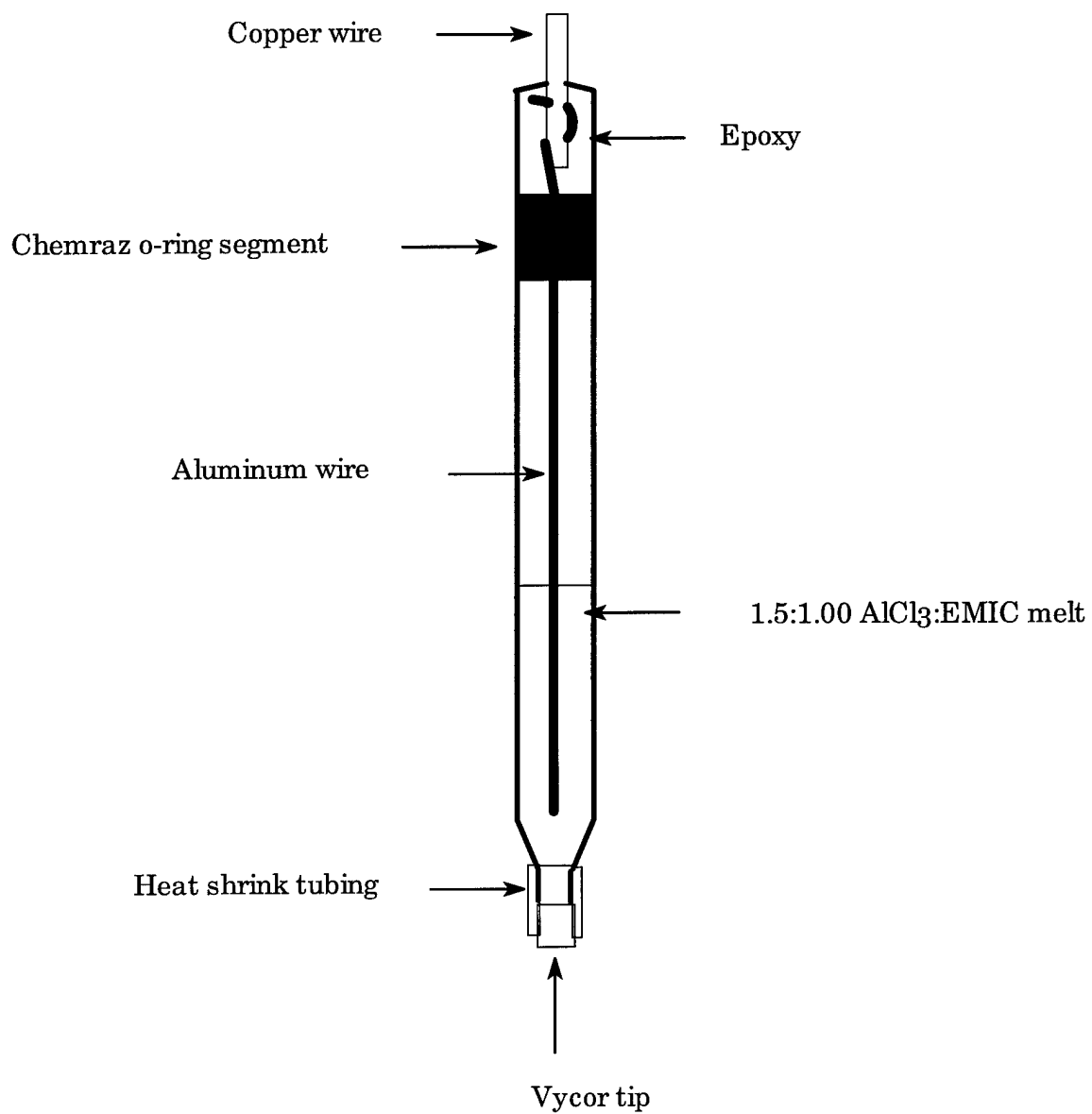


Figure 2.14. Reference electrode.

Vycor frit essentially eliminates leakage from the reference electrode.

Note. Do not touch the Vycor rod with your fingers. The Vycor tubing may absorb oils from your skin.

The loosely assembled body of the electrode was placed in a oven at 130 °C until the heat shrink tubing secured the Vycor tip to the glass tube.

After the body of the electrode had been assembled, a 4 cm length of 12 gauge copper wire was flattened slightly on one end with a hammer and two 1 mm holes were drilled into it. The aluminum wire was then laced through the two holes, and the assembled end was struck lightly with the hammer to ensure good electrical contact between the copper and the aluminum. A 6 mm length of Chemraz O-ring (Greene Tweed & Co., Part # M0400-8200-505) was frozen in dry ice / acetone and the segment drilled lengthwise using a 0.028 inch (Size 70) drill bit. The drilled O-ring segment was then slipped onto the aluminum wire.

The electrode components were then transferred into a dry box for final assembly. Once inside the box, the aluminum wire was lightly polished using a piece of fine jeweler's cloth to remove the oxide film. Next ≈ 1 mL of 1.5:1.0 melt was pipetted into the electrode body, and the O-ring and wire assembly were pushed into the open end of the glass tube. Five minute epoxy was then used to encase the aluminum and copper wires above the O-ring segment.

The assembled reference electrode must be soaked in a 1.5:1.0 melt to ensure electrical conductivity through the Vycor and should be stored when not in use in the same fashion.

Chapter 2 References

- (1) Wilkes, J. S.; Levisky, J. A.; Wilson, R. A.; Hussey, C. L. "Dialkylimidazolium Chloroaluminate Melts: A New Class of Room-Temperature Ionic Liquids for Electrochemistry, Spectroscopy, and Synthesis." *Inorg. Chem.* **1982**, *21*, 1263-1264.
- (2) Trulove, P. C.; Osteryoung, R. A. "Proton Speciation in Ambient-Temperature Chloroaluminate Ionic Liquids." *Inorg. Chem.* **1992**, *31*, 3980-3985.
- (3) Trulove, P. C. Ph. D. Thesis, State University of New York at Buffalo, 1992.
- (4) Gale, R. J.; Osteryoung, R. A.; In *Molten Salt Techniques*; Lovering, d. G.; Gale, R. J., Eds.; Plenum Press: New York, 1983; Chapter 3.
- (5) Melton, T. J.; Joyce, J.; Maloy, J. T.; Boon, J. A.; Wilkes, J. S. "Electrochemical Studies of Sodium Chloride as a Lewis Buffer for Room Temperature Chloroaluminate Molten Salts." *J. Electrochem. Soc.* **1990**, *137*, 3865-3869.

- (6) Scordilis-Kelley, C.; Fuller, J.; Carlin, R. T.; Wilkes, J. S. "Alkali Metal Reduction Potentials Measured in Chloroaluminate Ambient-Temperature Molten Salts." *J. Electrochem. Soc.* **1992**, *139*, 694-699.
- (7) Eubanks, D.; Aboot, F. J. "Gas Purification and Pressure Control System for Inert Atmosphere Boxes." *Anal. Chem.* **1969**, *41*, 1708-1709.
- (8) Ludwig, S. N. "The Use of Solid Aluminum Heat Transfer Devices in Organic Chemistry Laboratory Instruction and Research." *J. Chem. Ed.* **1989**, *66*, 77-84.
- (9) Abdul-Sada, A. K.; Avent, A. G.; Parkington, M. J.; Ryan, A.; Seddon, K. R.; Welton, T. "The Removal of Oxide Impurities from Room Temperature Halogenoaluminate Ionic Liquids." *J. Chem. Soc., Chem. Comm.* **1987**, 1643-1644.
- (10) Sun, I. W.; Ward, E. H.; Hussey, C. L. "Reactions of Phosgene with Oxide-Containing Species in a Room-Temperature Chloroaluminate Ionic Liquid." *Inorg. Chem.* **1987**, *26*, 4309-4311.
- (11) Noël, M. A. M.; Trulove, P. C.; Osteryoung, R. A. "Removal of Protons from Ambient-Temperature Chloroaluminate Ionic Liquids." *Anal. Chem.* **1991**, *63*, 2892-2896.

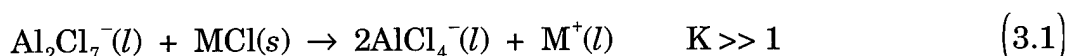
- (12) The Merck Index, Budvari, S; O'Neil, M. J.; Smith, A.; Heckelman, P. E., Eds.; Marck & Co.; Rahaway, NJ, 1989; 11th ed.; p. 1165.
- (13) Mehlman, M. A. *Def. Sci. J.* **1987**, *37*, 269-279.
- (14) Diller, W. F.; Zante, R. *J. Toxicol. and Indust. Health.* **1985**, *1*, 117-128.
- (15) Hussey, C. L., University of Mississippi, personal communication, 1991.
- (16) Trulove, P. C., United States Naval Academy, personal communication, 1994.
- (17) Carlin, R. T.; Crawford, W.; Bersch, M. "Nucleation and Morphology Studies of Aluminum Deposited from an Ambient-Temperature Chloroaluminate Molten Salt" *J. Electrochem. Soc.* **1992**, *139*, 2720-2727.
- (18) Brumleve, T. R.; O'Dea, J. J.; Osteryoung, R. A.; Osteryoung, J. G. "Differential Normal Pulse Voltammetry in the Alternating Pulse Mode for Reversible Electrode Reactions." *Anal. Chem.* **1981**, *53*, 702-706.
- (19) O'Dea, J. J. *Wotan: Instructions to Users*. 1993, Unpublished.

Chapter 3

Quantification of Latent Acidity

3.1 Introduction

In 1990 Wilkes and coworkers reported the preparation of neutral buffered chloroaluminate salts.¹ Neutral buffered melts are prepared through the addition of an alkali metal chloride salt (MCl) to an acidic melt.¹⁻³ The following reaction occurs when MCl is added to an acidic melt:



The melt that results contains M^+ , EMI^+ , and AlCl_4^- . Because Cl^- and Al_2Cl_7^- are absent the melt is not basic or acidic but is neutral. The melts are buffered from both strong Lewis acids and bases because solid MCl can react with added strong Lewis acids and M^+ can react with strong Lewis bases and precipitate as MCl.

The buffering mechanism alters the composition of the melt so that:

$$[\text{EMI}^+] + [\text{M}^+] = [\text{AlCl}_4^-] \quad (3.2)$$

This is in contrast to neutral unbuffered melts:

$$[\text{EMI}^+] = [\text{AlCl}_4^-] \quad (3.3)$$

These changes in ionic composition do not affect the electrochemistry when comparing neutral non-buffered and neutral buffered melts where the observed electrochemical window is the same (≈ 4.4 V).⁴

Although the electrochemistry appears the same between neutral unbuffered melts and neutral buffered melts there are large differences in the chemical properties of the two. Quarmby and Osteryoung observed that neutral buffered melts exhibit what they called a "latent acidity," generating AlCl_3 adducts when weak Lewis bases are added to the melts.⁵ Neutral unbuffered melts show no adduct formation when weak Lewis bases are added. Semi-quantitative results from cyclic voltammetric experiments suggested that speciation of weak Lewis bases in the buffered melts was controlled by the equilibrium:



where B: is a Lewis base.⁵ Cheek had already reported that aromatic ketones also form AlCl_3 adducts in neutral buffered melts but had not investigated this further.⁶

This chapter reports on the quantitative electrochemical and spectroscopic investigation of the behavior of Lewis bases in NaCl neutral buffered melts.

3.2 Specialized Experimental Procedures

3.2.1 Materials

Acetylferrocene ($\text{Fc}(\text{COMe})$ or AcFc , Aldrich) was sublimed twice at 70 °C and 1 torr and was transferred into the dry box. *N,N*-dimethylaniline (DMA, Fluka, >99.95%) was used without further purification.

3.2.2 Equipment and Procedures

3.2.2.1 UV-vis Measurements

UV-Visible spectra were recorded on a Hewlett-Packard 8452A Diode Array Spectrophotometer using 1 cm square air-tight silica cells. Short path lengths were obtained with precision silica inserts (Wilma Glass Co.) (Figure 3.1) and calibrated with K_2CrO_4 in 0.05 N aqueous KOH as described by Smith et al.⁷

3.3 Results And Discussion

3.3.1 Acetylferrocene

The chemistry of acetylferrocene is dependent upon melt composition.⁸

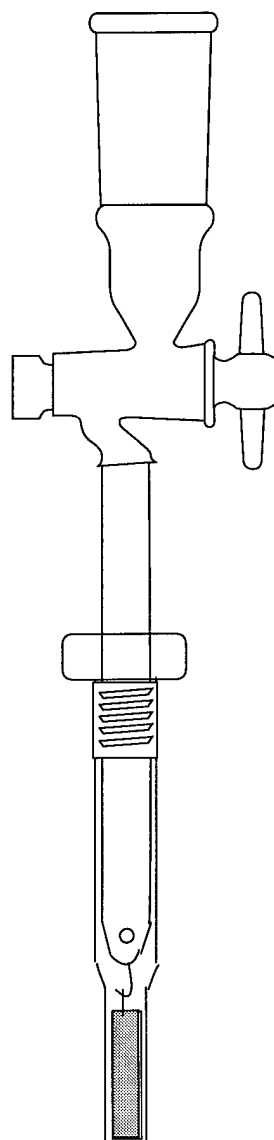
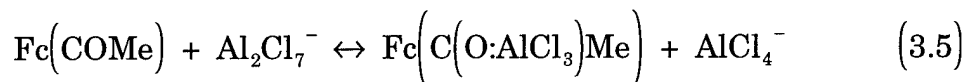


Figure 3.1 Sealed UV-vis cell used for acetylferrocene measurements.

In acidic melts an aluminum chloride adduct is formed at the carbonyl group:

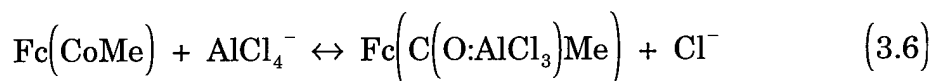


where $\text{Fc} = (\text{C}_5\text{H}_5)\text{Fe}(\text{C}_5\text{H}_4^-)$. Adduct formation at Lewis basic moieties such as carbonyl, cyanide and ferrocyanide has been reported.⁹⁻¹¹ In basic melts no adduct formation occurs. The oxidation potential of the adduct is 350 mV more positive than that of free acetylferrocene.

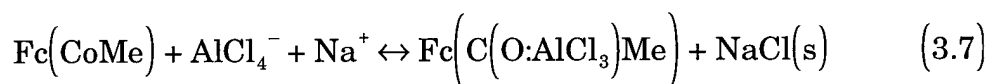
We observed that the behavior of acetylferrocene in unbuffered neutral melts varies from batch to batch of melt. Typically, a mixture of adduct and free acetylferrocene was observed. Occasionally only free acetylferrocene was detected. The maximum concentration of adduct observed was 2 millimolar. The acetylferrocene concentration present in the melts during these experiments was on the order of tens of millimolar. The presence of the adduct probably arises from experimental difficulties encountered when preparing a "neutral" melt. A neutral melt is generally prepared from a slightly basic melt. The disappearance of the Cl^- oxidation wave is monitored electrochemically as AlCl_3 is added. However the detection levels of Cl^- and Al_2Cl_7^- are approximately 5 millimolar.¹² Thus "neutral" melts may be slightly acidic or basic and the observed speciation will vary from batch to batch.

In contrast, upon addition of acetylferrocene to a NaCl buffered melt, $[\text{Na}^+] = 0.36 \text{ M}$, the free species was not observed even at concentrations up to 20 mM. The formation of the adduct requires a source of AlCl_3 in the buffered melts. The concentration of Al_2Cl_7^- is very low as no deposition or stripping

waves were evident at either platinum or glassy carbon electrodes. A report has suggested that buffered melts are slightly Lewis acidic, the upper limit on the concentration of Al_2Cl_7^- being $\approx 4 \text{ mM}$.¹³ It is more likely that the Al_2Cl_7^- concentration is far lower, and the Al_2Cl_7^- is in a rapid equilibrium with Na^+ and AlCl_4^- for the experiments employed. Either way this is significantly lower than the concentration of adduct that we have observed. We propose that the source of AlCl_3 is AlCl_4^- , a very weak Lewis acid. In an unbuffered neutral or basic melt the equilibrium:



lies far to the left. Tetrachloroaluminate is not a sufficiently strong Lewis acid for the reaction to occur which is why adduct is not observed in the unbuffered neutral or basic melts. However, in a buffered melt, the equilibrium is modified by the presence of sodium ions:



The generation of chloride ion during adduct formation results in the precipitation of Na^+ as NaCl(s) , thus providing a driving force to pull the equilibrium to the right. This modified equilibrium was characterized semi-quantitatively using cyclic voltammetry (Figure 3.2). When $[\text{Fc}(\text{COMe})]$ is less than $[\text{Na}^+]$ only adduct is observed and when $[\text{Fc}(\text{COMe})]$ is greater than $[\text{Na}^+]$ a mixture of adduct and free species is observed.⁵

A more quantitative analysis was performed with rotating disk electrode (RDE) voltammetry and UV-Visible spectroscopy. An acidic melt which was ≈ 80 mM Al_2Cl_7^- , and in which aluminum deposition was evident, was buffered with NaCl(s) . A neutral melt electrochemical window was observed. Acetylferrocene was then added to the melt and its electrochemistry examined. RDE voltammograms were run over a range of rotation rates and acetylferrocene concentrations. The adduct was the only species present at concentrations under 80 millimolar. On increasing the concentration of acetylferrocene, a second wave, due to uncomplexed acetylferrocene, appeared (Figure 3.3). Limiting currents were measured for each species for a range of rotation rates. Plots of limiting current of each species against $\omega^{1/2}$ were linear for both waves throughout the rotation range at each concentration (Figure 3.4). From the Levich equation:

$$I_{\text{lim}} = 0.62 n F A D^{2/3} \nu^{-1/6} \omega^{1/2} C_0 \quad (3.8)$$

the slope of the I_{lim} vs. acetylferrocene concentration plot at a fixed rotation rate is proportional to the concentration (C_0) of the electroactive species in the bulk of the solution (Table 3.1). A plot of I_{lim} at 2000 rpm against total acetylferrocene concentration is shown in Figure 3.5. It clearly illustrates that below 75 millimolar the adduct is the sole species present, and at higher concentrations the adduct concentration is constant and equal to the initial concentration of sodium ions in the buffered melt. The concentration of the free species increases linearly with total acetylferrocene concentration above 80 millimolar, as predicted by Equation 3.7. That is, once all the sodium ions have

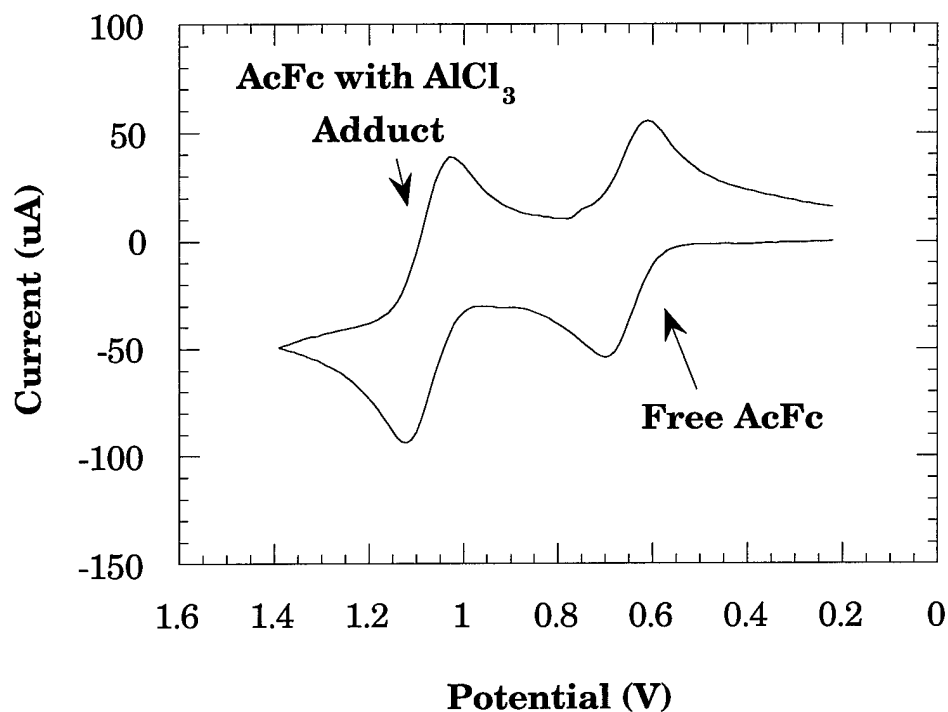


Figure 3.2 Cyclic staircase voltammogram of acetylferrocene in a sodium chloride neutral buffered melt. Prior to the addition of acetylferrocene $[\text{Na}^+] \approx 40 \text{ mM}$. The acetylferrocene concentration is 61 mM . Scan rate 500 mV/sec . Working electrode glassy carbon disk (area = 0.071 cm^2). Both the free acetylferrocene and the AlCl_3 adduct were observed.

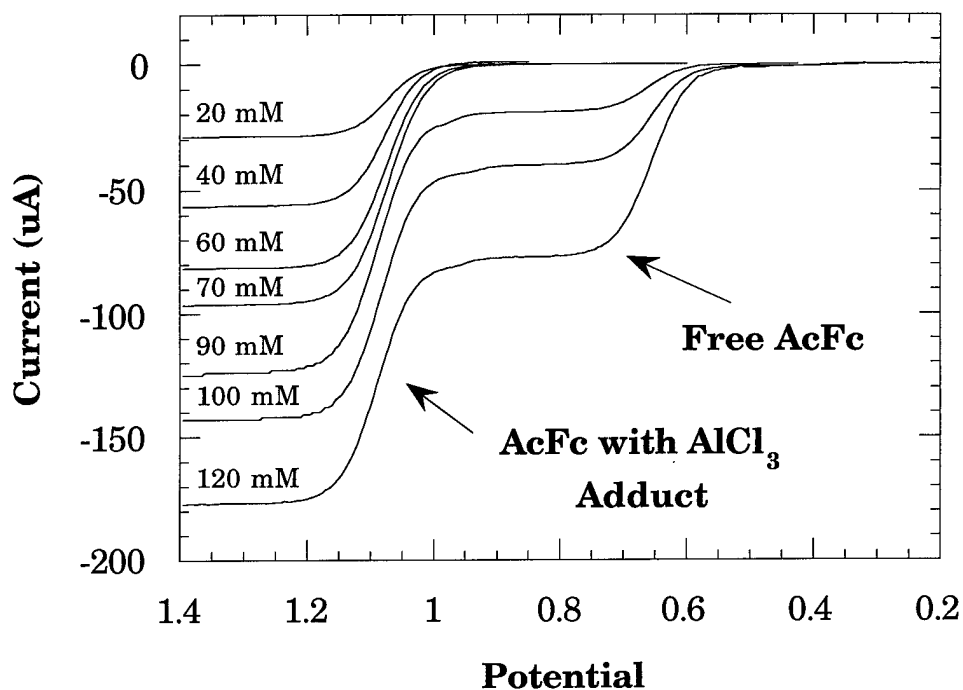


Figure 3.3 RDE voltammograms of Acetylferrocene in a NaCl neutral buffered melt $[\text{Na}^+] = 80 \text{ mM}$. Rotation rate is 2000 rpm. Working electrode was a platinum disk (area = 0.020 cm^2). When the acetylferrocene concentration reached 90 mM current due to the free form of acetylferrocene was observed. As the concentration was further raised the current due to the free form of the acetylferrocene increased while that due to the AlCl_3 adducts remained constant.

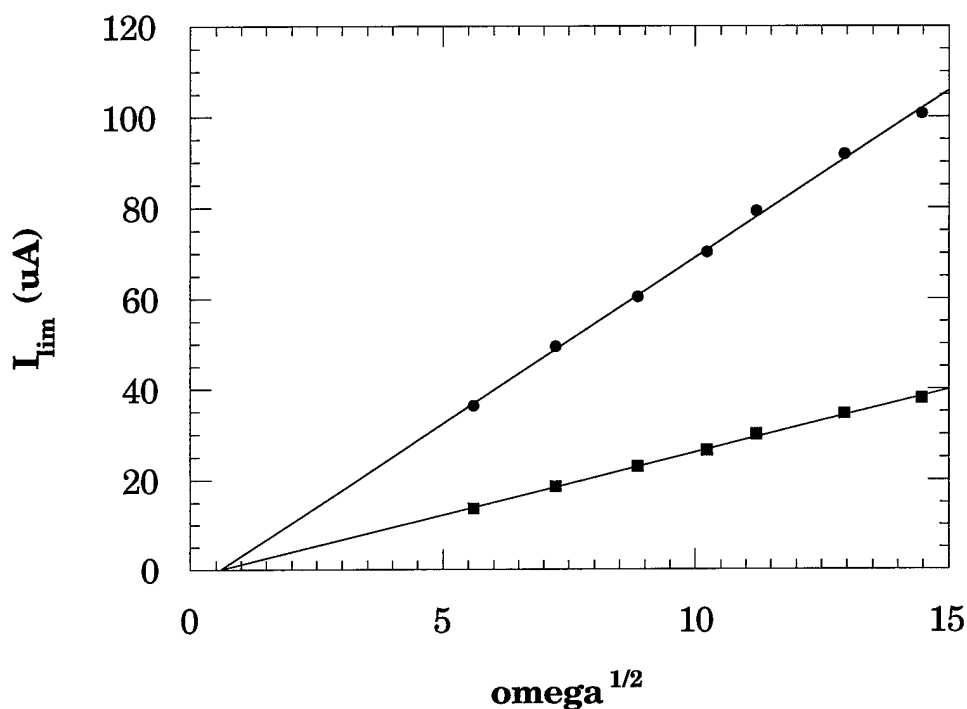


Figure 3.4 Limiting current of each species against $\omega^{1/2}$. for melt containing 120 mM acetylferrocene. Prior to the addition of base $[Na^+] = 80$ mM. Working electrode was a platinum disk (area = 0.020 cm^2). (●) Limiting current due to the acetylferrocene $AlCl_3$ adduct. (■) Limiting current due to free acetylferrocene. The lines are the least squared fits of the data. The slopes of the lines are proportional to the concentrations of the species. Both acetylferrocene species are taken to have the same diffusion coefficient and the concentration calculated from the sum of the slopes is equal to the total acetylferrocene added.

Concentration AcFc (mM)	I_{lim} Free AcFc (μA)	I_{lim} AcFc:AlCl ₃ Adduct (μA)
0	0	0
20	0	28.1
40	0	56.0
60	0	81.3
70	0	94.1
90	17.8	100.7
100	38.0	100.8
120	73.8	97.7

Table 3.1 Concentrations of free and bound acetylferrocene as the concentration of acetylferrocene is increased in a sodium chloride neutral buffered melt. $[\text{Na}^+] = 80 \text{ mM}$

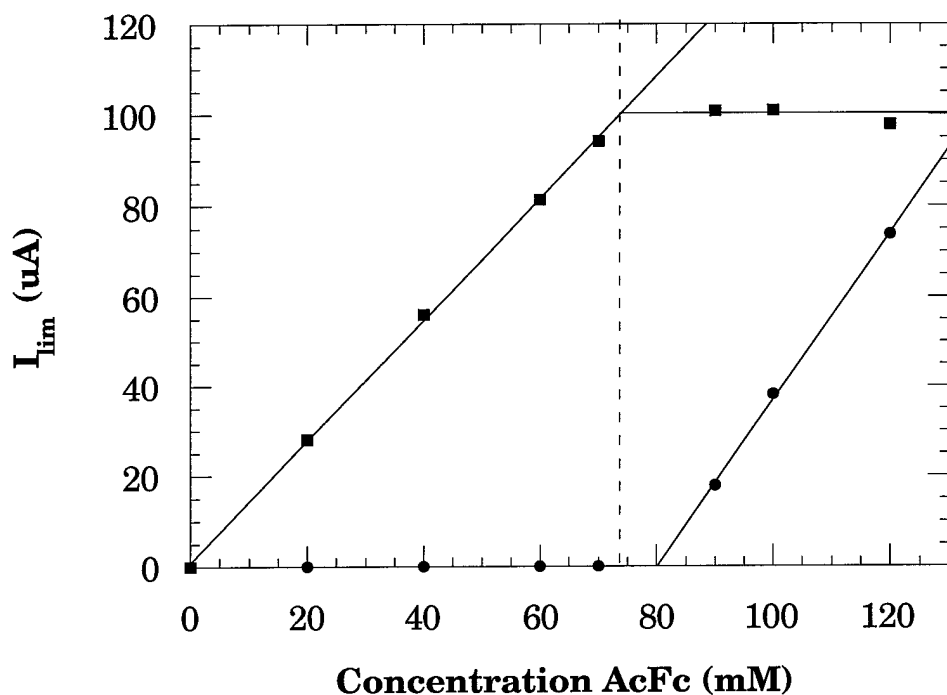


Figure 3.5 Plot of RDE I_{lim} at 2000 rpm. against total acetylferrocene concentration. Prior to the addition of acetylferrocene the $[Na^+] = 80$ mM. Working Electrode was a Pt disk (0.020 cm^2). (■) Acetylferrocene $AlCl_3$ adduct. (●) Free Acetylferrocene. Lines are the least squared fits to each portion of the data. The vertical dotted line shows the point at which I_{lim} due to the Acetylferrocene $AlCl_3$ adduct plateaus.

precipitated the equilibrium reverts to Equation 3.6 and no further adduct formation occurs.

Qualitative information on the stability of the adduct in the neutral and oxidized state can be obtained from the difference in the half-wave potentials of acetylferrocene and the adduct. The chemical and electrochemical reactions are represented by Figure 3.6.

Nernst equations for the free species and the adduct are given in Equations 3.9 and 3.10 respectively.

$$E = E_1^\circ + \frac{RT}{F} \ln \left(\frac{[B^+]}{[B]} \right) \quad (3.9)$$

$$E = E_2^\circ + \frac{RT}{F} \ln \left(\frac{[B:AlCl_3^+]}{[B:AlCl_3]} \right) \quad (3.10)$$

The chemical equilibrium constants for adduct formation in the neutral and oxidized states are given in Equations 3.11 and 3.12 respectively.

$$K_{eq}^1 = \frac{[B:AlCl_3]}{[B][AlCl_4^-][Na^+]} \quad (3.11)$$

$$K_{eq}^2 = \frac{[B:AlCl_3^+]}{[B^+][AlCl_4^-][Na^+]} \quad (3.12)$$

Substituting for [B] and [B⁺] in Equation 3.9 gives Equation 3.13,

$$E = E_1^\circ + \frac{RT}{F} \ln \left(\frac{K_{eq}^1}{K_{eq}^2} \right) + \frac{RT}{F} \ln \left(\frac{[B:AlCl_3^+]}{[B:AlCl_3]} \right) \quad (3.13)$$

which, by inspection with respect to Equation 3.10 gives Equation 3.14.

$$E_2^\circ = E_1^\circ + \frac{RT}{F} \ln \left(\frac{K_{eq}^1}{K_{eq}^2} \right) \quad (3.14)$$

$E_2^\circ - E_1^\circ$ can be approximated from the difference in half-wave potentials (420 mV) which implies that K_{eq}^1/K_{eq}^2 is approximately 1.2×10^7 . This indicates B is

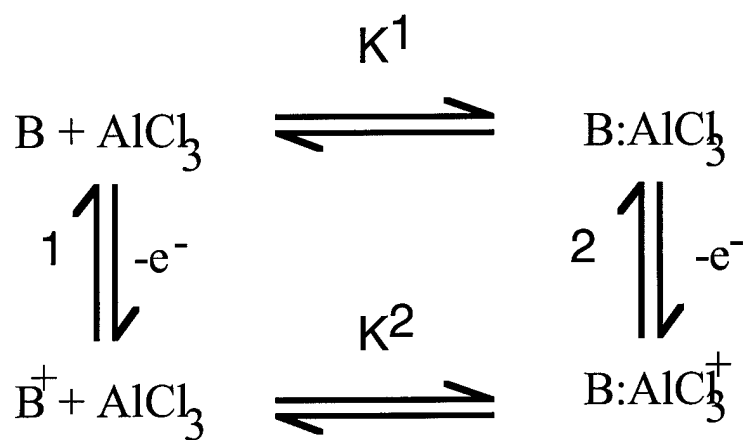


Figure 3.6 Scheme for chemical and electrochemical reactions of acetylferrocene in the melts.

much more tightly complexed than B^+ .

The equilibrium in Equation 3.7 was also characterized using UV-Visible spectroscopy. The adduct and free acetylferrocene exhibit markedly different spectra (Table 3.2 and Figure 3.7), with both species obeying Beer's law. At 580 nm the molar absorptivity of the adduct is two orders of magnitude greater than the free species and thus absorbance at 580 nm gives, to a first approximation, a measure of adduct concentration. A plot of absorbance at 580 nm vs. acetylferrocene concentration is shown in Figure 3.8 (Table 3.3). The absorbance rises linearly to a maximum at 80 millimolar and remains constant above this concentration. The molar absorptivities determined from the experimental data agree with those obtained from a Beer's law calibration plot of acetylferrocene in an acidic melt ($[Na^+] = 0.5\text{ M}$). This is in good agreement with the electrochemical data above.

3.3.2 Dimethylaniline (DMA)

DMA is a stronger Lewis base than acetylferrocene and has been shown to form an aluminum chloride adduct in acidic room temperature molten salts¹⁴ according to Equation 3.15:



The equilibrium lies far to the right when $Al_2Cl_7^-$ is in excess over DMA. When DMA is in excess, a mixture of adduct and free DMA results. The 1H NMR spectrum of the methyl region shows a single line whose chemical shift (δ) is

$\epsilon \pm 5\%$ (dm ³ mol ⁻¹ cm ⁻¹)				
Melt	Species	454 nm	518 nm	580 nm
Basic	Free	426	140	12
Acidic	Adduct	872	2137	1083
Buffered	Adduct	904	2176	1106

Table 3.2 Molar absorptivity of acetylferrocene in AlCl₃:EMIC and alkali metal chloride neutral buffered melts

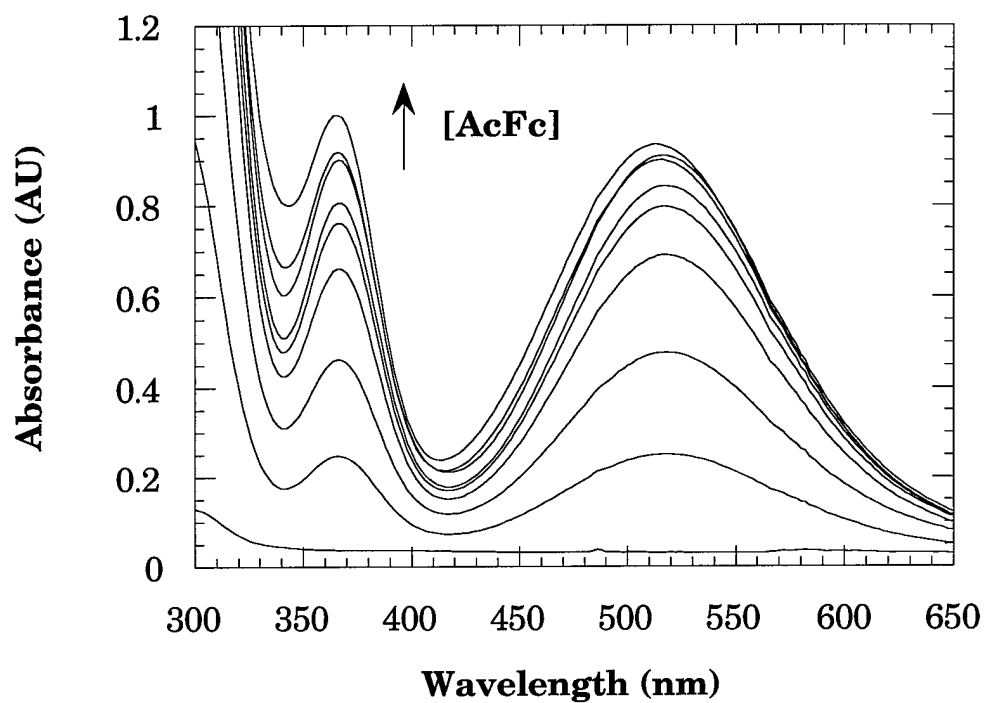


Figure 3.7 UV-vis spectra of acetylferrocene in a sodium chloride buffered melt.

The $[\text{Na}^+]$ concentration equals 80 mM. The UV-vis spectra are for a series of melts in which the acetylferrocene concentration equals: 0, 20, 40, 60, 70, 90, 95, 100, and 120 mM. The absorbance at 580 nm increases initially and then plateaus.

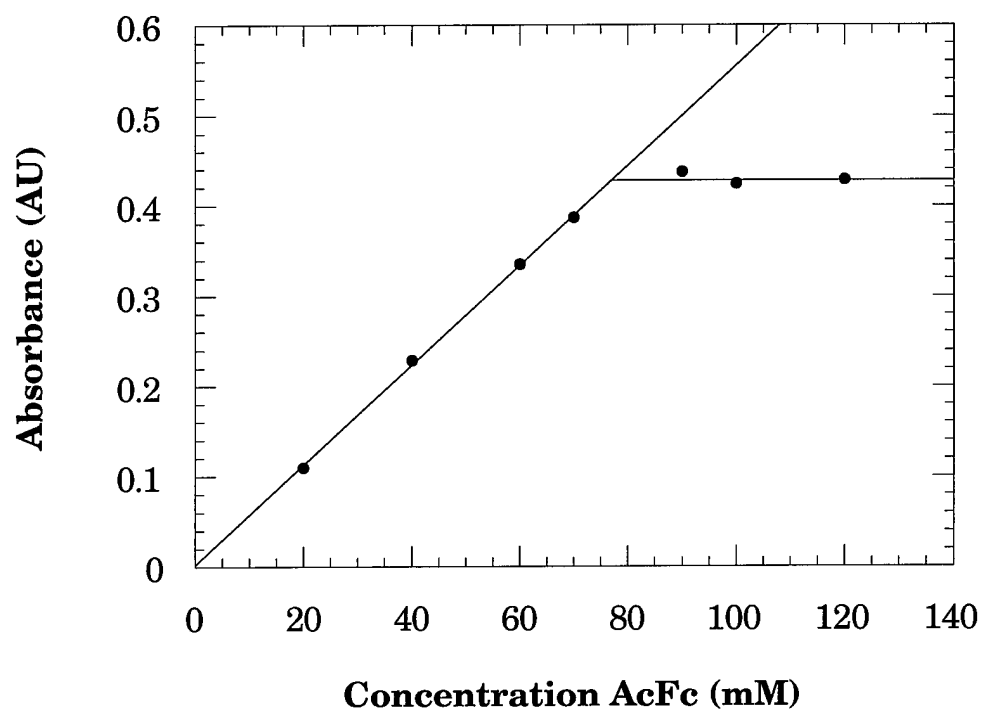


Figure 3.8 Plot of absorbance at 580 nm vs. acetylferrocene concentration in a 0.05 cm path length cell. Least squared fit lines show growth and plateau of the absorbance due to the acetylferrocene AlCl_3 adduct.

AcFc Concentration	580 nm	518 nm	454 nm
20	0.1097	0.2203	0.0896
40	0.2286	0.4459	0.1862
60	0.3354	0.6590	0.2718
70	0.3866	0.7650	0.3170
90	0.4378	0.8782	0.3844
100	0.4245	0.8672	0.4039
120	0.4283	0.8987	0.4578

Table 3.3 UV-vis data for absorbance at 580 nm vs. acetylferrocene concentration in a 0.05 cm path length cell. Prior to the addition of base $[\text{Na}^+] = 80 \text{ mM}$.

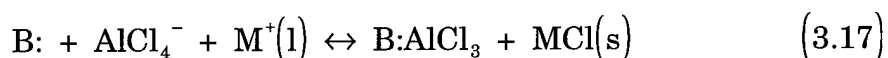
the population weighted average of the spectrum of the adduct and the free DMA (Equation 3.16).

$$\delta \text{ Free DMA } \left(\frac{\text{DMA}}{\text{DMA}_{\text{total}}} \right) + \delta \text{ DMA Adduct } \left(\frac{\text{DMA:AlCl}_3}{\text{DMA}_{\text{total}}} \right) \quad (3.16)$$

This is the result of a fast exchange process on the NMR timescale between DMA and DMA:AlCl₃. Similarly, the chemical shift of the methyl protons in a buffered melt also depends on the population weighted average of the adduct and the free DMA (Figure 3.9, Table 3.4). When the stoichiometry of [DMA]/[Na⁺] is less than 1 the chemical shift is that of the adduct. Above this the chemical shift decreases linearly with mole fraction of free DMA in exactly the same fashion as in an acidic melt (Figure 3.10, Table 3.5).

3.4 Conclusions

Our observations are in agreement with Equation 3.17, a general description of the chemistry of a Lewis base (B:) in a buffered melt:



The principle anionic species in NaCl neutral buffered melts and unbuffered melts is AlCl₄⁻. However weak Lewis bases behave very differently in buffered and unbuffered neutral melts. In the former, precipitation of NaCl provides the driving force for the formation of aluminum chloride adducts. Such adduct formation is not observed in the latter melts. Thus NaCl neutral buffered melts possess a latent acidity. The acidity is controlled by the amount

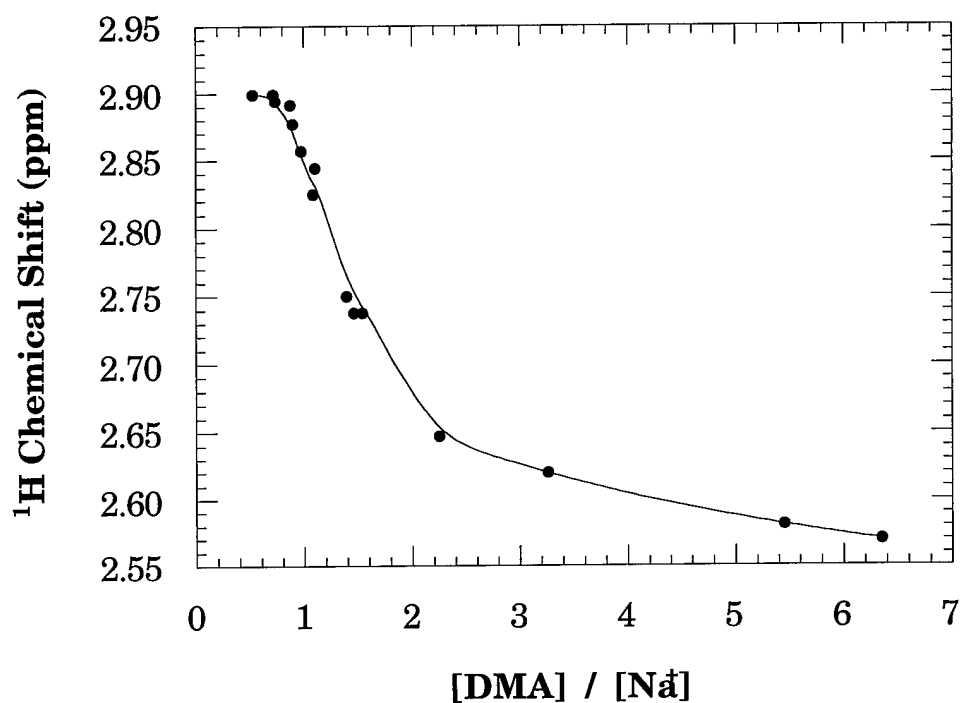


Figure 3.9 ^1H NMR chemical shift (ppm) of the DMA methyl hydrogen vs. DMA concentration divided by initial sodium cation concentration. When the $[\text{DMA}]/[\text{Na}^+]$ is less than one the chemical shift is 2.9 ppm which is the chemical shift of the DMA AlCl_3 adduct. As the ratio drops below 1 the chemical shift changes as more free DMA is in solution

[DMA] / [Na]	¹ H Chemical Shift (ppm)
0.52	2.899
0.71	2.899
0.73	2.894
0.87	2.891
0.89	2.877
0.97	2.857
1.08	2.825
1.10	2.844
1.39	2.750
1.46	2.738
1.54	2.738
2.25	2.647
3.26	2.620
5.45	2.581
6.35	2.570

Table 3.4 ¹H NMR chemical shift (ppm) of the DMA methyl hydrogen vs. DMA concentration divided by the initial sodium cation concentration.

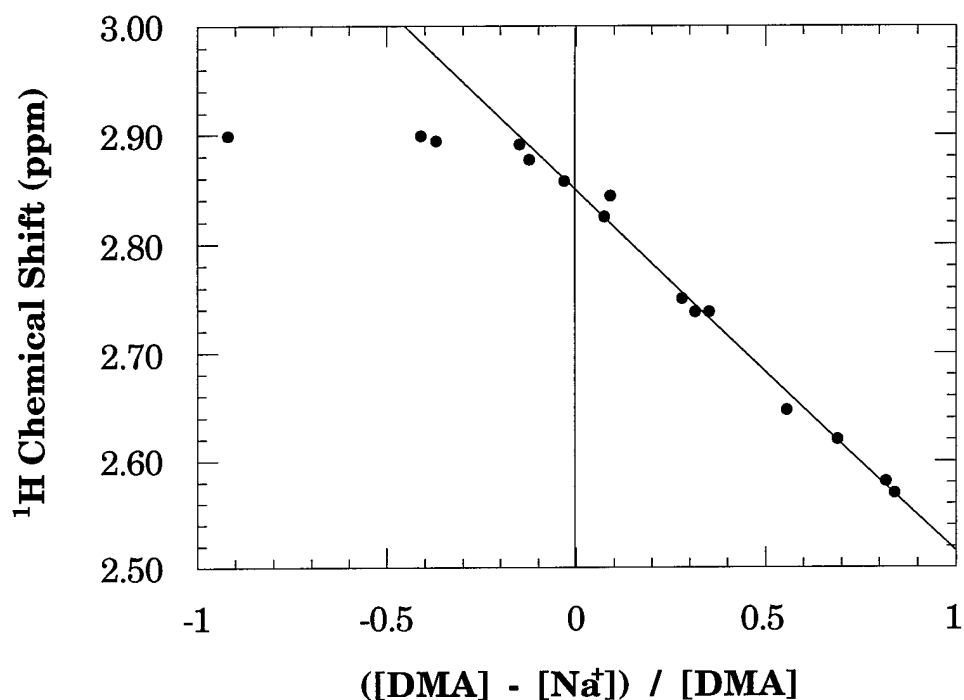


Figure 3.10 ^1H NMR shift (ppm) of dimethylaniline (DMA) methyl hydrogen vs. $([\text{DMA}]_t - [\text{Na}^+]) / [\text{DMA}]_t$. This shows the change in the chemical shift of the DMA methyl hydrogen as the AlCl_3 adduct is formed. When less DMA has been added than the $[\text{Na}^+]$ then only the adduct form is present and the chemical shift does not change. The chemical shift starts to change after the $[\text{DMA}]$ exceeds the initial $[\text{Na}^+]$ because now free DMA is present. The free DMA and the $\text{DMA}:\text{AlCl}_3$ adduct are in fast exchange on the NMR time scale. The observed chemical shift is the weighted average of the individual chemical shifts of each species.

$([\text{DMA}] / [\text{Na}]) / [\text{DMA}]$	^1H Chemical Shift (ppm)
-0.920	2.899
-0.410	2.899
-0.370	2.894
-0.150	2.891
-0.124	2.877
-0.031	2.857
0.074	2.825
0.090	2.844
0.280	2.750
0.315	2.738
0.350	2.738
0.556	2.647
0.690	2.620
0.817	2.581
0.840	2.570

Table 3.5 ^1H NMR shift (ppm) of dimethylaniline (DMA) methyl hydrogen vs. $([\text{DMA}]_t - [\text{Na}^+]) / [\text{DMA}]_t$.

of sodium ions in solution.¹⁵ These melts are an excellent medium in which to study AlCl_3 complexation, allowing precise control of the amount of AlCl_3 available for complexation and possessing a very large electrochemical window in which to observe complexed species.

Chapter 3 References

- (1) Melton, T. J.; Joyce, J.; Maloy, J. T.; Boon, J. A.; Wilkes, J. S. "Electrochemical Studies of Sodium Chloride as a Lewis Buffer for Room Temperature Chloroaluminate Molten Salts." *J. Electrochem. Soc.* **1990**, *137*, 3865-3869.
- (2) Scordilis-Kelley, C.; Fuller, J.; Carlin, R. T.; Wilkes, J. S. "Alkali Metal Reduction Potentials Measured in Chloroaluminate Ambient-Temperature Molten Salts." *J. Electrochem. Soc.* **1992**, *139*, 694-699.
- (3) Riechel, T. L.; Wilkes, J. S. "The Lewis Acidity of Room Temperature Chloroaluminate Molten Salts Buffered with Sodium Chloride." *J. Electrochem. Soc.* **1993**, *140*, 3104-3107.
- (4) Lipsztajn, M.; Osteryoung, R. A. "Increased Electrochemical Window in Ambient Temperature Neutral Ionic Liquids." *J. Electrochem. Soc.* **1983**, *130*, 1968-1969.
- (5) Quarmby, I. C.; Osteryoung, R. A. "Latent Acidity in Buffered Chloroaluminate Ionic Liquids." *J. Am. Chem. Soc.* **1994**, *116*, 2649-2650.
- (6) Cheek, G. *Proceedings of the Eighth International Symposium on Molten Salts* : The Electrochemical Society Softbound Series; Vol. 92-16, Gale, R. J.,

Blomgren, G., and Kojima, H., Editors, The Electrochemical Society: Pennington, NJ, 1992, pp.426-437.

(7) Zingg, S. P.; Dworkin, A. S.; Sørli, M.; Chapman, B. M.; Buchanan, A. C., III; Smith, G. P. "Brønsted Superacidity of HCl in a Liquid Chloroaluminate. AlCl_3 -1-Ethyl-3-methyl-1H-imidazolium Chloride." *J. Am. Chem. Soc.* **1989**, *111*, 525-530.

(8) Slocum, D. W.; Edgecombe, A. L.; Fowler, J. S.; Gibbard, H. F.; Phillips, J. "Substituent Effects on Ferrocenes in Aluminum Chloride-Butylpyridinium Chloride Molten-Salt Mixtures." *Organometallics* **1990**, *9*, 307-311.

(9) Cheek, G.; Osteryoung, R. A. "Electrochemical and Spectroscopic Studies of 9,10-Anthraquinone in a Room Temperature Molten Salt." *J. Electrochem. Soc.* **1982**, *129*, 2488-2496.

(10) Woodcock, C.; Shriver, D. F. "Electrochemistry and Spectroscopy of $\text{Fe}(\text{phen})_2(\text{CN})_2$, $\text{Cp}_4\text{Fe}_4(\text{CO})_4$, and $\text{CpFe}(\text{CO})_2\text{CN}$ in an Acidic Molten Salt." *Inorg. Chem.* **1986**, *25*, 2137-2141.

(11) Das, B.; Carlin, R. T.; Osteryoung, R. A. "The Ferro/ Ferricyanide Couple in an Aluminum Chloride-1-Methyl-3-ethylimidazolium Chloride Ambient-Temperature Molten Salt." *Inorg. Chem.* **1989**, *28*, 421-426 .

- (12) Karpinski, Z. J.; Osteryoung, R. A. "Spectrophotometric Studies of Iodine Complexes in an Aluminum Chloride-Butylpyridinium Chloride Ionic Liquid." *Inorg. Chem.* **1984**, *23*, 4561-4565.
- (13) Riechel, T. L.; Wilkes, J. S. "The Lewis Acidity of Room Temperature Chloroaluminate Molten Salts Buffered with Sodium Chloride." *J. Electrochem. Soc.* **1993**, *140*, 3104-3107.
- (14) Trulove, P. C.; Carlin, R. T.; Osteryoung, R. A. "Lewis and Bronsted Acid Adducts in Ambient Temperature Chloroaluminate Molten Salts: NMR Observations." *J. Am. Chem. Soc.* **1990**, *112*, 4567-4568.
- (15) Quarmby, I. C.; Mantz, R. A.; Goldenburg, L. M.; Osteryoung, R. A. "Stoichiometry of Latent Acidity in Buffered Chloroaluminate Ioinic Liquids." *Anal. Chem.* **1994**, *66*, 3558-3561.

Chapter 4

Gutmann Acceptor Numbers

4.1 Introduction

Gutmann acceptor numbers are a non-thermodynamic measure of the Lewis acidity of a solvent. They give a qualitative description of the solvent Lewis acidity and can be used to compare disparate solvents and to predict the chemistry of different solutes in these systems (Table 4.1).¹⁻³ Prior work in this laboratory described the Gutmann donor and acceptor number parameters for 1-ethyl-3-methylimidazolium and N-butylpyridinium based chloroaluminate melts, where EMIC is 1-ethyl-3-methylimidazolium chloride (Figure 4.1).⁴ However, since that time “neutral buffered” chloroaluminate melts have emerged.⁵ These new ternary melts provide researchers with systems that allow additional control of the melt properties.^{6,7} The acidity of these new melts is of interest and Gutmann acceptor numbers provide a way to make comparisons between the neutral buffered melts as well as between the neutral buffered melts and ethylmethylimidazolium-based melts.

The work reported here further characterizes these unique buffered chloroaluminate melt systems. A comparison is made between the Gutmann acceptor numbers of the LiCl, NaCl, KCl neutral buffered melts and the binary AlCl_3 / EMIC melts and how the acceptor numbers vary with melt composition for the four systems.

Solvent	Acceptor Number (AN)
Hexane (0 reference)	0.0
Diethyl Ether	3.9
Benzene	8.2
Acetonitrile	19.3
Ethyl alcohol	37.1
Water	54.8
Et ₃ O-SbCl ₅ in 1,2-dichloroethane (100 reference)	100
Trifluoroacetic acid	105.3
Methylsulfonic acid	126.1

Table 4.1 Typical Gutmann acceptor numbers.

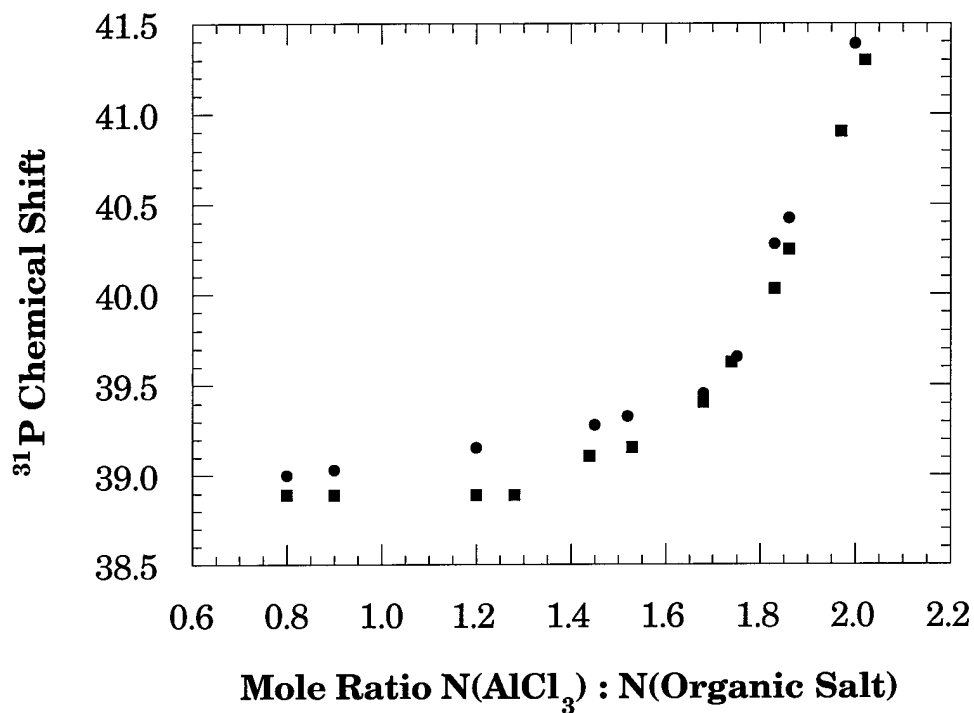


Figure 4.1 ^{31}P chemical shift of TEPO dissolved of N-butylpyridinium chloride and 1-ethyl-3-methylimidazolium chloride based chloroaluminate ionic liquids. The Gutmann acceptor numbers are proportional to this data after correction for concentration and magnetic susceptibility effects. (●) AlCl_3 :EMIC melts. (■) AlCl_3 :BuPyCl melts.

Gutmann acceptor numbers have been determined using ^{31}P nuclear magnetic resonance (NMR) for AlCl_3 / EMIC melts as well as LiCl , NaCl , and KCl neutral buffered melts. In AlCl_3 / EMIC melts the change in the Gutmann acceptor number is a function of the AlCl_3 :EMIC melt ratio and is attributed to an equilibrium between a mono- and diadduct of triethylphosphine oxide and AlCl_3 . In neutral buffered melts the changes in the Gutmann acceptor numbers appear linear with respect to the melt initial mole ratio of AlCl_3 :EMIC prior to buffering. The lithium cation appears to be the most Lewis acidic followed by the sodium and potassium. Possible reasons for the change in acceptor number as a function of changing alkali metal cation concentration are presented here.

4.2 Specialized Experimental Procedures

4.2.1 Materials

Triethylphosphine oxide (TEPO) (Alfa Chemical) was purified by sublimation under vacuum (1×10^{-3} torr) at room temperature and collected in a trap held at 0°C prior to use.²

4.2.2 Equipment and Procedures

4.2.2.1 NMR Preparation

10 mm nuclear magnetic resonance (NMR) tubes were prepared by soaking in 50% HNO_3 heated to 90 °C, rinsing with deionized water, soaking in a solution of the tetrasodium salt of EDTA for 12 hours at room temperature, and again rinsing with deionized water. ^{31}P NMR spectra (121.50 MHz) were obtained with the probe temperature maintained at 31.0 °C, and each sample was allowed to equilibrate while rotating at 10 Hz for at least 5 minutes prior to spectral acquisition. Spectra consisted of 64 scans with a sweep width of 128.6 ppm and a relaxation delay time of 2.0 seconds. An exponential multiplication with a line broadening of 2.0 Hz was applied to the acquired free induction decay (FID). The chemical shift was externally referenced to an 85% phosphoric acid in water sample (0 ppm) whose spectrum was obtained using identical acquisition and processing parameters.

4.2.2.2 Triethylphosphine Oxide Concentration Effect On Chemical Shift

Experiments were conducted to determine the change in chemical shift of the triethylphosphine oxide (TEPO) versus the concentration of the TEPO in the melt. Four melts were prepared, a 1.30:1.00 melt, a 1.15:1.00 LiCl buffered melt, a 1.30:1.00 NaCl buffered melt, and a 1.30:1.00 KCl buffered melt. Each

melt was divided into six portions and TEPO was added to make 5, 10, 25, 50, 100, and 300 mM solutions. The solutions were allowed to stir for 24 hours at $\approx 60^\circ\text{C}$ to ensure complete dissolution of the TEPO. After stirring for 24 hours, the samples were allowed to cool to room temperature. The resultant solution was filtered through a 0.1 mm PTFE (Whatman) filter disk (13 mm diameter) using a 5 mL syringe (B&D tuberculine, polyethylene, natural rubber latex) into a 9 inch long 10 mm Wilmad NMR tube that had been constricted at 8 inches. For the buffered melts a tip-off manifold was placed on each tube, the sealed assembly was removed from the dry box and flame sealed under vacuum ($\approx 1 \times 10^{-2}$ torr). The unbuffered melts were capped and sealed with Parafilm. ^{31}P spectra were obtained for each sample (Table 4.2).

4.2.2.3 Change in ^{31}P Chemical Shift of TEPO vs. Melt Composition

Experiments were conducted to determine the change in the chemical shift of the TEPO versus the melt composition. Melt compositions of the unbuffered and of the LiCl, NaCl, and KCl buffered melts were made that corresponded to initial AlCl_3 :EMIC mole ratios of 1.05:1.00, 1.10:1.00, 1.15:1.00, 1.20:1.00, 1.30:1.00, 1.40:1.00, 1.50:1.00, 1.70:1.00, and 1.90:1.00. In addition, an unbuffered melt with a mole ratio of 0.99:1.00 was prepared. TEPO was added to each melt to make 10 mM solutions. The solutions were prepared as described above. ^{31}P spectra were obtained for each sample (Table 4.3).

TEPO Concentration (mM)	Acidic Melt	LiCl Neutral Buffered Melt	NaCl Neutral Buffered Melt	KCl Neutral Buffered Melt
5.0	82.803	82.783	82.988	82.897
10.0	82.795	82.773	82.985	82.874
25.0	82.782	82.776	82.978	82.930
50.0	82.771	82.751	82.961	82.863
100.0	82.757	82.717	82.950	82.830
300.0	82.666	82.623	82.854	82.750

Table 4.2 Dependence of the ^{31}P chemical shift of TEPO on TEPO concentration

Melt Composition	Binary Melt	LiCl Neutral Buffered Melt	NaCl Neutral Buffered Melt	KCl Neutral Buffered Melt
0.80	82.703	–	–	–
0.99	82.532	–	–	–
1.00	82.529	–	–	–
1.05	82.564	82.638	82.634	82.601
1.10	82.584	82.693	82.716	82.663
1.15	82.619	82.773	82.802	82.715
1.20	82.667	82.870	82.860	82.730
1.30	82.787	83.08	83.022	82.809
1.40	82.948	83.303	83.16	82.869
1.50	83.179	83.498	83.321	82.903
1.70	83.867	83.867	83.565	–
1.90	85.393	84.196	–	–

Table 4.3 ^{31}P chemical shift of TEPO vs. melt composition. This is the NMR data prior to the concentration and magnetic susceptibility corrections.

4.2.2.4 Identification of Small Downfield Peak

Most ^{31}P NMR spectra consisted of a single peak (Figure 4.2). However, some spectra contained a small downfield peak. In order to determine the cause of the small downfield peak three samples whose preparation is described above were modified. These three samples consisted of a 1.30:1.00 unbuffered melt containing 50 mM, 100 mM and 300 mM TEPO. To the 100 mM and 300 mM TEPO containing melts, 1-ethyl-3-methylimidazolium hydrogen dichloride was added so that the same concentration of HCl as TEPO was present in the melt.⁸ A ten-fold excess of H_2O was added to the sample containing 50 mM TEPO. This sample was warmed and stirred for several hours to allow the water to fully react and to allow the resulting crust to dissolve in the melt. The samples were flame sealed under vacuum as described above.

4.2.2.5 Determination of Volume Magnetic Susceptibilities

Volume magnetic susceptibilities were determined using a variation of Becconsall's method.^{9,10} Samples were prepared by flame sealing benzene-*d*6 in the inner coaxial tube from a Wilmad 10 mm coaxial tube pair. The melt of interest was placed in the outer tube to which approximately 5% by weight of benzene-*d*6 had been added (Figure 4.3). The chemical shift of the benzene-*d*6 dopant in the outer tube did not appear to change due to any reaction between the melt and the benzene although the benzene does decompose over time.

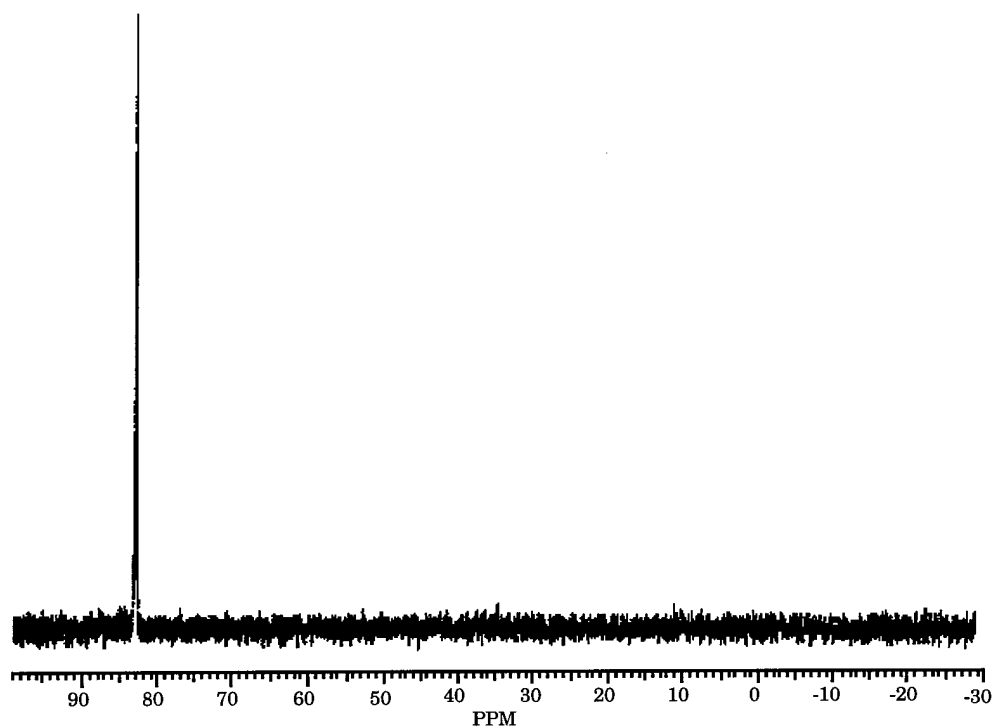


Figure 4.2 Typical ^{31}P NMR spectrum. This spectrum is of 10 mM TEPO dissolved in a LiCl neutral buffered melt. The initial melt ratio prior to buffering was 1.5:1.0.

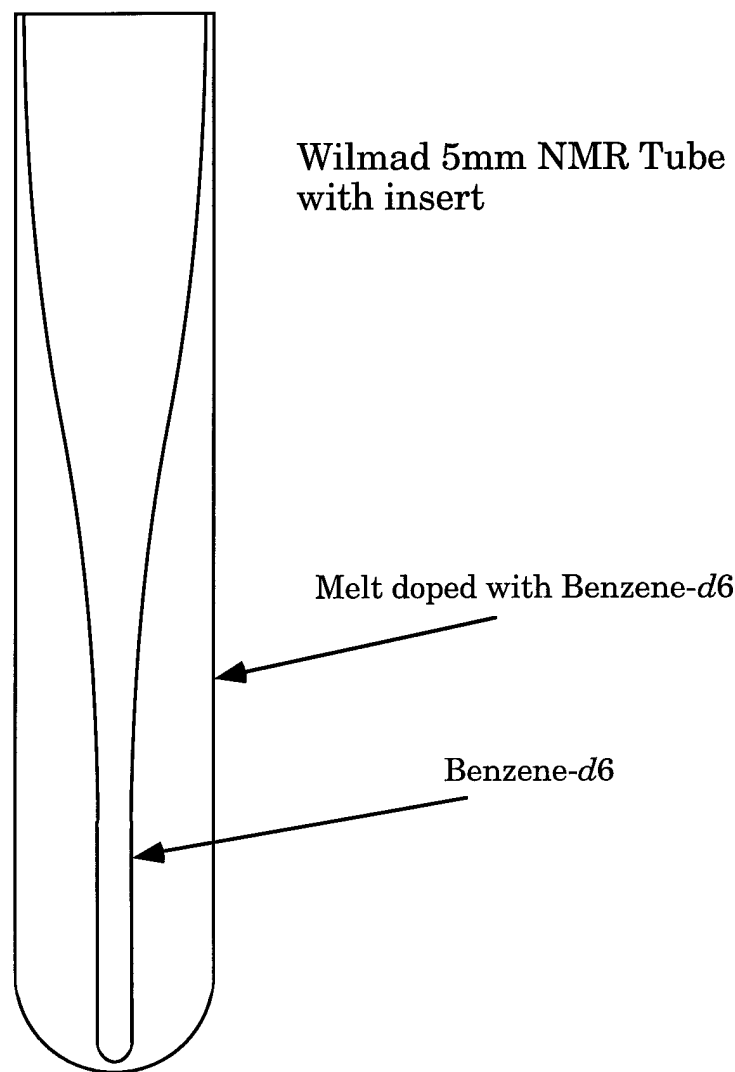


Figure 4.3 Coaxial tube configuration for volume magnetic susceptibility (χ_v) measurements.

The inner coaxial tube was inserted into the 10 mm NMR tube and the entire apparatus was then capped and sealed with Parafilm. These samples were analyzed in both a Bruker AC-300 (75.47 MHz) and a JEOL FX-90Q (22.48 MHz) using ^{13}C NMR. The probe on each spectrometer was maintained at 31 °C, and each sample was allowed to equilibrate for at least 5 minutes while rotating at 10 Hz in the Bruker and 15-20 Hz in the JEOL prior to spectral acquisition. Each spectrometer was locked on the benzene-*d*6 in the sample. Spectra on the Bruker AC-300 consisted of 16 scans with a sweep width of 161.6 ppm and a relaxation delay time of 2.0 seconds. An exponential multiplication with a line broadening of 2.0 Hz was applied to the acquired FID. Spectra on the JEOL FX-90Q consisted of 64 scans with a sweep width of 111.0 ppm and a relaxation delay of 2.0 seconds. An exponential multiplication with a line broadening of 1.0 Hz was applied to the acquired FID. The volume magnetic susceptibility was then calculated from the differences in ^{13}C chemical shifts with the two different field axes between the benzene-*d*6 in the inner and annular region of the coaxial pair (Table 4.4).

Assuming cylindrical samples of infinite length, the chemical shift contribution due to the volume bulk susceptibility for an electromagnet when the sample direction is perpendicular to the magnetic field is:⁹

$$\delta_{\text{b}}^{\perp} = \frac{2}{3} \pi \chi_{\text{v}} \quad (4.1)$$

χ_{v} is the volume bulk magnetic susceptibility, and δ_{b} is the bulk magnetic susceptibility contribution. Making the sample assumptions stated above for a superconducting magnet when the sample direction is parallel to the magnetic

A

Melt Ratio	Binary Melt	LiCl Neutral Buffered Melt	NaCl Neutral Buffered Melt	KCl Neutral Buffered Melt
0.99	1.2152	–	–	–
1.00	1.2196	–	–	–
1.05	1.1876	1.2511	1.2422	1.1832
1.10	1.2209	1.2192	1.2378	1.2782
1.15	1.2196	1.2374	1.2738	1.2600
1.20	1.2467	1.2644	1.2422	1.2689
1.40	1.2915	1.2866	1.3008	–
1.50	1.2711	1.3097	1.3186	–
1.90	1.3595	1.4318	1.3279	–

B

Melt Ratio	Binary Melt	LiCl Neutral Buffered Melt	NaCl Neutral Buffered Melt	KCl Neutral Buffered Melt
0.99	0.1194	–	–	–
1.00	0.1206	–	–	–
1.05	0.1190	0.1076	0.1109	0.1268
1.10	0.1095	0.0988	0.1034	0.1201
1.15	0.1094	0.0880	0.0981	0.1078
1.20	0.1040	0.0863	0.0918	0.1127
1.40	0.0897	0.0588	0.0769	–
1.50	0.0892	0.0439	0.0437	–
1.90	0.0798	0.0318	0.0459	–

Table 4.4 ^{13}C chemical shift differences (ppm) of benzene- d_6 between inner and annular regions of coaxial pair A. Perpendicular (Electromagnet), B. Parallel (Superconducting Magnet)

field the chemical shift due to the volume bulk susceptibility is:⁹

$$\delta_b^{\parallel} = - \frac{4}{3} \pi \chi_v \quad (4.2)$$

By comparing the same solvent in the inner and annular portions of a coaxial NMR tube and observing the chemical shift difference, one can solve for the volume magnetic susceptibility using the following two equations.⁹

$$\delta_{\text{sol}}^{\perp}(\text{y}) - \delta_{\text{sol}}^{\perp}(\text{x}) = \frac{2}{3} \pi \left[\chi_v(\text{y}) - \chi_v(\text{x}) \right] + \delta_{\text{loc}}(\text{y}) - \delta_{\text{loc}}(\text{x}) \quad (4.3)$$

$$\delta_{\text{sol}}^{\parallel}(\text{y}) - \delta_{\text{sol}}^{\parallel}(\text{x}) = - \frac{4}{3} \pi \left[\chi_v(\text{y}) - \chi_v(\text{x}) \right] + \delta_{\text{loc}}(\text{y}) - \delta_{\text{loc}}(\text{x}) \quad (4.4)$$

δ_{sol} in these two equations is the chemical shift of the benzene-*d*6 in the inner and annular region of the coaxial pair. δ_{loc} is the chemical shift due to "local" effects (effects other than bulk susceptibility). "y" is the solvent of which the magnetic susceptibility is being determined, and "x" is a solvent with known magnetic susceptibility. δ_{sol} is what is actually measured experimentally.

Combining the above equations results in:⁹

$$\delta_{\text{loc}}(\text{y}) - \delta_{\text{loc}}(\text{x}) = \frac{1}{3} \left[\delta_{\text{sol}}^{\parallel}(\text{y}) - \delta_{\text{sol}}^{\parallel}(\text{x}) + 2 \left(\delta_{\text{sol}}^{\perp}(\text{y}) - \delta_{\text{sol}}^{\perp}(\text{x}) \right) \right] \quad (4.5)$$

δ_{sol} is the measured chemical shift of the solvent in the coaxial NMR tube. After measuring the chemical shift differences in both the electromagnet and the superconducting magnet, $\delta_{\text{loc}}(\text{y}) - \delta_{\text{loc}}(\text{x})$ can be calculated. Next, this value is substituted into either Equation 4.1 or Equation 4.2 for δ_b to give:

$$\chi_v^\perp = \frac{3}{2\pi} \left(\delta_{\text{loc}}^\perp(\text{y}) - \delta_{\text{loc}}^\perp(\text{x}) \right) \quad (4.6)$$

$$\chi_v^{\parallel} = - \frac{3}{4\pi} \left(\delta_{\text{loc}}^{\parallel}(\text{y}) - \delta_{\text{loc}}^{\parallel}(\text{x}) \right) \quad (4.7)$$

χ_v^\perp should equal χ_v^{\parallel} . Finally, this χ_v must be corrected using the x solvent magnetic susceptibility, which is known, to obtain the magnetic susceptibility of the solvent of interest (Table 4.5):

$$\chi_v(\text{y}) = \chi_v(\text{x}) + \chi_v^{\parallel} \quad (4.8)$$

Once the magnetic susceptibility is known, the correction to the chemical shift in a superconducting magnet is calculated using:

$$\delta_{\text{corr}} = - \frac{4}{3} \pi \left(\chi_v(\text{hexane}) - \chi_v(\text{melt}) \right) \quad (4.9)$$

4.2.2.6 Determination of Alkali Metal Concentration in Neutral Buffered Melts

Neutral buffered melt samples for inductively coupled plasma (ICP) analysis were prepared by first pipetting 100 μL of melt into a 100 mL volumetric flask. The flask was then fitted with a rubber septum and transferred out of the dry box. Approximately 20 mL of water (18 M Ω) was added through the septum with a syringe and needle. The water was then swirled until all the melt dissolved. Finally, the septum was removed and water added to make the volume total 100 mL.

Elemental analysis was performed by using a Leeman Lab PS Series

Melt Composition	Binary Melt	LiCl Neutral Buffered Melt	NaCl Neutral Buffered Melt	KCl Neutral Buffered Melt
0.99	-0.79439	—	—	—
1.00	-0.79491	—	—	—
1.05	-0.79008	-0.80200	-0.80005	-0.78812
1.10	-0.79689	-0.79831	-0.80054	-0.80432
1.15	-0.79670	-0.80293	-0.80712	-0.80338
1.20	-0.80186	-0.80750	-0.80310	-0.80401
1.40	-0.81128	-0.81542	-0.81480	—
1.50	-0.80811	-0.82147	-0.82291	—
1.90	-0.82366	-0.84282	-0.82404	—

Table 4.5 Volume magnetic susceptibility of melts (ppm) determined for the binary and alkali chloride neutral buffered melts.

1000 Sequential ICP (Leeman Labs, Lowell, MA) with an Echelle spectrometer and Hildebrand Grid nebulizer system. The ICP is a computer controlled, sequential instrument allowing rapid elemental analysis. For this analysis each element was determined using the emission lines 670.784 nm for lithium, 589.592 nm for sodium, and 766.490 nm for potassium (Table 4.6). Additional instrumental parameters used for this study were 1.0 kW of power, 40.68 MHz Flagg Oscillator, 14 Lpm coolant flow rate, a nebulizer pressure of 40 psi, and sample introduction of 1.0 mL/min.

4.3 Results and Discussion

4.3.1 NMR Data

^{31}P NMR spectra of pure solutions of triethylphosphine oxide (TEPO) in all melts generally consisted of a single line and did not change over the course of several days. The ^{31}P NMR chemical shift data must be corrected prior to acceptor number determination. The first correction is the extrapolation of the ^{31}P chemical shift to infinite dilution of TEPO in the melt. The second correction is for the contribution made to the observed ^{31}P chemical shift by the volume bulk magnetic susceptibility (χ_v).

The effect of the TEPO concentration on the ^{31}P chemical shift was determined for AlCl_3 / EMIC melts as well as melts buffered with lithium, sodium, and potassium. A linear equation was fitted to the resultant data and

Melt Composition	LiCl Neutral Buffered Melt	NaCl Neutral Buffered Melt	KCl Neutral Buffered Melt
1.05	0.26797	0.28491	0.24068
1.10	0.54603	0.50022	0.47828
1.15	0.81400	0.80906	0.61640
1.20	0.96960	1.1135	0.63686
1.30	1.4119	1.4354	0.58570
1.40	1.8369	1.7138	—
1.50	2.1179	1.7312	—
1.70	—	—	—
1.90	3.7603	—	—

Table 4.6 Alkali metal concentrations determined from ICP data for a series of alkali metal chloride neutral buffered melts in which the melt composition prior to buffering has been varied.

the resultant function extrapolated to infinite dilution (Figure 4.4 and Table 4.7). The TEPO concentration used to determine the acceptor numbers was 10 mM, thus the correction by extrapolating to infinite dilution of TEPO was ≈ 0.005 ppm.

Correction for magnetic susceptibility effects required additional experiments as mentioned above, but they did result in a much larger chemical shift correction, approximately 1 ppm. The magnetic susceptibility was measured as outlined previously, and a linear function was fit to the data (Figure 4.5 and Table 4.8). This resultant function was then used to determine the chemical shift correction necessary for each melt composition.

Experiments were conducted in which the melt composition and the buffering alkali metal chloride were varied. After applying both corrections to the observed chemical shift data, the data were converted into Gutmann acceptor numbers using:¹

$$AN = 2.348 \times (\delta_{\text{CORR}}) \quad (4.10)$$

δ_{CORR} is the ^{31}P chemical shift using TEPO in hexane as the zero reference chemical shift (Tables 4.9 and 4.10). It should be noted that the melt ratio in the neutral buffered cases is the original melt ratio prior to addition of alkali halide. After buffering, the only anion present is AlCl_4^- and the alkali metal concentration is equal to the original Al_2Cl_7^- concentration.

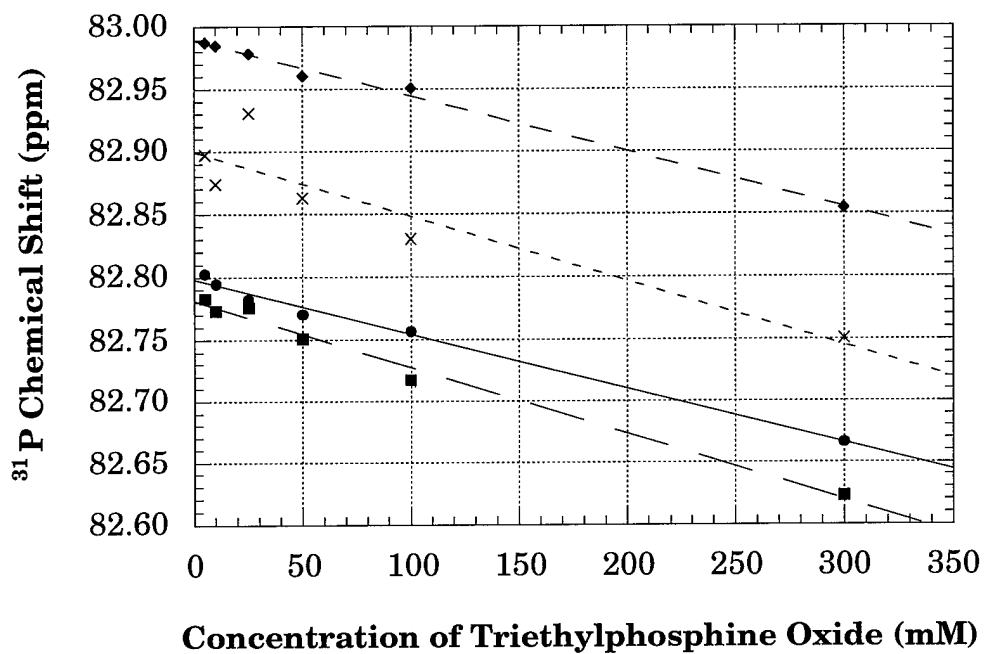


Figure 4.4 ^{31}P NMR chemical shift dependence of triethylphosphine oxide upon the concentration of triethylphosphine oxide in the melt (—●— Acidic melt, —■— LiCl buffered melt, —◆— NaCl buffered melt, --×-- KCl buffered melt).

^{31}P NMR Shift (ppm) = m [TEPO (mM)] + b		
Melt	m	b
Unbuffered	$-4.4 \times 10^{-4} \pm 2 \times 10^{-5}$	82.798 ± 0.003
LiCl Buffered	$-5.3 \times 10^{-4} \pm 3 \times 10^{-5}$	82.781 ± 0.003
NaCl Buffered	$-4.4 \times 10^{-4} \pm 2 \times 10^{-5}$	82.989 ± 0.002
KCl Buffered	$-5 \times 10^{-4} \pm 1 \times 10^{-4}$	82.90 ± 0.01

Table 4.7 ^{31}P NMR Chemical Shift Dependence on TEPO Concentration for the $\text{AlCl}_3\text{:EMIC}$ binary and alkali chloride neutral buffered melts. The data is the result of a linear least squares fit of the data.

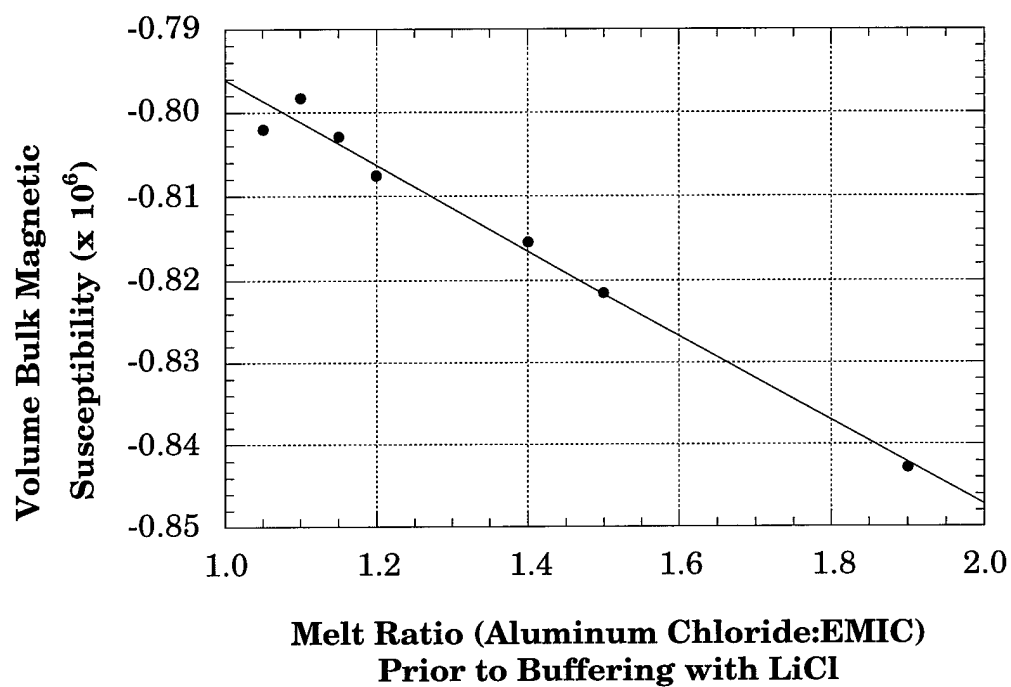


Figure 4.5 Volume bulk magnetic susceptibility (χ_v) of LiCl neutral buffered AlCl_3 / EMIC ionic liquid. The plot shows the change in magnetic susceptibility as the mole ratio of the melt prior to buffering is altered. The line is the linear least squared fit of the data points.

Magnetic Susceptibility ($\times 10^6$) = m (Melt Ratio) + b		
Melt	m	b
Unbuffered	-0.034 ± 0.003	-0.759 ± 0.004
LiCl Buffered	-0.051 ± 0.003	-0.745 ± 0.004
NaCl Buffered	-0.031 ± 0.006	-0.769 ± 0.008
KCl Buffered	-0.09 ± 0.06	-0.69 ± 0.06

Table 4.8 Volume bulk magnetic susceptibility of the binary and alkali chloride neutral buffered melts.

Melt Ratio	Acceptor Number
1.05	95.895
1.10	95.959
1.15	96.058
1.20	96.188
1.30	96.503
1.40	96.915
1.50	97.491
1.70	99.174
1.90	102.820

Table 4.9 Gutmann acceptor numbers of binary $\text{AlCl}_3\text{:EMIC}$ melts. The data shows the change in Gutmann acceptor number as the mole ratio of the melt is altered.

Initial Melt Ratio	LiCl Neutral Buffered Melt	NaCl Neutral Buffered Melt	KCl Neutral Buffered Melt
1.05	96.105	96.125	95.962
1.10	96.260	96.333	96.154
1.15	96.473	96.550	96.322
1.20	96.725	96.702	96.403
1.30	97.269	97.113	96.680
1.40	97.843	97.468	96.913
1.50	98.351	97.877	97.085
1.70	99.318	98.511	—
1.90	100.190	—	—

Table 4.10 Gutmann acceptor numbers for each of the alkali metal chloride neutral buffered melts and the melts initial mole ratio prior to buffering.

4.3.2 ICP Data

In addition, a series of experiments were conducted in which ICP was used to determine the lithium, sodium, and potassium concentrations in the different compositions of neutral buffered melts (Figure 4.6). These data were originally obtained with units of parts per million. In order to allow direct comparison between the different alkali metals, these data were corrected by dividing each data point by the atomic weight of the alkali metal. One experimental complication was revealed by the ICP data, which were taken much later than the NMR data. The ICP data for both the NaCl and KCl neutral buffered melts show a plateau for the alkali metal concentration at lower mole ratios even though the NMR data showed Gutmann acceptor number changes in the same region. This indicates that the NaCl and KCl neutral buffered melts prepared from acidic melts with mole ratios greater than $\approx 1.1:1.0$ for KCl and $1.4:1.0$ for NaCl were initially supersaturated.

More importantly the ICP results represent the first determination of the extent of buffering possible with different alkali metal chloride salts. When an acidic melt is buffered with an alkali metal chloride salt, usually the metal salt dissolves as it reacts with the Al_2Cl_7^- and excess metal chloride salt remains in solid form. In some cases, when the melt was heated, the alkali metal salt would dissolve, but upon cooling a solid would precipitate. In these cases we found that as we increased the initial concentration of Al_2Cl_7^- more solid would precipitate. This solid is presumably MAlCl_4 . The buffering limit would therefore depend upon the solubility of MAlCl_4 in a neutral melt. When

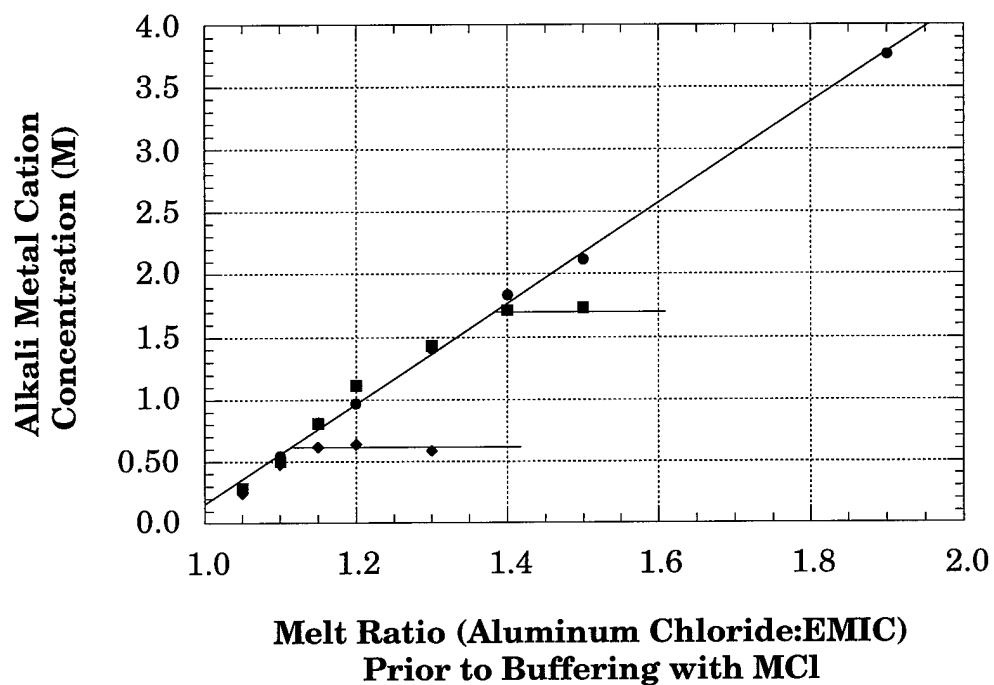
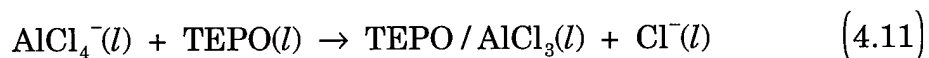


Figure 4.6 Alkali metal cation concentration determined using ICP versus the mole ratio of AlCl_3 to EMIC prior to buffering (—●— LiCl buffered melt, --■-- NaCl buffered melt, --◆-- KCl buffered melt). The horizontal lines are the maximum concentration of the alkali metal in the melt.

the solubility limit has been reached, MAlCl_4 will precipitate from solution. If a melt contains additional Al_2Cl_7^- , the MCl will continue to react with the additional Al_2Cl_7^- as the MAlCl_4 that is formed precipitates. Therefore, the solubility limit of MAlCl_4 defines the maximum concentration of metal cation in solution. Using ICP, the solubility of MAlCl_4 was determined, and the buffering limits were determined for LiCl , NaCl and KCl neutral buffered melts. The buffering ability of LiCl is greater than an initial mole ratio of 1.9:1.0, whereas for NaCl the limit is $\approx 1.4:1.0$, and for the KCl it is $\approx 1.1:1.0$.

4.3.3 Gutmann Acceptor Numbers of Binary AlCl_3 / EMIC Melts

The results for the binary AlCl_3 / EMIC melts have been interpreted based upon earlier results which demonstrated that the observed acceptor number in binary AlCl_3 / EMIC was a function of melt composition.⁴ Our results for the binary melts are in agreement with this prior work. In basic and neutral melts, the acceptor number is a constant 95.8 for an AlCl_3 monoadduct and does not change. This appears to be due to solvent leveling (Equation 4.11).⁴



In melts with acidic compositions, the change in acceptor number is due to the formation of an $\text{TEPO} / 2\text{AlCl}_3$ diadduct caused by the strong Lewis acidity of Al_2Cl_7^- .



Only a single ^{31}P NMR peak is observed, indicating the monoadduct and diadduct species are in fast equilibrium on the NMR timescale. Thus, contributions from both sides of the equilibrium (Equation 4.12) must be considered. The observed chemical shift is a weighted average of the concentration of the two species multiplied by their respective chemical shifts. The acceptor number is directly related to the ^{31}P NMR chemical shift (Equation 4.10). In order to quantitate this observed phenomenon, the equilibrium based on the above equation and the anionic composition were calculated for each melt composition. Because significant contributions from $\text{Al}_3\text{Cl}_{10}^-$ are present only in melt compositions above $\approx 1.7:1.0$ ($\text{AlCl}_3:\text{EMIC}$), melt compositions were calculated neglecting the $\text{Al}_3\text{Cl}_{10}^-$ contributions and only AlCl_4^- and Al_2Cl_7^- contributions were considered. Fitting the results with Equation 4.12 results in an equilibrium constant, K for Equations 4.12 and 4.13 of 0.158 ± 0.008 , an acceptor number for the diadduct of 108.1 ± 0.3 , and R^2 of 0.9993 (Figure 4.7).

$$\text{AN} = \frac{95.8}{\frac{\text{Equilibrium Constant} \times [\text{Al}_2\text{Cl}_7^-]}{[\text{AlCl}_4^-]} + 1} + \frac{\text{Diadduct Acceptor Number}}{\frac{[\text{Al}_2\text{Cl}_7^-]}{\text{Equilibrium Constant} \times [\text{AlCl}_4^-]} + 1} \quad (4.13)$$

Fitting the data using a function that contains the $\text{Al}_3\text{Cl}_{10}^-$ contributions simply results in greater uncertainty for the equilibrium constants and the diadduct acceptor number. It should be noted that given the data above, the maximum acceptor number that is theoretically possible is ≈ 108 , and it should also be noted that the magnitude of K shows that even at large Al_2Cl_7^-

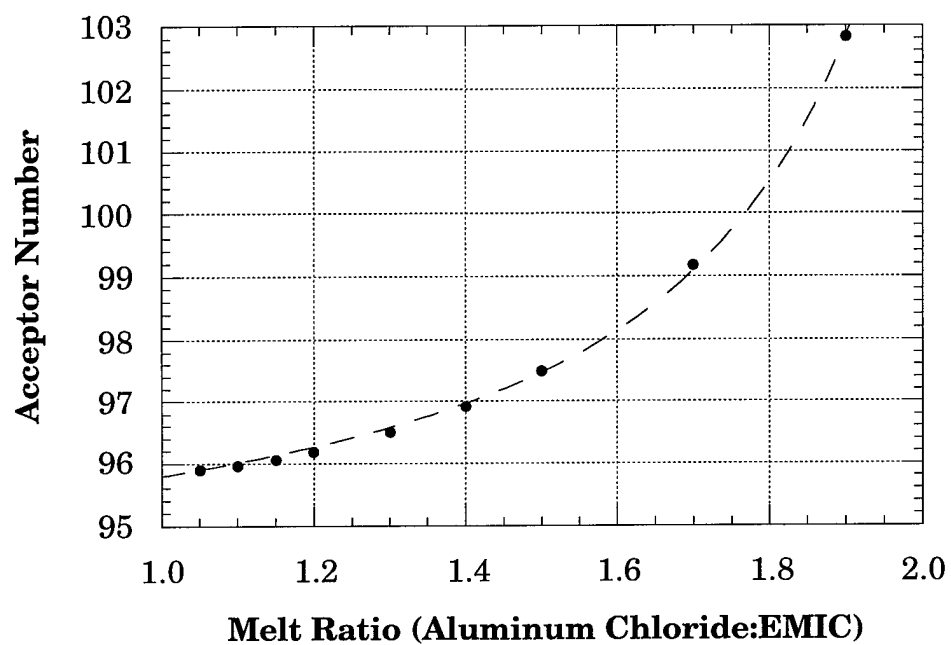


Figure 4.7 Dependence of the Gutmann acceptor number for binary melts upon the mole ratio of AlCl_3 to EMIC. Points are experimental data while the line is the fit using Equation 4.13.

concentrations there is only a small amount of diadduct formed. The TEPO / AlCl_3 monoadduct is such a weak base that Al_2Cl_7^- does not react with it to any substantial degree.

To calculate the Gutmann acceptor number (AN) of a binary melt of known composition, the AlCl_4^- and Al_2Cl_7^- anionic mole fractions must first be calculated from the melt ratio.⁵ Taking these values and substituting them into Equation 4.14 gives the expected Gutmann acceptor number for the melt.

$$\text{AN} = \frac{95.8}{\frac{0.158 [\text{Al}_2\text{Cl}_7^-]}{[\text{AlCl}_4^-]} + 1} + \frac{108.1}{\frac{[\text{AlCl}_4^-]}{0.158 [\text{Al}_2\text{Cl}_7^-]} + 1} \quad (4.14)$$

4.3.4 Gutmann Acceptor Numbers of Alkali Metal Neutral Buffered Melts

The determination of the acceptor numbers of the alkali metal neutral buffered melts was completed in the same fashion as those for the binary melts using Equation 4.10. The plot of acceptor number versus the melt ratio of AlCl_3 :EMIC prior to buffering is linear. It is important to remember that the melt ratio prior to buffering corresponds to the alkali metal cation concentration in the buffered melt. The linear function results in very good fits for the LiCl, NaCl, and KCl buffered melts, with $R^2 = 0.9981$, 0.9982 , and 0.9888 , respectively (Figure 4.8 and Table 4.11). Using the linear functions for each of the three buffered melts, the acceptor numbers can be estimated. It

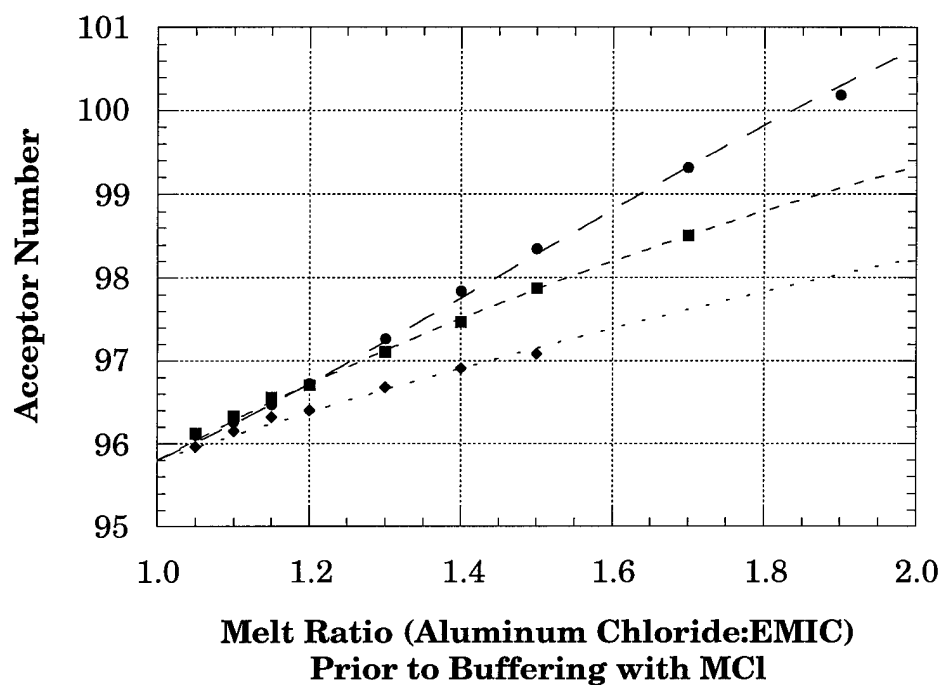


Figure 4.8 Dependence of the Gutmann acceptor number for alkali metal chloride neutral buffered melts upon the mole ratio of AlCl_3 to EMIC. (Note: This is the mole ratio prior to buffering. During buffering the Al_2Cl_7^- anions react with an equal number of alkali metal chlorides.) The data fit has been performed using the equilibrium explanation from the text (—●— LiCl buffered melt, —■— NaCl buffered melt, --◆-- KCl buffered melt).

AN = m (Melt Ratio) + b			
Buffering Agent	m	b	R ²
LiCl	4.97 ± 0.08	90.8 ± 0.1	0.9981
NaCl	3.70 ± 0.06	92.28 ± 0.08	0.9982
KCl	2.5 ± 0.1	93.4 ± 0.1	0.9888

Table 4.11 Least squared fit values of the Gutmann acceptor numbers of alkali metal chloride neutral buffered melts to a linear equation.

should be noted that because the melts prior to buffering are acidic and because the neutral buffered melts still appear more acidic than the basic melts, no anionic species such as LiCl_2^- , which has been observed in basic melts, are expected to be present.

Attempts to model the neutral buffered melts are not nearly as straightforward as the binary melts. The results for the neutral buffered melts can be interpreted in two ways. Both models explain portions of the data better, but neither offers an all encompassing explanation for the observed data.

The first model is that the observed acceptor number is simply a function of two different ionic systems, $\text{EMI}^+ / \text{AlCl}_4^-$ and $\text{M}^+ / \text{AlCl}_4^-$. The second model is that the observed acceptor number is a function of an equilibrium between a $\text{TEPO} / \text{AlCl}_3$ monoadduct and a $\text{TEPO} / 2 \text{AlCl}_3$ diadduct formed via the driving force provided by the precipitation of the alkali metal chloride salt.

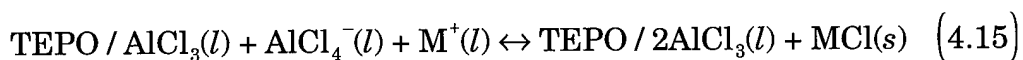
4.3.4.1 Weighted Average Model to Describe Neutral Buffered Acceptor Numbers

On the basis of the first model, one would expect the observed acceptor number to simply be a weighted average of the acceptor numbers of the two types of melt based upon the mole fractions. When the data are plotted in this fashion, what is actually observed are curvilinear lines for each of the melts

(Figure 4.9). This can be attributed to preferential solvation by one of the components of the melts.¹ The differences between alkali metal chloride neutral buffered melts buffered with different alkali metal chlorides appear to correlate with the alkali metal cation size. The Li^+ cation, being the smallest cation, would be expected to approach the $\text{TEPO} / \text{AlCl}_3$ monoadduct more closely. A possible explanation for the nonlinearity is that the Li^+ cation is also the hardest and strongest Lewis acid of the three alkali metal cations. Because the $\text{TEPO} / \text{AlCl}_3$ monoadduct is a Lewis base, the Li^+ cation may preferentially solvate the $\text{TEPO} / \text{AlCl}_3$ monoadduct. The Na^+ cation would be expected to show less of this behavior and the K^+ still less. Although the data seem to be in accord with these explanations, these observations are not quantifiable.

4.3.4.2 Equilibrium Model to Describe Neutral Buffered Acceptor Numbers

The second explanation uses a model similar to that used for the binary melts and results in an equilibrium expression:



The driving force for this equilibrium is the precipitation of the alkali metal chloride. Using this model, the maximum acceptor number would be 108.1 as determined in the $\text{AlCl}_3 / \text{EMIC}$ melts. Using Equation 4.15 to fit the data and using the diadduct acceptor number of 108.1 results in equilibrium constants K

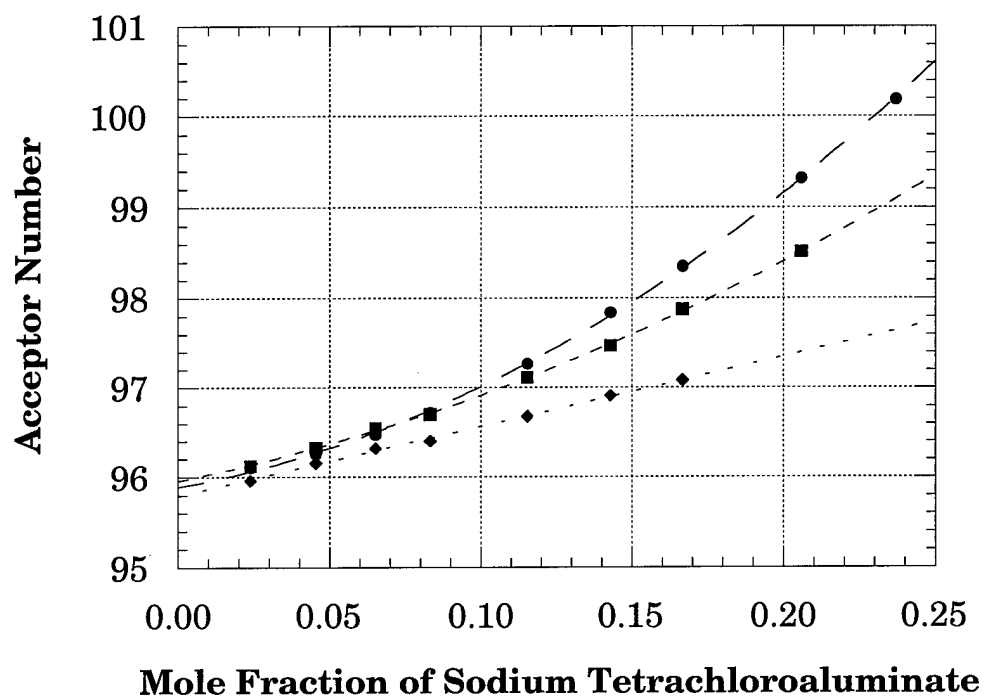


Figure 4.9 Dependence of the Gutmann acceptor number upon the mole fraction of alkali metal tetrachloroaluminate present in the ionic liquid (—●— LiCl buffered melt, —■— NaCl buffered melt, --◆-- KCl buffered melt). The lines have been added to highlight the data.

(M^{-2}) of 0.342 ± 0.004 , 0.27 ± 0.01 , and 0.18 ± 0.01 for the lithium, sodium, and potassium buffered melts, respectively. R^2 for each of the fits are 0.9980, 0.9540, and 0.9164 respectively. The magnitude of the equilibrium constants are still relatively small. These results show quantitatively the differences between melts buffered with different alkali metal cations as well as the dependence of the acceptor number on the original melt composition prior to buffering. These results also fit the model presented by Zawodzinski et al.⁴ where the TEPO forms an aluminum chloride diadduct. It should also be noted, that due to the small size of the equilibrium constants and because the melt ratios investigated only vary between 1.0:1.0 to 1.9:1.0, that the expressions would be expected to appear linear.

These results indicate that the alkali metal buffered melts are more Lewis acidic than the $AlCl_3$ / EMIC melts at low melt ratios (below mole ratios $\approx 1.4:1.0$). This was not expected and may only be true with the triethylphosphine oxide probe molecule. In addition the R^2 's of 0.9980, 0.9540, and 0.9164 for the data fit using Equation 4.15 are not compelling.

4.3.5 Effect of Oxide / Hydroxide on Acceptor Numbers

In some samples, a very small downfield peak (larger chemical shift) in the ^{31}P NMR spectrum appeared. Several experiments were conducted to determine the origin of this peak. Proton in the form of 1-ethyl-3-methylimidazolium hydrogen dichloride was added to several samples.⁸ To another sample, water was added. Water acts not only as a proton source, but

also as an oxide source.^{11,12} The sample to which the water had been added showed a marked increase in the intensity of the downfield peak. This suggests that the presence of the peak is due to either an aluminum oxide or aluminum hydroxide species and that this species is more Lewis acidic than the native melt (Figure 4.10). The Lewis acidity of the oxide species had not been investigated to date and further experiments are underway to investigate this phenomenon.

4.4 Conclusions

Gutmann acceptor numbers of the AlCl_3 / EMIC melts, as well as their alkali metal neutral buffered counterparts have been determined. The data from the binary AlCl_3 / EMIC melts have been fitted using the equilibrium expression derived from the model in which triethylphosphine oxide forms an AlCl_3 diadduct with an acceptor number of 108.1. This expression allows us to predict the Gutmann acceptor number of binary AlCl_3 / EMIC melts.¹³

The Gutmann acceptor numbers of the alkali metal chloride neutral buffered melts can be predicted using a linear expression.¹³ The LiCl neutral buffered melts show the greatest Lewis acidity followed by the NaCl and the KCl buffered melts. These data indicate that the potassium chloride neutral buffered melt is more Lewis acidic than its binary counterpart up to an AlCl_3 :EMIC mole ratio of 1.3:1.0; for the sodium chloride neutral buffered melt this ratio is 1.6:1.0 while for the lithium chloride it is 1.7:1.0. These results provide insight into the differences between the unbuffered and alkali metal

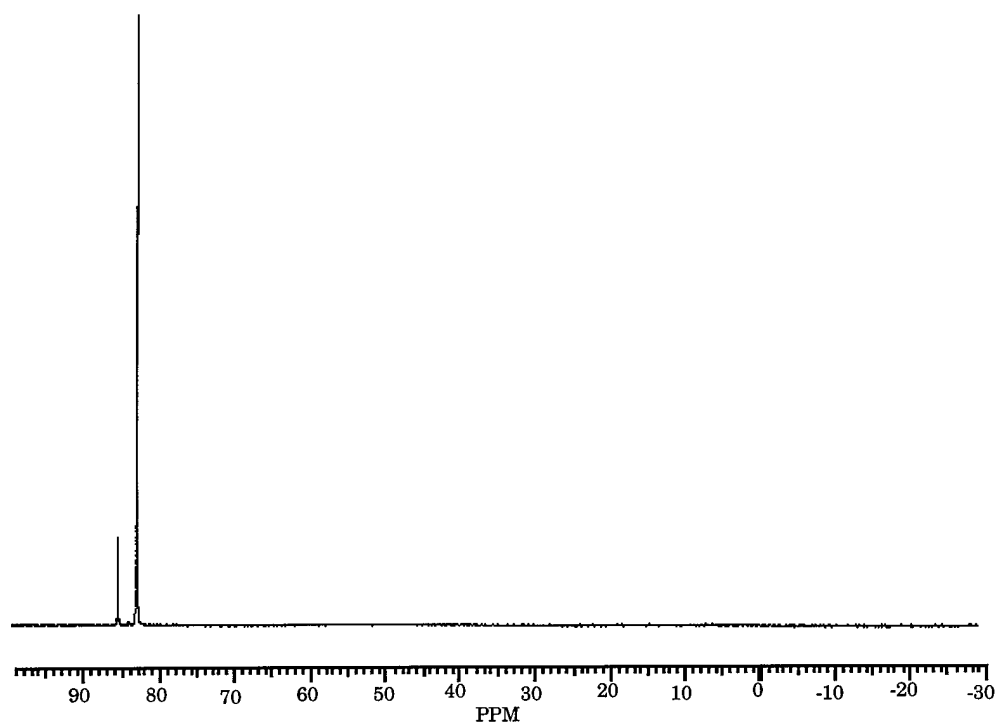


Figure 4.10 ^{31}P NMR Spectra of melt containing oxide and hydroxide. Sample was prepared by adding water to a melt containing TEPO. The peak at 86 ppm has appeared.

buffered melts as well as between the different alkali buffered melts themselves.

The buffering capacities for the LiCl, NaCl, and KCl neutral buffered melts have been determined using ICP. The buffering limit for LiCl is greater than an AlCl_3 :EMIC initial mole ratio of 1.9:1.0. The buffering limit for a NaCl buffered melt is $\approx 1.4:1.0$, and the buffering limit for a KCl buffered melt is $\approx 1.1:1.0$.

Chapter 4 References

- (1) Gutmann, V. *The Donor-Acceptor Approach to Molecular Interactions*; Plenum Press: New York, 1978.
- (2) Mayer, U.; Gutmann, V.; Gerger, "The Acceptor Number -- A Quantitative Empirical Parameter for the Electrophilic Properties of Solvents." *W. Mh. Chem.* **1975**, *106*, 1235-1257.
- (3) Gutmann, V. "Empirical Parameters for Donor and Acceptor Properties of Solvents." *Electrochimica Acta.* **1976**, *21*, 661-770.
- (4) Zawodzinski, T. A. Jr.; Osteryoung, R. A. "Donor-Acceptor Properties of Ambient-Temperature Chloroaluminate Melts." *Inorg. Chem.* **1989**, *28*, 1710-1715.
- (5) Melton, T. J.; Joyce, J.; Maloy, J. T.; Boon, J. A.; Wilkes, J. S. "Electrochemical Studies of Sodium Chloride as a Lewis Buffer for Room Temperature Chloroaluminate Molten Salts." *J. Electrochem. Soc.* **1990**, *137*, 3865-3869.
- (6) Quarmby, I. C.; Osteryoung, R. A. "Latent Acidity in Buffered Chloroaluminate Ionic Liquids." *J. Am. Chem. Soc.* **1994**, *116*, 2649-2650.

- (7) Quarmby, I. C.; Mantz, R. A.; Goldenberg, L. M.; Osteryoung, R. A. "Stoichiometry of Latent Acidity in Buffered Chloroaluminate Ionic Liquids." *Anal. Chem.* **1994**, *66*, 3558-3561.
- (8) Zawodzinski, T. A. Jr.; Osteryoung, R. A. "1-Methyl-3-ethylimidazolium Hydrogen Dichloride: Synthesis and Application to the Study of Protons in Ambient-Temperature Chloroaluminate Ionic Liquids." *Inorg. Chem.* **1988**, *27*, 4383-4384.
- (9) Beconsall, J. K.; Daves, G. D. Jr.; Anderson, W. R. Jr. "Reference-Independent Nuclear Magnetic Resonance Solvent Shifts." *J. Am. Chem. Soc.* **1970**, *92*, 430-432.
- (10) Becker, E. D. *High Resolution NMR: Theory and Chemical Applications*, 2nd ed.; Academic Press: New York, 1980; pp 59-61.
- (11) Zawodzinski, T. A. Jr.; Osteryoung R. A. "Aspects of the Chemistry of Water in Ambient-Temperature Chloroaluminate Ionic Liquids: ^{17}O NMR Studies." *Inorg. Chem.* **1987**, *26*, 2920-2922.
- (12) Zawodzinski, T. A. Jr.; Osteryoung, R. A. "Oxide and Hydroxide Species Formed on Addition of Water in Ambient-Temperature Chloroaluminate Melts: An ^{17}O NMR Study." *Inorg. Chem.* **1990**, *29*, 2842-2847.

Chapter 5

ROESY NMR of Basic Ambient-Temperature Chloroaluminate Ionic Liquids

5.1 Introduction

5.1.1 Physical and Structural Properties of the Chloroaluminate Ionic Liquids

Various physical and spectroscopic properties of ambient temperature chloroaluminate ionic liquids vary with melt composition. One of the most obvious properties affected by melt composition is melt viscosity.¹ Figure 5.1 shows that at 25 °C the viscosity of the acidic melts are relatively constant. However, in basic melts the viscosity increases dramatically as the melt becomes more basic. The viscosity increases from 17.75 cP in a 1.0:1.0 neutral melt to 411.95 cP in a 0.4:1.0 basic melt. In comparison, water has a viscosity of 0.89 cP at 25 °C, and glycerol has a viscosity of 984 cP at 25 °C.²

Lipsztajn and Osteryoung³ analyzed the conductivity and viscosity data of the melts. They concluded that the data could be explained on the basis of ion pair formation.

Initial NMR studies of the ambient temperature melts showed that imidazolium ring carbon and hydrogen chemical shifts (Figure 5.2) were highly

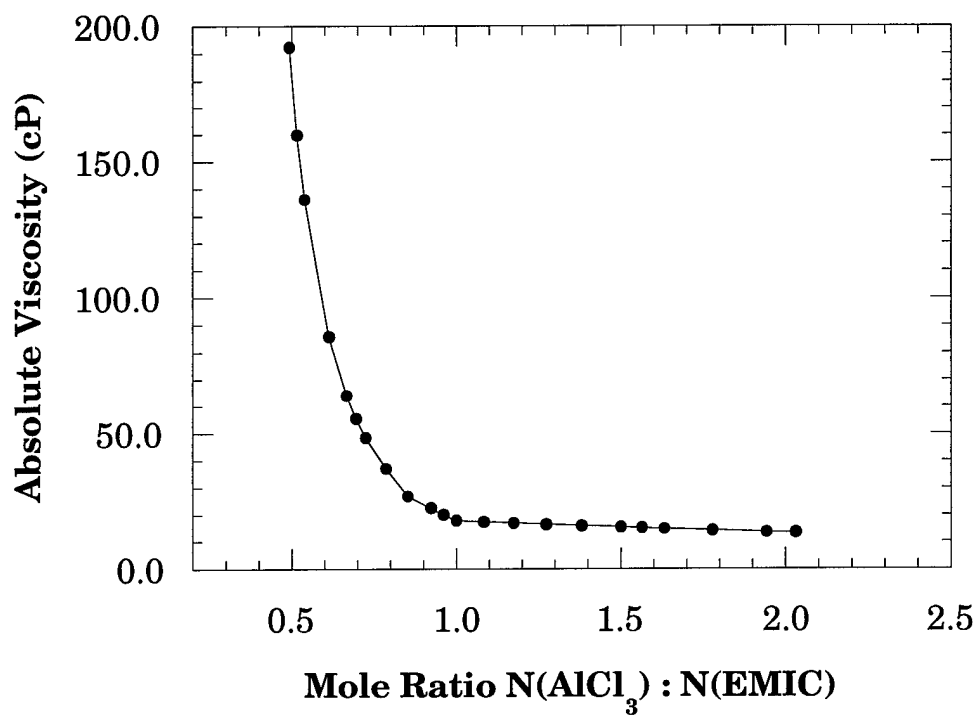


Figure 5.1 Absolute viscosity (cP) vs. the mole ratio of AlCl_3 :EMIC at 25 °C. The viscosity is essentially constant in the acidic region and then drastically increases as the mole ratio drops below 1.0:1.0.

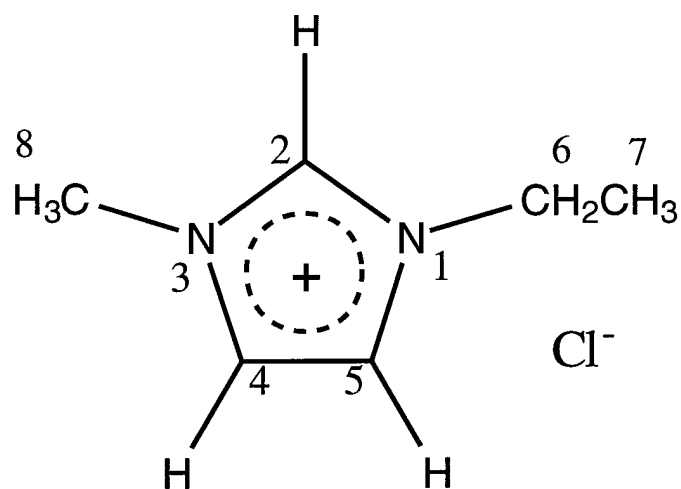


Figure 5.2 Structure and numbering of the positions of 1-ethyl-3-methylimidazolium chloride (EMIC).

dependent upon the melt composition.⁴⁻⁸ The ^1H NMR chemical shift (δ) of the imidazolium H-2 is an example of this dependence (Figure 5.3). In acidic melts the chemical shift is basically constant at 6.0 ppm, while the chemical shift moves dramatically downfield to 7.6 ppm in a 0.5:1.0 basic melt.⁶ The NMR results for both the EMIC and butylpyridinium based melts, which measured the dependence of chemical shift on melt composition, were attributed to ion pairing. Other experiments measured the chemical shift dependence with respect to added solvents.⁴ It was shown that the addition of benzene, a low dielectric solvent, resulted in changes to the chemical shifts in the ^1H NMR spectrum that were ascribed to ion pairing.

Osteryoung and Tait⁹ completed infrared measurements on acidic and basic melts. The changes that occurred in the infrared spectrum in basic melts were attributed to strong cation anion interactions. In addition, they obtained data from acidic and basic melts which suggested the presence of hydrogen bonding between H-2 and the chloride present in the basic melts.

Wilkes and coworkers⁷ proposed a model to describe the composition dependent behavior of the melts based on the NMR data described above. The model involves the formation of ion aggregates which are composed of oligomeric chains of alternating cations and anions (Figure 5.4). In acidic melts the EMI^+ alternates with either AlCl_4^- or Al_2Cl_7^- , while in the basic melts the EMI^+ alternates with either Cl^- or AlCl_4^- . This model was only electrostatic and precluded hydrogen bonding. The model successfully fit the NMR⁴⁻⁸ and viscosity data¹ but it did not sufficiently describe the infrared observations of

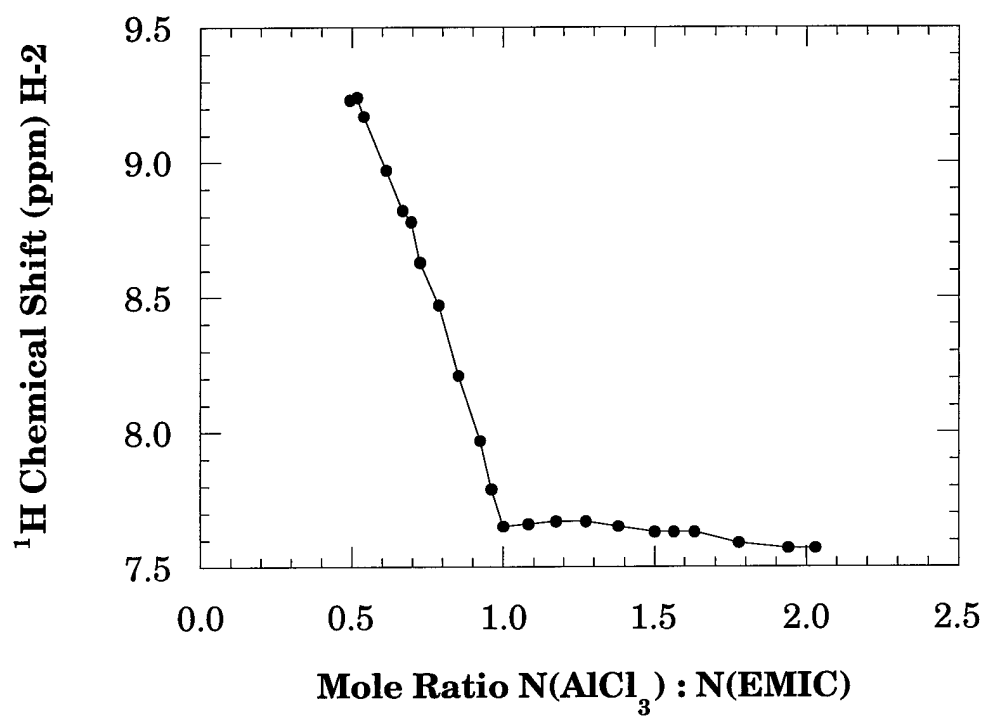


Figure 5.3 ^1H NMR chemical shift (δ) dependence of H-2 hydrogen upon mole ratio of AlCl_3 :EMIC in the melts. Similarly to the viscosity the chemical shift is essentially constant in the acidic melts but changes drastically for the basic melts.

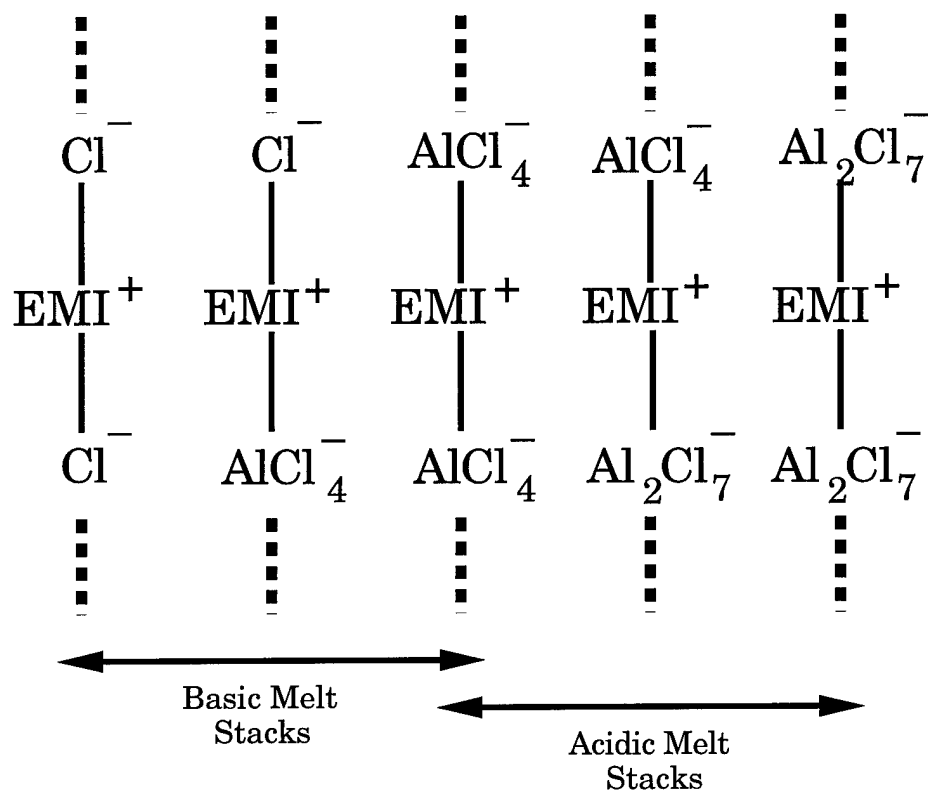


Figure 5.4 Wilkes proposed model of alternating oligomeric chains in the melts proposed to explain the ^1H NMR data.

Tait and Osteryoung.⁹

The crystal structure of several EMIC analogues including 1-ethyl-3-methylimidazolium iodide indicated the presence of hydrogen bonding through the H-2 hydrogen.^{10,11} This result agreed with the results of Tait and Osteryoung.⁹ It was obvious that the model proposed by Wilkes and coworkers¹ did not fully describe the variation in melt characteristics on melt composition.

Wilkes and co-workers¹² re-investigated the properties of the melts with respect to melt composition using infrared spectroscopy. They deuterated the ring positions of EMIC and prepared basic and neutral melts with the deuterated EMIC. Infrared spectroscopy revealed that not only the H-2 hydrogen was hydrogen bonding to the Cl^- anion, but the H-4 and H-5 hydrogens were hydrogen bonding to the Cl^- as well. Using this additional hydrogen bonding data, Wilkes and coworkers¹² attempted to modify their stack model and used AM1 and MNDO semi-empirical calculations to predict a stable configuration with the Cl^- anion centered between two imidazolium rings. The infrared spectra were calculated from this configuration using the semi-empirical methods. They were unable to predict the shifts in the C-H stretching frequencies of the ring hydrogen atoms with respect to the Cl^- concentration.

Dymek and coworkers^{13,14} used X-ray crystallography, infrared spectroscopy, and semi-empirical calculations to explain the experimental results which showed variation with melt composition. The crystal structure of EMIC consists of stacks of imidazolium cations (Figure 5.5).¹³ The Cl^- anions

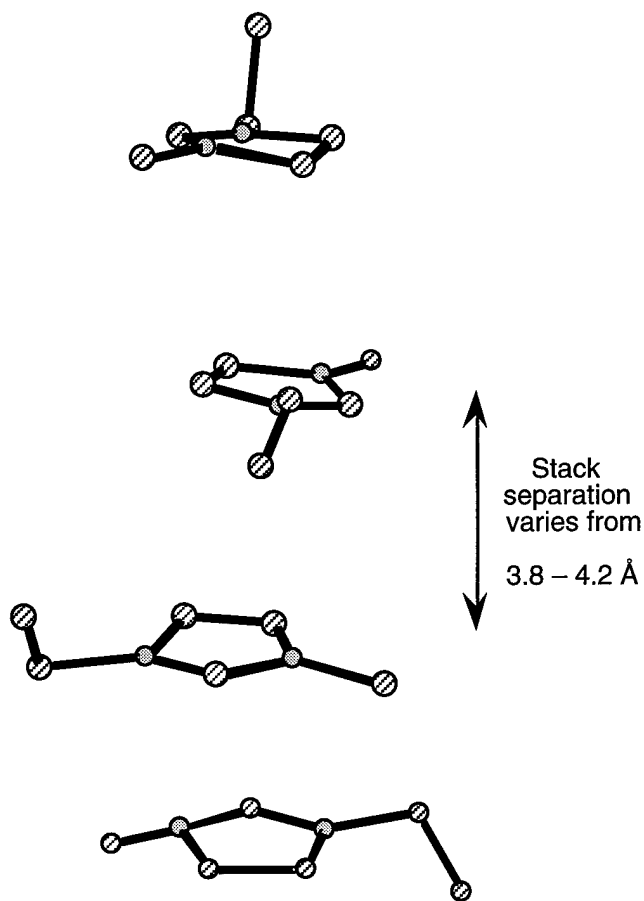


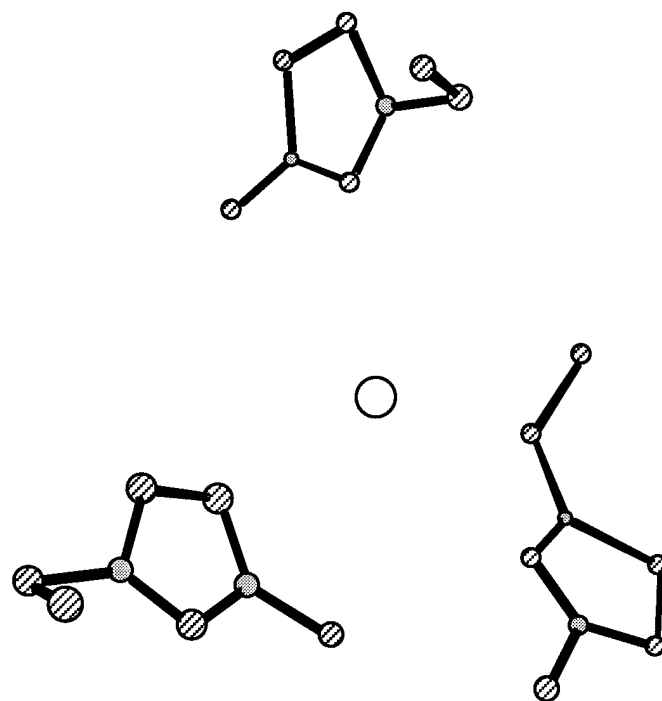
Figure 5.5. Stacks of EMI⁺ ions in the in crystalline EMIC obtained using X-ray crystallography

are also layered such that each Cl^- anion can hydrogen bond to three imidazolium cations (Figures 5.6 and 5.7). Dymek and coworkers utilized infrared spectroscopy to compare EMIC crystals and liquid EMIC in basic melts. They discovered that the infrared stretching bands due to hydrogen bonded ring hydrogens on the imidazolium cation did not change going from crystalline solid to liquid EMIC. This indicates that the hydrogen bonding interactions present in the crystalline solid remain in the liquid.¹³ In addition, the infrared stretching region due to the hydrogen bonding is also present in basic melts and may only be slightly altered due to the presence of AlCl_4^- because the infrared stretching bands remain virtually the same.¹³ From this data they were able to conclude that the structure present in crystalline EMIC was preserved in basic melts.

Using this new structural model, which includes the hydrogen bonding between the H-2, H-4, and H-5 hydrogen with the Cl^- anion, Dymek and Stewart¹⁴ were able to predict the changes in the infrared spectra as the melt composition is changed using the AM1 semi-empirical molecular orbital method.

More recently Welton et al^{15,16} have used ^1H , ^{35}Cl , ^{127}I NMR and conductivity measurements to further demonstrate experimentally the presence of hydrogen bonding between the H-2, H-4, and H-5 hydrogen to the Cl^- anion.

The work completed to date suggests that an interaction is present in basic melts that is absent in acidic melts, and this interaction results in local



H-Bond Distances
Average 3.45 Å

Figure 5.6. Chloride hydrogen bonding to three EMI⁺ cations in EMIC crystal.

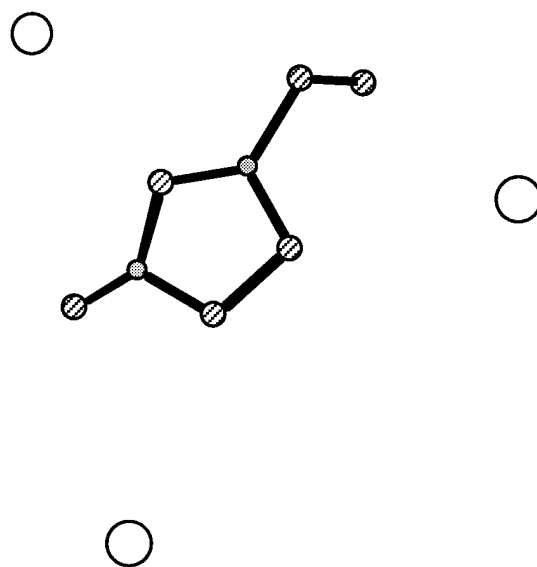


Figure 5.7. EMI⁺ cation hydrogen bonding to three chloride anions in crystalline EMIC.

structure in basic chloroaluminate melts. However, there have been no direct measurements of the internuclear distances between molecules in the basic melts.

5.1.2 Nuclear Overhauser Effect Spectroscopy

The nuclear Overhauser effect (NOE) is a powerful tool used in nuclear magnetic resonance (NMR) to study chemical exchange, nuclear relaxation, and molecular structure and conformation.^{17,18} The NOE was demonstrated early in the life of nuclear magnetic resonance when Solomon published a paper in 1955 that described the fundamentals of the NOE and also presented the first experimental demonstration of the effect.¹⁹ Ten years later the NOE would be demonstrated as a tool for elucidating molecular structure by Anet and Bourn.²⁰ They were able to utilize NOE difference spectroscopy to assign NMR spectra and confirm the structure of a cage molecule and several other small molecules.

Simply described, NOE is the dipole-dipole interaction through space between two nuclei. This manifests itself when a single resonance in a spectrum is irradiated and the intensities of other resonances are changed. In early experiments, NOE difference spectroscopy was the only means available to measure the NOE. In NOE difference spectroscopy the integral of a peak is measured with and without the irradiation of other NMR peaks in the sample (Figure 5.8). Those peaks, which when irradiated change the integral of the peak of interest, are interacting through space, i.e. the NOE. The NOE at

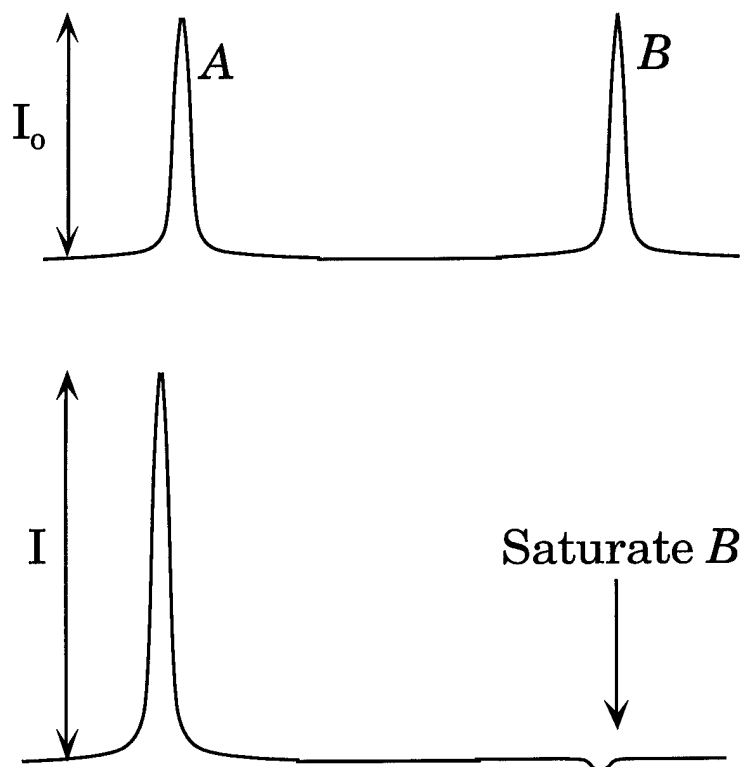


Figure 5.8. Depiction of a steady-state NOE difference measurement. I_0 is the original intensity of peak *A*. *I* is the intensity of peak *A* while peak *B* is being saturated.

nuclei A due to irradiation of spin B ($\eta_A(B)$) is given by:²¹

$$\eta_A(B) = (I - I_0)/I_0 \quad (5.1)$$

The NOE can be understood using a simple energy level diagram.^{21,22} Using a homonuclear system consisting of two spins, the energy diagram shown in Figure 5.9 is obtained. Four energy levels exist because the presence of the spin state of each of the nuclei has an effect on the magnetic field that the other nucleus feels. Figure 5.9 starts with the nuclear spins in an equilibrium state defined by the Boltzmann equation. If one of the spins, A, is irradiated then both energy levels for that nucleus are equally populated. The other nucleus now tries to re-establish the equilibrium population. Two pathways are available in order to re-establish equilibrium. The first pathway is a zero quantum transition in which nucleus A and nucleus B exchange spin states. The other pathway consists of both nucleus A and nucleus B simultaneously changing spin states. This is a double quantum transition. These two transitions are called cross relaxation.²³

The factors that determine which pathway is predominately available are the correlation time (τ_c) and the precession frequency (ω). The correlation time is defined as the average time it takes for a molecule to rotate one radian.¹⁷ If the correlation time is short, as it generally is for small molecules in non-viscous solutions, then the double quantum transition predominates resulting in a positive NOE.¹⁷ The regime in which ($\omega * \tau_c$) \ll 1 is referred to as the extreme narrowing limit because the NMR lines are narrow due to motional averaging.¹⁷ If the correlation time is long, as it generally is for large molecules,

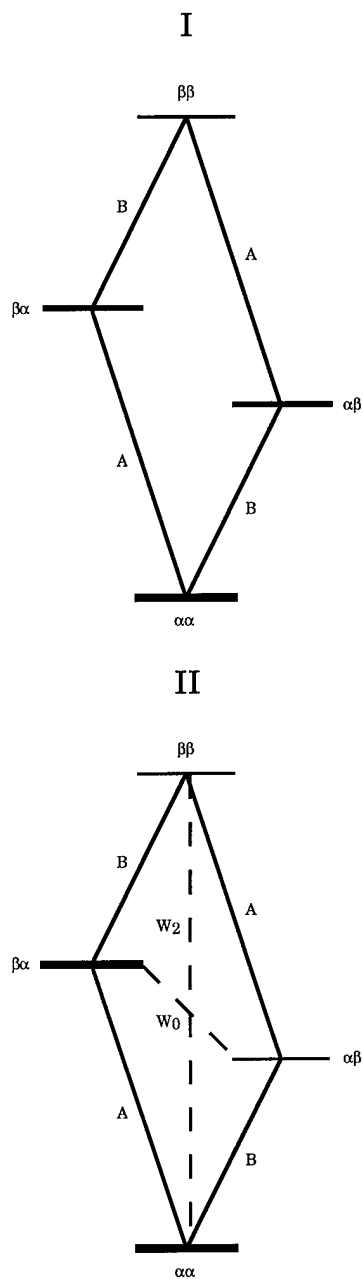


Figure 5.9 Energy level diagram to describe the NOE. α is the low energy spin state of the nucleus while β is the high energy spin state. A and B are the single quantum transitions of the respective nuclei. W_0 and W_2 are the zero and double quantum transitions. I is the Boltzmann determined equilibrium population. II is the population when nucleus A is saturated. The thickness of the energy state is representative of its population.

then the zero quantum transition predominates and a negative NOE is observed (Figure 5.10).¹⁷

Molecules with intermediate molecular weights or those in viscous solutions often do not have a predominate cross relaxation pathway. The absence of a predominate cross relaxation pathway results in no net observable NOE because the two pathways cancel each other.

Not only is the correlation time important to NOE, but the distance between the nuclei also drastically effects the observed NOE. The distance dependence of NOE is what makes the technique so important for structural determination studies. The dependence of the NOE for a two-spin system on the internuclear distance (r_{AB}) is given by:²⁴

$$1/\eta_A(B) = K(r_{AB})^6 \quad (5.2)$$

$\eta_A(B)$ is the NOE enhancement at nucleus A due to the saturation of spin B. K is a constant which includes the effects of molecular tumbling and alternative relaxation pathways; normally, the value of K is difficult to determine. The ratio between two NOE's is proportional to the ratios of the distances. Therefore, if an internuclear distance is known, the NOE enhancements can be compared to determine the unknown internuclear distance.

$$(r_{CD})^6 \left(\frac{\eta_C(D)}{\eta_A(B)} \right) = (r_{AB})^6 \quad (5.3)$$

This equation assumes K is the same for both NOE enhancements. This assumption is valid when similar molecules are being compared under identical conditions.²⁵

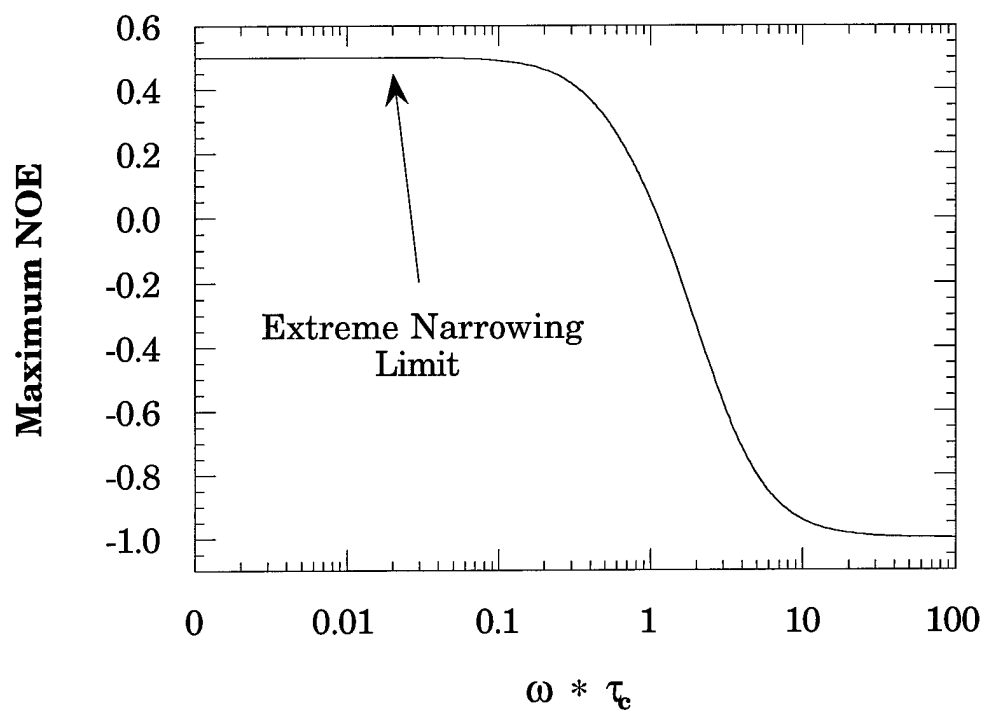


Figure 5.10 Maximum observable steady-state NOE vs. the molecular correlation time and spectrometer frequency. When $\omega * \tau_c$ is approximately 1 no NOE is observable. For small molecules $\omega * \tau_c$ is less than one and positive NOEs are observed while for large molecules $\omega * \tau_c$ is greater than one and negative NOEs are observed.

Two limitations on the observed NOE have been discussed. The first is the molecular correlation time and the second the distance between the two nuclei. A third limitation upon the observed NOE is that the nuclei have other relaxation pathways available that dilute the contributions of cross relaxation to the overall relaxation rate and thus limits the NOE enhancement.²³

Although there are significant limitations that limit the observed NOE, the technique is very important in determining internuclear distances. Many studies have used the observed NOE to obtain qualitative structural information. However, the careful measurement of NOE's not only gives qualitative information but quantitative internuclear distances as well. Bell and Saunders, by using a variety of molecules were able to obtain quantitative internuclear distances with a maximum observable internuclear distance of approximately 3.7 Å.²⁵

5.1.3 Rotating Frame Nuclear Overhauser Enhancement Spectroscopy (ROESY)

In basic melts the extreme narrowing limit condition is not met due to the high viscosity. To overcome this, Rotating Frame Nuclear Overhauser Enhancement Spectroscopy (ROESY) can be used (Figure 5.11).^{26,27} The experiment was originally called CAMELSPIN (cross-relaxation appropriate for minimolecules emulated by locked spins).²⁸ The ROESY experiment was developed by Bothner et al to overcome limitations of the nuclear Overhauser effect spectroscopy (NOESY) pulse sequence.¹⁷ The NOESY experiment is

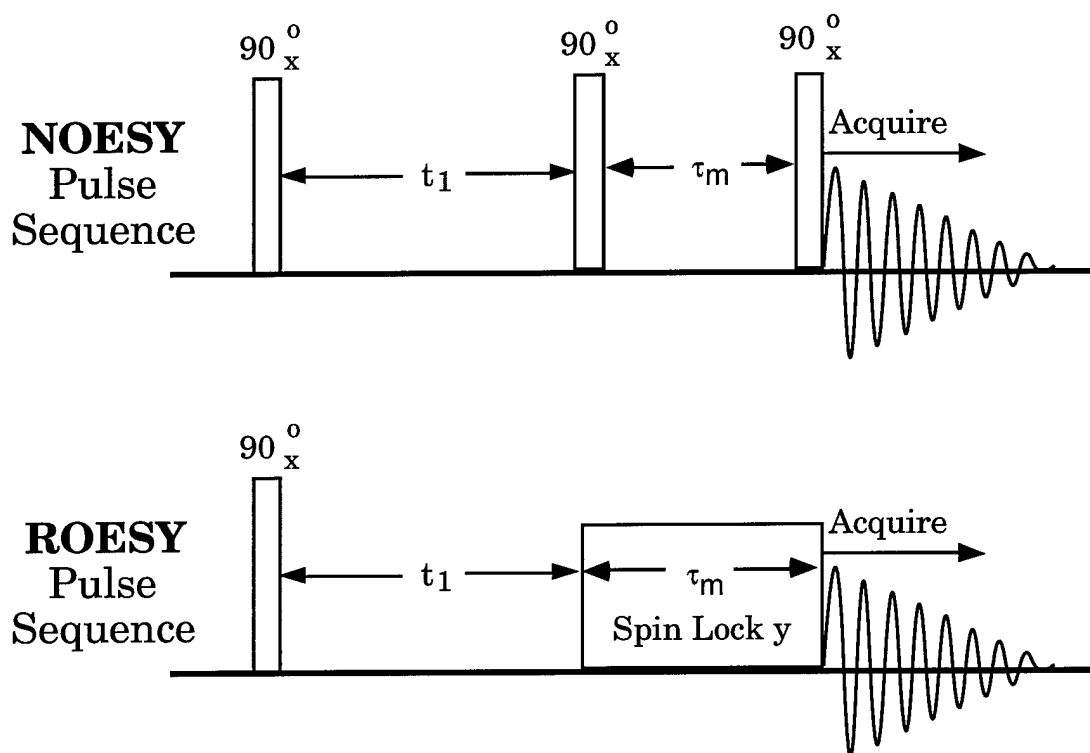


Figure 5.11. NOESY and ROESY pulse sequences. The pulse lengths and along which axis are depicted. In both experiments t_1 is incremented.

limited by superimposition of cross peaks due to J-coupling on the NOE peaks.^{17,21} Both ROESY and NOESY measure transient NOE; however, NOESY is restricted by disappearing NOE with mid-sized molecules and viscous solutions (Figure 5.12).¹⁷ The ROESY experiment is conducted in such a way that the nuclei are always in the extreme narrowing condition (Figure 5.13).^{17,28} Another advantage of the ROESY experiment is that the NOE build-up rates are greater than for the NOESY experiment (Figure 5.14).²⁷ The ROESY experiment can have two artifacts; both are due to scalar J-coupling. The first is due to the length of the mixing pulse. The long mixing time acts as a mixing pulse similar to that used in a COSY (correlation spectroscopy) experiment.²⁶ The integral of a COSY type artifact is zero.¹⁷ The other artifact is due to Hartmann-Hahn transfer. Hartmann-Hahn transfer depends on the strength of the mixing pulse, the scalar J-coupling, the offset between the spins and the transmitter, and the angles between the effective rf (radio frequency) fields and the Z axis.^{26,29,30} The peaks due to Hartmann-Hahn transfer have the opposite sign as the NOE peaks. By limiting the strength of the mixing pulse and carefully choosing the transmitter frequency both artifacts can be minimized.²⁶

The buildup of Intensity (I) of NOE cross-peaks versus time (dI/dt) in the ROESY experiment is inversely proportional to the internuclear distance to the sixth power and can be substituted into Equation 5.3 for NOE enhancement (η) to yield:²¹

$$(r_{CD})^6 \left(\frac{dI/dt_{CD}}{dI/dt_{AB}} \right) = (r_{AB})^6 \quad (5.4)$$

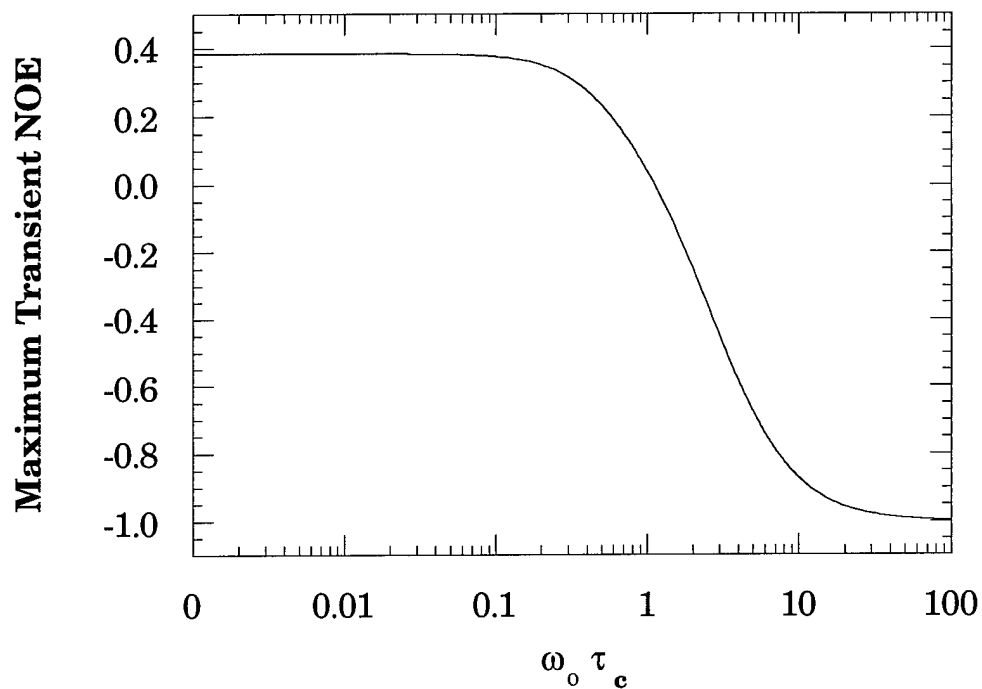


Figure 5.12 Maximum observable transient NOE vs. the molecular correlation time and spectrometer frequency. The NOE observed follow the same trends as the steady state NOE, however, the maximum NOE when $\omega * \tau_c$ is less than 1 is $\approx 40\%$ rather than 50% for steady state NOE.

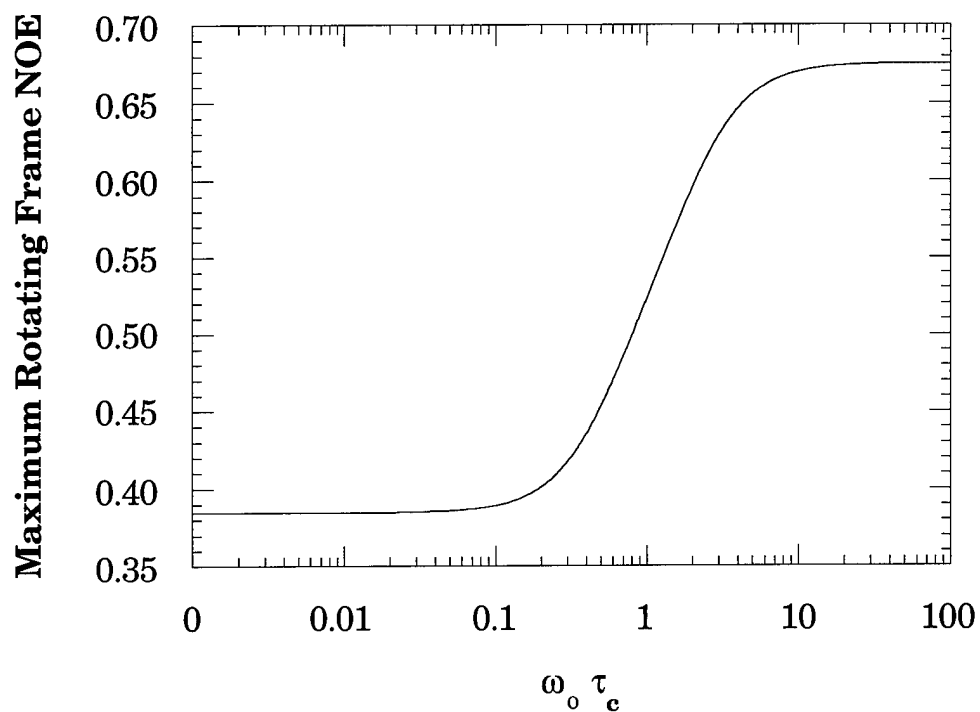


Figure 5.13 Maximum observable transient NOE using a spin locking experiment vs. the molecular correlation time and spectrometer frequency. Unlike both steady state and transient NOEs in the spin locking experiment the NOE is always positive.

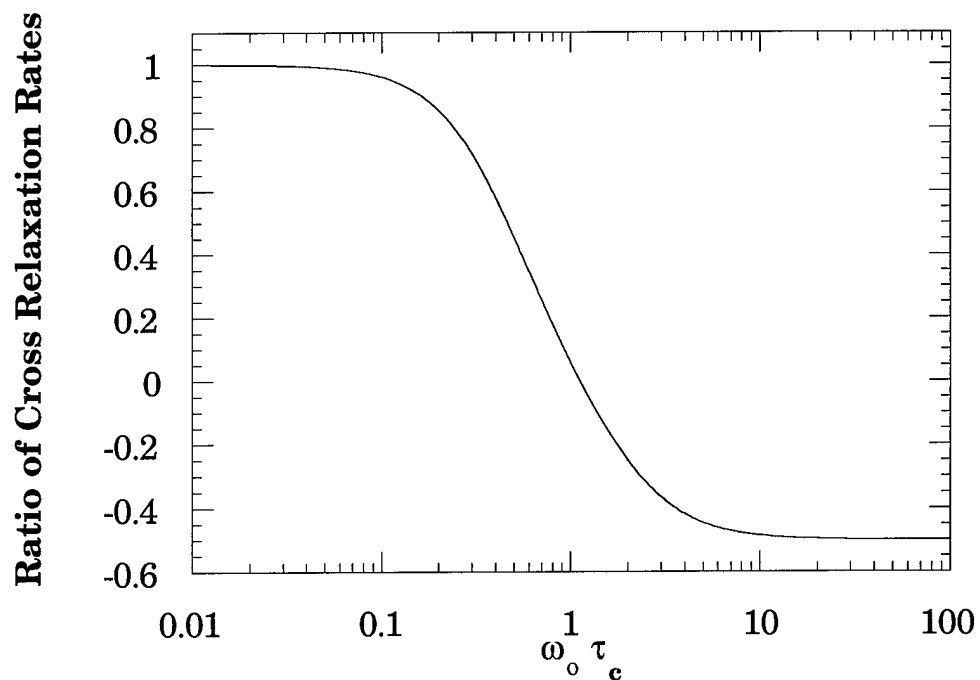


Figure 5.14 Ratio of the cross relaxation rates of the NOESY and ROESY pulse sequences. At $\tau_c = 0$ the rates are the same, otherwise the cross relaxation rate for the ROESY experiment is always greater. Experimentally this means the cross peaks will grow more rapidly for the ROESY experiment.

The subscripts indicate the NOE transfer and distance between two pairs of nuclei A and B, or C and D. The rate of NOE buildup is determined by varying the mixing time and determining the resulting change in volume of the two-dimensional cross-peak. The change in volume of the cross-peaks is inversely proportional to the internuclear distance to the sixth power.

Very little work has been published on intermolecular NOE. Studies to date have emphasized the solution structure of molecules but not the spatial relationships of molecules in solution. Kaiser published the first example of intermolecular NOE.³¹ The sample Kaiser chose was an 80% by volume solution of cyclohexane in chloroform. Chloroform was chosen because of the absence of intramolecular NOE so that an appreciable NOE could be observed between chloroform and the abundant cyclohexane hydrogen. Kaiser was able to observe a 31% NOE enhancement in the chloroform peak height when the cyclohexane peak was saturated in a steady state NOE experiment.³¹ Macura and Ernst used the same sample to demonstrate the utility of the NOESY experiment.³² Macura and Ernst also calculated the maximum cross peak intensities that could be expected for intermolecular NOE. In an ideal case where each molecule only contained one hydrogen, the maximum cross peak intensity to autpeak (peak lying along the diagonal) intensity ratio for the NOESY experiment was 0.333.³² For comparison the observed maximum cross peak intensity for the chloroform cyclohexane sample was 0.12.³²

5.2 Specialized Experimental Procedures

5.2.1 Materials

5.2.1.1 Synthesis of *d*11-1-Ethyl-3-Methylimidazolium Chloride

The synthesis of perdeuterated 1-ethyl-3-methylimidazolium chloride is described elsewhere.³³⁻³⁵

5.2.2 Equipment and Procedures

5.2.2.1 NMR Preparation

Three NMR samples were prepared: a basic, 0.4:1.0 melt, a neutral 1.0:1.0 melt, and a 95% perdeuterated 0.4:1.0 melt. The deuterated melt was prepared by mixing 5% protium-containing EMIC with 95% fully deuterated EMIC and then mixing the resulting EMIC with AlCl_3 . Each sample was loaded into a 5 mm co-axial tube (Figure 5.15). The ^1H containing samples were loaded into a Wilmad 5 mm co-axial tube (Wilmad Part # WGS-5BL) while the ^2H containing sample was loaded into a different style Wilmad 5 mm coaxial tube (Wilmad Part # 516-CC-5). The center portion of the coaxial tube contained the melt sample and was flame sealed. A lock solvent, generally *d*3-acetonitrile, was loaded into the annular region of the tube pair.

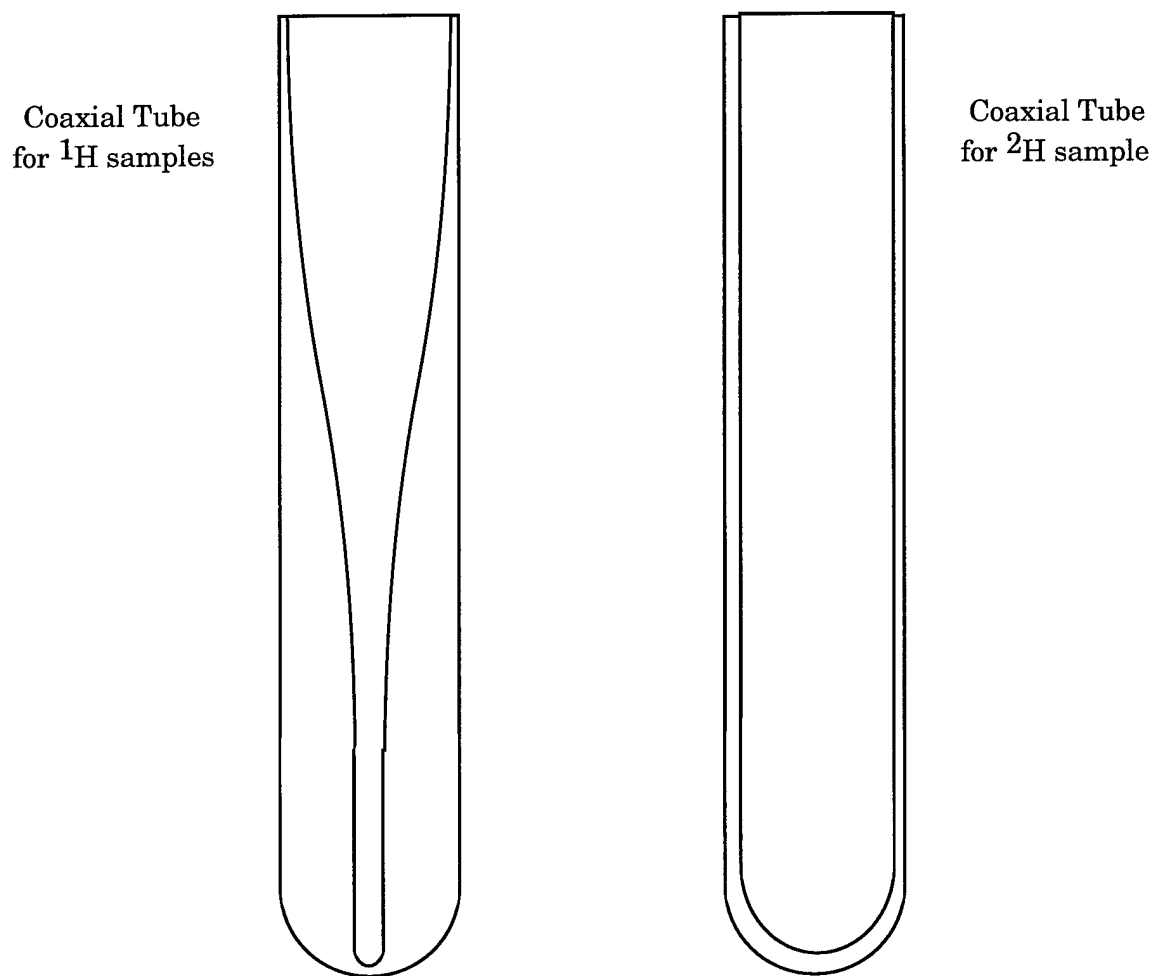


Figure 5.15 Wilmad coaxial NMR tubes (Part # WGS-5BL and 516-CC-5) which were utilized to acquire ROESY spectra. The center tube contains the melt while the annular region is filled with a deuterated solvent to provide a lock signal.

5.2.2.2 NMR Experiments

NMR spectra were acquired on GE 500 MHz Omega and Bruker 500 MHz ARX spectrometers. ^1H spectra were generally acquired with a sweep width of 11 ppm which covers all the ^1H resonances due to the imidazolium cation. Pulse widths were calibrated for the melts. For example a 90° pulse on the Bruker spectrometer was 12 μsec with the transmitter attenuated 0 dB.

Four pulse sequences were used in the course of this study: T1 inversion recovery, T2 spin echo, T1 ρ , and ROESY. The NMR sample was maintained at the temperatures 25 and 40 $^\circ\text{C}$. ROESY and T1 ρ pulse sequences were acquired with a spin locking pulse strength of 2 kHz. ROESY spectra were acquired with a relaxation delay of 5 seconds between scans while T1, T2, and T1 ρ were acquired with relaxation delays of 20 seconds. ROESY spectra consisted of 256 experiments in which the evolution time was varied. Within each experiment, 32 scans were acquired with 2048 points. The T1, T2, and T1 ρ experiments consisted of between 30 and 48 experiments in which either the pulse time or delay was varied. Each experiment consisted of 16 scans with 16,384 points.

5.2.2.3 NMR Data Treatment

After acquisition, the NMR data had to be Fourier transformed. Prior to transformation, window functions were applied to remove artifacts and to enhance the signal to noise ratio. The free induction decay (FID) for the T1, T2 and T1 ρ experiments was multiplied by an exponential multiplication window function with a line broadening of 1 Hz. The F2 FID for the ROESY experiment was multiplied by an exponential window function with a line broadening of 5 Hz and then the F1 FID for the ROESY experiment was multiplied by a cosine window function.

5.3 Results and Discussion

5.3.1 Relaxation Studies

5.3.1.1 T1 Relaxation

Proton NMR of basic chloroaluminate molten salts yields well-resolved one-dimensional spectra corresponding to the protons of the 1-ethyl-3-methylimidazolium chloride (Figure 5.16). Relaxation measurements were conducted on the 0.5:1.0 melt at 25 °C and 40 °C and also an 0.99:1.0 melt at 25 °C in order to determine the molecular correlation time of the EMIC molecule in the melts. Quantitative ^1H T1 measurements are generally very

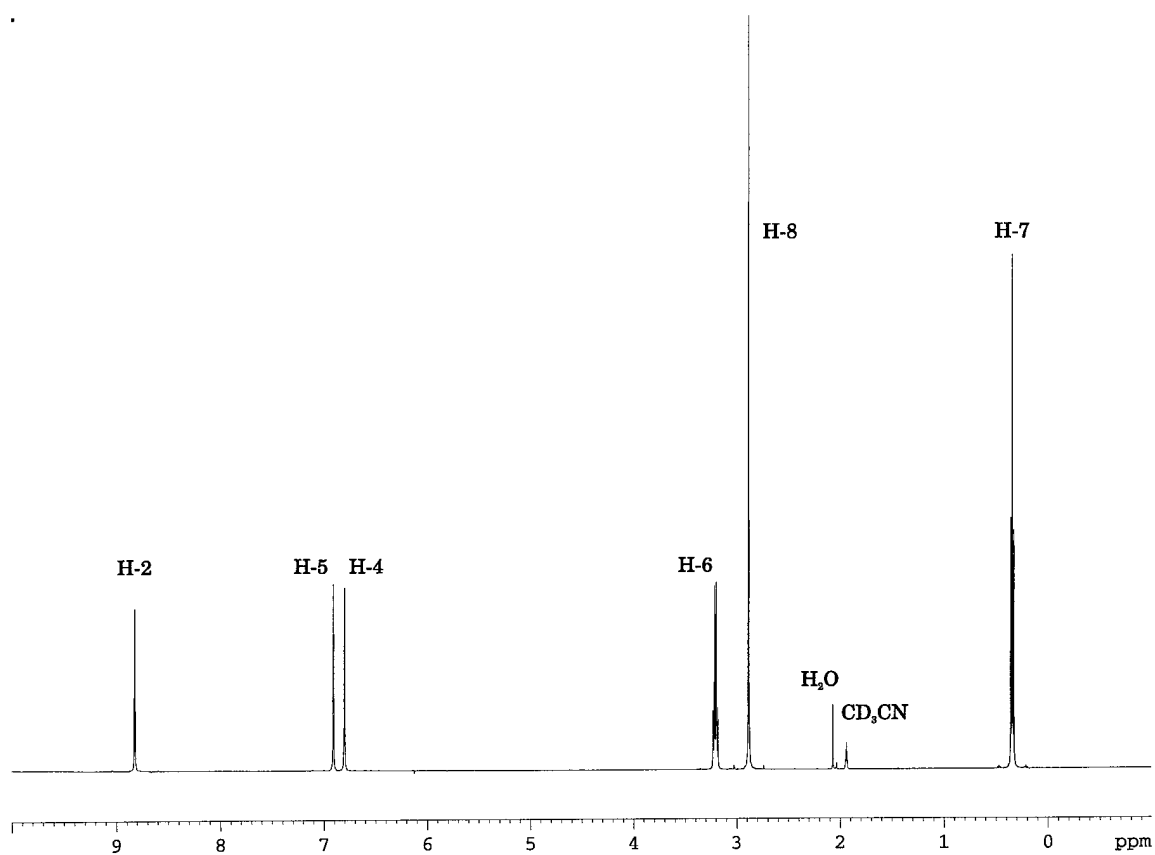


Figure 5.16 ^1H NMR spectrum of 0.5:1.0 EMIC / AlCl_3 melt. The numbers labeling each peak correspond to the numbering of the positions of the EMIC molecule.

difficult to obtain because the protons are generally part of strongly coupled spin systems in most organic molecules of interest. In addition cross relaxation effects interfere with the measurement of T1. This makes the exact analysis of relaxation data a forbidding task.³⁶ These interferences lead to retarded and non-exponential relaxation.³⁷ These problems limit the relaxation studies to a semi-quantitative nature.

When spins are perturbed in a magnetic field their behavior is predicted using the Bloch equations. These predict that the magnetization will tend toward its equilibrium value exponentially with a time constant, T1. For the recovery to equilibrium in the inversion recovery experiment, integration of the Bloch equation for the z component of the magnetization gives:

$$M_z(t) = M_0 \left(1 - e^{(-t/T_1)} \right) \quad (5.5)$$

The results of a typical inversion recovery T1 measurement are shown in Figure 5.17. The figure shows the intensity of a typical peak as a function of relaxation time. One difficulty in obtaining T1 data is the accuracy of the pulses. It is essential the pulse length be exactly 180°. A linearized plot is considerably less sensitive to pulse length errors. Rearranging Equation 5.5 gives:

$$-\ln \left(\frac{-M_z(t) - M_0}{2} \right) = \frac{t}{T_1} \quad (5.6)$$

The term to the left of the equal sign is Y. A plot of Y vs. t will have a slope of 1/T1 (Figure 5.18). The T1's calculated from both plots are equal. This indicates the 180° pulse length was set correctly. The T1 data for the imidazolium

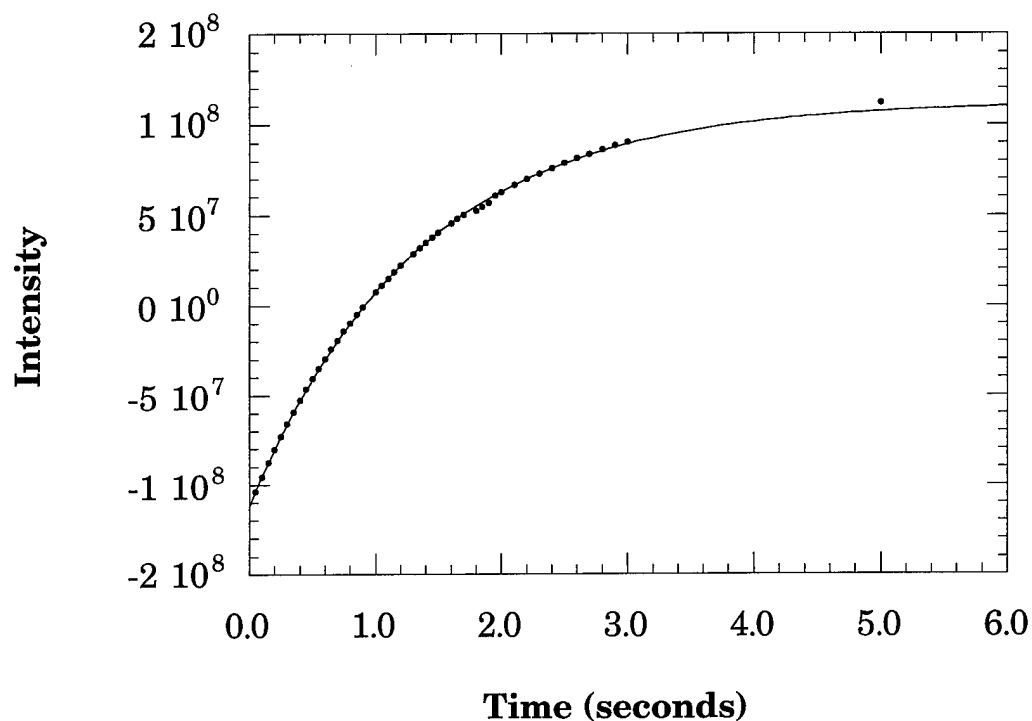


Figure 5.17 ^1H NMR inversion recovery experiment for H-6. Inversion recovery experiment consists of a 180° pulse, a waiting period, and a 90° pulse followed by the acquisition. The intensity of the peak of interest is then monitored as a function of the waiting time. The line is the least squared fit of the data using Equation 5.5.

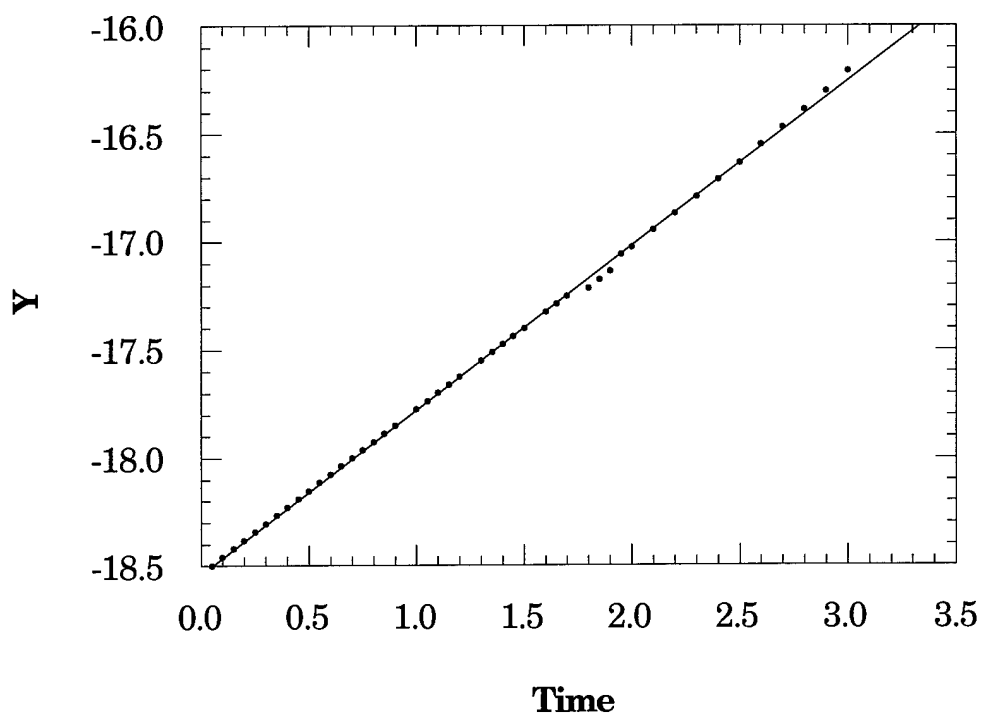


Figure 5.18 ^1H NMR inversion recovery experiment for H-6. Inversion recovery experiment consists of a 180° pulse, a waiting period, and a 90° pulse followed by the acquisition. The intensity of the peak of interest is then monitored as a function of the waiting time. The data can then be plotted according to equation 5.6. The line is the linear least squared fit of the data.

cation in the melts is presented in Table 5.1. The relaxation times for H-6 and H-8 are very short; this is most likely due to the close proximity of the nitrogen nucleus which is quadrupolar.

5.3.1.2 T2 Relaxation

Spin refocusing T2 relaxation measurements were conducted on the melts as well. T2 measurements involve the decay of observable magnetization. This decay is also exponential but slightly different than that for T1 relaxation.

$$M_z(t) = M_0 \left(e^{-t/T_1} \right) \quad (5.7)$$

The results of a typical spin refocusing T2 measurement are shown in Figure 5.19. These results are also only semi-quantitative. This is because as the spin refocusing time is increased the effects of diffusion within the sample become more pronounced. In a viscous liquid such as the molten salts, these effects should be minimal. In a similar fashion to that outlined above, linearization of Equation 5.7 gives:

$$-\ln \left(\frac{M(t)}{M_0} \right) = \frac{t}{T_2} \quad (5.8)$$

A plot of the left side of Equation 5.8 vs. t will have a slope of $1/T_2$ (Figure 5.20). The T_2 's calculated from Figures 5.19 and 5.20 differ by less than 10%. The T_2 data for the imidazolium cation in the melts is presented in Table 5.2.

T1 (seconds)						
Melt	Molecular Position					
	H-2	H-4	H-5	H-6	H-7	H-8
0.5:1.0 Melt 25 °C	2.3	2.6	2.4	1.4	1.2	1.6
0.5:1.0 Melt 40 °C	2.0	2.2	2.2	1.1	1.4	1.2
0.99:1.0 Melt 25 °C	2.8	3.5	3.4	1.6	2.1	1.4

Table 5.1 Results of ^1H T1 inversion recovery experiment for each position on the EMIC molecule for a 0.5:1.0 melt at 25 °C and 40 °C and for a 0.99:1.0 melt at 25 °C.

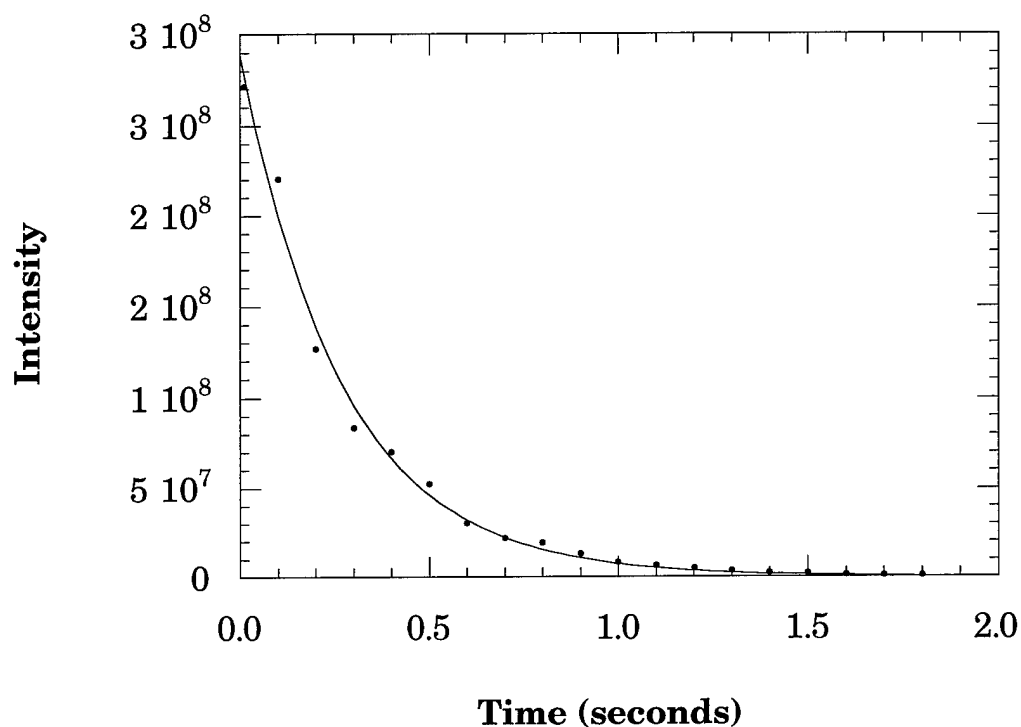


Figure 5.19 ^1H NMR spin refocusing experiment for H-7. The spin refocusing experiment consists of a 90° pulse along the X axis, a waiting period, a 180° pulse along the Y axis, another waiting period of equal length, and then the acquisition. The intensity of the peak of interest is then monitored as a function of the waiting time (waiting period $\times 2$). The line is the least squared fit of the data using Equation 5.7.

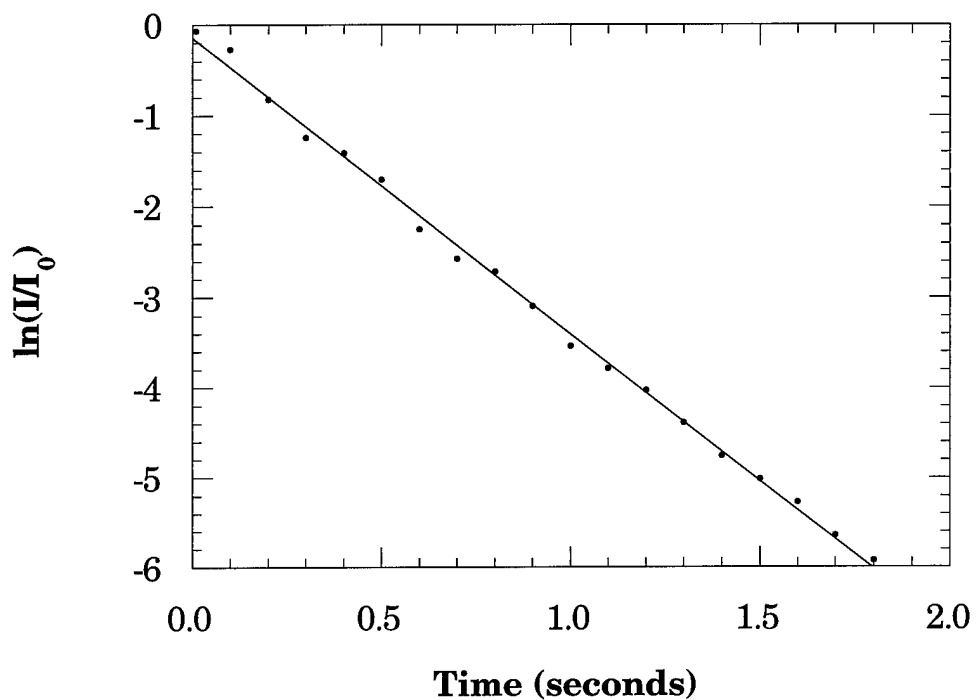


Figure 5.20 ^1H NMR spin refocusing experiment for H-7. The spin refocusing experiment consists of a 90° pulse along the X axis, a waiting period, a 180° pulse along the Y axis, another waiting period of equal length, and then the acquisition. The intensity of the peak of interest is then monitored as a function of the waiting time (waiting period $\times 2$). The data can be plotted according to Equation 5.8. The line is the linear least squared fit of the data.

T2 (milliseconds)						
Melt	Molecular Position					
	H-2	H-4	H-5	H-6	H-7	H-8
0.5:1.0 Melt 25 °C	83.2	90.2	93.6	94.6	276	176
0.5:1.0 Melt 40 °C	98.0	114	129	184	510	238
0.99:1.0 Melt 25 °C	104	278	324	234	844	294

Table 5.2 Results of ^1H T2 spin refocusing experiment for each position on the EMIC molecule for a 0.5:1.0 melt at 25 °C and 40 °C and for a 0.99:1.0 melt at 25 °C.

5.3.1.3 T1ρ Relaxation

T1ρ measurements were acquired using a pulse sequence where the magnetization is rotated into the XY plane and then spin locked. The spin locking time was varied and then the spectrum was acquired. T1ρ relaxation is described by the same expression as T2 relaxation (Equation 5.7 substitute T1ρ for T2). These experiments were acquired with a 2 kHz spin locking field while the spectra was acquired with a width of over 2.2 kHz on either side of the transmitter frequency. The weak spin locking field was necessary to allow spin locking times exceeding 1 second. When a weak spin locking field is used, the observed relaxation is a function of T1ρ, T1, the spin locking field strength, and the frequency difference between the spin locking field and the resonance of interest.³⁸ In order to obtain T1ρ, the following dependence can be used:

$$\frac{1}{T1\rho} = \frac{\cos^2(\theta)}{T1} + \frac{\sin^2(\theta)}{T1\rho} \quad (5.9)$$

where

$$\theta = \tan^{-1}\left(\frac{W_1}{\Delta}\right) \quad (5.10)$$

W_1 is the spin locking field strength and Δ is the frequency difference between the spin locking field and the peak of interest.

The results of the T1ρ measurements are shown in Table 5.3. These results are only qualitative. The data points arising from short spin locking

T1ρ (milliseconds)						
Melt	Molecular Position					
	H-2	H-4	H-5	H-6	H-7	H-8
0.5:1.0 Melt 25 °C	600	405	389	112	181	134
0.5:1.0 Melt 40 °C	-	971	1111	242	719	325
0.99:1.0 Melt 25 °C	-	3307	2315	790	2352	623

Table 5.3 Results of ^1H T1ρ spin locking experiment for each position on the EMIC molecule for a 0.5:1.0 melt at 25 °C and 40 °C and for a 0.99:1.0 melt at 25 °C.

times, < 80 msec, oscillate due to T2 ρ relaxation. In addition, the relaxation does not decay with a single exponential time constant. The exclusion of data points taken with varying spin locking times changes the relaxation time (Tables 5.4 - 5.6). This is indicative of the molecule being subject to motions with different molecular correlation times (τ_c).

5.3.1.4 Molecular Correlation Time

As mentioned earlier in the chapter, the molecular correlation time, τ_c , and the strength of the magnetic field are extremely important to determine whether the sample is in the extreme narrowing limit. Where the sample lies with respect to this dictates how the sample will respond to various NMR experiments, i.e. NOESY vs. ROESY. In addition, the variation of τ_c can allow us to compare molecular motion rates in different solvents. Because T1 and T2 are not equal, we immediately know we are not in the extreme narrowing region (Figure 5.21). Outside the extreme narrowing region τ_c can be estimated from the ratio of T1 and T2.³⁹

$$\tau_c \approx \frac{1}{\omega_0} \sqrt{\frac{2T1}{T2}} \quad (5.11)$$

The molecular correlation times for the hydrogen nuclei present on the imidazolium cation in the different melts is presented in Table 5.7. The molecular correlation times show two general trends. The first trend is that the

T1ρ (milliseconds) 0.5:1.0 Melt 25 °C						
	Molecular Position					
	H-2	H-4	H-5	H-6	H-7	H-8
0 to 1200 msec	600	405	389	112	181	124
80 to 1200 msec	1104	510	523	112	192	154
80 to 500 msec	454	267	370	124	280	165
500 to 1200 msec	-	1348	1581	-	-	-

Table 5.4 Results of ^1H T1ρ spin refocusing experiment for each position on the EMIC molecule for a 0.5:1.0 melt at 25 °C. The waiting time was varied from 0 to 1200 msec. If a single exponential decay is followed then the exclusion of portions of the data should not effect the value of T1ρ. In this case using portions of the available waiting times causes considerable variance in the calculated result.

T1ρ (milliseconds) 0.5:1.0 Melt 40 °C						
	Molecular Position					
	H-2	H-4	H-5	H-6	H-7	H-8
0 to 1200 msec	-	971	1111	242	719	325
80 to 1200 msec	-	1213	1202	248	1141	285
80 to 500 msec	2315	889	885	274	563	300
500 to 1200 msec	-	2053	2251	-	-	375

Table 5.5 Results of ^1H T1ρ spin refocusing experiment for each position on the EMIC molecule for a 0.5:1.0 melt at 40 °C. The waiting time was varied from 0 to 1200 msec. If a single exponential decay is followed then the exclusion of portions of the data should not effect the value of T1ρ. In this case using portions of the available waiting times causes considerable variance in the calculated result.

T1ρ (milliseconds) 0.99:1.0 Melt 25 °C						
	Molecular Position					
	H-2	H-4	H-5	H-6	H-7	H-8
0 to 1200 msec	-	3307	2315	790	2352	623
80 to 1200 msec	-	3833	2718	684	4596	684
80 to 500 msec	-	-	-	712	1564	671
500 to 1200 msec	-	-	-	628	-	732

Table 5.6 Results of ^1H T1ρ spin refocusing experiment for each position on the EMIC molecule for a 0.99:1.0 melt at 25 °C. The waiting time was varied from 0 to 1200 msec. If a single exponential decay is followed then the exclusion of portions of the data should not effect the value of T1ρ. In this case using portions of the available waiting times causes considerable variance in the calculated result.

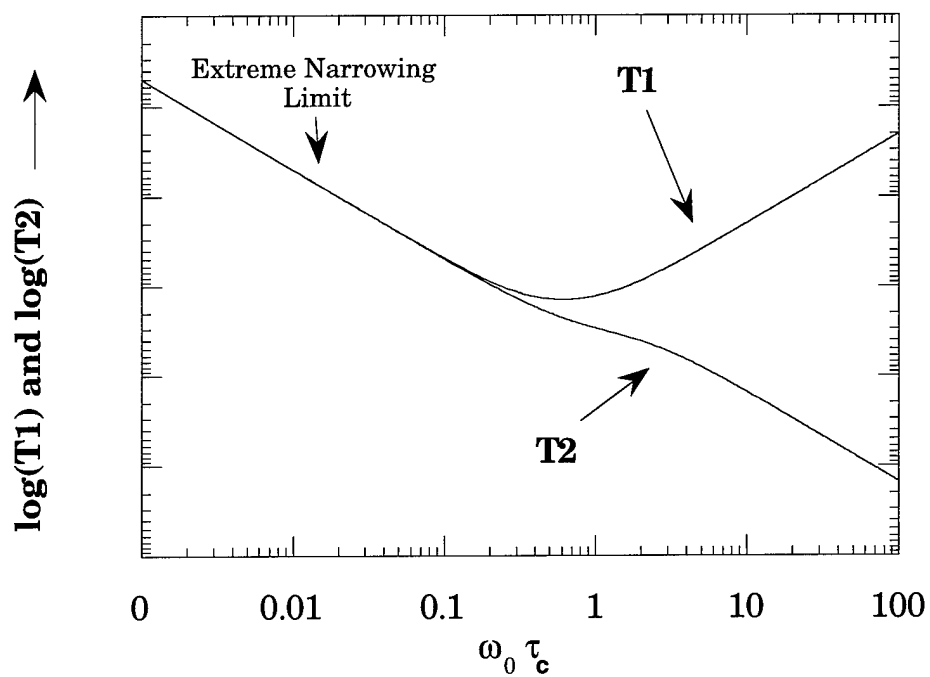


Figure 5.21 Plot of T_1 and T_2 vs. $\omega_0 \tau_c$. In the extreme narrowing region T_1 equals T_2 but in viscous liquids or with large molecular weight molecules the two values deviate.

τ_c (nanoseconds)						
Melt	Molecular Position					
	H-2	H-4	H-5	H-6	H-7	H-8
0.5:1.0 Melt 25 °C	14.9	15.2	14.3	10.9	5.9	8.5
0.5:1.0 Melt 40 °C	12.8	12.4	11.7	6.9	4.7	6.4
0.99:1.0 Melt	14.7	10.0	9.2	7.4	4.5	6.2

Table 5.7 Molecular correlation time calculated for each molecular position of EMIC from the T1 and T2 values determined previously.

0.5 : 1.0 basic melt at 25 °C has the longest molecular correlation times followed by the 0.5 : 1.0 basic melt at 40 °C and then the 0.99 : 1.0 near neutral melt. This indicates that the imidazolium cation in the 0.5 : 1.0 basic melts moves more slowly in solution. It also indicates that even heating the 0.5 : 1.0 melt to 40 °C does not speed up the imidazolium cation movement relative to that in a near neutral melt. The second trend is that the hydrogen near the nitrogen nuclei have the shortest molecular correlation times. This is either due to the quadrupolar nature of nitrogen or the fact that these hydrogen are at the end of alkyl chains hanging into solution.

5.3.2 ROESY Studies

ROESY experiments were used to estimate internuclear distances between the EMIC cations in basic AlCl_3 :EMIC melts. ROESY spectra were obtained for a 0.5:1.0 melt at 25 °C, a 0.5:1.0 melt at 40 °C, a 0.99 : 1.0 melt at 25 °C, and a 95% deuterated 0.5:1.0 melt at 25 °C. The mixing time used in the ROESY experiments was varied for each of the samples (Figures 5.22 - 5.34).

When the mixing time is increased in the ROESY experiment communication between ^1H nuclei increases as well. The increased mixing time allows the cross-peaks due to NOE to increase in size. Figures 5.22 - 5.29 are a series of ROESY experiments in which the mixing time is successively increased. As expected, the cross-peaks become more intense as the mixing time is increased.

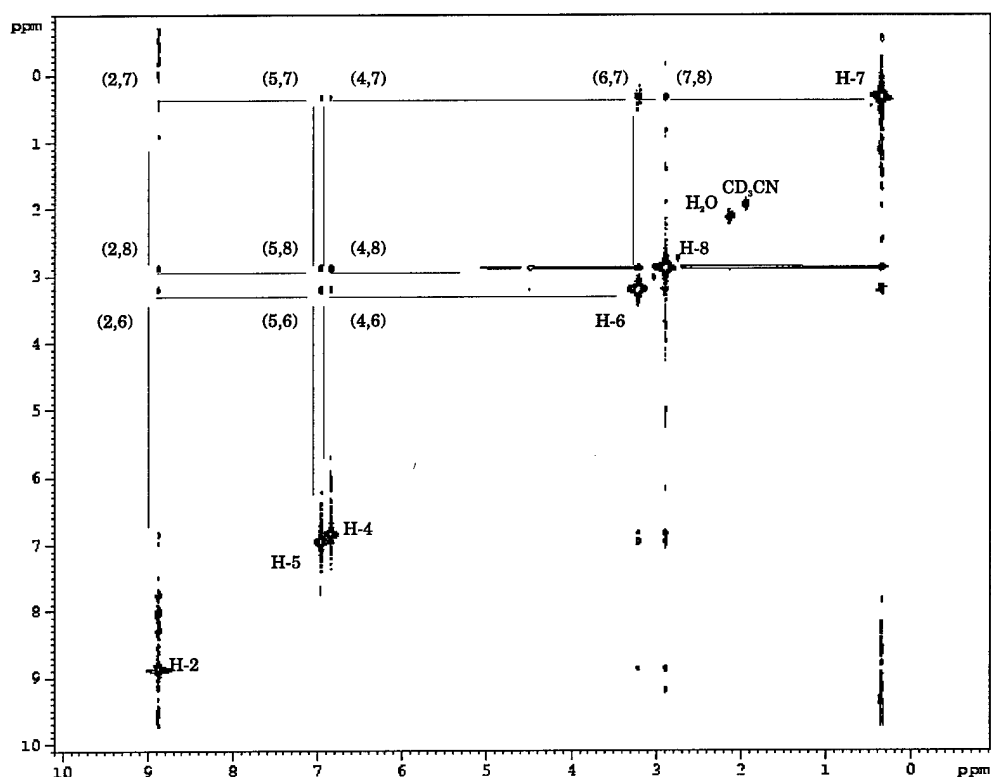


Figure 5.22 500 MHz ¹H NMR ROESY (spin locking time 50 msec) spectrum of 0.5:1 melt. Spectrum obtained using a Bruker ARX NMR spectrometer at 25 °C. Peaks labeled with an "H" such as H-1 or H-2 correspond to the numbering of the positions of the EMIC molecule. Peaks labeled with numbers in parenthesis are cross peaks and represent NOE communication between the two positions on the EMIC molecule. Lines have been added to aid in interpretation. Individuals unfamiliar with the interpretation of two-dimensional NMR spectra should refer to Reference 21.

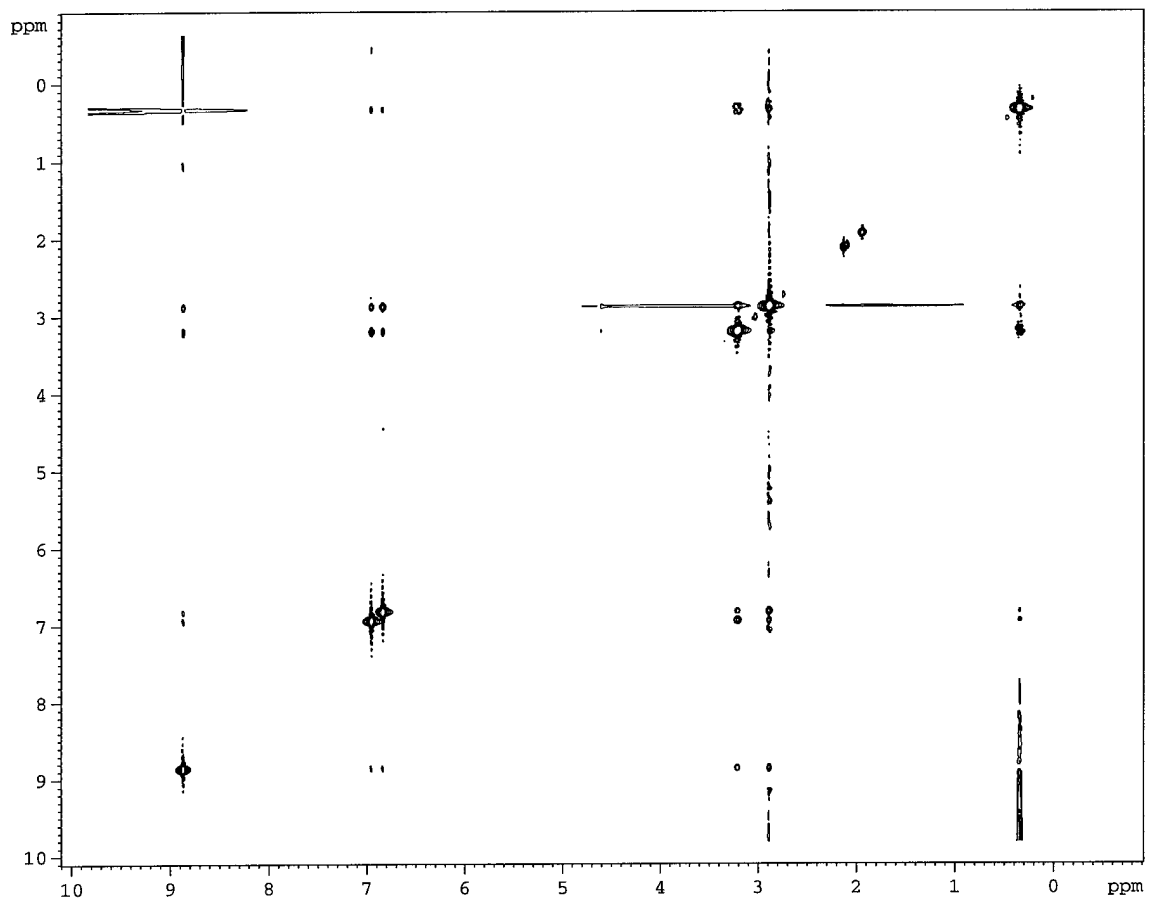


Figure 5.23 500 MHz ^1H NMR ROESY (spin locking time 100 msec) spectrum of 0.5:1 melt. Spectrum obtained using a Bruker ARX NMR spectrometer at 25 $^{\circ}\text{C}$.

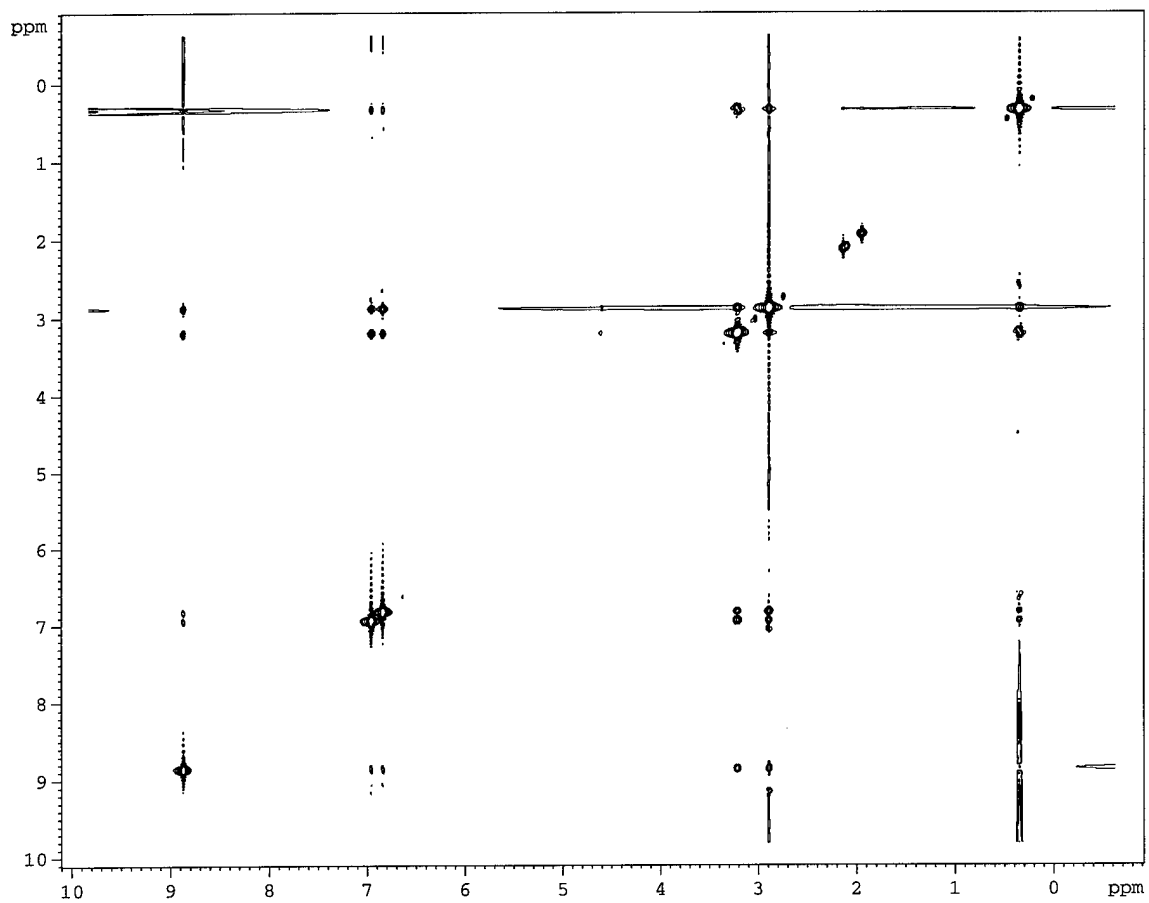


Figure 5.24 500 MHz ^1H NMR ROESY (spin locking time 150 msec) spectrum of 0.5:1 melt. Spectrum obtained using a Bruker ARX NMR spectrometer at 25 °C.

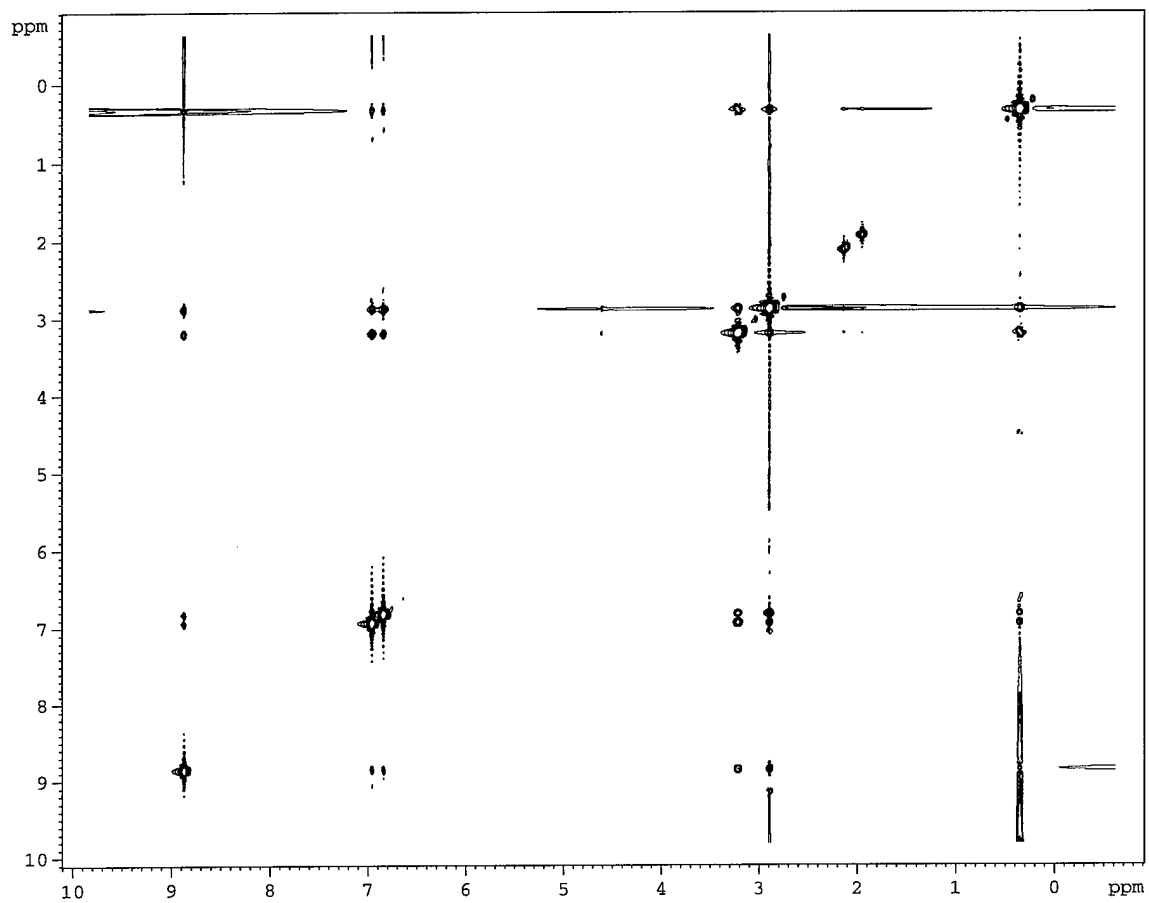


Figure 5.25 500 MHz ^1H NMR ROESY (spin locking time 200 msec) spectrum of 0.5:1 melt. Spectrum obtained using a Bruker ARX NMR spectrometer at 25 °C.

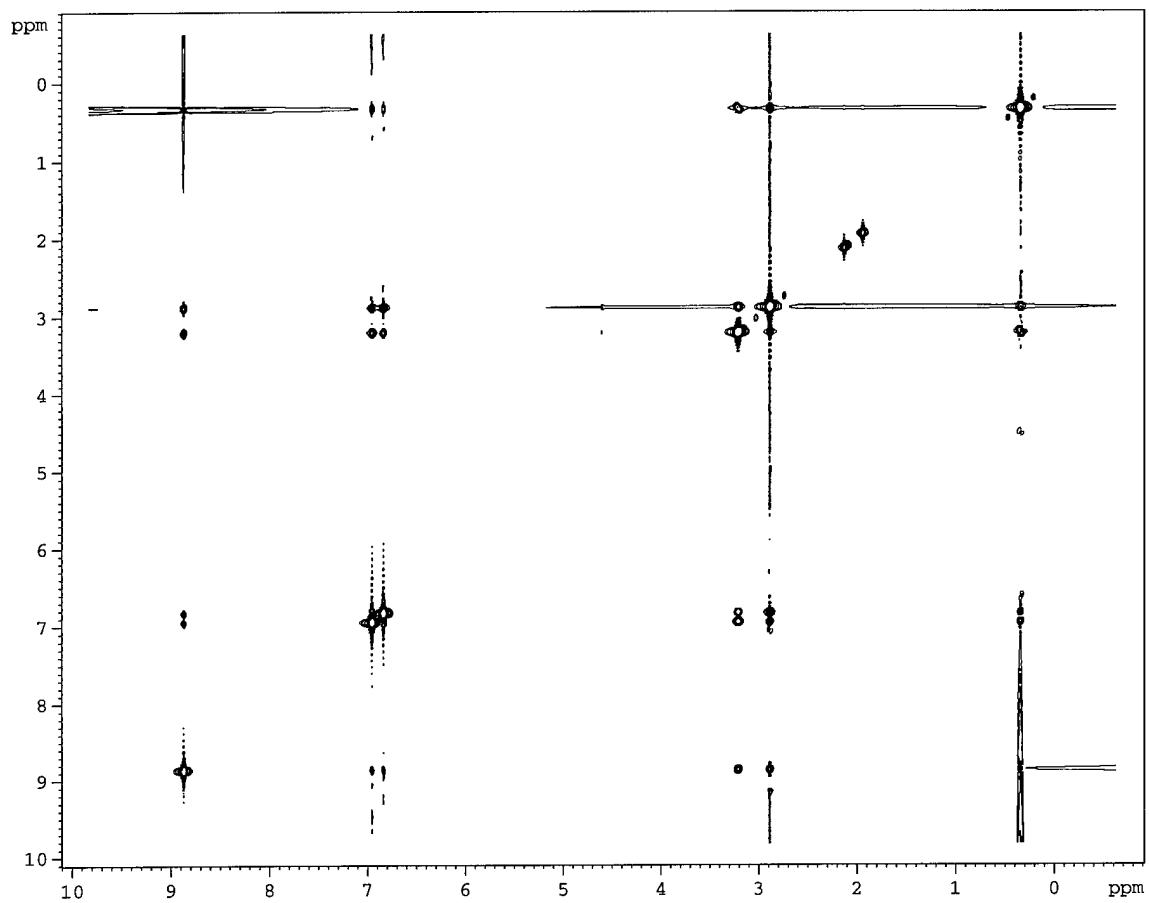


Figure 5.26 500 MHz ^1H NMR ROESY (spin locking time 250 msec) spectrum of 0.5:1 melt. Spectrum obtained using a Bruker ARX NMR spectrometer at 25 °C.

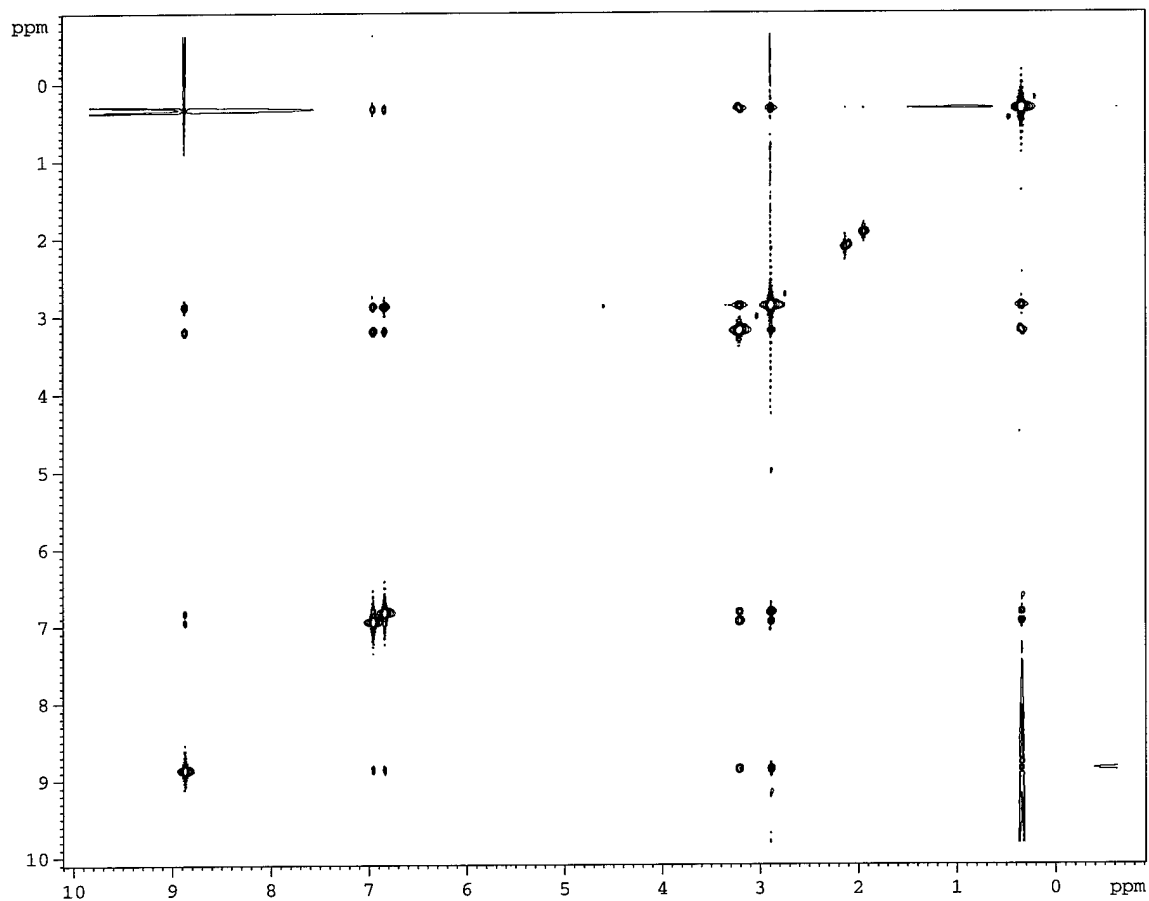


Figure 5.27 500 MHz ^1H NMR ROESY (spin locking time 300 msec) spectrum of 0.5:1 melt. Spectrum obtained using a Bruker ARX NMR spectrometer at 25 °C.

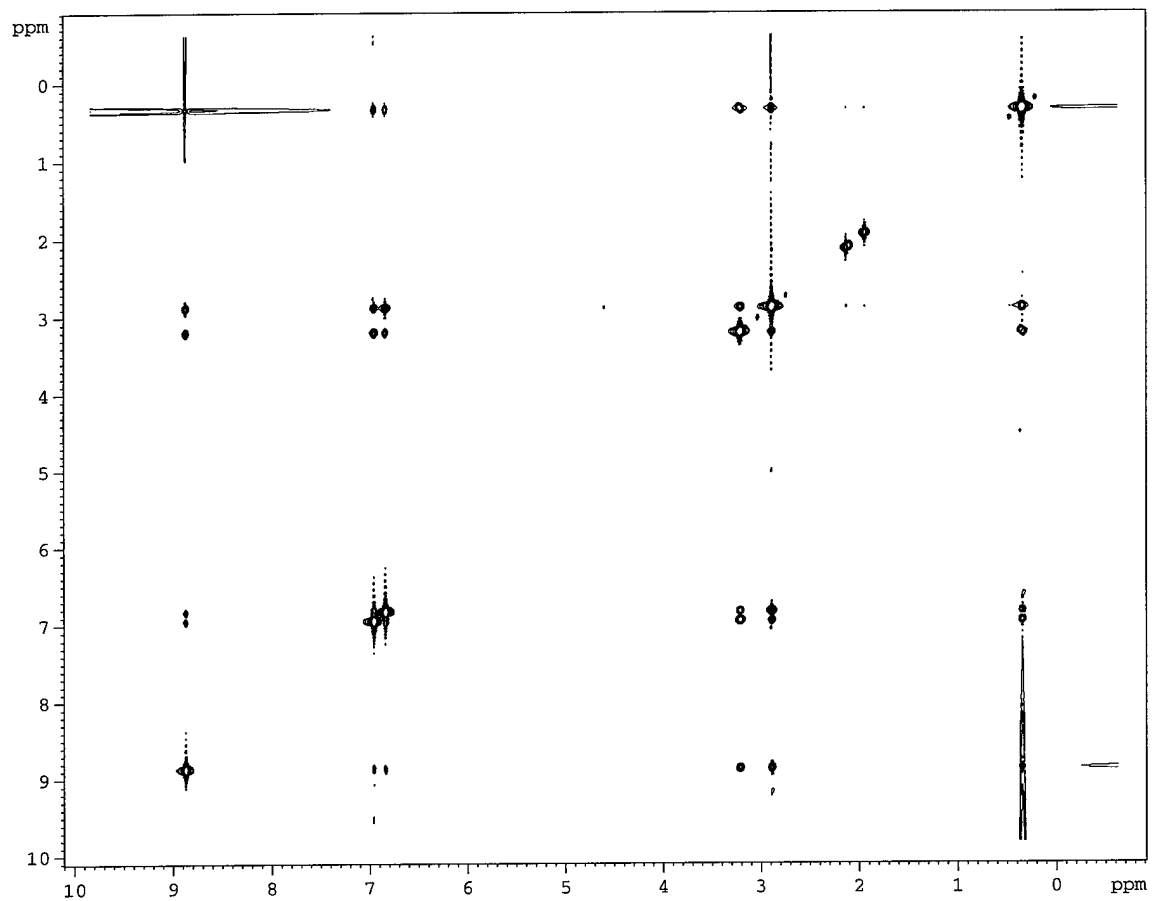


Figure 5.28 500 MHz ^1H NMR ROESY (spin locking time 350 msec) spectrum of 0.5:1 melt. Spectrum obtained using a Bruker ARX NMR spectrometer at 25 °C.

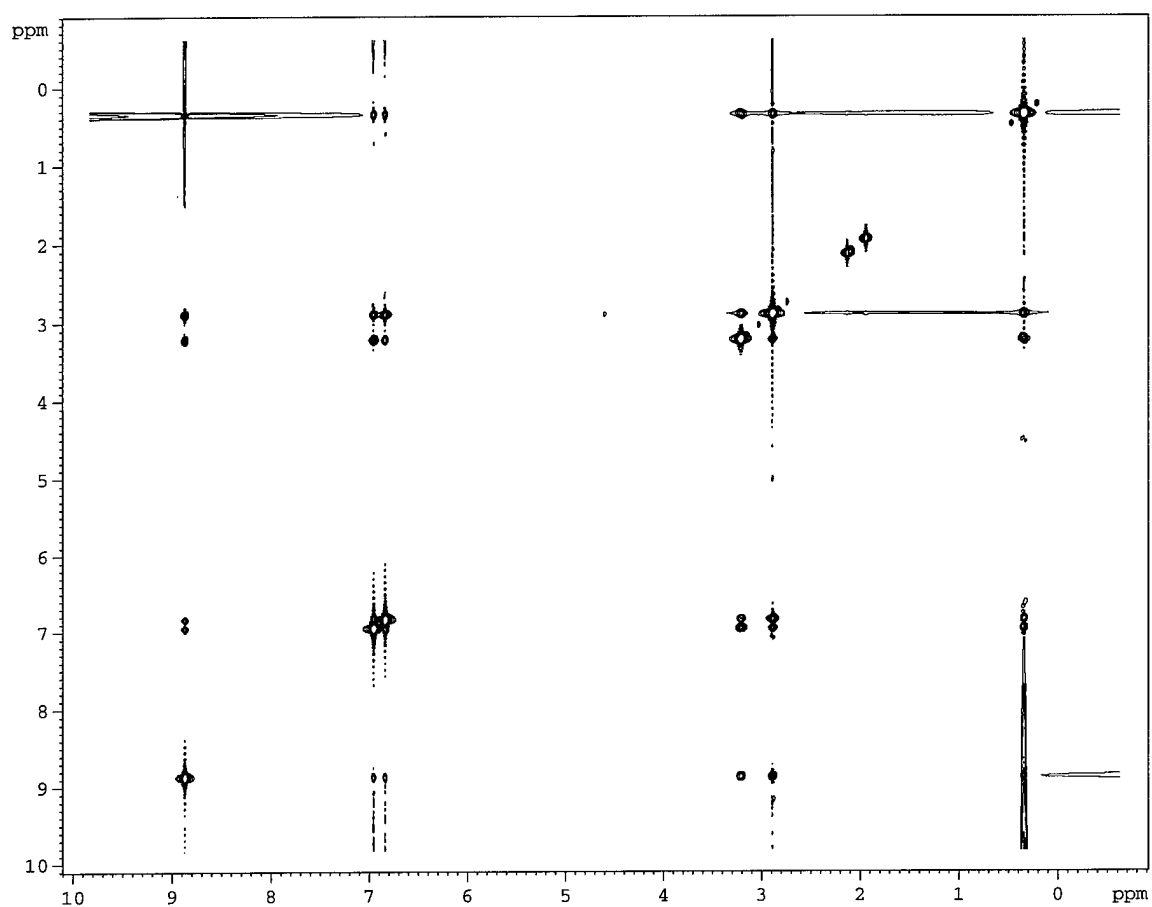


Figure 5.29 500 MHz ^1H NMR ROESY (spin locking time 400 msec) spectrum of 0.5:1 melt. Spectrum obtained using a Bruker ARX NMR spectrometer at 25 °C.

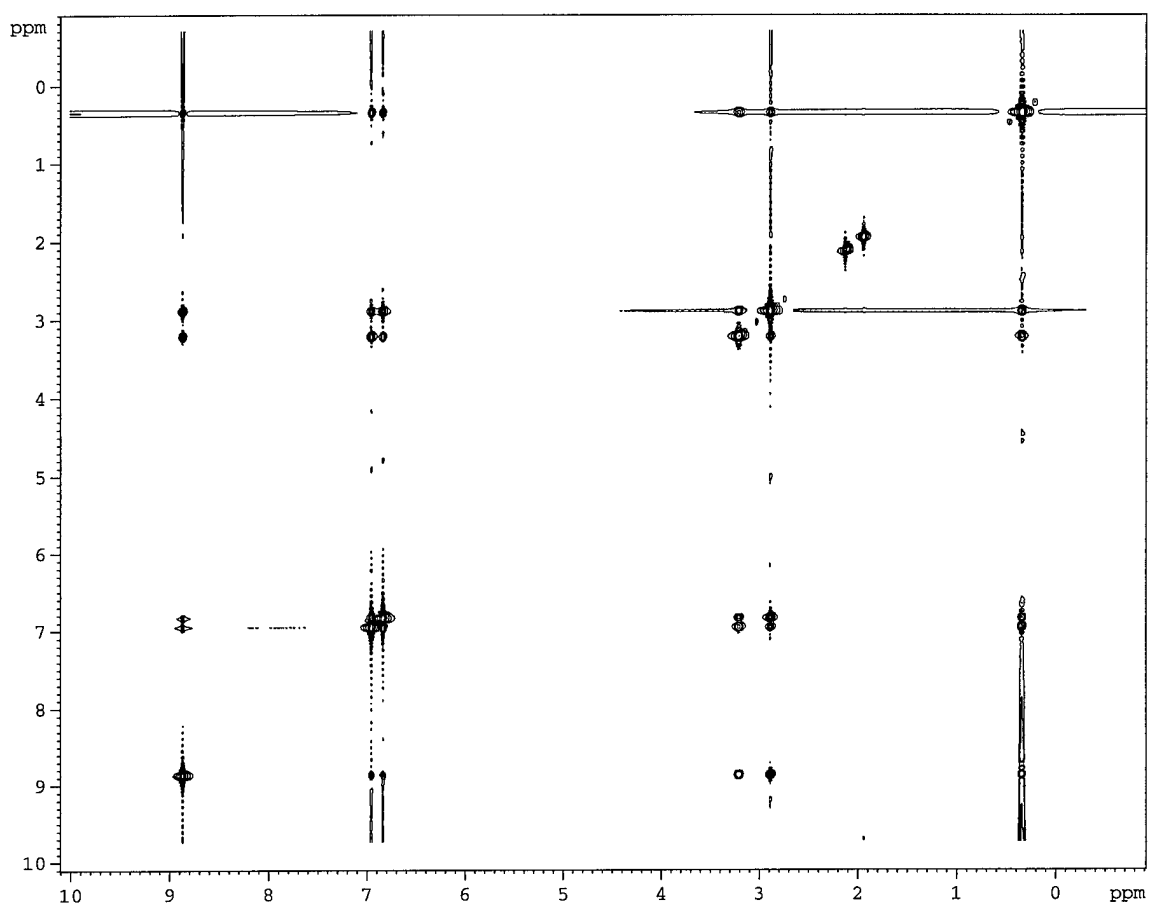


Figure 5.30 500 MHz ^1H NMR ROESY (spin locking time 500 msec) spectrum of 0.5:1 melt. Spectrum obtained using a Bruker ARX NMR spectrometer at 25 °C.

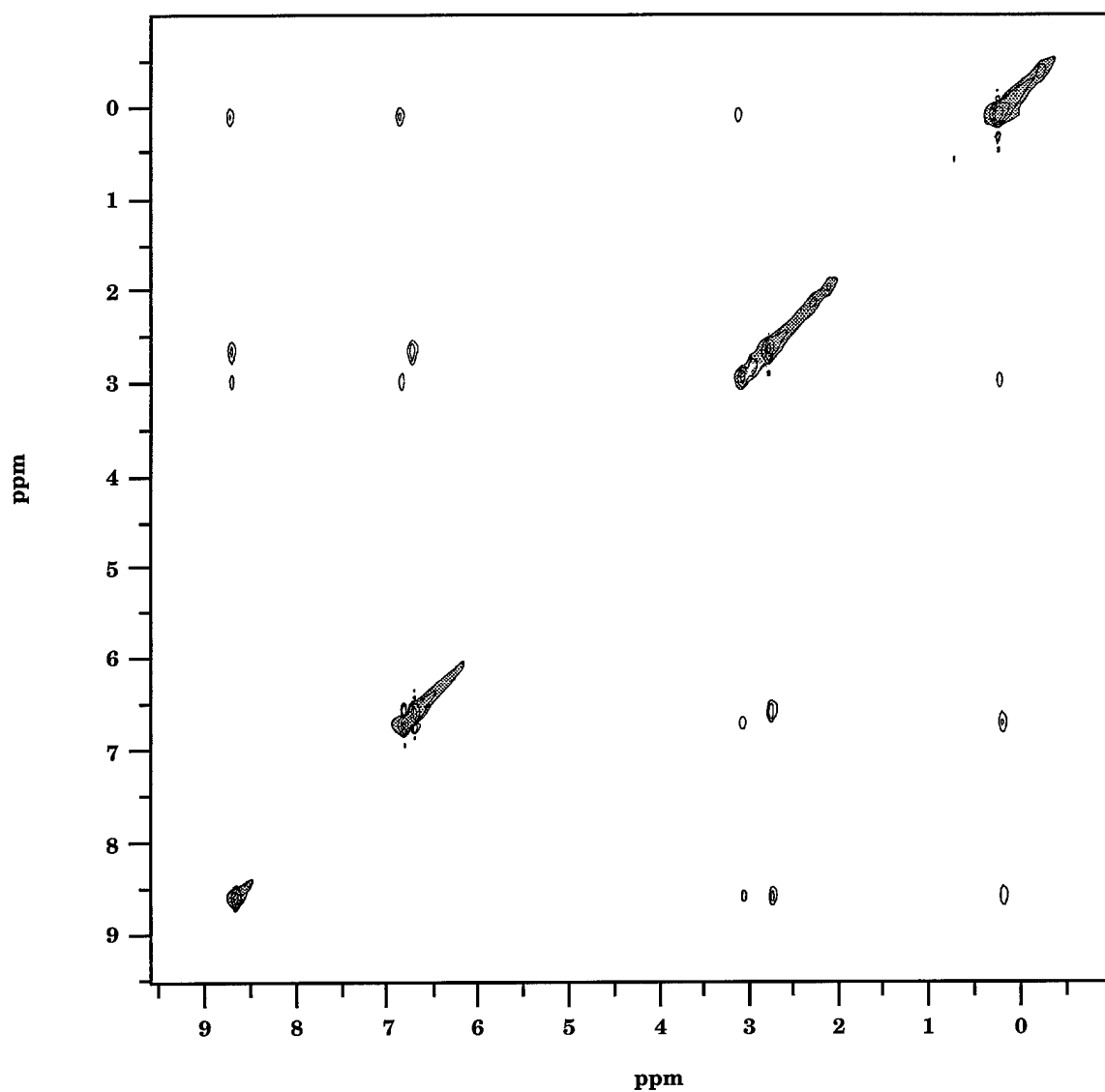


Figure 5.31 500 MHz ^1H NMR ROESY (spin locking time 250 msec) spectrum of a 95% perdeuterated EMIC 0.5:1 melt. In this sample 95% of the EMIC is perdeuterated and the other 5% is perprotiated. Spectrum obtained using a GE Omega NMR spectrometer at 25 $^{\circ}\text{C}$

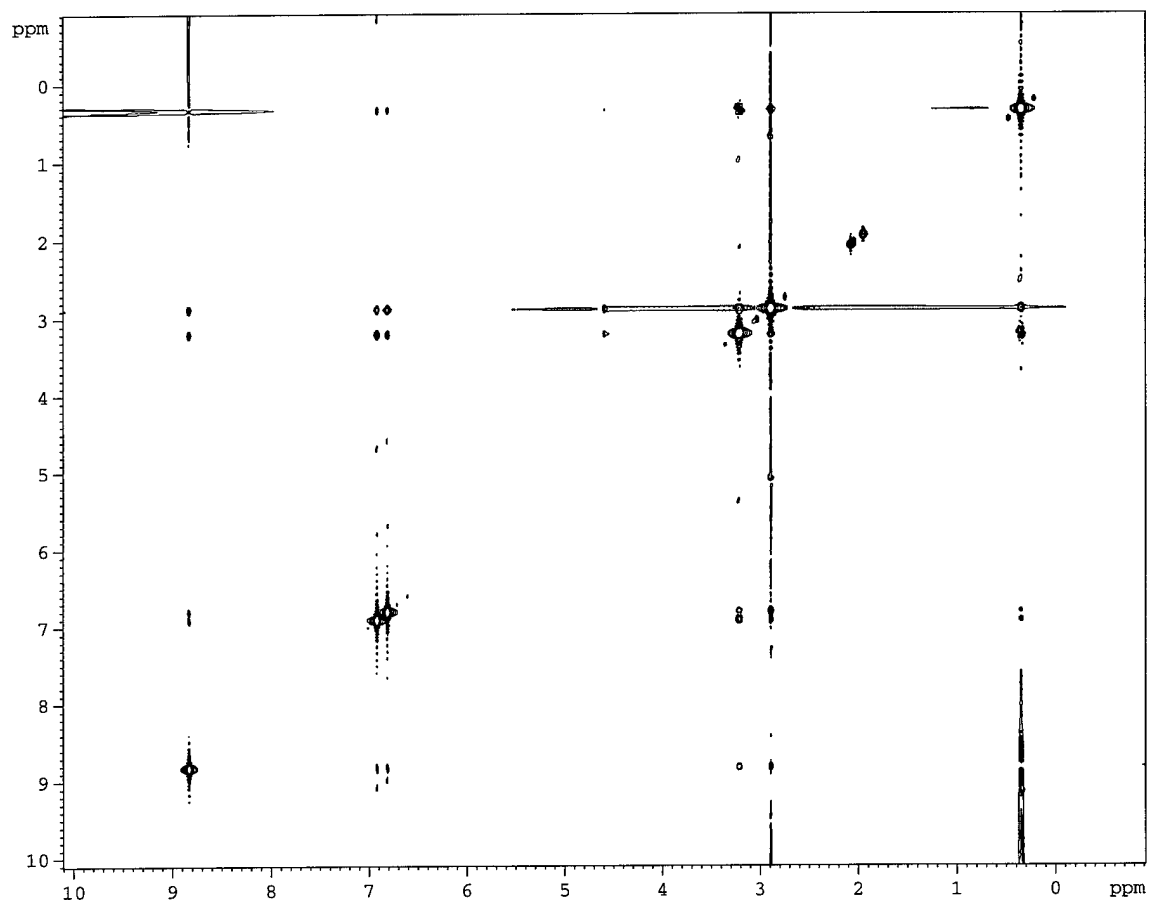


Figure 5.32 500 MHz ¹H NMR ROESY (spin locking time 200 msec) spectrum of 0.5:1 melt. Spectrum obtained using a Bruker ARX NMR spectrometer at 40 °C.

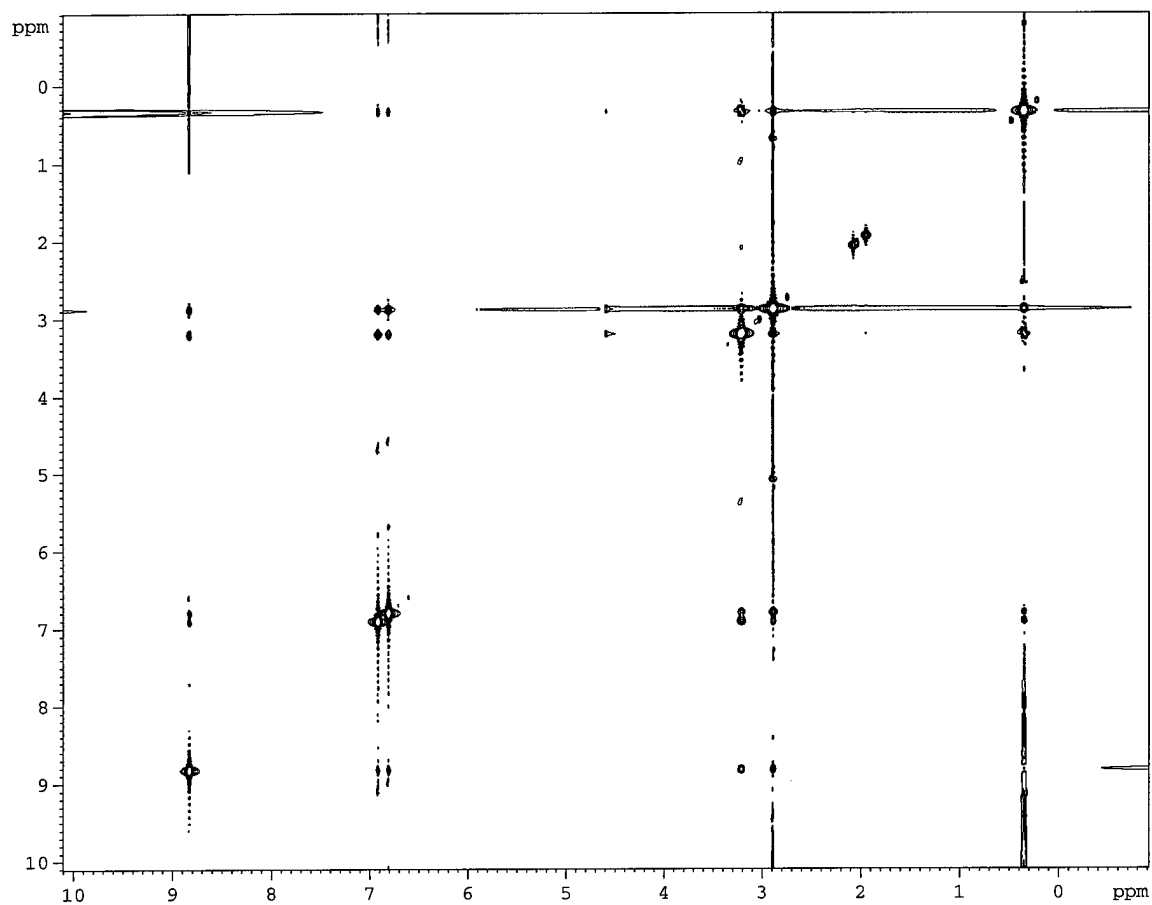


Figure 5.33 500 MHz ^1H NMR ROESY (spin locking time 300 msec) spectrum of 0.5:1 melt. Spectrum obtained using a Bruker ARX NMR spectrometer at 40 °C.

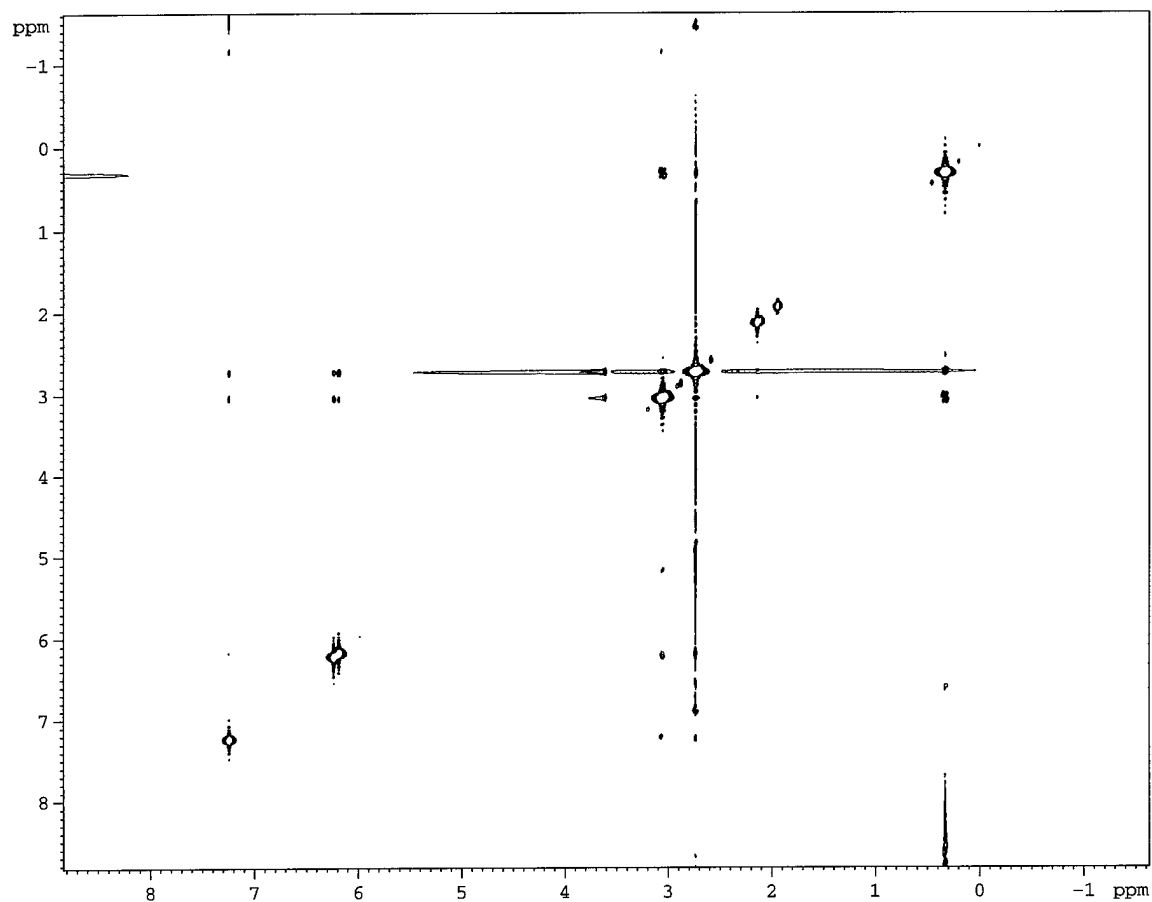


Figure 5.34 500 MHz ^1H NMR ROESY (spin locking time 200 msec) spectrum of 0.99:1.0 melt. Spectrum obtained using a Bruker ARX NMR spectrometer at 25 °C.

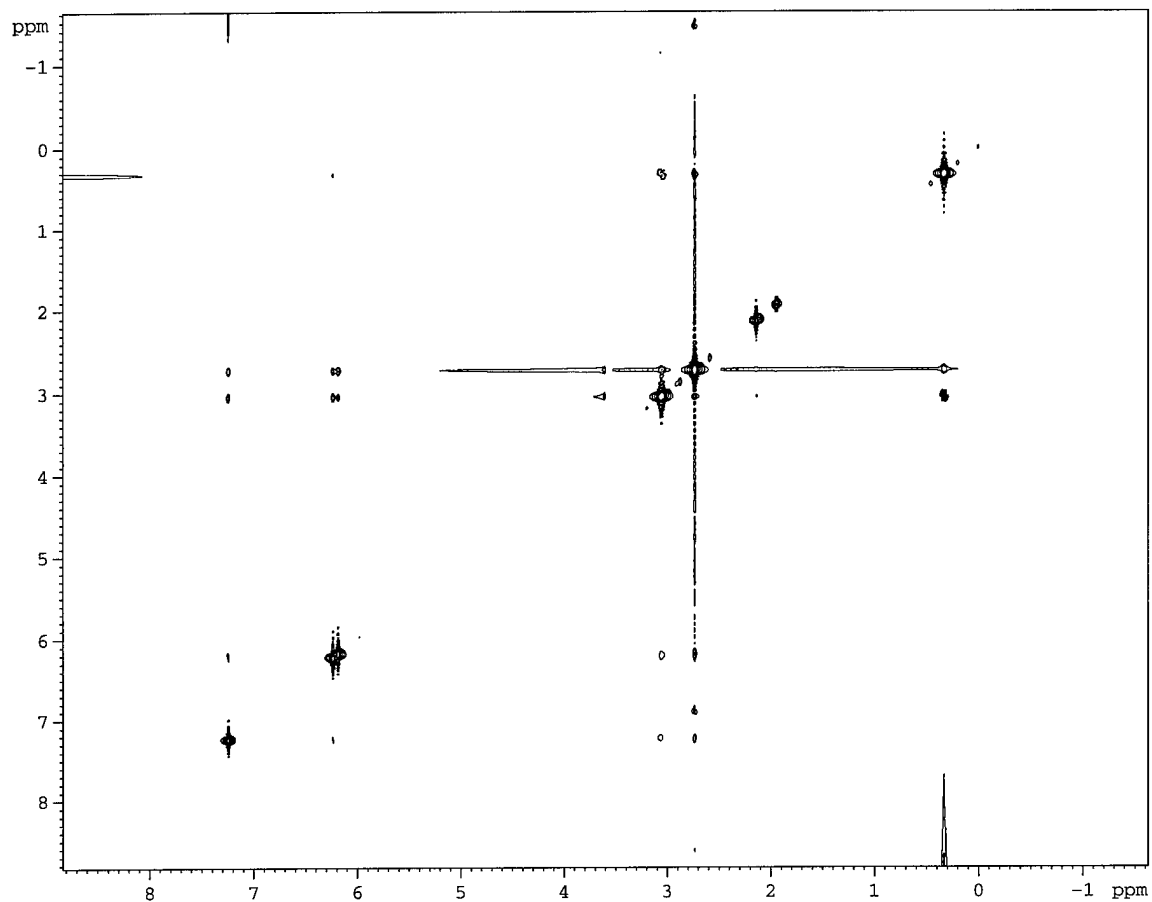


Figure 5.35 500 MHz ¹H NMR ROESY (spin locking time 400 msec) spectrum of 0.99:1.0 melt. Spectrum obtained using a Bruker ARX NMR spectrometer at 25 °C.

Intramolecular Distances in EMIC	
Interaction	Distance (Å)
H-4 H-5	2.70
H-2 H-8	2.94
H-2 H-4	4.30
H-2 H-5	4.30
H-5 H-8	4.70
H-4 H-6	4.80
H-6 H-8	5.13
H-4 H-7	5.24
H-7 H-8	5.75

Table 5.8 Intramolecular distances for the EMIC molecule. These distances are determined for crystalline EMIC.

In Figure 5.26, the ROESY spectrum shows cross-peaks due to NOE transfer. NOE cross-peaks are not normally observed for internuclear distances beyond 4 Å because of the r^{-6} dependence.²⁵ The ROESY spectrum (Figure 5.26) shows cross-peaks which are clearly due to intramolecular interactions (i.e. between H-4 and H-5) (Table 5.8). It should be noted that these peaks can contain intermolecular contributions as well. In addition, there are cross-peaks which are most likely due to intermolecular interactions. For example, H-2, which is separated across the imidazole ring from H-4 and H-5 by 4.3 Å, still shows cross-peaks to both H-4 and H-5, thus indicating some type of intermolecular interaction. In addition, although H-4 and H-7 are separated by a minimum of 5.2 Å, and H-5 and H-8 are separated by a similar distance, they both still show significant NOE interactions. If correct this further demonstrates the existence of intermolecular interactions in basic $\text{AlCl}_3\text{:EMIC}$ melts.⁴⁰

To clearly distinguish between intramolecular and intermolecular NOE transfer the 95% deuterated sample was utilized. The 95% deuterated melt contains two types of EMIC, EMIC that is fully deuterated and EMIC that is fully protiated. This mixture of two types of EMIC was then mixed with AlCl_3 to generate a 0.5:1.0 melt. Due to the highly deuterated environment, any EMIC that contains protium is surrounded by deuterated EMIC. This isolation of ^1H containing EMIC quenches any intermolecular NOE. The absence of cross-peaks from the deuterated ROESY spectrum that were initially present helps differentiate between inter- and intra-molecular NOE communication. Those peaks that disappear or become less intense have an intermolecular

contribution. The resulting spectrum (Figure 5.30) shows the absence of the peaks between H-2 and H-4 as well as between H-2 and H-5, H-4 and H-6, H-4 and H-7, H-5 and H-8, H-6 and H-8, and H-7 and H-8. These have been assigned as due to intermolecular NOE transfer. The cross-peaks between H-2 and H-6, H-2 and H-7, H-2 and H-8, H-4 and H-8, H-5 and H-6, H-5 and H-7, H-6 and H-7 are still present. These cross-peaks have been assigned as intramolecular NOE transfer.⁴⁰

ROESY spectra were acquired for the 0.5:1.0 melt at 40 °C. The higher temperature should increase molecular motion as evidenced by a drop in viscosity as the temperature is raised. Figures 5.33 and 5.34 show that indeed the cross peaks are less intense at a given mixing time. Intermolecular NOE is not expected to occur as rapidly if the molecules do not stay in close proximity.

Although the 95% perdeuterated sample allowed the cross peaks to be assigned as either predominately intermolecular or intramolecular in nature, the 0.99:1.0 near neutral sample was necessary to show that the interactions which allow the intermolecular NOE are absent in neutral melts. As expected the cross-peaks between H-2 and H-4, H-4 and H-7, are absent while the cross-peak between H-2 and H-5 is greatly diminished. However, the cross-peaks between H-4 and H-6, H-5 and H-8, H-6 and H-8, and H-7 and H-8 are still present. These cross-peaks were not expected to be present. To further complicate the situation the cross-peak between H-2 and H-7 which was assigned as intramolecular is absent. After reviewing the other ROESY spectra the cross-peak between H-2 and H-7 was generally very weak. The absence of this cross-peak is not entirely surprising.

The presence of some cross-peaks which had been assigned as intermolecular in the 0.99:1.0 melt suggests that even in neutral melts there is still some intermolecular hydrogen bonding; none-the-less it has diminished substantially.

5.4 Conclusions

Relaxation studies in which T1, T2 and T1 ρ were measured have shown that both 0.5:1.0 and 0.99:1.0 melts at 25 °C and 0.5:1.0 at 40 °C are not in the region of extreme narrowing in a 11.74 Tesla field (500 MHz). The molecular correlation times for the 1-ethyl-3-methylimidazolium cation have been estimated.

Evidence of intermolecular NOE transfer for basic ambient-temperature chloroaluminate melts has been presented. The intermolecular NOE transfer is possible due to the existence of intermolecular interactions in the basic melts (hydrogen bonding).⁴⁰ The presence of the cross-peaks indicates that the intermolecular distances between EMIC molecules is less than 4 Å. Upon heating the intensities of the cross-peaks is lowered. The presence of intermolecular interactions in near neutral melts is still unclear.

This area of research warrants future work. Further studies to quantitate the intermolecular NOE remain to be completed. In addition, the interpretation of the relaxation studies is presently still very uncertain. Further studies to minimize errors in measurement as well as characterize more

melts under various conditions may provide insight into this very complex system.

Chapter 5 References

- (1) Fannin, A. A.; Floreani, D. A.; King, D. A.; Landers, J. S.; Piersma, B. J.; Stech, D. J.; Vaughn, R. L.; Wilkes, J. S.; Williams, J. L. "Properties of 1,3-Dialkylimidazolium Chloride-Aluminum Chloride Ionic Liquids. 2. Phase Transitions, Densities, Electrical Conductivities, and Viscosities." *J. Phys. Chem.* **1984**, 88, 2614-2621.
- (2) *CRC Handbook of Chemistry and Physics*; Weast, R. C. Ed.; CRC Press: Boca Raton, Fl, 60th ed., 1980.
- (3) Lipsztajn, M.; Osteryoung, R. A. "On Ionic Association in Ambient Temperature Chloroaluminate Molten Salts." *J. Electrochem. Soc.* **1985**, 132, 1126-1130.
- (4) Robinson, J.; Bugle, R. C.; Chum, H. L.; Koran, D.; Osteryoung, R. A. "¹H and ¹³C Nuclear Magnetic Resonance Spectroscopy Studies of Aluminum Halide-Alkylpyridinium Halide Molten Salts and Their Benzene Solutions." *J. Am. Chem. Soc.* **1979**, 101, 3776-3779.
- (5) Taulelle, F.; Popov, A. I. "Nuclear Magnetic Resonance Study of Aluminum Chloride-n-Butylpyridinium Chloride Melts." *Polyhedron* **1983**, 2, 889-894.

- (6) Wilkes, J. A.; Frye, J. S.; Reynolds, G. F. " ^{27}Al and ^{13}C NMR Studies of Aluminum Chloride-Dialkylimidazolium Chloride Molten Salts." *Inorg. Chem.* **1983**, *22*, 3870-3872.
- (7) Fannin, A. A.; King, D. A.; Levisky, J. A.; Wilkes, J. S. "Properties of 1,3-Dialkylimidazolium Chloride-Aluminum Chloride Ionic Liquids. 1. Ion Interactions by Nuclear Magnetic Resonance Spectroscopy." *J. Phys. Chem.* **1984**, *88*, 2609-2614.
- (8) Wilkes, J. S.; Hussey, C. L.; Sanders, J. R. "NMR Chemical Shift Studies of Ion Association in Aluminum Halide-Organic Halide Melts." *Polyhedron* **1986**, *5*, 1567-1571.
- (9) Tait, S.; Osteryoung, R. A. "Infrared Study of Ambient-Temperature Chloroaluminates as a Function of Melt Acidity." *Inorg. Chem.* **1984**, *23*, 4352-4360.
- (10) Abdul-Sada, A. K.; Greenway, A. M.; Hitchcock, P. B.; Mohammed, T. J.; Seddon, K. R.; Zora, J. A. "Upon the Structure of Room Temperature Halogenoaluminate Ionic Liquids." *J. Chem. Soc., Chem. Commun.* **1986**, 1753-1754.
- (11) Dubois, R. H.; Zaworotko, M. J.; White, P. S. "Complex Hydrogen-Bonded Cations. X-ray Crystal Structure of $[(\text{C}_6\text{H}_5\text{CH}_2)\text{NH}_3]_4\text{Cl}][\text{AlCl}_4]_3$ and Its

Relevance to the Structure of Basic Chloroaluminate Room-Temperature Melts." *Inorg. Chem.* **1989**, 28, 2019-2020.

(12) Dieter, K. M.; Dymek, C. J.; Heimer, N. E.; Rovang, J. W.; Wilkes, J. S. "Ionic Structure and Interactions in 1-Methyl-3-ethylimidazolium Chloride- AlCl_3 Molten Salts." *J. Am. Chem. Soc.* **1988**, 110, 2722-2726.

(13) Dymek, C. J.; Grossie, D. A.; Fratini, A. V.; Adams, W. W. "Evidence for the Presence of Hydrogen-Bonded Ion-Ion Interactions in the Molten Salt Precursor 1-Methyl-3-ethylimidazolium Chloride." *J. Mol. Struc.* **1989**, 213, 25-34.

(14) Dymek, C. J.; Stewart, J. J. "Calculation of Hydrogen-Bonding Interactions between Ions in Room-Temperature Molten Salts." *Inorg. Chem.* **1989**, 28, 1472-1476.

(15) Avent, A. G.; Chaloner, P. A.; Day, M. P.; Seddon, K. R.; Welton, T. "Evidence for Hydrogen-Bonding in Solutions of 1-Methyl-3-ethylimidazolium Halides, as Determined by ^1H , ^{35}Cl and ^{127}I NMR Spectroscopy, and Its Implications for Room-Temperature Halogenoaluminate(III) Ionic Liquids." in *Proceedings of the Seventh International Symposium on Molten Salts*, The Electrochemical Society, Pennington, NJ, 1990, PV 90-17, 98-133.

- (16) Avent, A. G.; Chaloner, P. A.; Day, M. P.; Seddon, K. R.; Welton, T. "Evidence for Hydrogen Bonding in Solutions of 1-Ethyl-3-methylimidazolium Halides, and Its Implications for Room-Temperature Halogenoaluminate(III) Ionic Liquids." *J. Chem. Soc. Dalton Trans.* **1994**, 3405-3413
- (17) Neuhaus, D.; Williamson, M. In *The Nuclear Overhauser Effect In Structural and Conformational Analysis*. VCH: New York, NY. 1989.
- (18) Roberts, G. C. K. In *NMR of Macromolecules: A Practical Approach*. IRL Press at Oxford University Press: New York, NY. 1993.
- (19) Solomon, I. "Relaxation Processes in a System of Two Spins." *Physical Review* **1955**; 99, 559-565.
- (20) Anet, F. A. L.; Bourn, A. J. R. "Nuclear Magnetic Resonance Spectral Assignments from Nuclear Overhauser Effects." *J. Am. Chem. Soc.* **1965**, 87, 5250-5251.
- (21) Derome, A. E. In *Modern NMR Techniques for Chemistry Research*. Pergamon Press: Elmsford, NY. 1987, Chapters 5 and 6.
- (22) Friebolin, H. In *Basic One- and Two-Dimensional NMR Spectroscopy*. VCH: New York, NY. 1991, Chapter 10.

- (23) Ernst, R. R.; Bodenhausen, G.; Wokaun, A. In *Principles of Nuclear Magnetic Resonance in One and Two Dimensions*. Oxford University Press: New York, 1991, Chapter 9.
- (24) Akitt, J. W. *NMR and Chemistry: An Introduction to the Fourier transform-multinuclear era*; Chapman and Hall: New York, 1983; Chapter 4.
- (25) Bell, R. A.; Saunders, J. K. "Correlation of the Intramolecular Nuclear Overhauser Effect with Internuclear Distance." *Can J. Chem.* **1970**, *48*, 1114-1122.
- (26) Bax, A.; Davis, D. J. "Practical Aspects of Two-Dimensional Transverse NOE Spectroscopy." *J. Mag. Res.* **1985**, *63*, 207-213.
- (27) Kessler, H.; Gehrke, M.; Griesinger, C. "Two-Dimensional NMR Spectroscopy: Background and Overview of the Experiments." *Angew. Chem. Int. Ed. Engl.* **1988**, *27*, 490-536.
- (28) Bothner-By, A. A.; Stephens, R. L.; Lee J. "Structure Determination of a Tetrasaccharide: Transient Nuclear Overhauser Effects in the Rotating Frame." *J. Am. Chem. Soc.* **1984**, *106*, 811-813.
- (29) Neuhaus, D.; Keeler, J. "'False' Transverse NOE Enhancements in CAMELSPIN Spectra." *J. Mag. Res.* **1986**, *68*, 568-574

- (30) Griesinger, C.; Ernst, R. R. "Frequency Offset Effects and Their Elimination in NMR Rotating-Frame Cross-Relaxation Spectroscopy." *J. Mag. Res.* **1987**, *75*, 261-271.
- (31) Kaiser, R. "Intermolecular Nuclear Overhauser Effect in Liquid Solutions." *J. Chem. Phys.* **1965**, *42*, 1838-1839.
- (32) Macura, S.; Ernst, R. R. "Elucidation of Cross Relaxation in Liquids by Two-Dimensional NMR Spectroscopy." *Molecular Physics* **1980**, *41*, 95-117.
- (33) Dieter, K. M.; Dymek, C. J. Jr.; Heimer, N. E.; Rovang, J. W.; Wilkes, J. S. "Ionic Structure and Interactions in 1-Methyl-3-ethylimidazolium Chloride-AlCl₃ Molten Salts." *J. Am. Chem. Soc.* **1988**, *110*, 2722-2726.
- (34) Trulove, P. C.; Osteryoung, R. A. "Proton Speciation in Ambient-Temperature Chloroaluminate Ionic Liquids." *Inorg. Chem.* **1992**, *31*, 3980-3985.
- (35) Trulove, P. C.; Sukumaran, D. K.; Osteryoung, R. A. "Protons in Acidic Ambient-Temperature Chloroaluminate Molten Salts: Hydrogen-Deuterium Exchange between the Imidazolium Cation and Hydrogen Chloride." *J. Phys. Chem.* **1994**, *98*, 141-146.

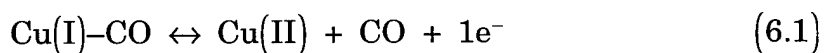
- (36) Vold, R. L.; Vold, R. R. *Prog. Nuc. Mag. Res. Spec.* **1978**, *12*, 79.
- (37) Werbelow, L. G.; Grant, D. M. In *Advances in Magnetic Resonance*; Waugh J. S., Ed.; Academic Press: New York, 1977; Vol. 9, pp 190-298.
- (38) Zhang, S.; Morgan, D. R.; Burgess, J. P.; Stejskal, E. O.; Fornes, R. E. "Strategies for Cross Polarization in the Tilted Frame: Spin Dynamics and Relaxation." 34th Experimental Nuclear Magnetic Resonance Conference, St. Louis, Missouri, Mar 14 - 18 1993, Poster Abstract 147.
- (39) Van de Ven, F. J. M. In *Multidimensional NMR in Liquids: Basic Principles and Experimental Methods*. VCH: New York 1995, Chapter 3, Sec. 4.
- (40) Mantz, R. A.; Trulove, P. C.; Carlin, R. T.; Osteryoung, R. A. "ROESY NMR of Basic Ambient-Temperature Chloroaluminate Ionic Liquids." *Inorg. Chem.* **1995**, *34*, 3846-3847.

Chapter 6

Characterization of the Cu(I/II) Couple in Ambient-Temperature Chloroaluminate Molten Salts

6.1 Introduction

Initial studies of the Cu(I) / Cu(II) couple in molten salts were geared toward using the couple in battery systems.¹⁻³ These studies concluded that the Cu(I) / Cu(II) couple electron transfer rate was diffusion controlled.³ In addition, they found that both the Cu(I) and Cu(II) species formed tetrachloroaluminate complexes in acidic molten salts.³ Carlin and Sullivan investigated Cu(I) in acidic 1-butylpyridinium chloride based melts for use in removing carbon monoxide from continuous flowing gas streams.⁴ Copper is used industrially in the COSORB process in which CuCl is combined with AlCl₃ in an aromatic solvent to absorb carbon monoxide.⁵ Carlin and Sullivan were able to identify the carbon monoxide stretching frequency in the infrared spectrum at 2142 cm⁻¹ in the room temperature molten salts. This stretching energy is typical for Cu(I)-CO complexes. They also went on to characterize the Cu(I)-CO complex using electrochemistry and found that the Cu(I) / Cu(II) redox couple shifts 132 mV positive in the presence of carbon monoxide.⁴ In addition, potentiometric measurements were able to determine an equilibrium constant for:



of $88 \pm 16 \text{ atm}^{-1}$.⁴ One other important discovery was that Cu(I) is not oxidized by oxygen to Cu(II) in room temperature molten salts as it is in many conventional solvents.⁴

Carlin et al re-investigated the behavior of Cu(I) / Cu(II) couple dissolved in 1-ethyl-3-methylimidazolium chloride (EMIC) based melts in the presence of carbon monoxide.⁶ They utilized a 250 μm diameter tungsten electrode and used cyclic staircase, square wave, and normal pulse voltammetry. A 250 μm diameter tungsten electrode was utilized in order to minimize the effects of IR drop. They were able to determine the diffusion coefficient of Cu(II) in a 1.5:1.0 AlCl_3 :EMIC melt as $5.6 \pm 0.3 \times 10^{-7} \text{ cm}^2 \text{ sec}^{-1}$. Carlin et al determined the electron transfer kinetic parameters for the Cu(I) / Cu(II) in the presence of carbon monoxide as $E_{1/2} = 2.060 \text{ V}$, $\beta = 0.15$, and $k_a^\circ = 1.5 \times 10^{-3} \text{ cm sec}^{-1}$.⁶

They were able to conclude that the observed electron transfer kinetics of the Cu(I)-CO complex were not caused by a traditional CE (chemistry followed by electrochemistry) mechanism but instead proposed a model in which Cu(I)-CO bond is stretched or partially broken as the complex approaches the electrode surface. This was explained using Marcus theory as summarized by Rieger.⁷ The apparent standard rate constant is given by:

$$k_a^\circ = Z * \exp\left(\frac{-\Delta G^\ddagger}{RT}\right) \quad (6.2)$$

Z is a pre-exponential factor. ΔG^\ddagger is the activation free energy for the electron transfer when $E = E^\circ$. The activation free energy is related to energy changes in the electrochemical process through:

$$\Delta G_o^\ddagger = + \frac{\lambda}{4} + \frac{w_o + w_R}{2} + \frac{(w_o - w_R)^2}{4\lambda} \quad (6.3)$$

λ is the intrinsic reorganization energy for the electrochemical process at the electrode surface. w_o and w_R are the work required to bring the oxidized species, Cu(II), and the reduced species, Cu(I)-CO, to the electrode surface as well as the energy required to cause the changes in conformation or complexation prior to electron transfer. Finally, β can be calculated using:

$$\beta = \frac{1}{2} - \frac{\left[F(E - E^\circ) - (w_o + w_R) \right]}{2\lambda} \quad (6.4)$$

At potentials near E° a β value of less than 0.5 will only result when $w_R \gg w_o$. This indicates that the work required to bring the Cu(I)-CO complex to the electrode is much greater than the work required to bring the Cu(II) and CO to the electrode.⁶

Trulove et al investigated the Cu(I) / Cu(II) couple in the presence of ethylene.^{8,9} Ethylene like carbon monoxide forms a weak copper complex in acidic room temperature melts. Using normal pulse and square wave voltammetry, the anodic transfer coefficient, β , was determined to be 0.18.^{8,9} This suggested that the ethylene ligand behaves in the same fashion as the carbon monoxide ligand where the Cu(I) ligand bond is stretched or partially broken as the complex approaches the electrode.

The characterization of the Cu(I) / Cu(II) couple in the absence of any solutes would provide a baseline to compare against the existing results.

6.2 Specialized Experimental Procedures

6.2.1 Materials

Cu(I)Cl (99+ % Aldrich) was used without further purification. The melts used in this chapter were 1.5 : 1.0 mole ratio melts.

6.2.2 Equipment and Procedures for Electrochemical Experiments

Results were obtained using a home-built potentiostat, Mr. Coffee II.^{10,11} This potentiostat is limited to a square wave frequency of approximately 80 kHz.¹² Mr. Coffee II was coupled to a QuaTech digitizer and a waveform generator both housed within a single IBM 486 personal computer. Mr. Coffee II is only capable of controlling the potential over a 4 V range, -2, to +2 V. In order to study the copper(I)/copper(II) couple which has an $E_{1/2}$ of ≈ 1.9 V versus the Al(0)/Al(III) reference electrode, the reference electrode was offset using a 2V voltage source. The 2 V voltage source was hooked in series with the reference electrode and the potentiostat in order to allow scans from 1.6 to 2.3 V.

Electrochemical experiments were conducted in a cell constructed of a EG&G PAR 303A static mercury drop electrode glass cell, a Buna-N or Viton gasket, and a custom-built cell holder (Figure 6.1). Holes were drilled through the gasket to accommodate both working electrodes, the reference electrode, and a Pt coil counter electrode. Experiments were conducted with 2 tungsten

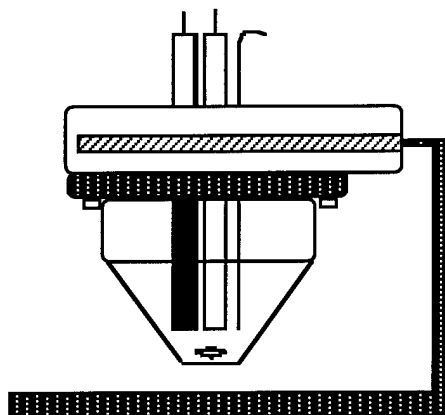


Figure 6.1 Sealed electrochemical cell used for Cu(I)/Cu(II) electron transfer parameter measurements.

working electrodes of 25 μm and 9 μm diameters. The use of microelectrodes minimizes effects due to IR drop and RC charging current contributions.¹³ Each working electrode was mechanically polished with diamond suspension. The cell in Figure 6.1 is sealed within a dry box and allows the electrochemical experiments to be conducted outside the dry box in the laboratory atmosphere. During the course of the electrochemical experiments, the cell and the potentiostat were enclosed in a grounded Faraday cage. The temperature inside the Faraday cage was monitored. The temperature fluctuated between 25 and 27 °C.

Prior to the acquisition of electrochemical data, each working electrode was electrochemically cleaned by cycling into the AlCl_4^- oxidation wave using cyclic staircase voltammetry. Three scans were performed with a scan rate of 500 mV / sec from 1 to 3 volts versus the Al(0) / Al (III) reference.¹⁴ After the electrochemical cleaning, a test square wave voltammogram was acquired in order to monitor the performance of the system as experiments were conducted. These voltammograms were acquired with a 10 mV step, 50 mV peak-to-peak square wave amplitude, and a square wave frequency of 1000 Hz. During the course of a series of voltammograms, several test square wave voltammograms were obtained with the same parameters as the first. These voltammograms were then compared to check for system degradation.

Two different pulse voltammetry techniques were utilized to characterize the Cu(I) / Cu(II) couple: normal pulse voltammetry and square wave voltammetry.¹⁵ The experimental parameters utilized are summarized in

Table 6.1. The square wave frequency was varied between 1 to 100 kHz while the normal pulse width was varied between 10 and 0.1 msec. Experiments were conducted using WOTAN, an in-house experimental-control and data-acquisition software package.

A 1.5 : 1.0 melt was prepared and a portion used to prepare a 20 mM solution of Cu(I) chloride. Background voltammograms were acquired using unadulterated melt, the same experimental parameters, and the same cell geometry.

Once the electrochemical data had been acquired, it was analyzed using FSQPLT, an in-house data-analysis program. FSQPLT utilizes the "COOL" algorithm (Chernoff, O'Dea, Osteryoung, and Lane) to determine electron transfer parameters.¹⁶ The COOL algorithm employs as a boundary condition the Erdey-Gruz and Volmer equation which can be written in the form:

$$i(t) = n F A \kappa \varepsilon^{-\alpha} \left[D_0^{\frac{1}{2}} C_0(0,t) - \varepsilon D_R^{\frac{1}{2}} C_R(0,t) \right] \quad (6.5)$$

where

$$\kappa = \frac{k_a^0}{D_0^{(1-\alpha)/2} D_R^{\alpha/2}} \quad (6.6)$$

and

$$\varepsilon = \exp \left(\frac{n F (E - E_{1/2}^r)}{R T} \right) \quad (6.7)$$

In these equations, α is the cathodic transfer coefficient, k_a^0 is the apparent standard rate constant (cm s^{-1}), D_0 and D_R are the diffusion coefficients ($\text{cm}^2 \text{s}^{-1}$)

Common Experimental Parameters	
Initial Potential 1.6 V	
Final Potential 2.3 V	
Step Height 10 mV	
Normal Pulse Parameters	Square Wave Parameters
Initial Potential Width 1 second	Square Wave Amplitude 50 mV
Number of Scans Averaged 20 - 100	Conditioning Time 1 second
	Number of Scans Averaged 100

Table 6.1. Common electrochemical experimental parameters used Cu(I)/Cu(II) electron transfer parameter measurements.

of the oxidized and reduced species, and $E_{1/2}^r$ (V) is the reversible half-wave potential. When $D_O = D_R$, the expression for κ simplifies to $k_a^*/D^{1/2}$.

Utilizing the Erdey-Gruz and Volmer equation, COOL treats the experimental current as a linear function of the calculated theoretical current function¹⁷

$$i(t) = a \psi(t, E, \alpha, \kappa) + c \quad (6.8)$$

where $i(t)$ is the observed current at the time of measurement, t , "a" is the slope, and ψ is the dimensionless current function. The quantity c is a constant which allows for bias in the location of the zero current. COOL uses an opportunistic search algorithm to vary initial estimates of $E_{1/2}$, β , and κ to obtain the minimum difference between the calculated voltammogram and the experimental voltammogram.

6.3 Results And Discussion

6.3.1 Normal Pulse Voltammetry Results

Normal pulse voltammetry was utilized in order to determine the electron transfer parameters for the Cu(I)/Cu(II) couple. A series of normal pulse voltammograms were obtained in which the pulse width was varied (5 μ sec to 50 μ sec). In general the normal pulse voltammograms were plagued by sloping backgrounds. Even with background subtraction, the voltammograms

seemed to have a residual curved background. Attempting to fit the normal pulse voltammograms to a quasi-reversible model resulted in poor fits with systematic deviations (Figures 6.2 and 6.3). The overall value for β was < 0.25 and for $\kappa \approx 150$ to 200. Although the fits have reasonable signal-to-noise ratios, the systematic deviations and the inability to remove the residual curved baseline, make normal pulse voltammetry unsuitable for kinetic analysis.

The curved background which makes the normal pulse voltammograms unsuitable for kinetic analysis does not limit their ability to be used for the determination of the diffusion coefficient for the Cu(I) species. Analysis of the observed data for the 25 μm diameter tungsten electrode yields a diffusion coefficient of $6.48 \times 10^{-7} \text{ cm}^2 \text{ sec}^{-1}$ (Figures 6.4 and 6.5). This is in very good agreement with a previously determined value of $7.51 \times 10^{-7} \text{ cm}^2 \text{ sec}^{-1}$.¹⁷

6.3.2 Square Wave Voltammetry Results

Square wave voltammetry can be used as a means of characterizing electrochemical couples with high electron transfer rates.¹⁸⁻²¹ In addition, square wave voltammetry is a differential technique and would hopefully not be susceptible to the same background subtraction problem that had plagued the normal pulse voltammetry results.

Square wave voltammograms were run, and the square wave frequency was varied from 10 kHz to 100 kHz. The net currents were background subtracted and the resulting data were analyzed using the COOL algorithm

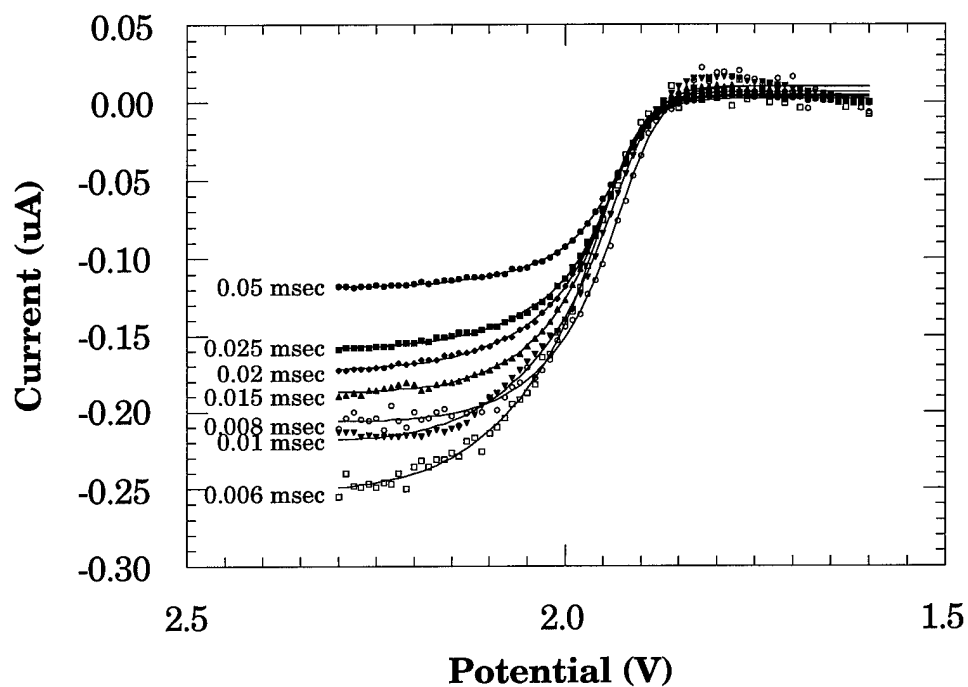


Figure 6.2 Normal pulse voltammograms of Cu(I)/Cu(II) in 1.5:1.0 melt using a 9 μm diameter tungsten electrode. Cu(I) concentration is 19.6 mM. t_p is shown next to each voltammogram. Points represent experimental data while the lines are the quasi-reversible fits from the COOL algorithm.

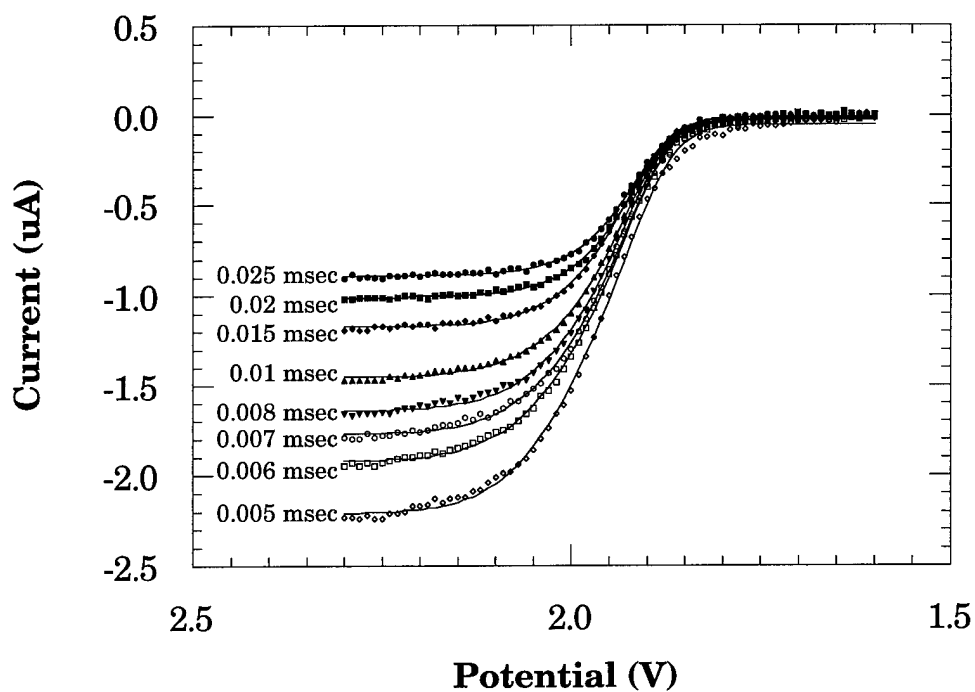


Figure 6.3 Normal pulse voltammograms of Cu(I)/Cu(II) in 1.5:1.0 melt using a 25 μm diameter tungsten electrode. Cu(I) concentration is 19.6 mM. t_p is shown next to each voltammogram. Points represent experimental data while the lines are the quasi-reversible fits from the COOL algorithm.

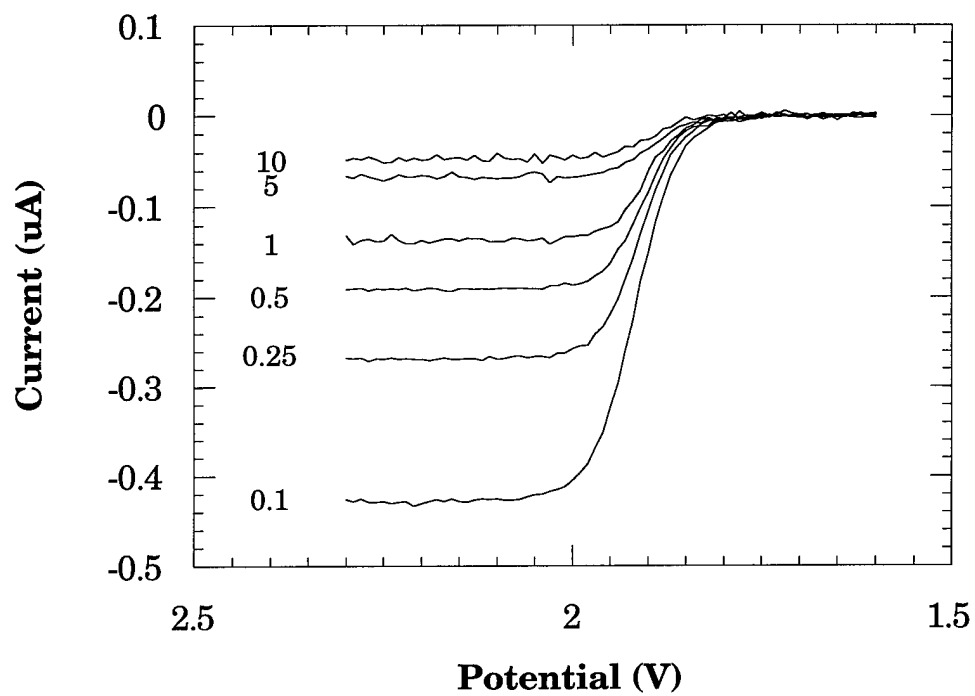


Figure 6.4 Normal pulse voltammograms of Cu(I)/Cu(II) in 1.5:1.0 melt using a 25 μm diameter tungsten electrode. Cu(I) concentration is 19.6 mM. t_p (msec) is shown next to each voltammogram.

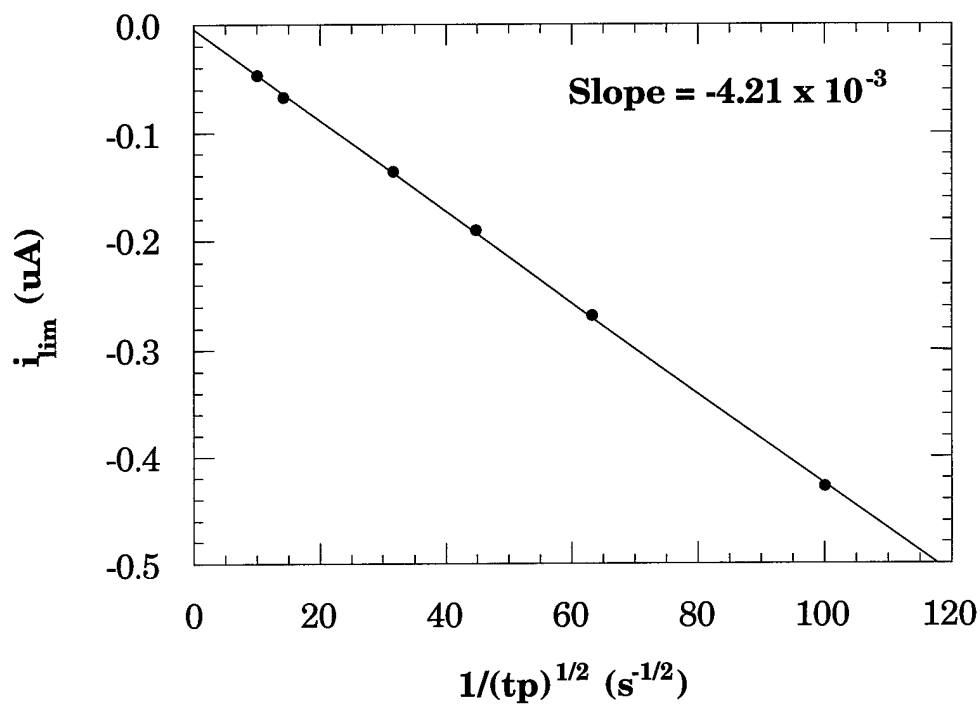


Figure 6.5 Limiting current of normal pulse voltammograms vs. $1 / \sqrt{tp}$ for Cu(I)/Cu(II) in 1.5:1.0 melt using a 25 μm diameter tungsten electrode. Cu(I) concentration is 19.6 mM. Points represent experimental data while the line is the least squared linear fit.

truncated from 1.7 to 2.2 V and truncated from 1.8 to 2.1 V. The results are plotted several ways in order to determine the quality of the data and to extract the diffusion coefficient and electron transfer parameters (Figures 6.6 to 6.23 and Tables 6.2 to 6.5).

By simple observation of Figures 6.8 to 6.11, the $E_{1/2}$ for the Cu(I)/Cu(II) couple vs. Al(0)/Al(III) is 1.94 V. The uncertainty in this measurement with both electrodes is less than 10 mV. This is the best that can be expected given the Al(0)/Al(III) reference electrode. The differences among the data, which were analyzed between 1.7 to 2.2 V and 1.8 to 2.1 V, is minimal and the additional truncation doesn't seem to have much effect on $E_{1/2}$. β is also well behaved and has good correlation between the two electrodes (Figures 6.12 to 6.15). Using the 9 μm electrode, β is 0.45 with an uncertainty of 0.05. Using the 25 μm electrode, β is 0.1. Given these results, β is 0.5 ± 0.1 . Although the uncertainty of 0.1 appears large initially, this uncertainty is actually very small when compared to other results in the literature. Once again, the differences between the data which were analyzed between 1.7 to 2.2 V and 1.8 to 2.1 V are minimal and the additional truncation doesn't seem to have much effect on β .

The diffusion coefficient and κ can also be calculated from the experimental data. The diffusion coefficient can be calculated from the slope obtained from the COOL algorithm. The slope (a) is usually referred to as a normalization factor; however, the slope is equal to:¹⁸

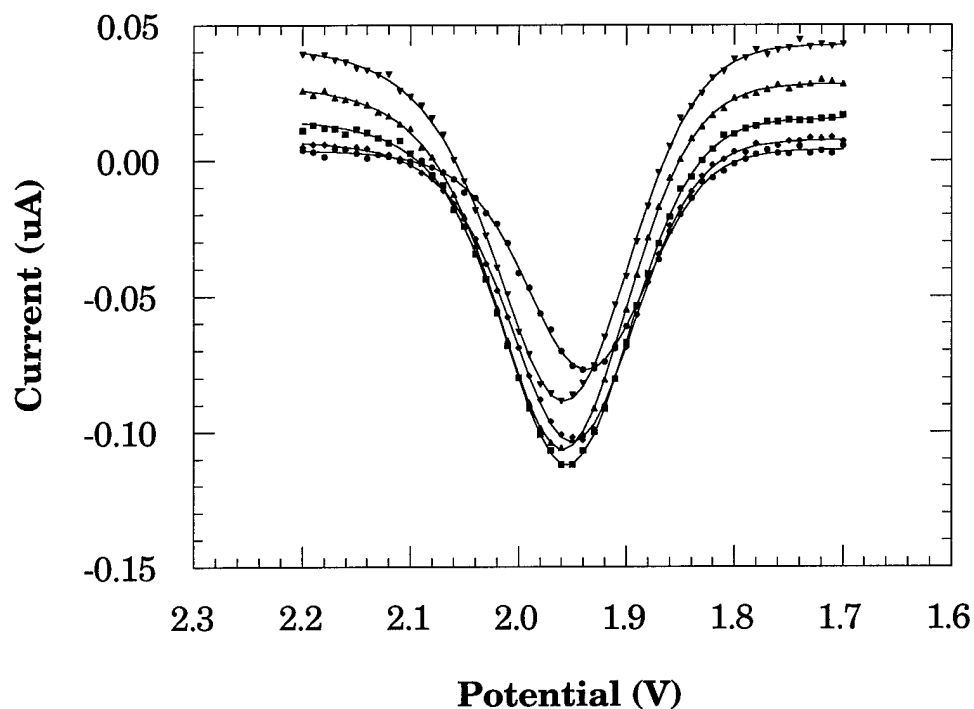


Figure 6.6 Square wave voltammograms of Cu(I)/Cu(II) in 1.5:1.0 melt using a 9 μm diameter tungsten electrode. Cu(I) concentration is 19.6 mM. Square wave frequencies are 10, 30, 50, 70, and 90 kHz. Points represent the experimental data while the lines are the quasi-reversible fits from the COOL algorithm. This data has a baseline offset which tends to increase at higher square wave frequencies. This makes it appear as if the net current is not increasing as the square wave frequency is increasing, although this is not the case.

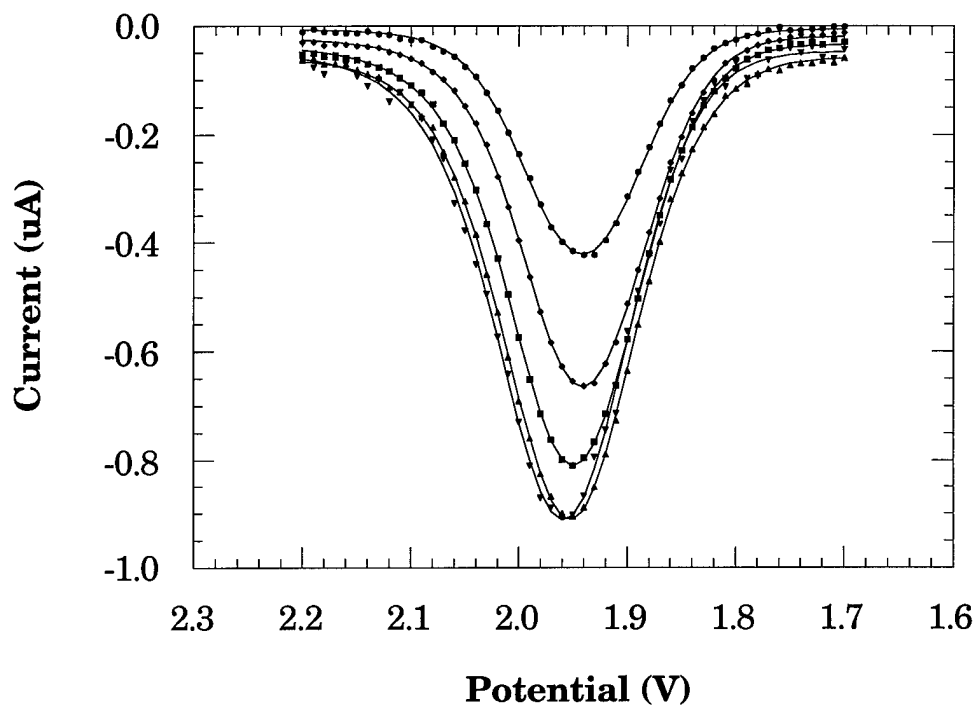


Figure 6.7 Square wave voltammograms of Cu(I)/Cu(II) in 1.5:1.0 melt using a 25 μm diameter tungsten electrode. Cu(I) concentration is 19.6 mM. Square wave frequencies are 10, 30, 50, 70, and 90 kHz. Points represent the experimental data while the lines are the quasi-reversible fits from the COOL algorithm.

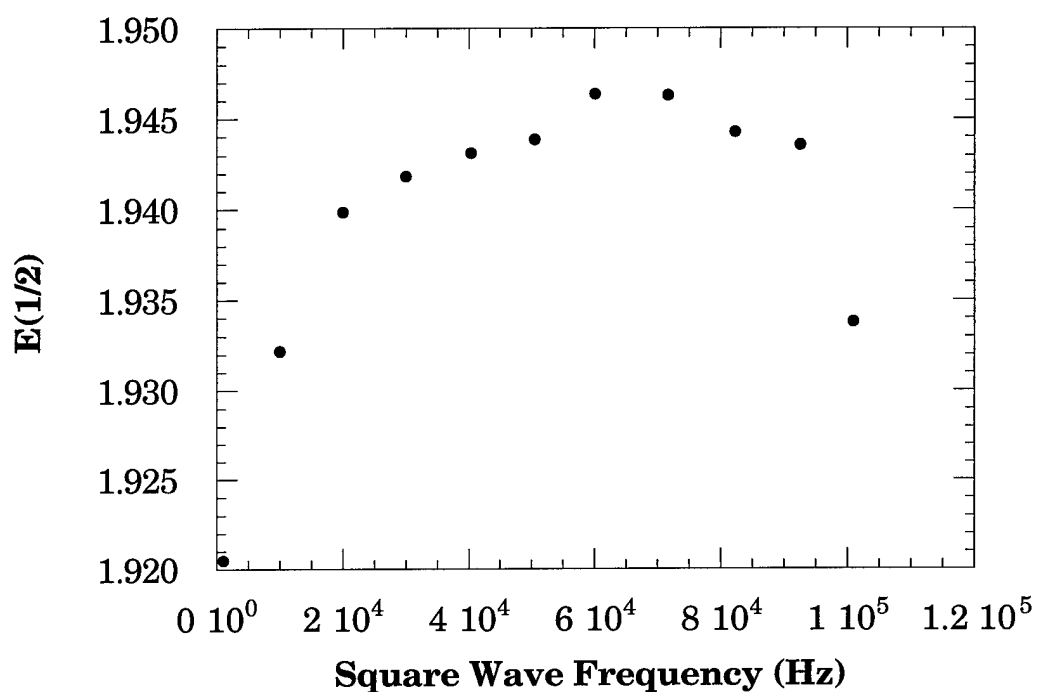


Figure 6.8 $E_{1/2}$ vs. square wave frequency from voltammograms of Cu(I)/Cu(II) in 1.5:1.0 melt using a 9 μm diameter tungsten electrode. Cu(I) concentration is 19.6 mM. Data obtained using quasi-reversible fits of the experimental data, between 1.7 to 2.2 V, from the COOL algorithm.

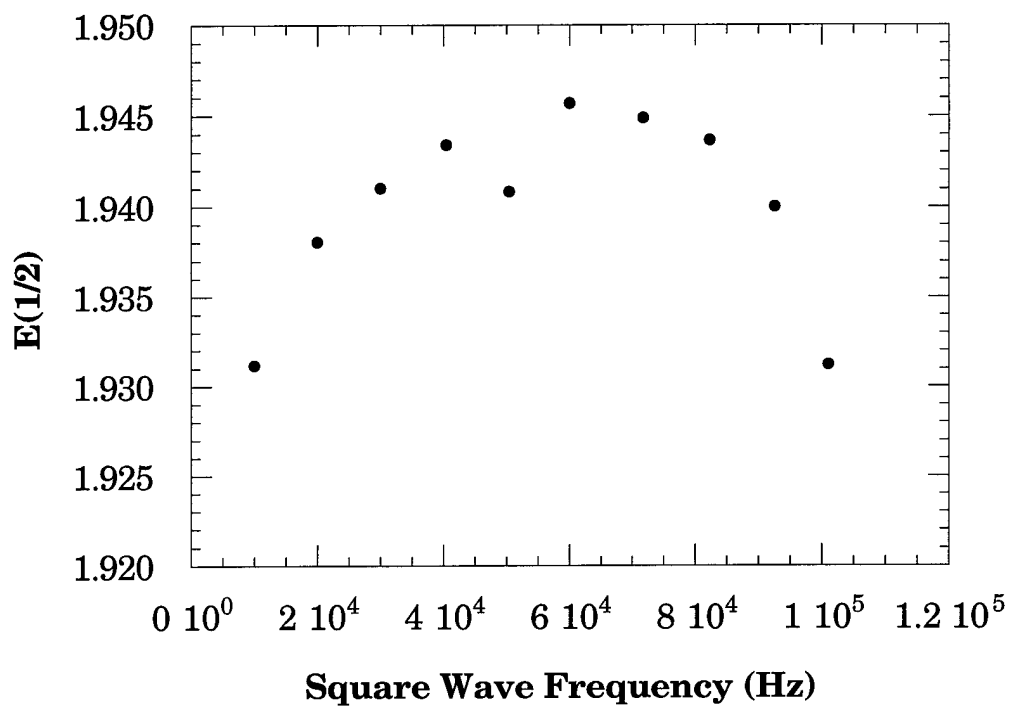


Figure 6.9 $E_{1/2}$ vs. square wave frequency from voltammograms of Cu(I)/Cu(II) in 1.5:1.0 melt using a 9 μm diameter tungsten electrode. Cu(I) concentration is 19.6 mM. Data obtained using quasi-reversible fits of the experimental data, between 1.8 to 2.1 V, from the COOL algorithm.

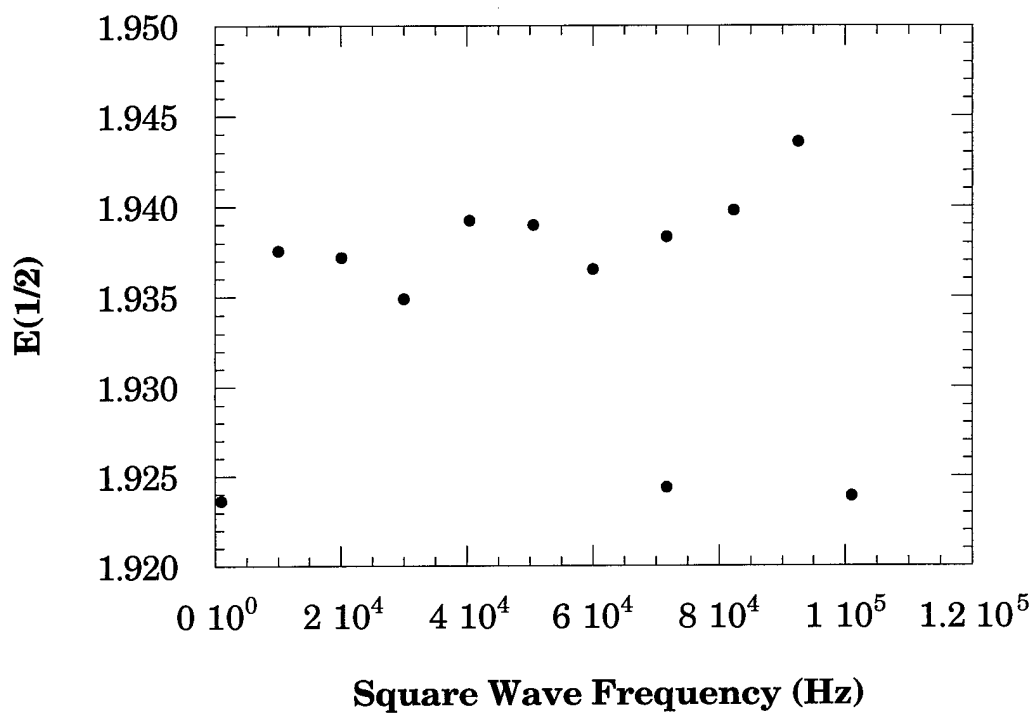


Figure 6.10 $E_{1/2}$ vs. square wave frequency from voltammograms of Cu(I)/Cu(II) in 1.5:1.0 melt using a 25 μm diameter tungsten electrode. Cu(I) concentration is 19.6 mM. Data obtained using quasi-reversible fits of the experimental data, between 1.7 to 2.2 V, from the COOL algorithm.

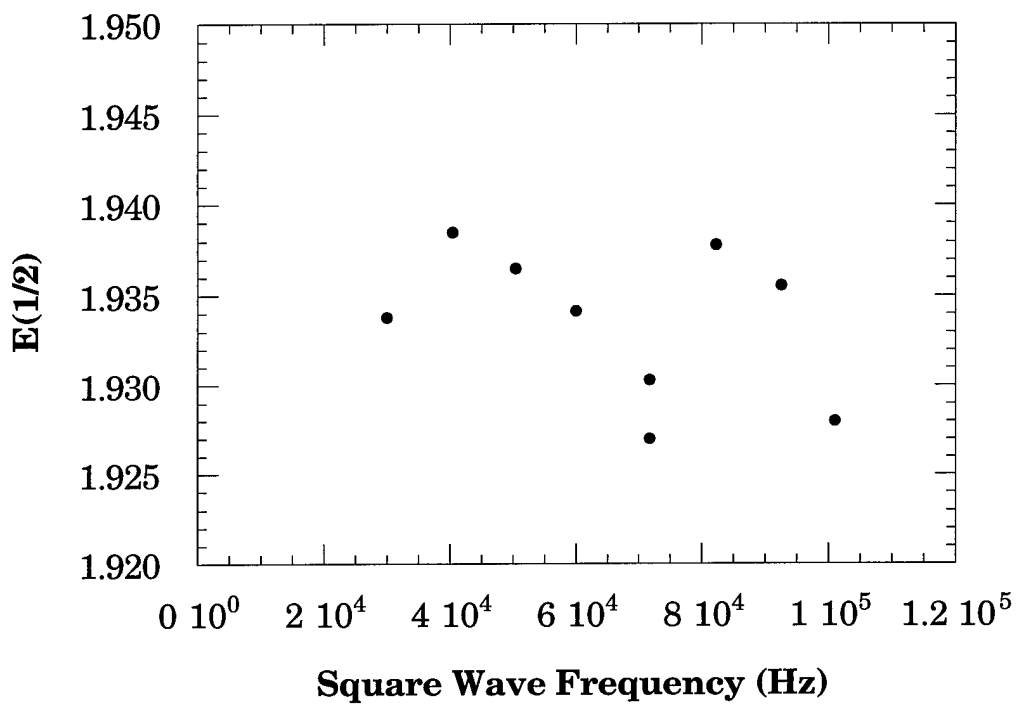


Figure 6.11 $E_{1/2}$ vs. square wave frequency from voltammograms of Cu(I)/Cu(II) in 1.5:1.0 melt using a 25 μm diameter tungsten electrode. Cu(I) concentration is 19.6 mM. Data obtained using quasi-reversible fits of the experimental data, between 1.8 to 2.1 V, from the COOL algorithm.

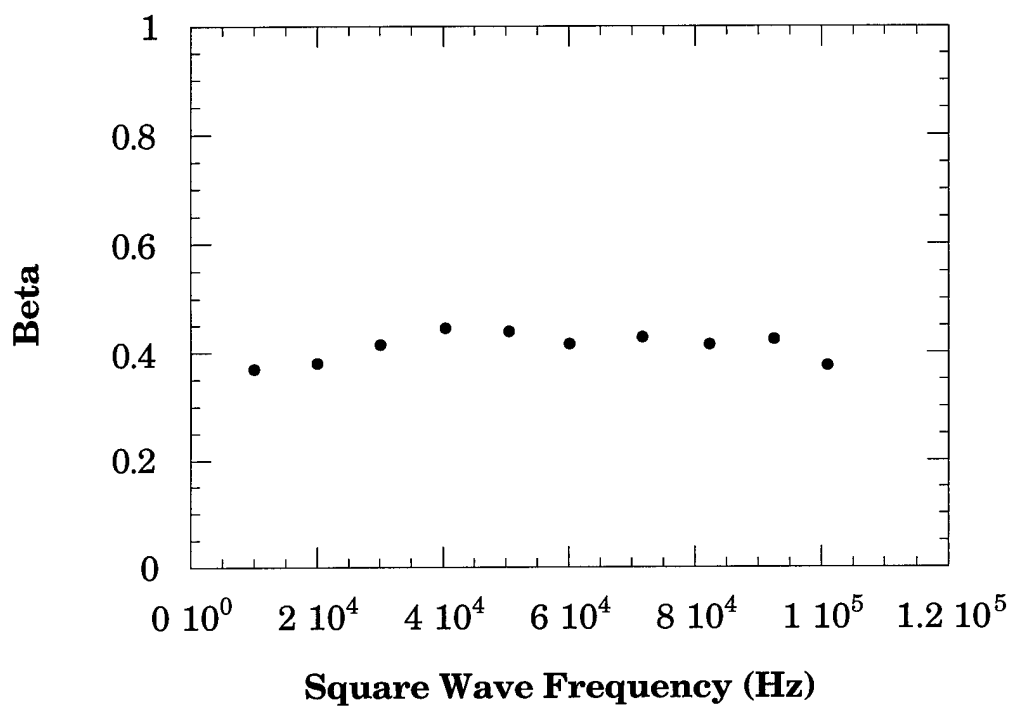


Figure 6.12 β vs. square wave frequency from voltammograms of Cu(I)/Cu(II) in 1.5:1.0 melt using a 9 μm diameter tungsten electrode. Cu(I) concentration is 19.6 mM. Data obtained using quasi-reversible fits of the experimental data, between 1.7 to 2.2 V, from the COOL algorithm.

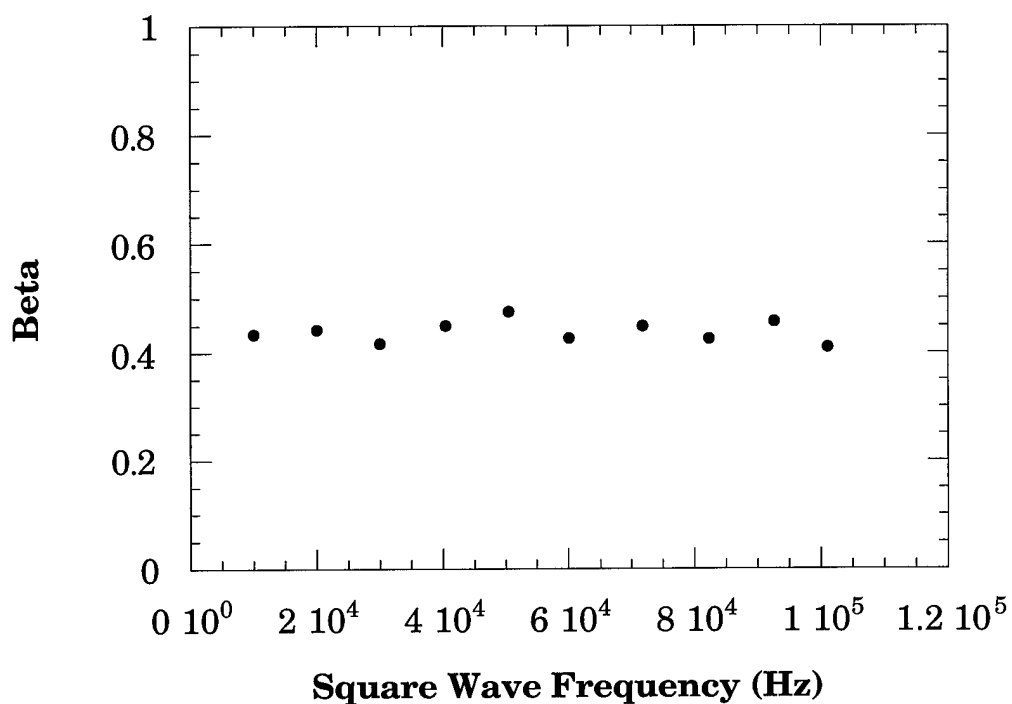


Figure 6.13 β vs. square wave frequency from voltammograms of Cu(I)/Cu(II) in 1.5:1.0 melt using a 9 μm diameter tungsten electrode. Cu(I) concentration is 19.6 mM. Data obtained using quasi-reversible fits of the experimental data, between 1.8 to 2.1 V, from the COOL algorithm.

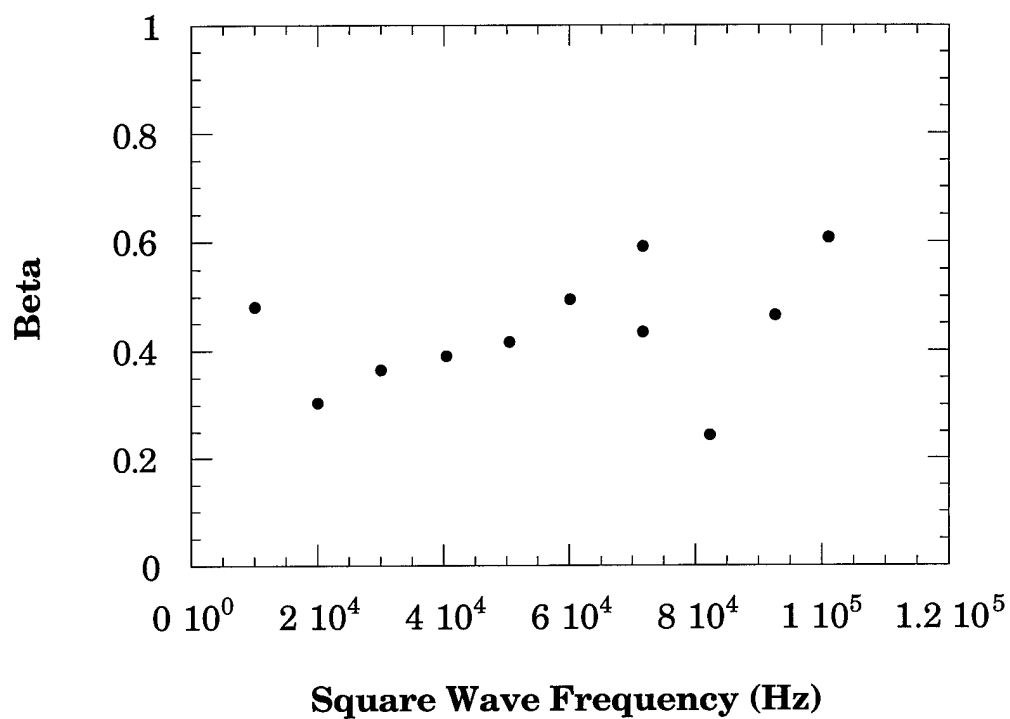


Figure 6.14 β vs. square wave frequency from voltammograms of Cu(I)/Cu(II) in 1.5:1.0 melt using a 25 μm diameter tungsten electrode. Cu(I) concentration is 19.6 mM. Data obtained using quasi-reversible fits of the experimental data, between 1.7 to 2.2 V, from the COOL algorithm.

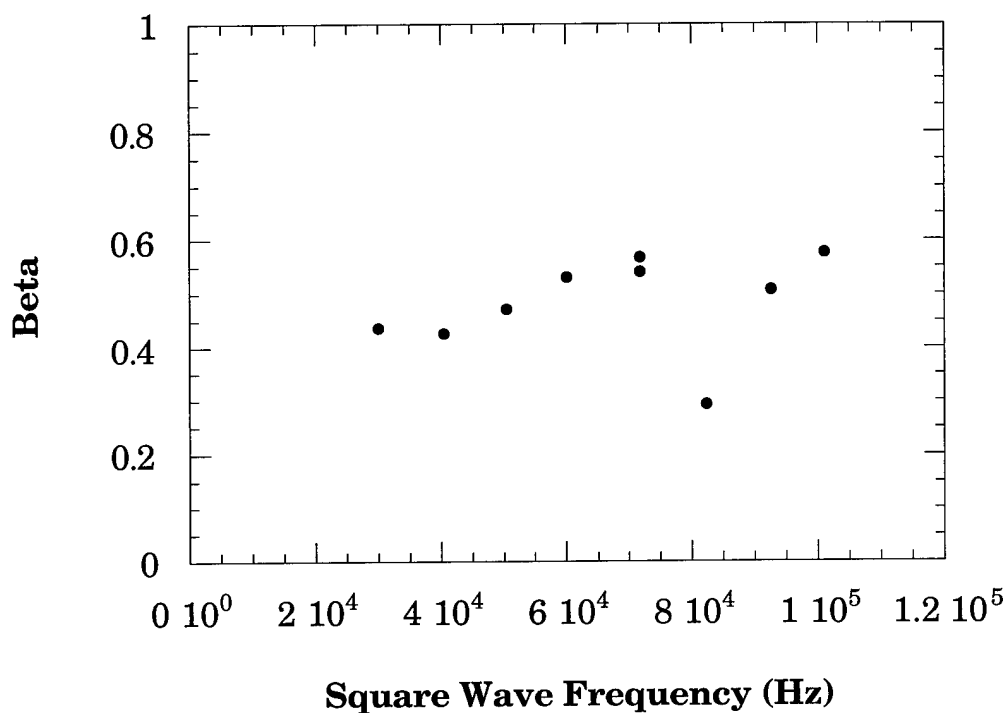


Figure 6.15 β vs. square wave frequency from voltammograms of Cu(I)/Cu(II) in 1.5:1.0 melt using a 25 μm diameter tungsten electrode. Cu(I) concentration is 19.6 mM. Data obtained using quasi-reversible fits of the experimental data, between 1.8 to 2.1 V, from the COOL algorithm.

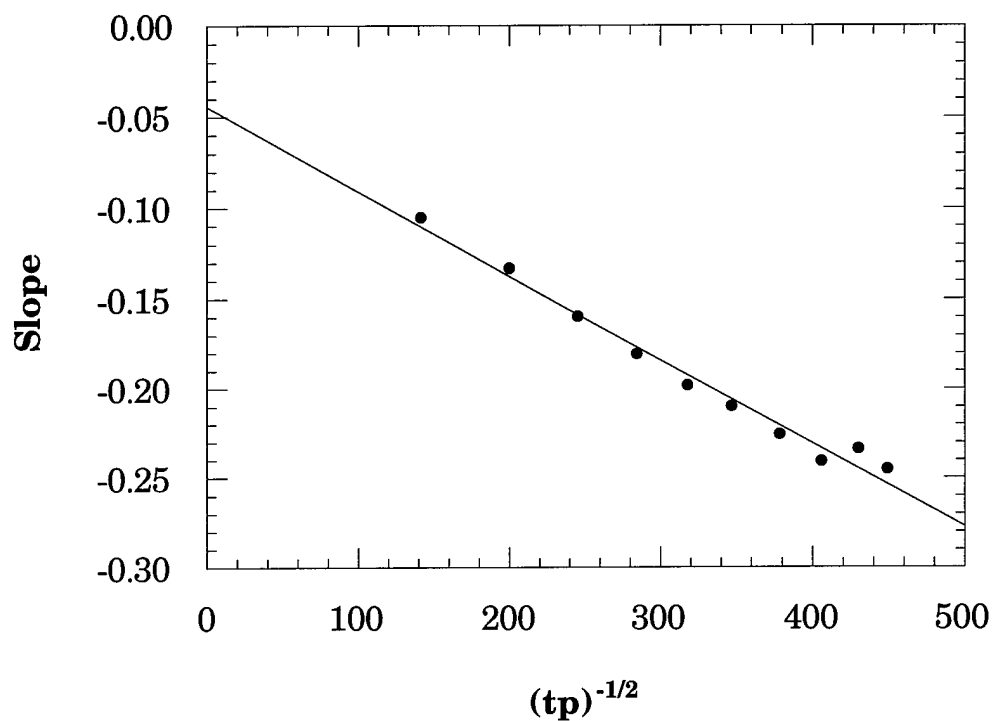


Figure 6.16 Slope vs. $1/\sqrt{tp}$ from voltammograms of Cu(I)/Cu(II) in 1.5:1.0 melt using a 9 μm diameter tungsten electrode. Cu(I) concentration is 19.6 mM. Data obtained using quasi-reversible fits of the experimental data, between 1.7 to 2.2 V, from the COOL algorithm. The points represent the experimental data while the line is the least squared fit of the experimental data.

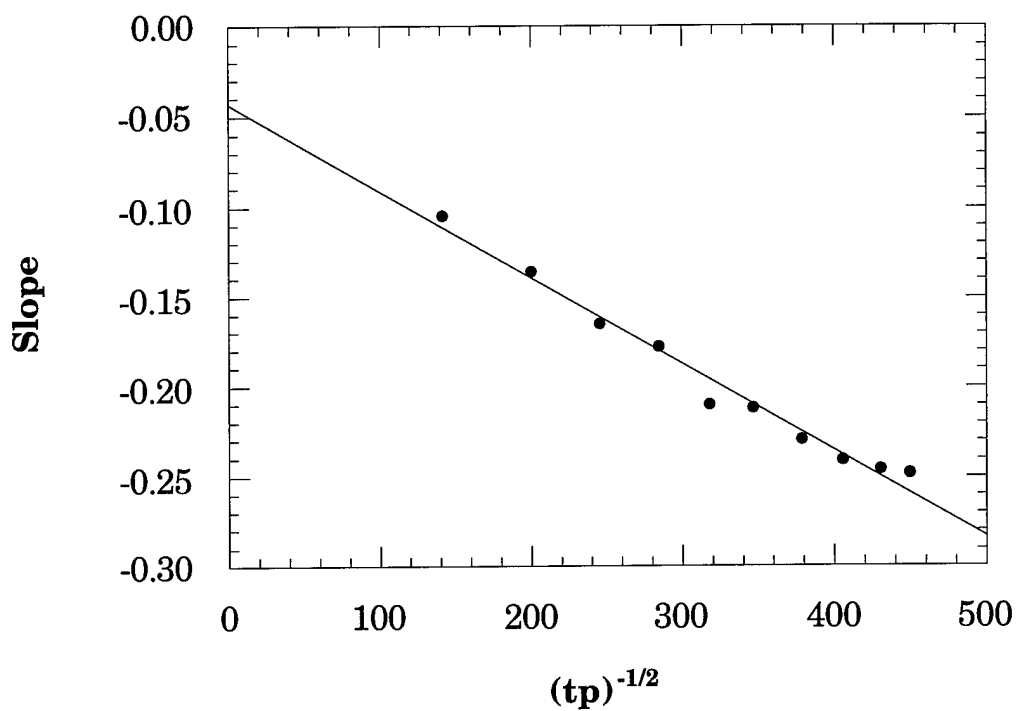


Figure 6.17 Slope vs. $1/\sqrt{tp}$ from voltammograms of Cu(I)/Cu(II) in 1.5:1.0 melt using a 9 μm diameter tungsten electrode. Cu(I) concentration is 19.6 mM. Data obtained using quasi-reversible fits of the experimental data, between 1.8 to 2.1 V, from the COOL algorithm. The points represent the data while the line is the least squared fit of the experimental data.

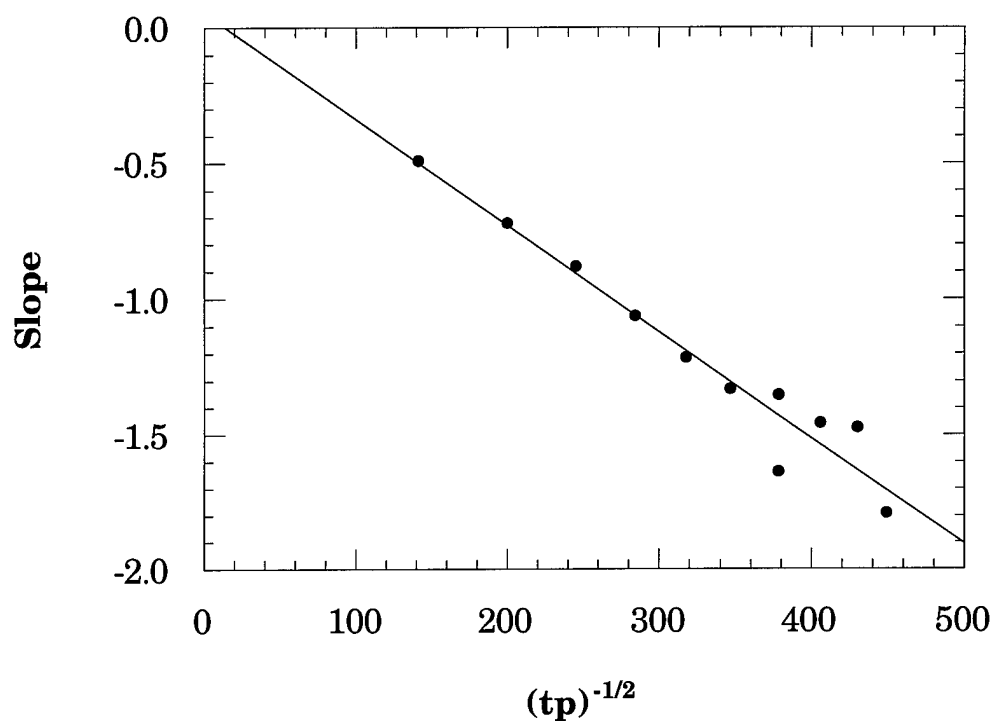


Figure 6.18 Slope vs. $1/\sqrt{tp}$ from voltammograms of Cu(I)/Cu(II) in 1.5:1.0 melt using a 25 μm diameter tungsten electrode. Cu(I) concentration is 19.6 mM. Data obtained using quasi-reversible fits of the experimental data, between 1.7 to 2.2 V, from the COOL algorithm. The points represent the experimental data while the line is the least squared fit of the experimental data.

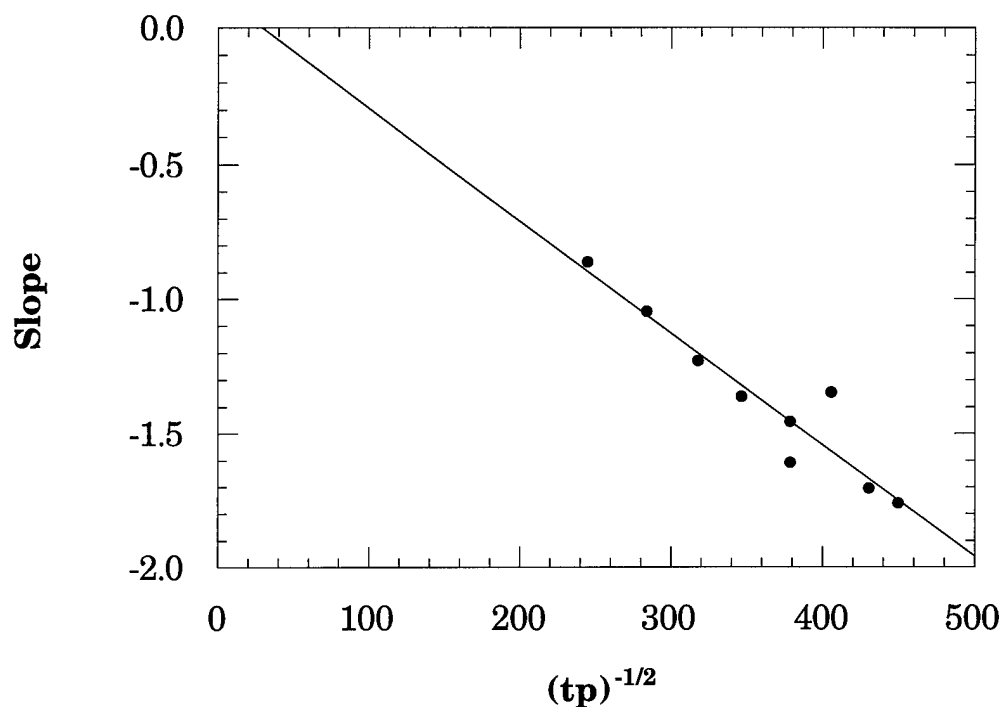


Figure 6.19 Slope vs. $1/\sqrt{tp}$ from voltammograms of Cu(I)/Cu(II) in 1.5:1.0 melt using a 25 μm diameter tungsten electrode. Cu(I) concentration is 19.6 mM. Data obtained using quasi-reversible fits of the experimental data, between 1.8 to 2.1 V, from the COOL algorithm. The points represent the experimental data while the line is the least squared fit of the experimental data.

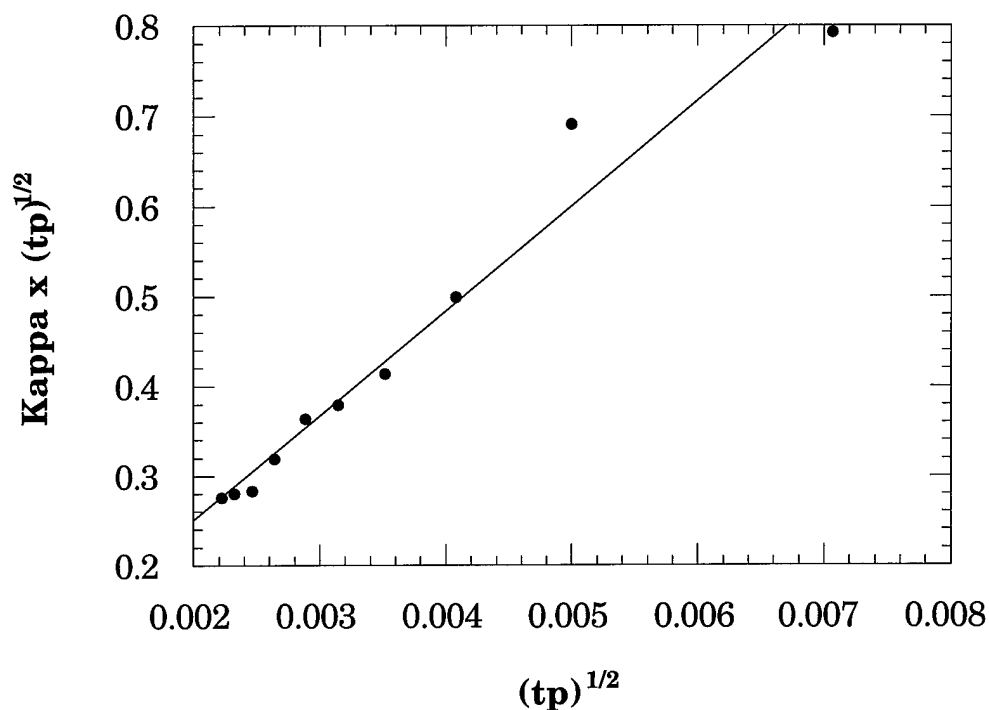


Figure 6.20 $\kappa \times \sqrt{tp}$ vs. \sqrt{tp} from voltammograms of Cu(I)/Cu(II) in 1.5:1.0 melt using a 9 μm diameter tungsten electrode. Cu(I) concentration is 19.6 mM. Data obtained using quasi-reversible fits of the experimental data, between 1.7 to 2.2 V, from the COOL algorithm. The points represent the experimental data while the line is the least squared fit of the experimental data.

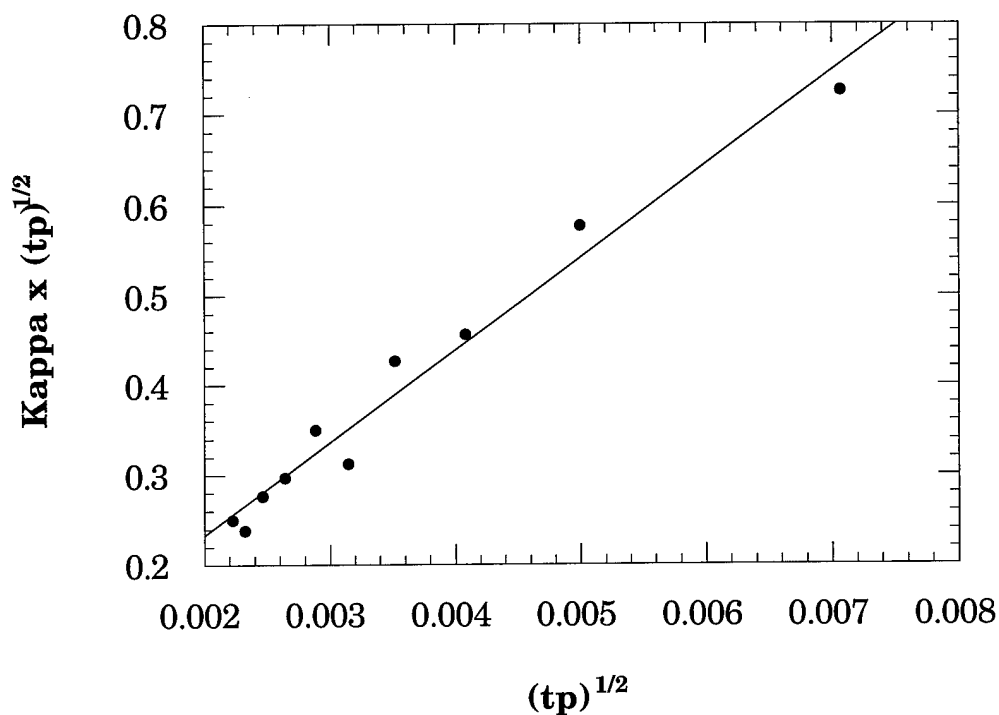


Figure 6.21 $\kappa \times \text{sqrt}(tp)$ vs. $\text{sqrt}(tp)$ from voltammograms of Cu(I)/Cu(II) in 1.5:1.0 melt using a 9 μm diameter tungsten electrode. Cu(I) concentration is 19.6 mM. Data obtained using quasi-reversible fits of the experimental data, between 1.8 to 2.1 V, from the COOL algorithm. The points represent the experimental data while the line is the least squared fit of the experimental data.

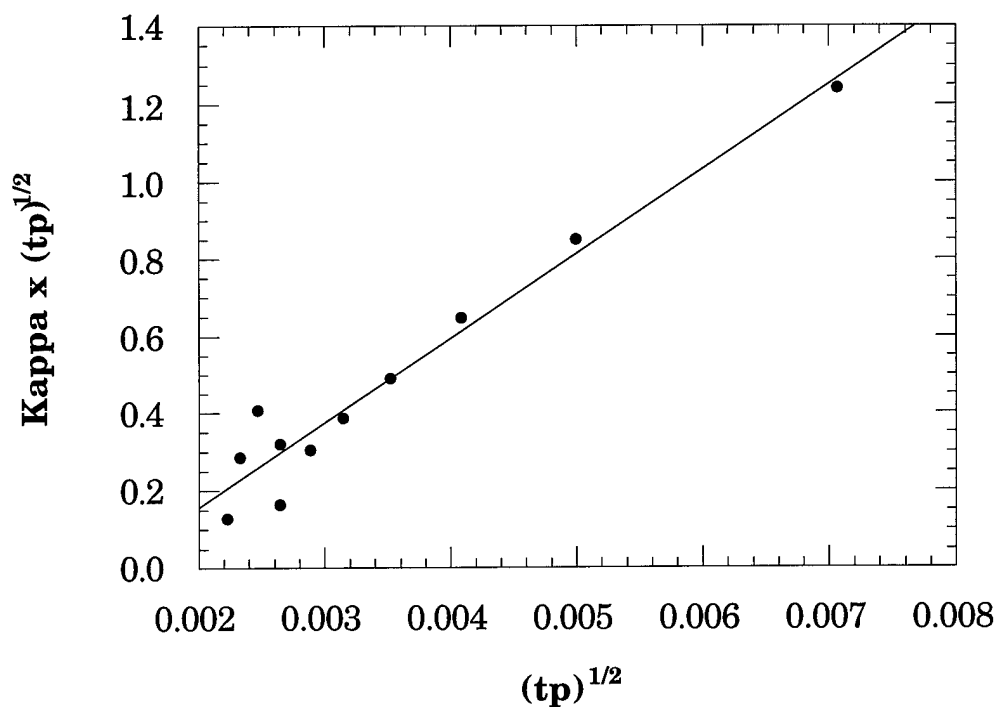


Figure 6.22 $\kappa \times \sqrt{tp}$ vs. \sqrt{tp} from voltammograms of Cu(I)/Cu(II) in 1.5:1.0 melt using a 25 μm diameter tungsten electrode. Cu(I) concentration is 19.6 mM. Data obtained using quasi-reversible fits of the experimental data, between 1.7 to 2.2 V, from the COOL algorithm. The points represent the experimental data while the line is the least squared fit of the experimental data.

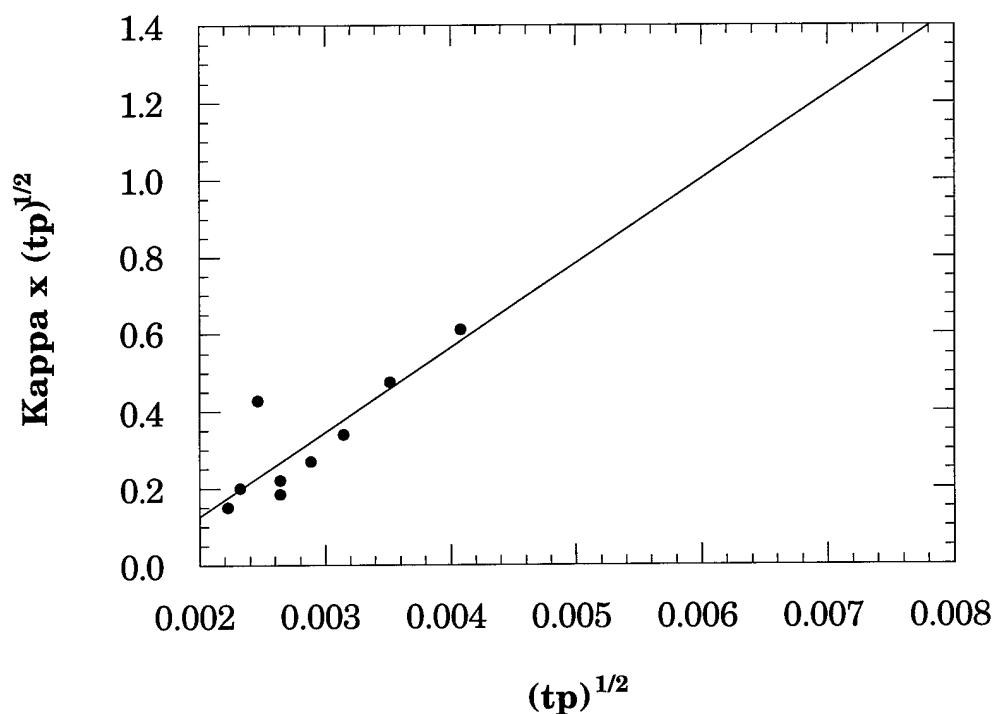


Figure 6.23 $\kappa \times \sqrt{tp}$ vs. \sqrt{tp} from voltammograms of Cu(I)/Cu(II) in 1.5:1.0 melt using a 25 μm diameter tungsten electrode. Cu(I) concentration is 19.6 mM. Data obtained using quasi-reversible fits of the experimental data, between 1.8 to 2.1 V, from the COOL algorithm. The points represent the experimental data while the line is the least squared fit of the experimental data.

9 μm Electrode 1.7 to 2.2 V				
Square Wave Frequency	E1/2	Beta	Slope	Kappa * $t_p^{1/2}$
10010	1.932(1)	0.37(6)	-0.105	0.793
20020	1.940(1)	0.38(5)	-0.133	0.691
30030	1.942(1)	0.42(3)	-0.159	0.499
40404	1.943(1)	0.45(2)	-0.181	0.414
50505	1.944(1)	0.44(2)	-0.198	0.379
60060	1.946(1)	0.42(1)	-0.210	0.364
71685	1.946(1)	0.43(1)	-0.226	0.319
82305	1.944(1)	0.41(2)	-0.241	0.283
92563	1.944(1)	0.42(2)	-0.234	0.280
101010	1.934(1)	0.38(1)	-0.245	0.275

Table 6.2 Electron transfer parameters for Cu(I)/Cu(II) determined using square wave voltammetric data obtained in 1.5:1.0 melt using a 9 μm diameter tungsten electrode. Cu(I) concentration is 19.6 mM. Data obtained using quasi-reversible fits of the experimental data, between 1.7 to 2.2 V, from the COOL algorithm.

9 μm Electrode 1.8 to 2.1 V				
Square Wave Frequency	E1/2	Beta	Slope	Kappa * $t_p^{1/2}$
10010	1.931(1)	0.43(8)	-0.105	0.725
20020	1.938(1)	0.44(6)	-0.136	0.577
30030	1.941(1)	0.42(3)	-0.165	0.457
40404	1.943(1)	0.45(3)	-0.178	0.427
50505	1.941(1)	0.48(2)	-0.210	0.313
60060	1.946(1)	0.43(2)	-0.212	0.350
71685	1.945(1)	0.45(2)	-0.230	0.297
82305	1.944(1)	0.43(2)	-0.241	0.276
92563	1.940(1)	0.46(2)	-0.246	0.239
101010	1.931(1)	0.41(2)	-0.248	0.251

Table 6.3 Electron transfer parameters for Cu(I)/Cu(II) determined using square wave voltammetric data obtained in 1.5:1.0 melt using a 9 μm diameter tungsten electrode. Cu(I) concentration is 19.6 mM. Data obtained using quasi-reversible fits of the experimental data, between 1.8 to 2.1 V, from the COOL algorithm.

25 μm Electrode 1.7 to 2.2 V				
Square Wave Frequency	E1/2	Beta	Slope	Kappa * $t_p^{1/2}$
10010	1.938(1)	0.48(8)	-0.491	1.241
20020	1.937(1)	0.40(3)	-0.721	0.850
30030	1.935(1)	0.36(2)	-0.881	0.648
40404	1.934(1)	0.39(2)	-1.061	0.490
50505	1.939(1)	0.42(2)	-1.216	0.387
60060	1.937(1)	0.50(2)	-1.329	0.305
71685	1.924(1)	0.59(1)	-1.637	0.165
71685	1.938(1)	0.43(4)	-1.353	0.320
82305	1.940(1)	0.24(2)	-1.456	0.408
92563	1.944(1)	0.47(4)	-1.474	0.286
101010	1.924(1)	0.61(2)	-1.792	0.128

Table 6.4 Electron transfer parameters for Cu(I)/Cu(II) determined using square wave voltammetric data obtained in 1.5:1.0 melt using a 25 μm diameter tungsten electrode. Cu(I) concentration is 19.6 mM. Data obtained using quasi-reversible fits of the experimental data, between 1.7 to 2.2 V, from the COOL algorithm.

25 μm Electrode 1.8 to 2.1 V				
Square Wave Frequency	E1/2	Beta	Slope	Kappa * $t_p^{1/2}$
30030	1.934(1)	0.44(3)	-0.862	0.611
40404	1.939(1)	0.43(3)	-1.047	0.475
50505	1.937(1)	0.47(2)	-1.230	0.339
60060	1.934(1)	0.53(3)	-1.361	0.270
71685	1.927(1)	0.57(2)	-1.609	0.183
71685	1.930(1)	0.54(6)	-1.455	0.220
82305	1.938(1)	0.29(3)	-1.347	0.428
92563	1.936(1)	0.51(5)	-1.705	0.199
101010	1.928(1)	0.58(4)	-1.761	0.149

Table 6.5 Electron transfer parameters for Cu(I)/Cu(II) determined using square wave voltammetric data obtained in 1.5:1.0 melt using a 25 μm diameter tungsten electrode. Cu(I) concentration is 19.6 mM. Data obtained using quasi-reversible fits of the experimental data, between 1.8 to 2.1 V, from the COOL algorithm.

$$a = \frac{n F A D_o^{1/2} C_o^*}{(\pi t p)^{1/2}} \quad (6.9)$$

If a is plotted against $1/(tp)^{1/2}$, then the slope of the resulting line is equal to:

$$\text{slope} = - \frac{n F A D_o^{1/2} C_o^*}{(\pi)^{1/2}} \quad (6.10)$$

If the slope of the fitted line is taken from Figures 6.16 to 6.19, the diffusion coefficient can be calculated (Table 6.6). The more truncated electrochemical data gives slightly higher diffusion coefficients for both electrodes. Even so, the differences are extremely small and well within experimental error. The average of the calculated diffusion coefficients is $5.41 \times 10^{-7} \text{ cm}^2/\text{sec}$. This is in very good agreement with the previously determined value of $7.51 \times 10^{-7} \text{ cm}^2/\text{sec}$.

Kappa can also be calculated from the experimental data. For quasi-reversible electron transfer, the dimensionless parameter is $\kappa t p^{1/2}$.¹⁵ The slope of a plot of $\kappa t p^{1/2}$ vs. $t p^{1/2}$ is κ (Figures 6.20 to 6.23). If the assumption is made that Cu(I) and Cu(II) have the same diffusion coefficient, k_a° can be calculated by multiplying κ by the square root of the diffusion coefficient (Table 6.7). The average of the k_a° values is 0.1423 cm/sec . One difficulty observed with the data from the $25 \mu\text{m}$ electrode is that the k determined from the slope of the plots is ≈ 2 times higher than the mean calculated for each data point (Table 6.8). This may imply that κ is a function of $t p^{1/2}$ for the $25 \mu\text{m}$ electrode. On the

Diffusion Coefficient of Cu(I) in 1.5:1.0 Melt				
	9 μm Electrode		25 μm Electrode	
Initial and Final Potential	Slope	Diffusion Coefficient (cm^2/sec)	Slope	Diffusion Coefficient (cm^2/sec)
1.7 to 2.2 V	-4.65×10^{-4}	4.70×10^{-7}	-3.92×10^{-3}	5.59×10^{-7}
1.8 to 2.1 V	-4.81×10^{-4}	5.03×10^{-7}	-4.16×10^{-3}	6.31×10^{-7}

Table 6.6 Diffusion coefficient of Cu(I) determined using square wave voltammetric data obtained in 1.5:1.0 melt using a 9 and 25 μm diameter tungsten electrodes. Cu(I) concentration is 19.6 mM. Data obtained using quasi-reversible fits of the experimental data, between 1.8 to 2.1 and 1.7 to 2.2 V, from the COOL algorithm.

k_a° of Cu(I) in 1.5:1.0 Melt				
	9 μm Electrode		25 μm Electrode	
Initial and Final Potential	κ	k_a° (cm/sec)	κ	k_a° (cm/sec)
1.7 to 2.2 V	116.6	0.1010	218.6	0.1894
1.8 to 2.1 V	102.9	0.0892	219.1	0.1897

Table 6.7 κ and k_a° of Cu(I)/Cu(II) determined using square wave voltammetric data obtained in 1.5:1.0 melt using a 9 and 25 μm diameter tungsten electrodes. Cu(I) concentration is 19.6 mM. Data obtained using the slopes of Figures 6.20 to 6.23 determined from quasi-reversible fits of the experimental data, between 1.8 to 2.1 and 1.7 to 2.2 V, from the COOL algorithm.

k_a° of Cu(I) in 1.5:1.0 Melt				
	9 μm Electrode		25 μm Electrode	
Initial and Final Potential	κ	k_a° (cm/sec)	κ	k_a° (cm/sec)
1.7 to 2.2 V	121.5	0.1053	121.3	0.1051
1.8 to 2.1 V	111.2	0.0964	107.2	0.0929

Table 6.8 κ and k_a° of Cu(I)/Cu(II) determined using square wave voltammetric data obtained in 1.5:1.0 melt using a 9 and 25 μm diameter tungsten electrodes. Cu(I) concentration is 19.6 mM. Data obtained using the mean of the data points in Tables 6.2 to 6.5 determined from quasi-reversible fits of the experimental data, between 1.8 to 2.1 and 1.7 to 2.2 V, from the COOL algorithm.

other hand, the 9 μm electrode does not exhibit the same behavior. The more truncated electrochemical data tends to give a slightly higher κ but the differences are within the error of the measurements. Using these values, the average of k_a° is 0.0999 cm/sec.

One final check that was applied to the experimental data was a direct comparison of the peak net current for both the 9 μm and 25 μm electrodes. The area of the 25 μm electrode was divided by that of the 9 μm electrode. By multiplying the peak net current of the 9 μm electrode by 6.25, it should equal that of the 25 μm electrode. Figure 6.24 shows that the 10 μm and 25 μm peak net currents behave in the same way with respect to the square root of the frequency (Table 6.9).

6.4 Conclusions

Using square wave voltammetry and normal pulse voltammetry, the diffusion coefficient and electron transfer parameters for the Cu(I)/Cu(II) couple can be determined. The diffusion coefficient for Cu(I) in a 1.5:1.0 melt is $6.8 \pm 1.0 \times 10^{-7} \text{ cm}^2/\text{sec}$ while $E_{1/2}$ is $1.94 \pm 0.01 \text{ V}$, β is 0.5 ± 0.1 , and k_a° is $0.10 \pm 0.06 \text{ cm/sec}$. These measurements were taken using two different size tungsten electrodes with 9 μm and 25 μm diameters. The close agreement of the results from both electrodes implies these measurements are not biased by

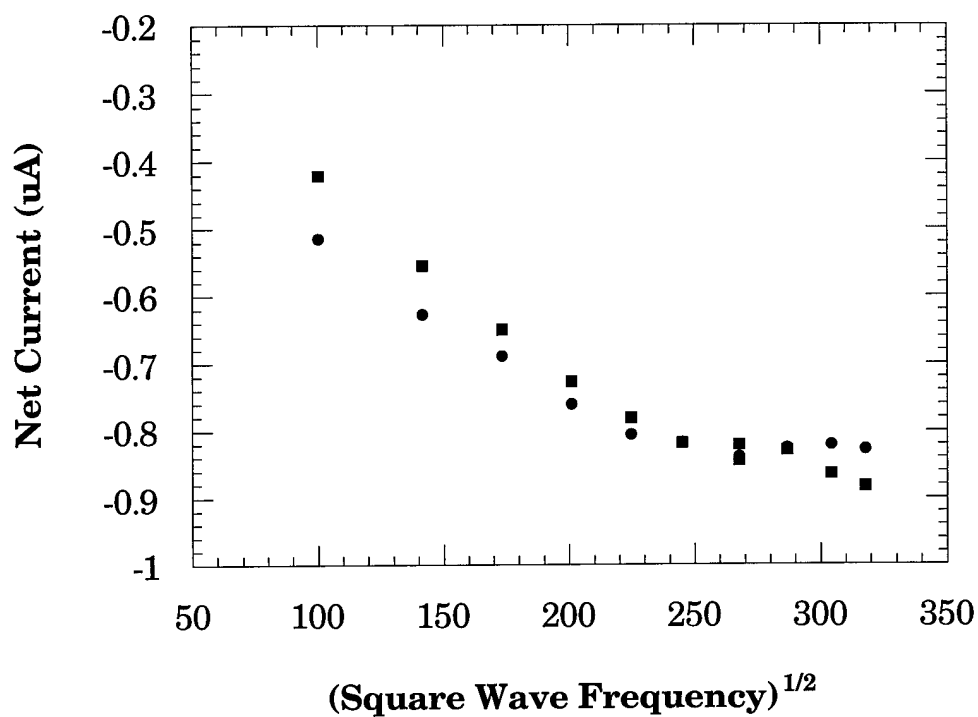


Figure 6.24 Comparison of the net square wave currents from the 9 μm and 25 μm diameter tungsten electrodes for 19.6 mM Cu(I) in a 1.5:1.0 melt. The net current from the 9 μm diameter electrode has been multiplied by 6.25 to correct for the difference in area between the two electrodes. The circles are the 9 μm net currents multiplied by 6.25 and the squares are the 25 μm net currents.

Square Wave Net Current		
Square Wave Frequency	Net Current 25 μm Electrode	Net Current 9 μm Electrode x 6.25
10010	-0.4214	-0.5143
20020	-0.5543	-0.6273
30030	-0.6497	-0.6887
40404	-0.7271	-0.7599
50505	-0.7806	-0.8052
60060	-0.8178	-0.8168
71685	-0.8450	-0.8383
82305	-0.8285	-0.8258
92593	-0.8638	-0.8206
101010	-0.8830	-0.8280

Table 6.9 The net square wave currents from the 9 μm and 25 μm diameter tungsten electrodes for 19.6 mM Cu(I) in a 1.5:1.0 melt. The net current from the 9 μm diameter electrode has been multiplied by 6.25 to correct for the difference in area between the two electrodes.

artifacts which would be caused by IR drop or RC time constant interferences. This study represents the most complete and thorough determination of these electron transfer parameters.

Chapter 6 References

- (1) Boxall, L. G.; Jones, H. L.; Osteryoung, R. A. "Electrochemical Studies on Ag, Fe, and Cu Species in AlCl_3 -NaCl Melts." *J. Electrochem. Soc.* **1974**, *121*, 212-219.
- (2) Hussey, C. L.; King, L. A.; Carpio, R. A. "The Electrochemistry of Copper in a Room Temperature Acidic Chloroaluminate Melt." *J. Electrochem. Soc.* **1979**, *126*, 1029-1034.
- (3) Nanjuniah, C.; Osteryoung, R. A. "Electrochemical Studies of Cu(I) and Cu(II) in an Aluminum Chloride-N-(n-Butyl)Pyridinium Chloride Ionic Liquid." *J. Electrochem. Soc.* **1983**, *130*, 1312-1318.
- (4) Carlin, R. T.; Sullivan, T. "Electrochemical Quantification of Carbon Monoxide Complexation to Copper(I) in a Chloroaluminate Molten Salt." *J. Electrochem. Soc.* **1992**, *139*, 144-147.
- (5) Walker, D. G. "Making and Using CO." *CHEMTECH* 1975, 308-311.
- (6) Carlin, R. T.; Sullivan, T.; Sherman, J. W.; Aspinwall, C. A. "Asymmetric Electrode Kinetics Induced by Concurrent Metal-Ligand Bond Dissociation." *Electrochimica Acta*, **1993**, *38*, 927-934.

- (7) Rieger, P. H. In *Electrochemistry*, Prentice Hall: Englewood Cliffs, 1987.
- (8) Trulove, P. C.; Carlin, R. T.; Mantz, R. A.; O'Dea, J. J.; Osteryoung, R. A. "Electrode Kinetics of Cu(I)-Ethylene Complex in Acidic Ambient-Temperature Chloroaluminate Molten Salts." *Electrochemistry in Non-Aqueous Media*, The Electrochemical Society, Fall meeting, New Orleans, Louisiana, Oct 10 - 15 1993.
- (9) Carlin, R. T.; Trulove, P. C.; Mantz, R. A.; O'Dea, J. J.; Osteryoung, R. A. "Electron Transfer Kinetics for Weakly Bonded, Labile Metal-Ligand Complexes." *J. Chem. Soc., Faraday Trans.*, **1996**, 92, 3969-3973.
- (10) Noël, M. A. M.; O'Dea, J. J.; Osteryoung, R. A. "Short Time Pulse Voltammetry in Ambient Temperature Chloroaluminate Ionic Liquids." *Electrochem. Soc.* **1992**, 139, 1231-1236.
- (11) Karpinski, Z. J.; Osteryoung, R. A. "Short Time Pulse Voltammetric Studies of Fast Heterogeneous Electron Transfer Reactions." *J. Electroanal. Chem.* **1993**, 349, 285-297.
- (12) O'Dea, J. J., North Carolina State University, personal communication.

- (13) Wightman, R. M.; Wipf, D. O. In *Electroanalytical Chemistry*; Bard A. J., Ed.; Marcel Dekker: New York, 1989, Vol. 15. pp 267-353.
- (14) Carlin, R. T.; Crawford, W.; Bersch, M. "Nucleation and Morphology Studies of Aluminum Deposited from an Ambient-Temperature Chloroaluminate Molten Salt" *J. Electrochem. Soc.* **1992**, *139*, 2720-2727.
- (15) Osteryoung, J.; O'Dea, J. J. In *Electroanalytical Chemistry*; Bard, A. J., Ed.; Marcel Dekker: New York, 1986, Vol. 14. pp. 209-308.
- (16) O'Dea, J. J.; Osteryoung, J.; Lane, T. "Determining Kinetic Parameters from Pulse Voltammetric Data." *J. Phys. Chem.* **1986**, *90*, 2761-2764.
- (17) Trulove, P. C., United States Naval Academy, personal communication, 1994.
- (18) O'Dea, J. J.; Osteryoung J.; Osteryoung, R. A. "Square Wave Voltammetry and Other Pulse Techniques for the Determination of Kinetic Parameters. The Reduction of Zinc(II) at Mercury Electrodes." *J. Phys Chem.* **1983**, *87*, 3911-3918.
- (19) Osteryoung, J.; O'Dea, J. J. In *Electroanalytical Chemistry*; Bard, A. J., Ed.; Marcel Dekker: New York, 1986, Vol. 14. pp 209-308.

(20) Wikiel, K.; Osteryoung, J "Square Wave Voltammetry at a Mercury Film Electrode: Exeperimental Results." *Anal. Chem.* **1989**, *61*, 2086-2092.

(21) O'Dea, J. J.; Wikiel, K.; Osteryoung, J. "Square-Wave Voltammetry for ECE Mechanisms." *J. Phys. Chem.* **1990**, *94*, 3629-9636.

Chapter 7

Behavior of Oxide Containing Melts

7.1 Introduction

Room temperature chloroaluminate molten salts are very hygroscopic and water reactive. In fact, both the AlCl_3 and the 1-ethyl-3-methylimidazolium chloride (EMIC) are very hygroscopic. Because water is an ubiquitous impurity it is very essential to know how water changes the melt characteristics. When a melt is exposed to water it reacts with the water to generate an aluminum oxide and/or an aluminum hydroxide species and hydrochloric acid. Several studies have been conducted in which either the oxide or the proton (hydrochloric acid) has acted as an interference with the chemistry of interest.¹⁻⁶

In order to remove the complications caused by the presence of either proton or oxide several removal procedures have been developed.⁷⁻⁹ Proton can be removed in two ways. The first removal method for proton is treatment of the melt with ethylaluminum sesquichloride (EtAlCl_2).⁷ One difficulty in using ethylaluminum sesquichloride was the difficulty in adding the exact amount needed to remove all the proton. Not adding enough ethylaluminum sesquichloride leaves residual protons while adding too much leaves ethylaluminum sesquichloride in solution.⁸ In addition, ethylaluminum sesquichloride changes the melt composition. Its addition makes a melt more

acidic while it removes proton. Proton can also be removed simply by applying high vacuum.⁹ The beauty of this technique is that the melt composition is not changed and nothing has to be added to the melt. This eliminates tedious titrations. One limitation of the vacuum technique is that it cannot be applied to acidic melts above $\approx 1.3:1.0$ mole ratio. At higher acidities the vapor pressure of AlCl_3 over the melt increases. The application of vacuum to these melts will remove AlCl_3 thereby changing the melt composition.⁹

Oxide can also be removed from the melts. Phosgene has been utilized to remove oxide from basic melts.^{10,11} In practice a basic melt is exposed to an excess of phosgene. The phosgene reacts with the oxide to generate carbon dioxide. Carbon dioxide and excess phosgene are then easily removed using vacuum.

The ability to remove proton and oxide from the melts is very important because it allows species to be studied in the melts without these potential interferences. In addition, the ability to remove proton and oxide has allowed researchers to study better these ubiquitous impurities. The characterization of oxide as a buffering agent is also extremely important. If the roles these two impurities play are known then the chemistry of species in the melts can be predicted.

Early work on oxide in the room temperature melts was conducted by Linga et al.¹ They found that Ti(IV) exhibited two reduction waves but only a single reoxidation in basic melts. The two waves were assigned to TiCl_6^{2-} and TiOCl_4^{2-} . The titanium oxychloride species was shown to reduce at a more

negative potential and the two species were found to be in slow equilibrium. None-the-less both species reduce to a common product TiCl_6^{3-} . In addition the equilibrium constant for the titanium chloride and titanium oxychloride was determined for melts of various compositions. The authors did note that the addition of water to the melt had the opposite of the expected effect. The addition of water decreased the concentration of titanium oxychloride. This was attributed to the formation of an aluminum hydroxychloride species which is not involved in the equilibrium with titanium.¹ Based on these results an analytical method for the determination of oxide concentration in the melts was developed.⁶ This study concluded that for the melts studied, the oxide concentration was generally about 2 mM.

Another technique to determine oxide concentrations in the melts was developed.³ This analytical method uses NbCl_6^- instead of TiCl_6^{2-} . Niobium chloride appears to react to completion with oxide added to basic melts. Niobium(V) chloride exhibits two reversible one electron reductions in basic melts.⁵ These two reductions waves are separated by about 1 V. When oxide is present in the melt or is added to the melt as lithium carbonate, another reduction appears between the first two.⁵ Using this analytical method, the oxide concentration in the melts studied was determined to be 3 - 5 mM.⁸

Electrochemistry has not been the method utilized to characterize oxide in the melts. Mass spectrometry (MS) has been used to determine the ionic make-up of the melts. Fast atom bombardment MS (FAB-MS) and secondary ion MS (SIMS) have both been utilized.¹²⁻¹⁶ In order to detect oxide and

hydroxide species in the melts, negative ion detection must be used.¹³⁻¹⁶ In these studies, contamination of the melt samples led to the formation of oxy- and hydroxychloroaluminate species.

Franzen et al. were the first to report the negative ion mass spectrum of the melts.¹³ Using SIMS they observed AlCl_4^- and Cl^- in basic melts and Al_2Cl_7^- in very acidic compositions. In addition they observed several oxide and hydroxide species including: $\text{Al}_2\text{OCl}_5^-$, $\text{Al}_3\text{O}_2\text{Cl}_6^-$, and $\text{Al}_2\text{Cl}_6\text{OH}^-$ in a 1.2:1.0 melt. In basic melts no oxide or hydroxide melt species were detected.

Wicelinski et al. used FAB-MS to conduct a similar study.¹⁴ In addition to detecting Cl^- and the characteristic chloroaluminate anions they detected numerous oxy- and hydroxychloroaluminate species in the acidic melts including: AlCl_3OH^- , $\text{Al}_2\text{OCl}_5^-$, $\text{Al}_2\text{Cl}_6\text{OH}^-$, $\text{Al}_3\text{Cl}_6\text{O}_2^-$, $\text{Al}_3\text{Cl}_7\text{O}_2\text{H}^-$, $\text{Al}_3\text{Cl}_8\text{O}^-$, and $\text{Al}_4\text{Cl}_9\text{O}_2^-$. In the basic melts they detected one oxide species, AlOCl_5^- .

Abdul-Sada et al. have conducted two studies using FAB-MS to characterize the anionic components in the melt.^{15,16} They initially observed the oxy- and hydroxychloroaluminate species: $\text{Al}_2\text{OCl}_5^-$ and $\text{Al}_3\text{Cl}_8\text{O}^-$ in acidic melts. After 30 minutes had elapsed, $\text{Al}_2\text{Cl}_6\text{OH}^-$, $\text{Al}_3\text{Cl}_6\text{O}_2^-$, $\text{Al}_3\text{Cl}_7\text{O}_2\text{H}^-$, and $\text{Al}_4\text{Cl}_9\text{O}_2^-$ were also detected. The authors noted that the primary hydroxychloroaluminate species is $\text{Al}_2\text{Cl}_6\text{OH}^-$, that this is the first formed hydroxide containing species, and this ion becomes dominant as the oxide impurity level increases. One flaw in the mass spectrometry data is that both HCl and AlCl_3 have a measurable vapor pressure above acidic melts with a

mole ratio above $\approx 1.3:1.0$. In these conditions various recombinations can occur above the melt in the mass spectrometer. This can lead to the detection of species that did not exist in the melt originally.

Zawodzinski et al conducted several ^{17}O NMR studies of the melts.^{8,17,18} These studies provide great insight to the speciation of oxide and hydroxide in both acidic and basic melts. In basic melts a single peak is observed in the ^{17}O NMR spectrum. However, the peak position is dependent on the HCl concentration. When HCl was bubbled through an oxide containing basic melt the chemical shift would move upfield (smaller ppm). Because only a single peak is observed, the exchange between oxide and hydroxide species must be rapid on the NMR timescale. In addition, this does not limit the number of species present to only two. Zawodzinski et al⁸ were able to confirm the explanation offered by Linga for the results observed previously with Ti(IV) in basic melts.¹

In acidic melts the ^{17}O NMR spectrum consists of three lines at 49.7 ppm, 73.8 ppm and 91.8 ppm. The peak positions are not dependent on melt composition. The peak at 49.7 ppm was assigned to a hydroxide species.^{8,17,18} This was done based upon the changes in the NMR spectrum when HCl was added to the melt. In this case the peak at 49.7 ppm grew in size while the other two peaks decreased in size at the same rate. When ethylaluminum sesquichloride was added to the melt the exact opposite occurred and the peak at 49.7 ppm decreased in size.

In the absence of hydroxide the remaining peak intensities are dependent on melt composition (Figure 7.1).⁸ As the acidity of the melt is

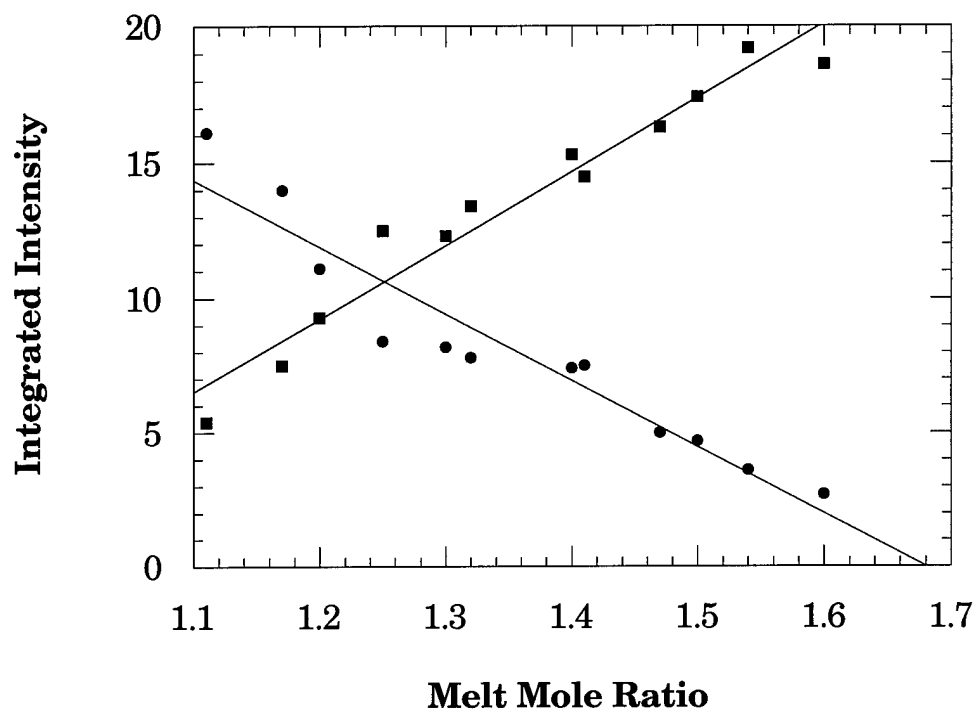
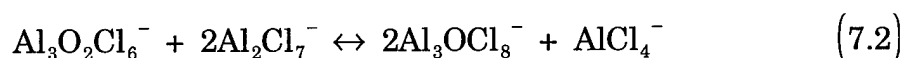


Figure 7.1 Plot of the integrated intensity of the ^{17}O NMR peaks present in acidic melts in the absence of proton vs. melt composition. (■ Peak at 91.8 ppm) (● Peak at 72.8 ppm).⁸

increased the intensity of the peak at 91.8 ppm increases as well. This was attributed to the oxygen nucleus being surrounded by more acidic groups in very acidic melts.⁸ Based on linewidths and chemical shifts they were able to conclude that three oxide containing species in slow exchange exist in acidic melts. One of the three species is a hydroxide. The other two species most likely have the oxygen bridged between two aluminum atoms.

Zawodzinski et. al. took steps to further try and determine the structures of the oxide and hydroxide species present in the acidic melts. A program was written to model six equilibrium between the two oxide species. Two of the six equilibrium fit the data reasonably well.



Taking these equilibrium and adding an additional equilibrium between HCl and hydroxide resulted in two probable hydroxide species $\text{Al}_2\text{Cl}_6\text{OH}^-$ and $\text{Al}_3\text{Cl}_9\text{OH}^-$. For the basic melts the following equilibrium was suggested:



Structures of species with the stoichiometry indicated by these models are depicted in Figure 7.2.

The most recent FAB-MS data presented suggested that the two oxide species present in acidic melts are: $\text{Al}_3\text{Cl}_8\text{O}^-$ and $\text{Al}_2\text{Cl}_5\text{O}^-$. They also suggested the favored oxide species is $\text{Al}_2\text{Cl}_6\text{OH}^-$.¹⁶

Preliminary studies by Summers suggested that oxide present in melts

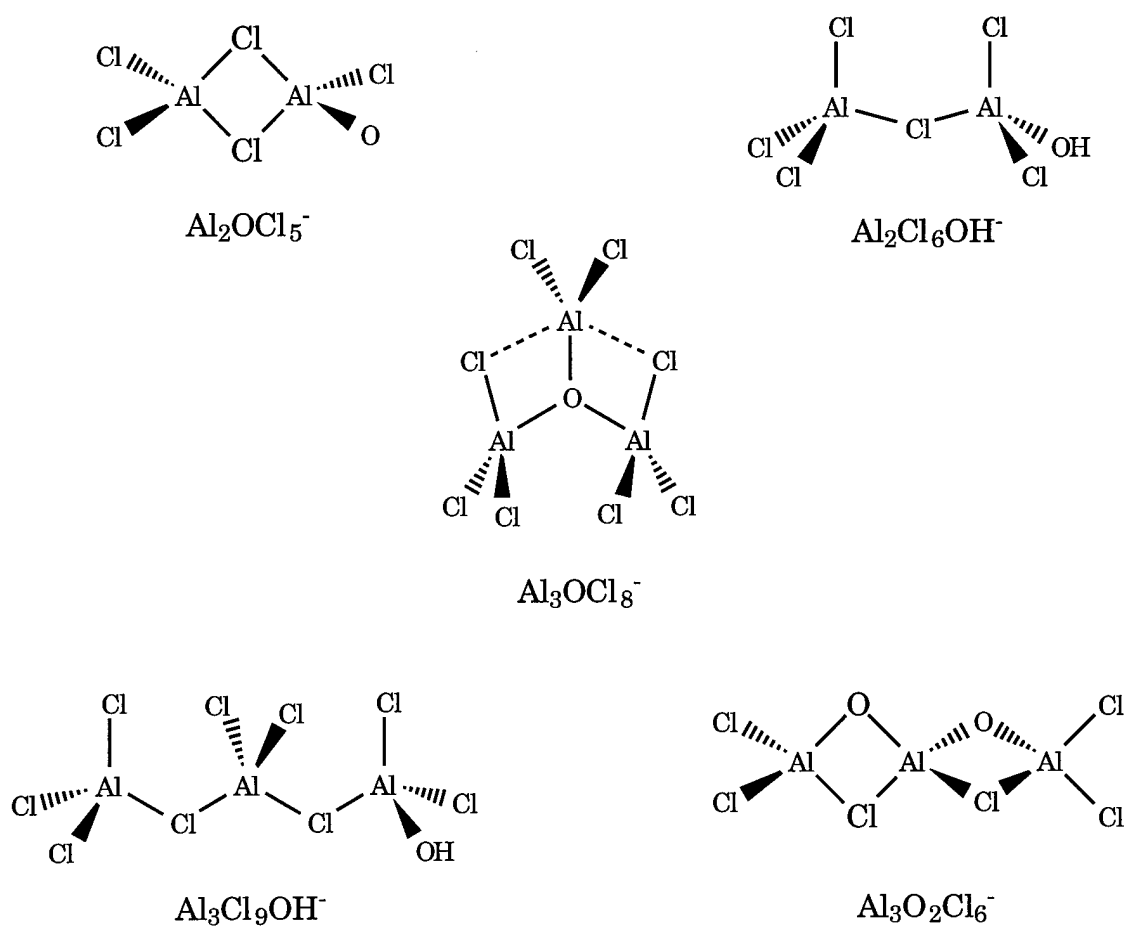


Figure 7.2 Structures of species with the stoichiometry indicated by the models proposed by Zawodzinski.⁸

acts as a neutral buffering agent. In the presence of oxide a region of melt compositions near neutral exist where no chloride wave was observed electrochemically and at the same time no aluminum deposition was observed electrochemically. In studies where the melt composition is close to neutrality it is very important to know if some buffering agent is present altering the melt behavior.

7.2 Specialized Experimental Procedures

7.2.1 Materials

H_2^{17}O (19% isotopic enrichment, Cambridge Isotopes) was used as received. Niobium(V)chloride (99.9+ %, Aldrich) was used without further purification.

7.2.2 Equipment and Procedures

7.2.2.1 Electrochemical Measurements

Electrochemical measurements were conducted in a nitrogen-filled dry box using a PAR EG&G 273 potentiostat, a Pentium personal computer, and Wotan, an in-house data-acquisition program. During the quantification of oxide concentration in a melt a Cypress Systems glassy carbon working

electrode was used. For all other portions of the study a single 250 μm diameter tungsten working electrode was used. The reference electrode consisted of an aluminum wire in a 1.5:1.0 melt and the counter electrode was a loop of 1 mm platinum wire. The working electrode was mechanically polished with diamond suspension prior to use. Prior to the acquisition of electrochemical data the working electrode was electrochemically cleaned by cycling into the AlCl_4^- oxidation wave using cyclic staircase voltammetry. Three scans were performed with a scan rate of 500 mV / sec from 1 to 3 volts versus the $\text{Al}(0)$ / $\text{Al}(\text{III})$ reference.²⁰

Before electrochemical data were acquired using oxide containing samples, the optimum normal pulse voltammetry conditions to quantitate the Al_2Cl_7^- and Cl^- concentrations were determined (Table 7.1). In addition, square wave voltammetry was utilized with Nb(V)Cl to quantitate the oxide level in a stock melt. The square wave parameters are listed in Table 7.2.

Once the electrochemical data had been acquired it was analyzed using FSQPLT, an in-house data-analysis program. The analysis for the square wave voltammograms consisted of measuring the peak net current. The analysis of the normal pulse data consisted of an applied 15 point moving average smoothing routine followed by a three line graphical analysis to determine the limiting current.

Normal Pulse Experimental Parameters	
Parameters to Detect Cl^-	Parameters to Detect Al_2Cl_7^-
Initial Potential 0.50 V	Initial Potential 0.25 V
Final Potential 2.30 V	Final Potential -1.10 V
Step Height 10 mV	Step Height 10 mV
Potential Width 1 msec	Potential Width 8 msec
Time Between Pulses 3 seconds	Time between Pulses 15 seconds
Number of Scans 1	Number of Scans 1
Temperature 25 °C	Temperature 25 °C

Table 7.1 Normal pulse voltammetry parameters for the detection of oxidation of chloride and deposition of aluminum used throughout the study.

Square Wave Experimental Parameters
Initial Potential 0.75 V
Final Potential -1.50 V
Step Height 10 mV
Square Wave Amplitude 50 mV
Square Wave Frequency 10 Hz
Conditioning Time 5 seconds
Number of Scans 1
Temperature 40 °C

Table 7.2 Square wave voltammetry parameters used during the Nb(V)Cl titration with oxide containing melt to determine the oxide concentration.

7.2.2.2 ^{17}O NMR Experiments

10 mm nuclear magnetic resonance (NMR) tubes were prepared by soaking in 80% HNO_3 , rinsing with deionized water, soaking in a solution of the tetrasodium salt of EDTA for 12 hours, and again rinsing with deionized water.

NMR samples were prepared by combining the stock solutions to prepare a melt with a known acidity and oxide concentration. The resulting melt was then stirred for several hours. After sufficient time had elapsed the melt was transferred into a 9 inch long 10 mm Wilmad NMR tube that had been constricted at 8 inches. A tip-off manifold was placed on the tube, and the sealed assembly was removed from the dry box and flame sealed under vacuum ($\approx 1 \times 10^{-2}$ torr).

^{17}O NMR experiments were acquired with the probe temperature set to 85 °C, and each sample was allowed to equilibrate for at least 10 minute prior to spectral acquisition. ^{17}O NMR spectra consisted of 32769 scans of 4096 points with a sweep width of 250 ppm, and a relaxation delay of 0.5 seconds. An exponential multiplication with a line broadening factor of 40 Hz was applied to the acquired free induction decay (FID) prior to Fourier transformation. The 90° pulse width was calibrated using D_2O containing natural abundance ^{17}O and set to 22 μsec throughout the experiments. The chemical shift was externally referenced to D_2O containing natural abundance ^{17}O (0 ppm) whose spectrum was obtained using identical acquisition and processing parameters.

7.2.2.3 Sample Preparation

In order to minimize error due to the uncertainty of melt composition a single 315 g 0.988:1.0 melt was prepared. The oxide and proton impurities were removed from the melt using phosgene and vacuum as described previously. From this melt, three stock solutions were prepared (Figure 7.3). The first stock solution was simply 175 g of the initial melt. This melt should be oxide and proton free and have a mole ratio of 0.988:1.0. This corresponds to a Cl^- concentration of 56.2 mM

The second stock solution was obtained by titrating 53 g of the first solution using AlCl_3 and monitoring the Cl^- and Al_2Cl_7^- concentrations using electrochemistry (Figure 7.4 and Table 7.3). The titration of this melt using AlCl_3 served three purposes. First, it allowed testing of the experimental parameters used to ensure that the response of the experiment was linear with respect to Cl^- and Al_2Cl_7^- concentrations. Second, the exact acidity of the melt was now known because the titration goes through a zero point at neutrality. Neutrality is a precise melt condition and any AlCl_3 added after this point simply increases the Al_2Cl_7^- concentration. Thirdly, the titration allowed the exact determination of the original melt composition. Based on this experiment the initial melt composition was determined to be 0.990:1.0 rather than 0.988:1.0. This seemingly minor difference has consequences because a 0.988:1.0 melt has a Cl^- concentration of 56.2 mM while the Cl^- concentration of a 0.990:1.0 melt is 44.5 mM. This is approximately a 20% difference. The

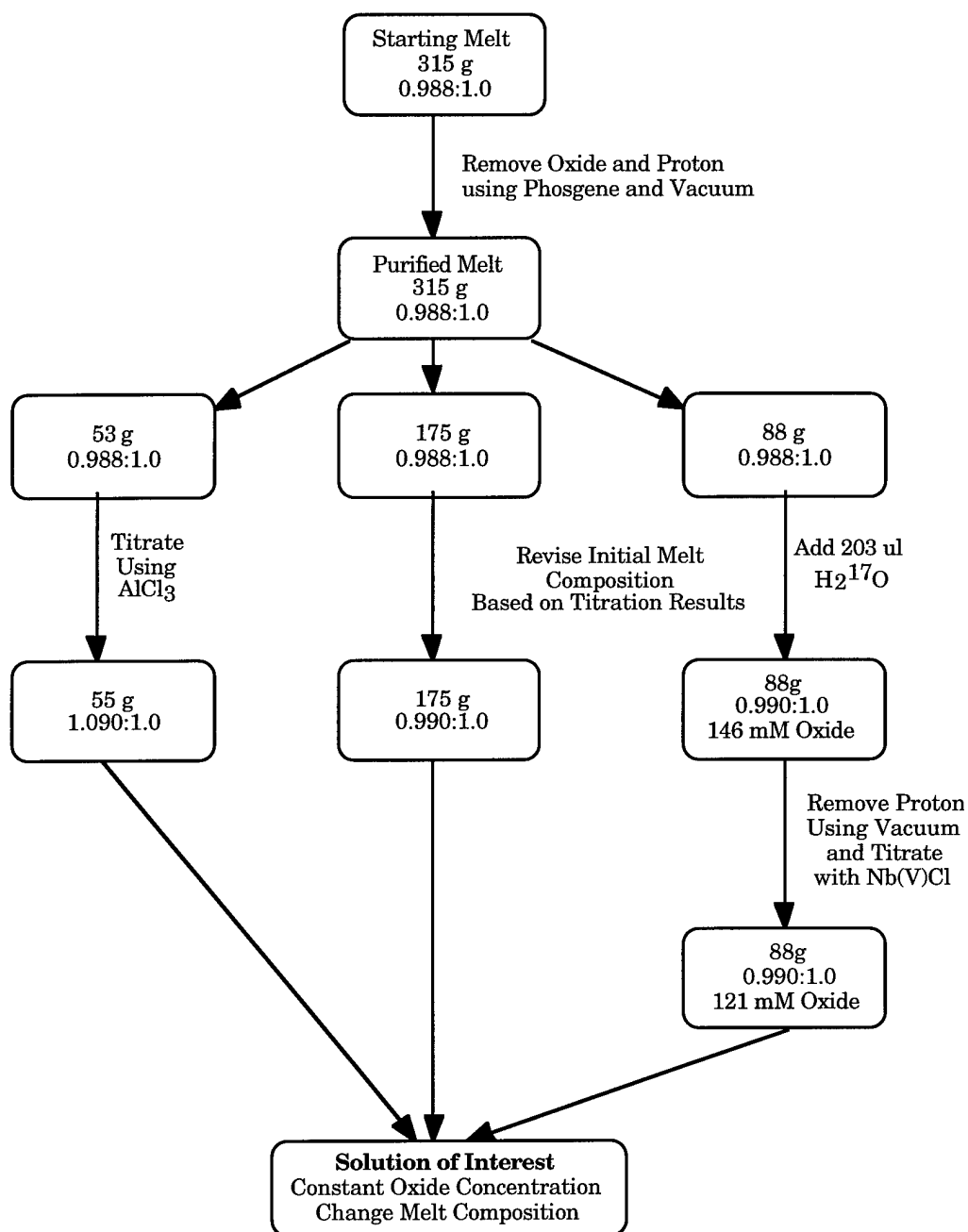


Figure 7.3 Experimental flow chart for the generation of proton free melts with know composition and oxide concentration.

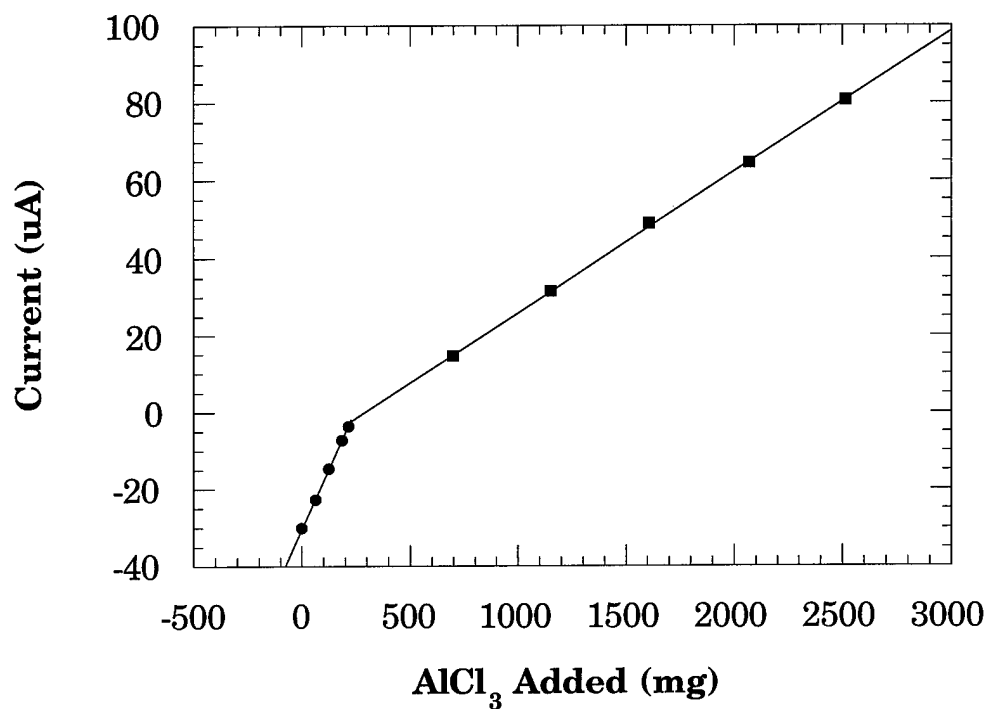


Figure 7.4. Titration of initial melt using AlCl_3 . AlCl_3 is added and either the Cl^- oxidation (●), or the aluminum deposition (■), is monitored. In the basic melt compositions, Cl^- oxidation is monitored. In acidic melt compositions, the aluminum deposition is monitored. The break point is a neutral melt. Lines are the linear least squared fit to the data points.

AlCl ₃ Titration of the Stock Basic Melt	
Amount AlCl ₃ added (mg)	Observed Current (μA)
0.0	-30.00
61.8	-22.66
122.8	-14.60
183.8	-7.28
214.7	-3.70
697.3	14.69
1152.1	31.44
1607.3	48.91
2069.8	64.54
2513.2	80.69

Table 7.3 Titration of initial melt using AlCl₃. AlCl₃ is added and either the Cl⁻ oxidation (negative currents), or the aluminum deposition (positive currents), is monitored. In the basic melt compositions Cl⁻ oxidation is monitored. In acidic melt compositions the aluminum deposition is monitored.

melt composition of stock solution two is 1.090:1.0 which corresponds to a Al_2Cl_7^- concentration of 400 mM.

The third stock solution is the stock solution that contained the oxide. This melt was prepared by taking 88 g of the original melt and adding 203 μl of H_2^{17}O (19% isotopic enrichment). The resultant melt should contain 145 mM oxide. The resulting crust on the melt was allowed to dissolve while the solution was stirred. After the melt had stirred 48 hours the melt was deprotonated using vacuum as described above. After deprotonation procedure the melt was returned to the dry box and a 200 μl aliquots were added to a 0.9:1.0 melt containing 249 mM of Nb(V)Cl . Nb(V)Cl has been shown to react quantitatively with oxide in the melts and has been suggested as a means to determine oxide concentrations in basic melts.⁸ A problem that arose was the oxide added in each aliquot took days to fully react with the niobium. An explanation for the discrepancy between these results and those just mentioned is that Hussey and coworkers added oxide as lithium carbonate to a melt that already contained Nb(V)Cl . What they measured was the ability of niobium to compete with the melt in order to react with the free oxide. In this case the niobium must abstract the oxide from the melt species. It seems this abstraction process is much slower. Titrating the oxide using Nb(V)Cl resulted in the determination of the oxide concentration as 121 mM. The difference in the oxide concentration from that expected from the addition of the H_2O , 146 mM, and that from the titration, 121 mM, is not entirely surprising because of the difficulty of the niobium titration. However the niobium titration is

reasonably close to the predicted value. The oxide containing stock solution was taken to have an oxide concentration of 146 mM.

Four series of samples were prepared from the three stock solutions. Within each set of samples the oxide concentration is held constant while the melt composition is incremented from basic to acidic. The four oxide concentrations studied were: 0 mM, 25 mM, 50 mM and 75 mM (Tables 7.4 to 7.7). In the case of the 75 mM set, larger samples were prepared to allow a portion of the sample to be examined using ^{17}O NMR.

7.3 Results and Discussion

7.3.1 Electrochemical Results

The electrochemical window available in AlCl_3 / EMIC melts is strongly dependent on melt composition. When the mole ratio of AlCl_3 :EMIC is greater than one, the melt is acidic and aluminum deposition is possible. When the mole ratio is less than one the chloride species is present and its oxidation is observable. Both the oxidation of chloride and the reduction of Al(III) to Al(0) are absent in neutral melts and alkali metal chloride neutral buffered melts. The presence of an aluminum oxychloride or an aluminum hydroxychloride species also seems to buffer the melts (Figure 7.5). This study evaluates which species, aluminum oxide or aluminum hydroxide is buffering the melt.

Each sample was examined using normal pulse voltammetry. Samples that were close to neutrality were examined for both chloride oxidation and

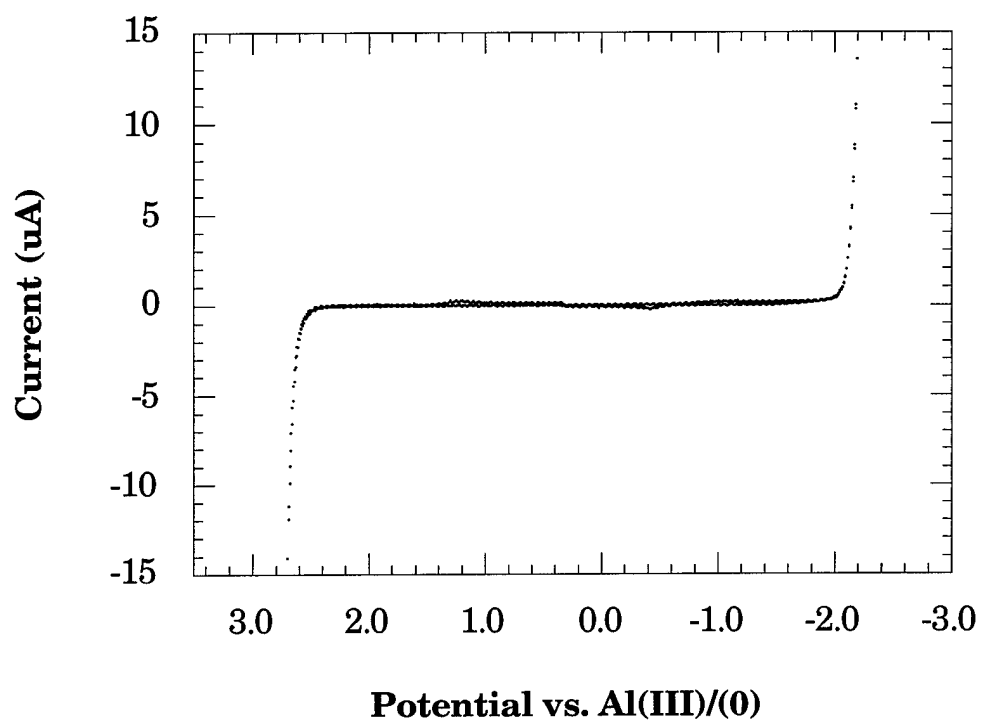


Figure 7.5 Electrochemical window present in oxide buffered melts. 250 μm diameter tungsten electrode with Al(0) / Al(III) in a 1.5:1.0 melt reference electrode.

Oxide Melt Weight (g)	Acidic Melt Weight (g)	Basic Melt Weight (g)	Al_2Cl_7^- Concentration (mM)	Oxide Concentration (mM)
3.3796	2.5158	0.6613	118.35	75.33
3.3799	2.3680	0.8103	108.38	75.32
3.3796	2.2348	0.9560	99.16	75.17
3.3788	2.0788	1.0997	88.96	75.31
3.3797	1.9291	1.2467	78.94	75.35
3.3796	1.7827	1.3974	69.02	75.30
3.3790	1.7825	1.3966	69.04	75.30
3.3793	1.6357	1.5476	59.10	75.26
3.3800	1.4900	1.6907	49.34	75.29
3.3789	1.4165	1.7678	44.37	75.24
3.3794	1.3431	1.8379	39.48	75.28
3.3787	1.2701	1.9148	34.54	75.23
3.3791	1.1956	1.9868	29.56	75.26
3.3787	1.1241	2.0635	24.71	75.20
3.379	1.0535	2.1362	19.95	75.18
3.3786	0.9026	2.2836	9.85	75.22
3.3802	0.9806	2.2880	14.34	74.30
3.3803	0.7724	2.4231	1.04	75.13

Table 7.4 Actual stock solution weights used to generate a series of samples with 75 mM oxide and to vary the melt composition from slightly acidic melt to a basic melt.

Oxide Melt Weight (g)	Acidic Melt Weight (g)	Basic Melt Weight (g)	Al_2Cl_7^- Concentration (mM)	Oxide Concentration (mM)
0.8863	0.9476	0.7697	111.93	49.75
0.8867	0.8858	0.8256	101.77	49.88
0.8856	0.8244	0.8860	91.47	49.86
0.8864	0.7663	0.9430	81.62	49.91
0.8854	0.7115	1.0019	72.18	49.79
0.8859	0.6546	1.0650	62.26	49.69
0.8867	0.5908	1.1178	51.84	49.93
0.8869	0.5416	1.1776	43.12	49.74
0.8862	0.4727	1.2316	31.93	50.00
0.8860	0.4165	1.2971	22.13	49.81
0.8848	0.3553	1.3506	11.96	49.91
0.8855	0.2983	1.4091	2.22	49.91
0.8862	0.2404	1.4685	-7.66	49.91
0.8846	0.1832	1.5316	-17.41	49.74
0.8856	0.1238	1.5817	-27.43	49.95
0.8861	0.0638	1.6566	-37.67	49.68

Table 7.5 Actual stock solution weights used to generate a series of samples with 50 mM oxide and to vary the melt composition from slightly acidic melt to a basic melt. Negative Al_2Cl_7^- concentrations correspond to Cl^- concentrations.

Oxide Melt Weight (g)	Acidic Melt Weight (g)	Basic Melt Weight (g)	Al_2Cl_7^- Concentration (mM)	Oxide Concentration (mM)
0.4457	0.5273	1.632	42.94	25.00
0.4493	0.4982	1.652	38.17	25.26
0.4435	0.4464	1.7142	29.29	24.89
0.4446	0.3890	1.7710	19.56	24.95
0.4448	0.3245	1.8308	8.74	25.00
0.4439	0.2675	1.8887	-0.92	24.95
0.4491	0.2084	1.9420	-10.95	25.25
0.4495	0.1454	2.0009	-21.60	25.31

Table 7.6 Actual stock solution weights used to generate a series of samples with 25 mM oxide and to vary the melt composition from slightly acidic melt to a basic melt. Negative Al_2Cl_7^- concentrations correspond to Cl^- concentrations.

Oxide Melt Weight (g)	Acidic Melt Weight (g)	Basic Melt Weight (g)	Al_2Cl_7^- Concentration (mM)	Oxide Concentration (mM)
0	0.7256	1.9816	74.08	0
0	0.7210	1.9795	73.63	0
0	0.6615	2.0420	63.80	0
0	0.6609	2.0455	63.58	0
0	0.6015	2.1089	53.77	0
0	0.6013	2.1078	53.78	0
0	0.5402	2.3873	37.29	0
0	0.5400	2.1624	44.03	0
0	0.4794	2.2242	34.11	0
0	0.4195	2.2860	24.30	0
0	0.3591	2.3436	14.52	0
0	0.2992	2.4058	4.71	0
0	0.2694	2.4475	-0.34	0
0	0.2381	2.4675	-5.25	0
0	0.2078	2.4965	-10.17	0
0	0.1774	2.5288	-15.15	0
0	0.1468	2.557	-20.11	0
0	0.1186	2.5887	-24.73	0
0	0.0595	2.6491	-34.35	0
0	0.0045	2.7032	-43.30	0

Table 7.7 Actual stock solution weights used to generate a series of samples with 0 mM oxide and to vary the melt composition from slightly acidic melt to a basic melt. Negative Al_2Cl_7^- concentrations correspond to Cl^- concentrations.

aluminum deposition. Under no conditions were both the chloride oxidation and the aluminum deposition present in the same sample. Figures 7.6 to 7.9 plot the observed current against the melt composition. The melt composition is calculated from the compositions of the stock solutions. Two details are qualitatively obvious from the plots. First, the plateau is larger the greater the oxide concentration. The width of the plateau represents the buffering capacity of the melt. It is clear that the presence of oxide buffers the melts and that higher concentrations of oxide species buffer the melts to a larger degree.

Second, the plots are offset from zero on the X axis. The melt composition predicted by the compositions of the stock melts does not agree with experiment. In all cases the melts are more basic than the calculated value. Something has caused the X axis to shift. This was very surprising considering the various calibrations that were performed on the stock solutions. The offset is most likely due to one of two possibilities. The first possibility is simply that there was an error in preparing the melt and that the melt composition differed from that used to calculate the expected melt composition. This is not entirely unlikely due to the sensitivity of these measurements. For example, in the preparation of a 25 g melt a weighing error of 0.29 g results in a 100 mM change in either Cl^- or Al_2Cl_7^- concentration. Given that the balance is in a dry box, static electricity as well as changes in box pressure are a problem. The second possibility is that not all the aluminum hydroxychloride species were removed using vacuum. For every aluminum hydroxychloride there is an extra chloride in solution that was assumed to be removed by vacuum as HCl .

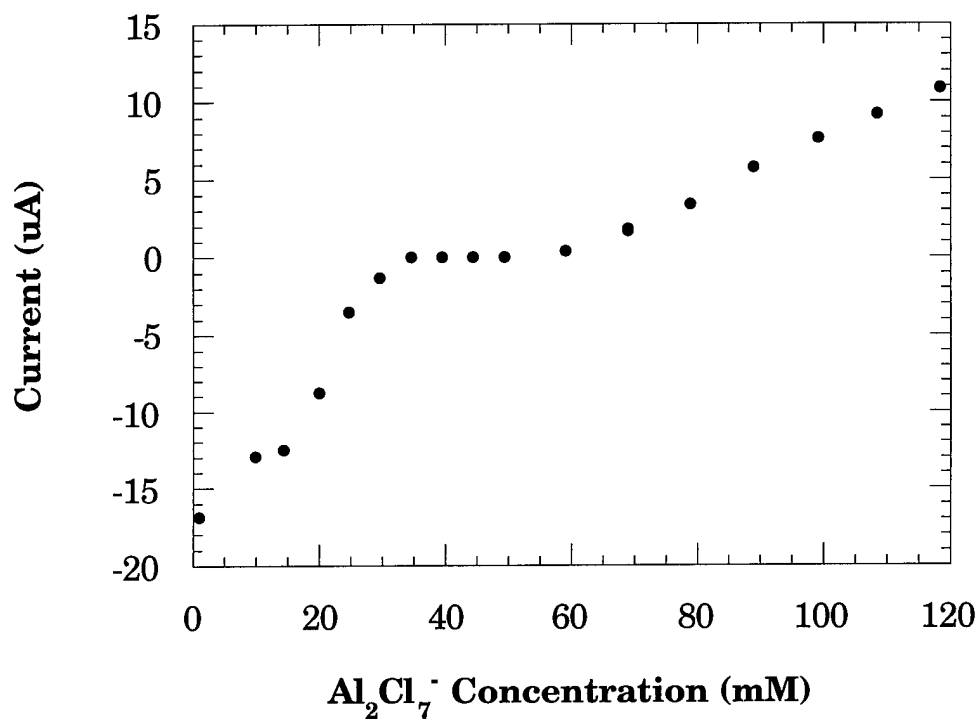


Figure 7.6 Observed current obtained using normal pulse voltammograms and a 250 μm diameter tungsten electrode vs. Al_2Cl_7^- concentration in a series of melts with a 75 mM concentration of oxide. Negative currents correspond to the oxidation of chloride while positive currents correspond to the deposition of aluminum.

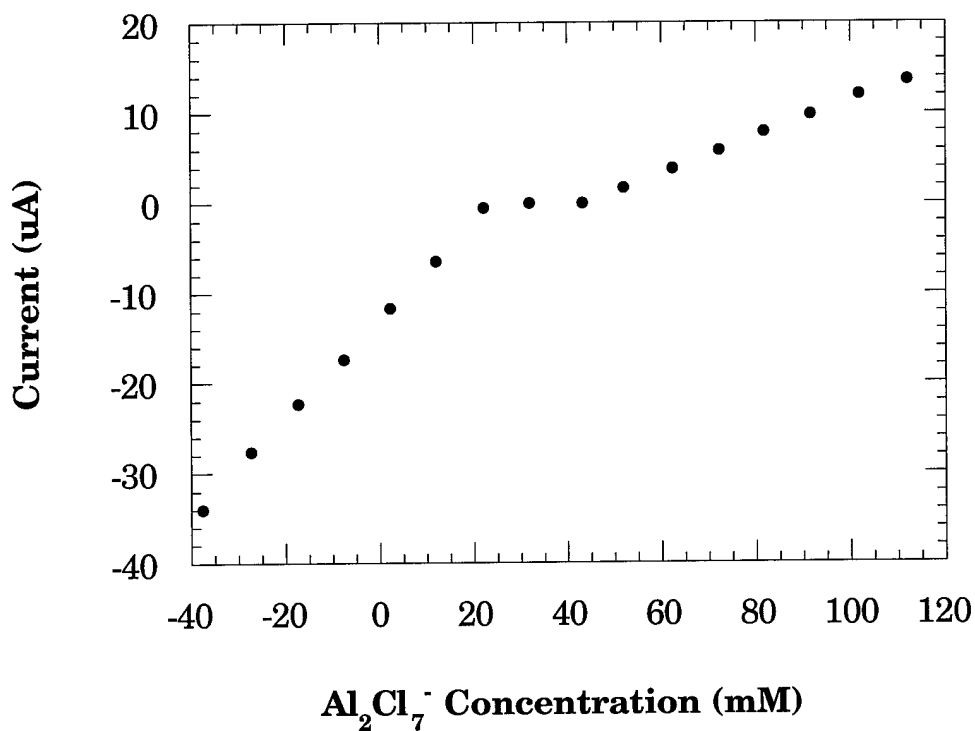


Figure 7.7 Observed current obtained using normal pulse voltammograms and a 250 μm diameter tungsten electrode vs. Al_2Cl_7^- concentration in a series of melts with a 50 mM concentration of oxide. Negative currents correspond to the oxidation of chloride while positive currents correspond to the deposition of aluminum. Negative Al_2Cl_7^- concentrations correspond to Cl^- concentration.

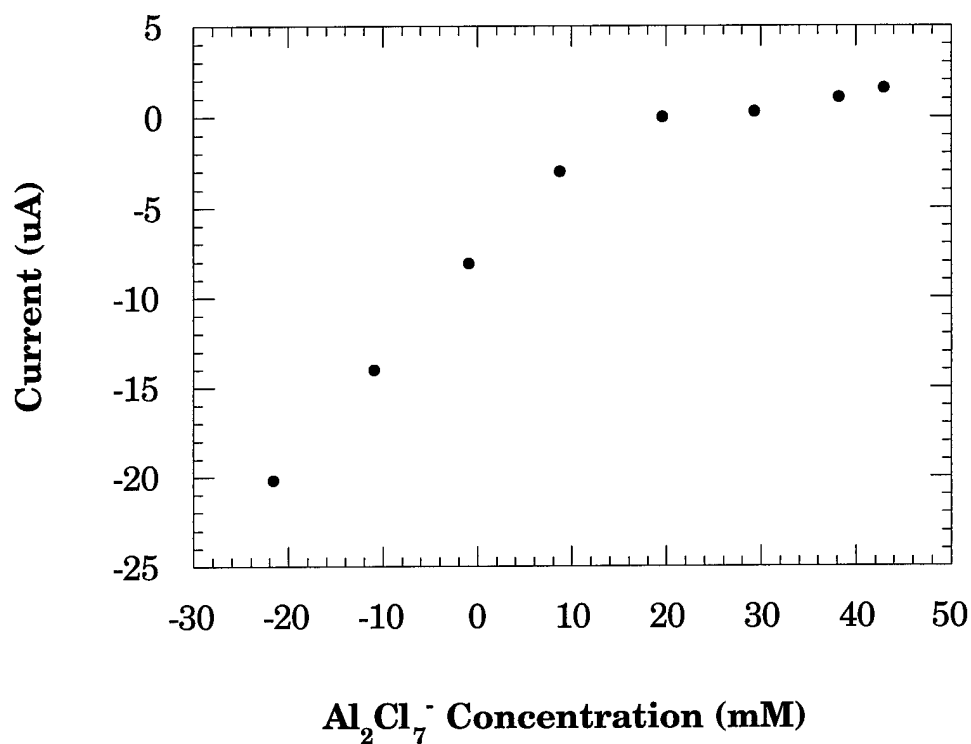


Figure 7.8 Observed current obtained using normal pulse voltammograms and a 250 μm diameter tungsten electrode vs. Al_2Cl_7^- concentration in a series of melts with a 25 mM concentration of oxide. Negative currents correspond to the oxidation of chloride while positive currents correspond to the deposition of aluminum. Negative Al_2Cl_7^- concentrations correspond to Cl^- concentration.

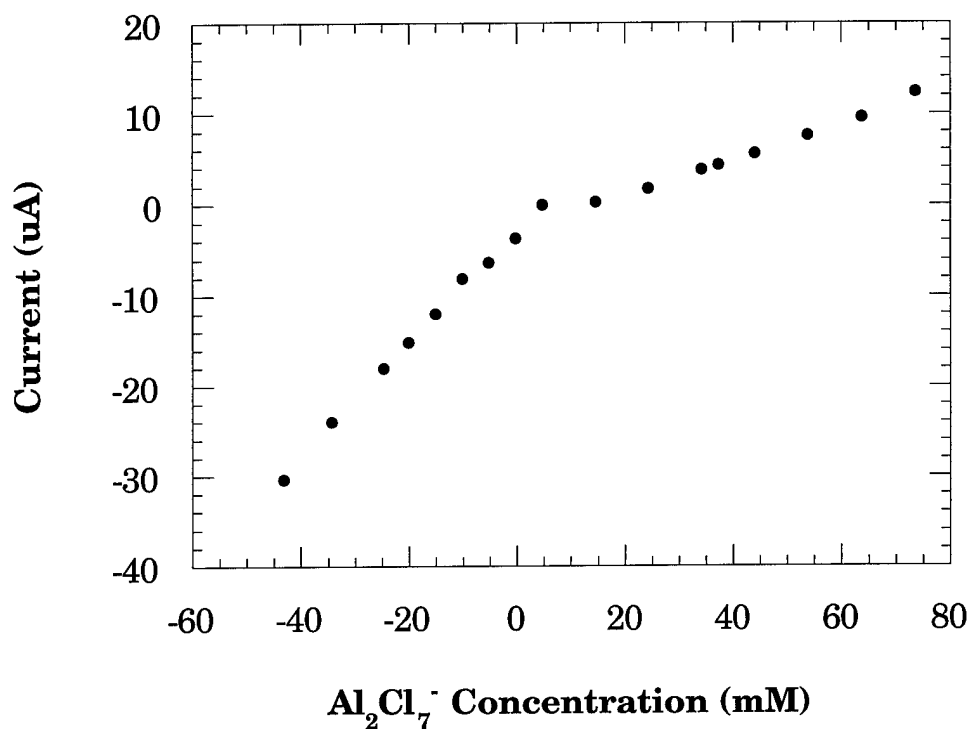


Figure 7.9 Observed current obtained using normal pulse voltammograms and a 250 μm diameter tungsten electrode vs. Al_2Cl_7^- concentration in a series of melts with no oxide. Negative currents correspond to the oxidation of chloride while positive currents correspond to the deposition of aluminum. Negative Al_2Cl_7^- concentrations correspond to Cl^- concentration.

In order to determine if the oxide containing melt was causing the X axis displacement, the offset of the plateau was plotted against the oxide concentration in each series of melts (Figure 7.10 and Table 7.8). The slope of this line is 0.336 mM of Al_2Cl_7^- for every 1 mM of oxide in the melt. The oxide stock solution contains 146 mM oxide and had a calculated chloride concentration of 57 mM. Calculating the chloride concentration from the slope of Figure 7.8 results in an actual chloride concentration of 106 mM. In order for this effect to have been caused by residual aluminum hydroxychloride species roughly 33% of the oxide species in the melt would have to be hydroxide.

Using this new chloride concentration for the oxide stock solution Figures 7.6 to 7.9 can be plotted with the X axis corrected to within a few mM (Figures 7.11 to 7.14 and Tables 7.9 to 7.12). Using these plots to determine the width of the plateau from the linear least squared fits of data the buffering capacity of the oxide containing melts and how it varies with oxide concentration can be determined. A plot of the buffering capacity vs. the oxide concentration is shown in Figure 7.15 (Table 7.13). The slope of the linear least squared fit to the data is 0.2. This means to buffer the melt against 1 millimole of the Lewis acid AlCl_3 takes 5 millimoles of oxide in the melt.

7.3.2 ^{17}O NMR Results

^{17}O NMR provides unique insight about oxide speciation in the melts. The NMR data coupled with the electrochemical results was able to offer a reasonable explanation for the limited buffering capacity of the oxide

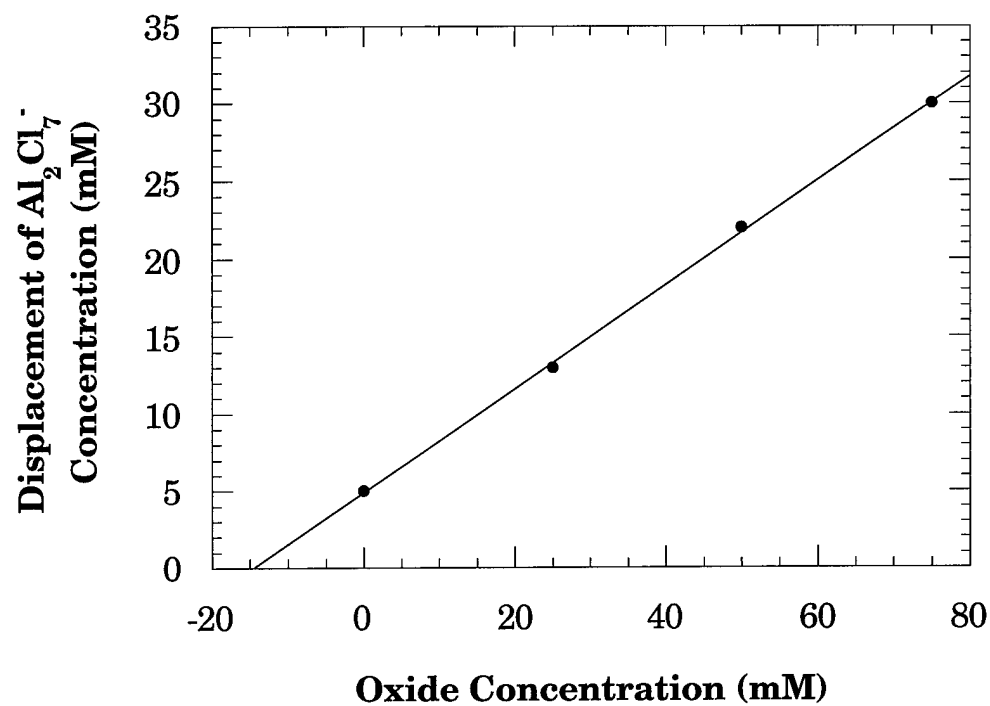


Figure 7.10 Plot of displacement of Al_2Cl_7^- concentration for Figures 7.6 to 7.9 against the oxide concentration for each set of samples. Line is the linear least squared fit to the data points.

Displacement of Al_2Cl_7^- Concentration (mM)	Oxide Concentration for Set of Samples (mM)
5	0
13	25
22	50
30	75

Table 7.8 The displacement of Al_2Cl_7^- concentration for Figures 7.6 to 7.9 and the oxide concentration for each set of samples.

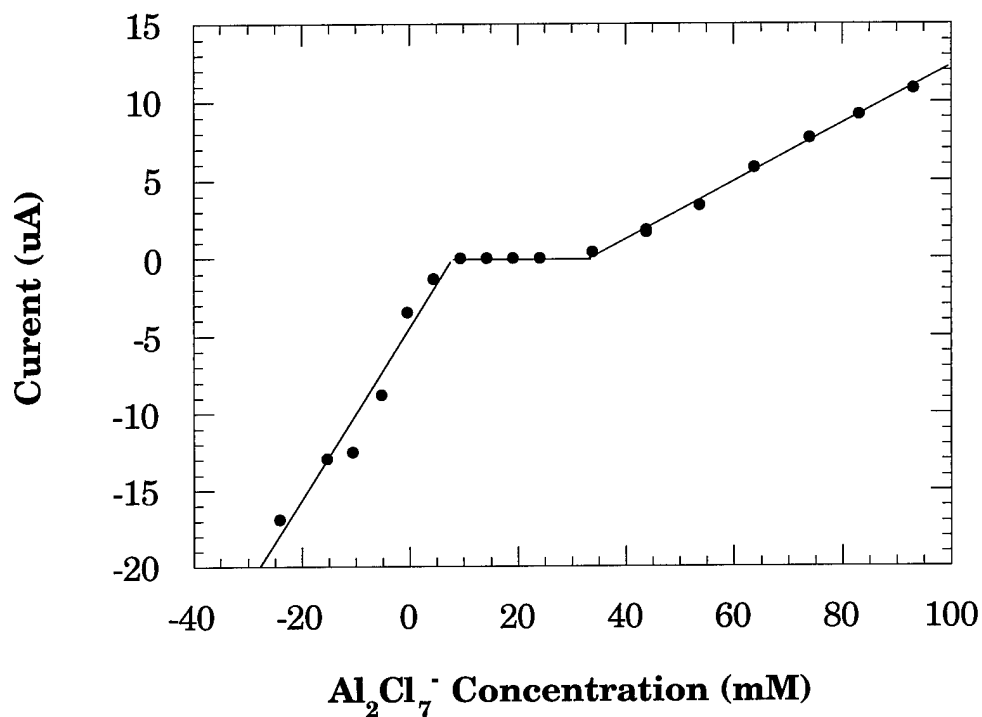


Figure 7.11 Observed current obtained using normal pulse voltammograms and a 250 μm diameter tungsten electrode vs. Al_2Cl_7^- concentration in a series of melts with a 75 mM concentration of oxide. Al_2Cl_7^- concentration has been adjusted to remove X axis offset. Negative currents correspond to the oxidation of chloride while positive currents correspond to the deposition of aluminum. Negative Al_2Cl_7^- concentrations correspond to Cl^- concentration. Lines are linear the least square fit to that portion of the data.

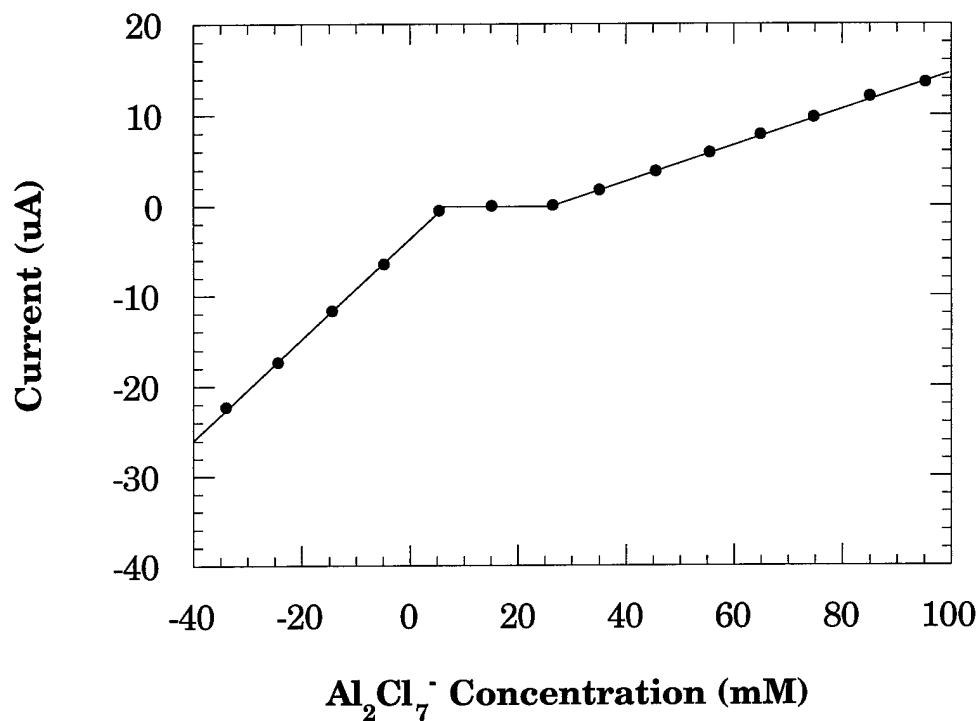


Figure 7.12 Observed current obtained using normal pulse voltammograms and a 250 μm diameter tungsten electrode vs. Al_2Cl_7^- concentration in a series of melts with a 50 mM concentration of oxide. Al_2Cl_7^- concentration has been adjusted to remove X axis offset. Negative currents correspond to the oxidation of chloride while positive currents correspond to the deposition of aluminum. Negative Al_2Cl_7^- concentrations correspond to Cl^- concentration. Lines are linear the least square fit to that portion of the data.

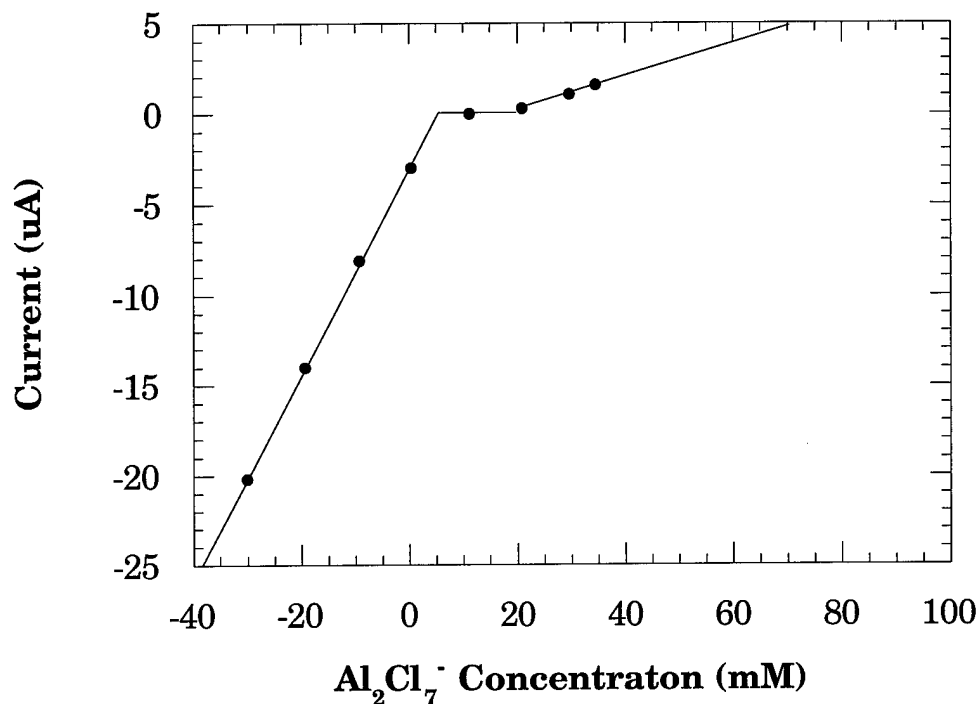


Figure 7.13 Observed current obtained using normal pulse voltammograms and a 250 μm diameter tungsten electrode vs. Al_2Cl_7^- concentration in a series of melts with a 25 mM concentration of oxide. Al_2Cl_7^- concentration has been adjusted to remove X axis offset. Negative currents correspond to the oxidation of chloride while positive currents correspond to the deposition of aluminum. Negative Al_2Cl_7^- concentrations correspond to Cl^- concentration. Lines are linear the least square fit to that portion of the data.

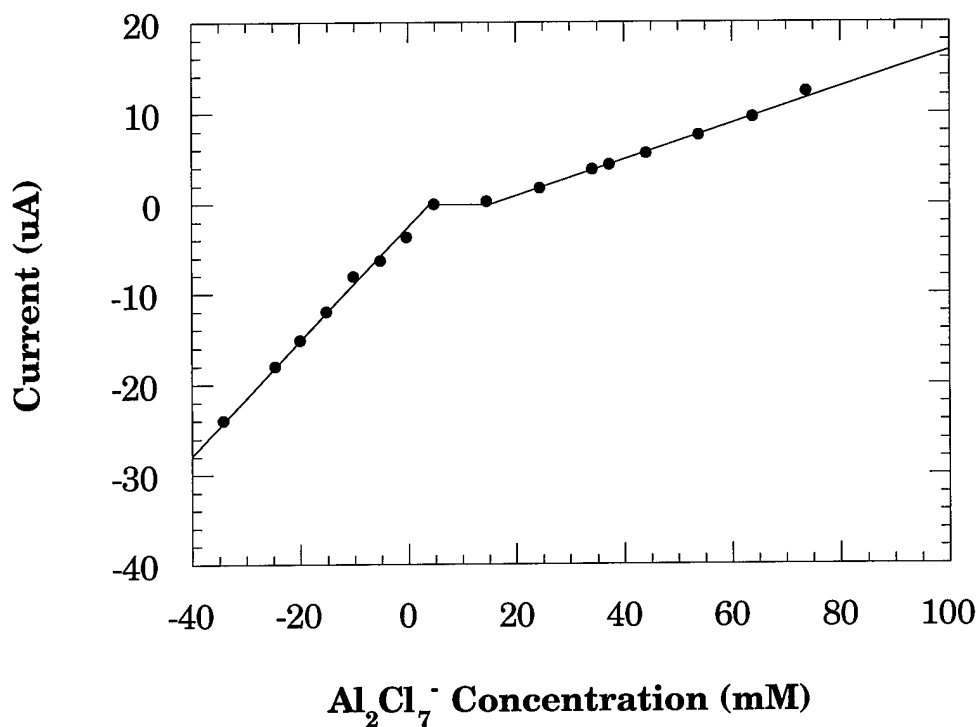


Figure 7.14 Observed current obtained using normal pulse voltammograms and a 250 μm diameter tungsten electrode vs. Al_2Cl_7^- concentration in a series of melts with no oxide. Al_2Cl_7^- concentration has been adjusted to remove X axis offset. Negative currents correspond to the oxidation of chloride while positive currents correspond to the deposition of aluminum. Negative Al_2Cl_7^- concentrations correspond to Cl^- concentration. Lines are linear the least square fit to that portion of the data.

Al_2Cl_7^- Concentration (mM)	Current (μA)
93.06	10.85
83.10	9.19
73.93	7.67
63.69	5.79
53.65	3.40
43.75	1.69
43.76	1.83
33.84	0.39
24.07	0.00
19.12	0.00
14.21	0.00
9.29	0.00
4.30	-1.32
-0.53	-3.49
-5.29	-8.78
-15.39	-12.95
-10.60	-12.50
-24.18	-16.38

Table 7.9 Observed current obtained using normal pulse voltammograms and a 250 μm diameter tungsten electrode vs. Al_2Cl_7^- concentration in a series of melts with a 75 mM concentration of oxide. Al_2Cl_7^- concentration has been adjusted to remove X axis offset. Negative currents correspond to the oxidation of chloride while positive currents correspond to the deposition of aluminum. Negative Al_2Cl_7^- concentrations correspond to Cl^- concentration.

Al_2Cl_7^- Concentration (mM)	Current (μA)
95.23	13.63
85.03	12.04
74.74	9.77
64.87	7.90
55.47	5.87
45.58	3.85
35.08	1.76
26.43	0.06
15.15	0.00
5.42	-0.48
-4.79	-6.46
-14.53	-11.67
-24.41	-17.37
-34.10	-22.29
-44.19	-27.60
-54.35	-34.00

Table 7.10 Observed current obtained using normal pulse voltammograms and a 250 μm diameter tungsten electrode vs. Al_2Cl_7^- concentration in a series of melts with a 50 mM concentration of oxide. Al_2Cl_7^- concentration has been adjusted to remove X axis offset. Negative currents correspond to the oxidation of chloride while positive currents correspond to the deposition of aluminum. Negative Al_2Cl_7^- concentrations correspond to Cl^- concentration.

Al_2Cl_7^- Concentration (mM)	Current (μA)
34.55	1.57
29.70	1.06
20.94	0.29
11.19	0.00
0.35	-3.00
-9.29	-8.10
-19.43	-14.00
-30.10	-20.20

Table 7.11 Observed current obtained using normal pulse voltammograms and a 250 μm diameter tungsten electrode vs. Al_2Cl_7^- concentration in a series of melts with a 25 mM concentration of oxide. Al_2Cl_7^- concentration has been adjusted to remove X axis offset. Negative currents correspond to the oxidation of chloride while positive currents correspond to the deposition of aluminum. Negative Al_2Cl_7^- concentrations correspond to Cl^- concentration.

Al_2Cl_7^- Concentration (mM)	Current (μA)
73.63	12.34
63.80	9.58
53.77	7.54
37.29	4.30
44.03	5.60
34.11	3.84
24.30	1.80
14.52	0.30
4.71	0.00
-0.34	-3.68
-5.25	-6.29
-10.17	-8.12
-15.15	-1.97
-20.11	-15.13
-24.73	18.02
-34.35	-23.98
-43.30	-30.38

Table 7.12 Observed current obtained using normal pulse voltammograms and a 250 μm diameter tungsten electrode vs. Al_2Cl_7^- concentration in a series of melts with no oxide. Al_2Cl_7^- concentration has been adjusted to remove X axis offset. Negative currents correspond to the oxidation of chloride while positive currents correspond to the deposition of aluminum. Negative Al_2Cl_7^- concentrations correspond to Cl^- concentration.

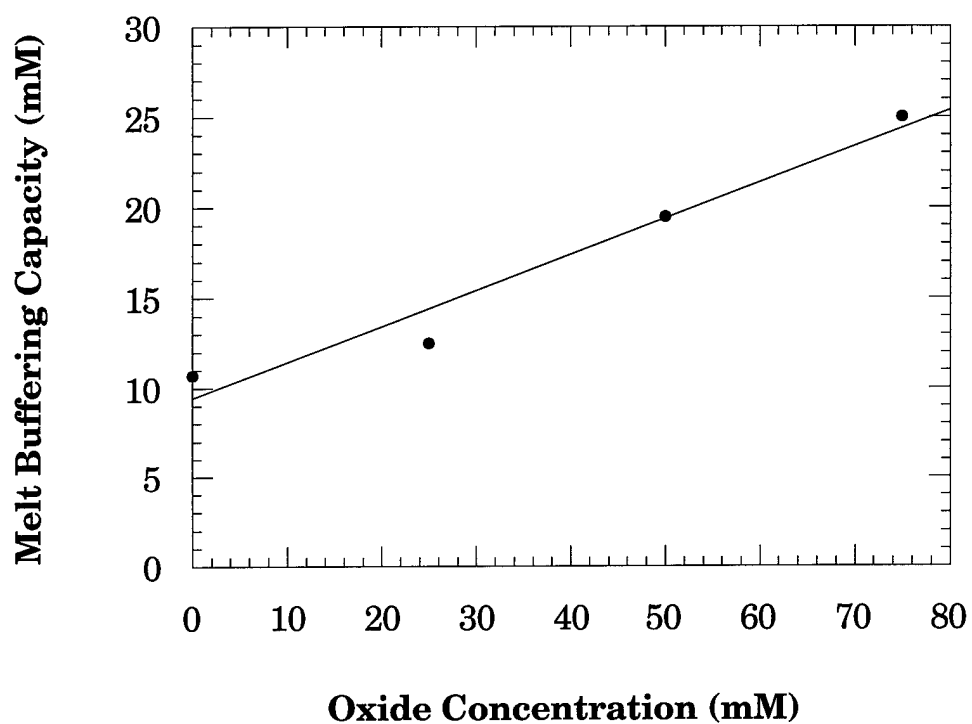


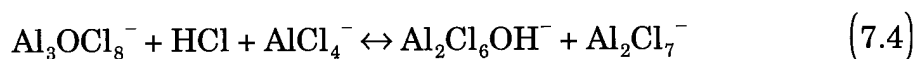
Figure 7.15 Melt buffering capacity against the oxide concentration determined from Figures 7.11 to 7.14. This is an indicator of how much oxide is needed to buffer against a given concentration of Lewis acid or base. For example, a melt that contains 80 mM oxide can have 25 mM AlCl_3 added before the melt is no longer buffered.

Oxide Concentration (mM)	Melt Buffering (mM)
75	25.0
50	19.4
25	12.6
0	10.7

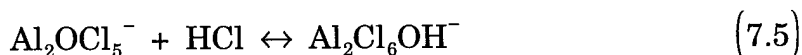
Table 7.13 Melt oxide concentration and melt buffering capacity determined from Figures 7.11 to 7.14.

containing melts. As mentioned previously the NMR samples were portions of the same 75 mM oxide containing samples which were examined electrochemically. This was done so the samples could be directly compared without having to correct for oxide concentration changes or melt composition differences. Ten sample spectra were obtained. These samples varied in melt composition from 93 mM Al_2Cl_7^- to 24 mM Cl^- using the adjusted stock solution composition and from 75 mM Al_2Cl_7^- to 44 mM Cl^- using the original stock solution compositions (Figures 7.16 to 7.25). Each spectrum was run under identical conditions and the scaling of the Y axis has not been modified. This allows the intensities of peaks to be directly compared.

In the basic melts a single peak is observed. This is in agreement with Zawodzinski et. al.^{8,17,18} In the acidic melts three lines are observed. The peaks have the intensities expected for a near neutral acidic melt.⁸ Although the melt had been placed under vacuum to remove all proton and aluminum hydroxychloride species the ^{17}O NMR spectrum shows the presence of a substantial amount of aluminum hydroxychloride. Two equilibria have been proposed for the removal of proton from acidic melts²¹



and



for basic melts. The equilibrium constants have not been measured for either reaction. At high oxide concentrations it may not be possible to remove all hydroxide from the melts.

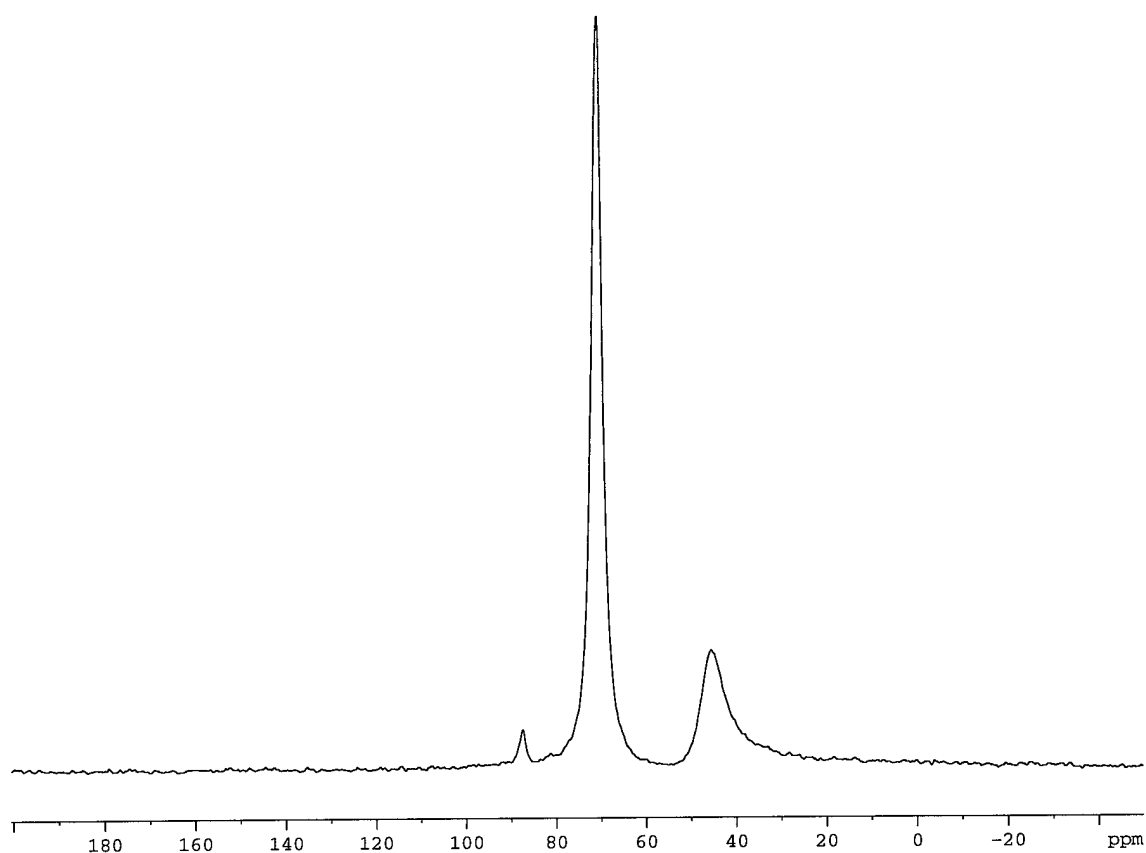


Figure 7.16 ^{17}O NMR spectrum of melt containing 75 mM oxide at 85 °C. This sample contained 75 mM Al_2Cl_7^- using the original stock solution compositions and 93 mM Al_2Cl_7^- using the modified stock solution compositions. The portion of the sample which was characterized using normal pulse voltammetry had a current of 10.85 μA for aluminum deposition.

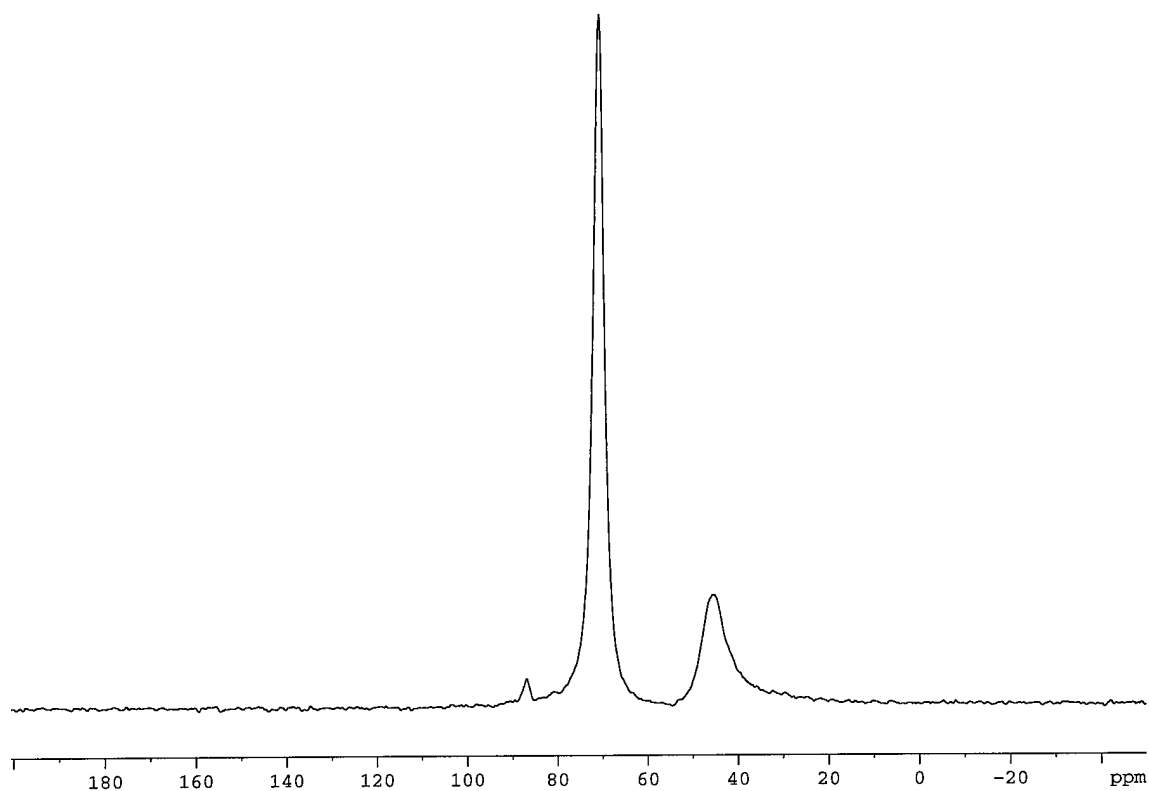


Figure 7.17 ^{17}O NMR spectrum of melt containing 75 mM oxide at 85 °C. This sample contained 55 mM Al_2Cl_7^- using the original stock solution compositions and 74 mM Al_2Cl_7^- using the modified stock solution compositions. The portion of the sample which was characterized using normal pulse voltammetry had a current of 7.67 μA for aluminum deposition.

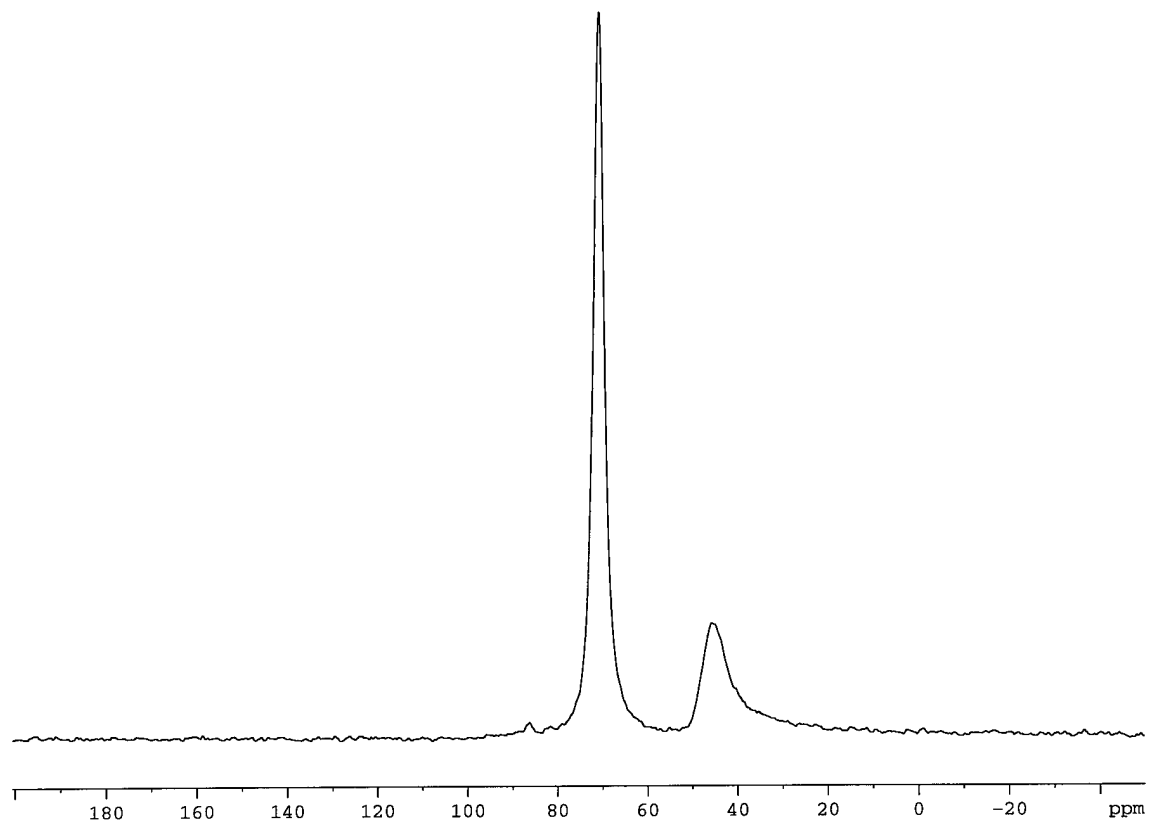


Figure 7.18 ^{17}O NMR spectrum of melt containing 75 mM oxide at 85 °C. This sample contained 45 mM Al_2Cl_7^- using the original stock solution compositions and 64 mM Al_2Cl_7^- using the modified stock solution compositions. The portion of the sample which was characterized using normal pulse voltammetry had a current of 5.79 μA for aluminum deposition.

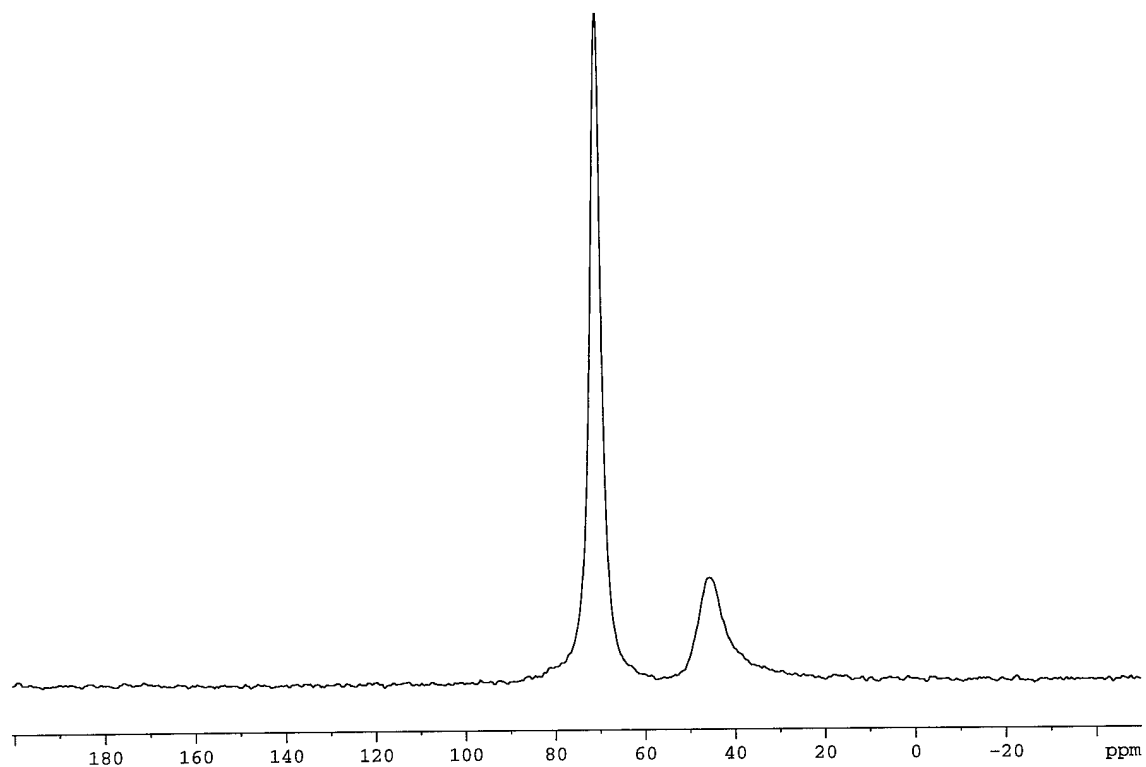


Figure 7.19 ^{17}O NMR spectrum of melt containing 75 mM oxide at 85 °C. This sample contained 25 mM Al_2Cl_7^- using the original stock solution compositions and 44 mM Al_2Cl_7^- using the modified stock solution compositions. The portion of the sample which was characterized using normal pulse voltammetry had a current of 1.69 μA for aluminum deposition.

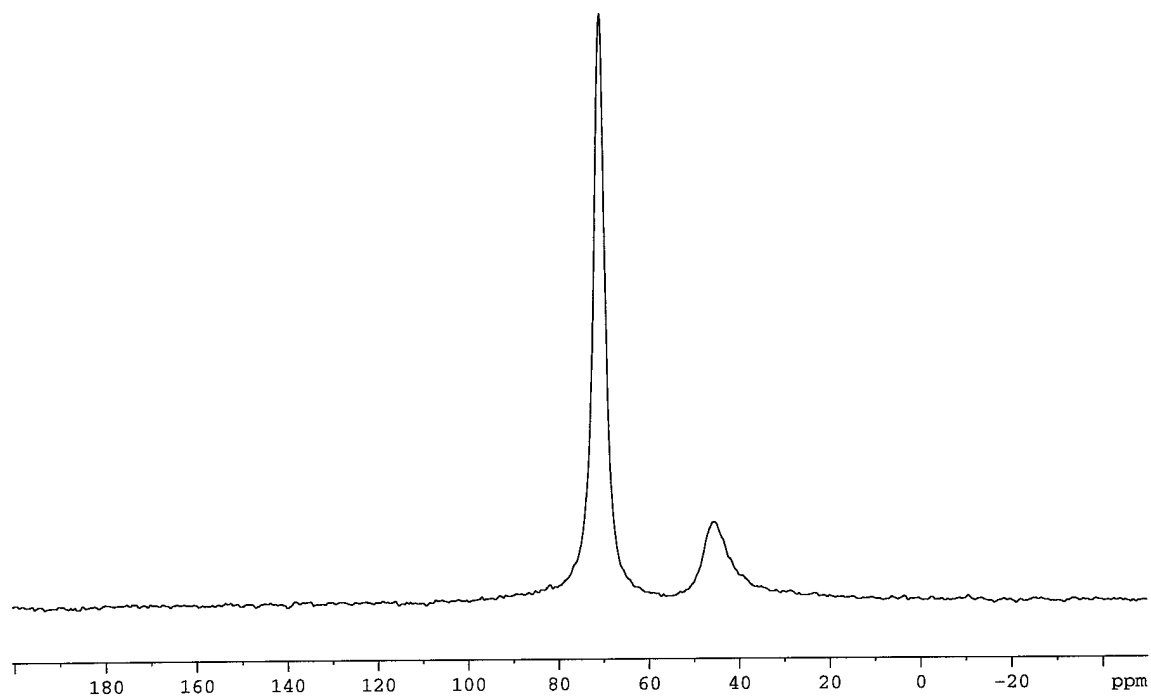


Figure 7.20 ^{17}O NMR spectrum of melt containing 75 mM oxide at 85 °C. This sample contained 15 mM Al_2Cl_7^- using the original stock solution compositions and 34 mM Al_2Cl_7^- using the modified stock solution compositions. The portion of the sample which was characterized using normal pulse voltammetry had a current of 0.39 μA for aluminum deposition.

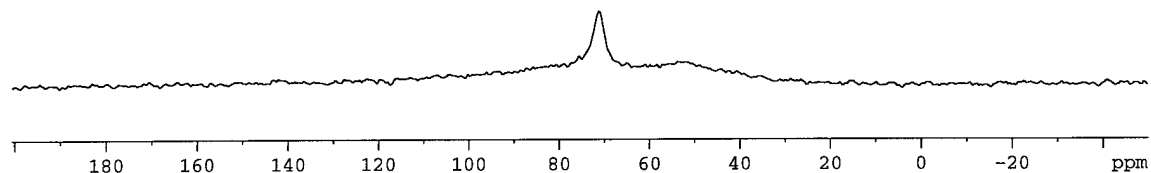


Figure 7.21 ^{17}O NMR spectrum of melt containing 75 mM oxide at 85 °C. This sample contained 0 mM Al_2Cl_7^- using the original stock solution compositions and 19 mM Al_2Cl_7^- using the modified stock solution compositions. The portion of the sample which was characterized using normal pulse voltammetry had a current of 0 μA .

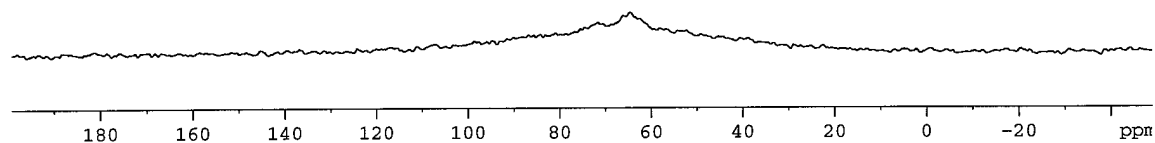


Figure 7.22 ^{17}O NMR spectrum of melt containing 75 mM oxide at 85 °C. This sample contained 5 mM Cl^- using the original stock solution compositions and 14 mM Al_2Cl_7^- using the modified stock solution compositions. The portion of the sample which was characterized using normal pulse voltammetry had a current of 0 μA .

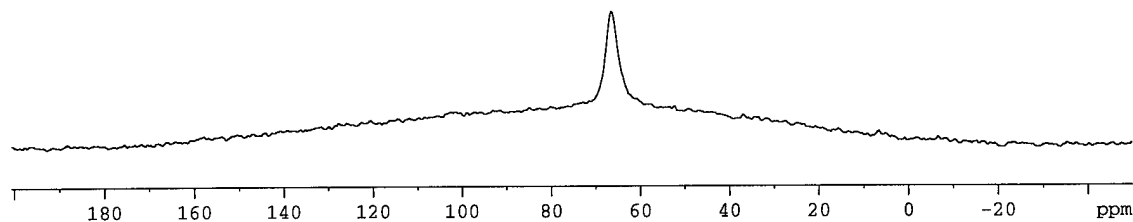


Figure 7.23 ^{17}O NMR spectrum of melt containing 75 mM oxide at 85 °C. This sample contained 15 mM Cl^- using the original stock solution compositions and 4 mM Al_2Cl_7^- using the modified stock solution compositions. The portion of the sample which was characterized using normal pulse voltammetry had a current of 1.32 μA for chloride oxidation.

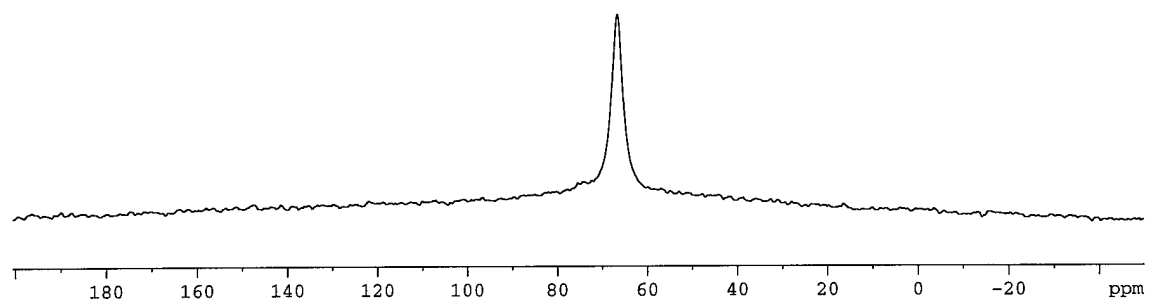


Figure 7.24 ^{17}O NMR spectrum of melt containing 75 mM oxide at 85 °C. This sample contained 25 mM Cl^- using the original stock solution compositions and 5 mM Cl^- using the modified stock solution compositions. The portion of the sample which was characterized using normal pulse voltammetry had a current of 8.78 μA for chloride oxidation.

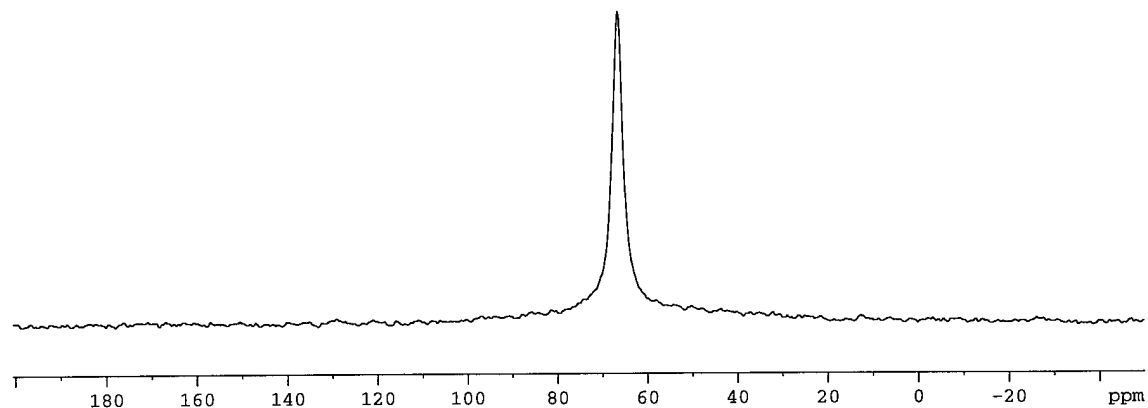


Figure 7.25 ^{17}O NMR spectrum of melt containing 75 mM oxide at 85 °C. This sample contained 44 mM Cl^- using the original stock solution compositions and 24 mM Cl^- using the modified stock solution compositions. The portion of the sample which was characterized using normal pulse voltammetry had a current of 16.38 μA for chloride oxidation.

As the Al_2Cl_7^- concentration is decreased the ^{17}O NMR peak at ≈ 90 ppm becomes smaller. At the same time other oxide species and the hydroxide species remain essentially constant in size. This upfield peak disappears at the same time the aluminum deposition current goes to zero. As the melt becomes more basic the remaining two peaks broaden until they are replaced by the oxide peak associated with basic melts. As the oxide peak associated with basic melts appears, the chloride oxidation becomes possible.

7.4 Conclusions

It appears that the buffering of room temperature molten salts with oxide is not actually due to an aluminum oxychloride species but to the aluminum hydroxychloride species. The parallel electrochemical and NMR experiments show that aluminum is not deposited until the species associated with the 90 ppm peak is present. Aluminum is not deposited when only the hydroxide or oxide species associated with the 73 ppm peak are present. The buffering capacity measured using normal pulse voltammetry is in error. The buffering capacity was based upon the total concentration of oxide species present. In order to assess the buffering capacity the aluminum hydroxychloride concentration would have to be determined. A rough estimate of the area under the ^{17}O NMR peak at 73 ppm is about 1/5 of the total. This would explain the buffering capacity slope of 1/5. This result is very qualitative and further studies would be necessary to test this premise.

The NMR experiments also offer an explanation for the offset in melt composition experienced with the electrochemical experiments. The inability to remove all the aluminum hydroxychloride leads to a melt that has more chloride than would be expected. The additional chloride causes the melt to be more basic.

Chapter 7 References

- (1) Linga, H.; Stojek, Z.; Osteryoung, R. A. "Electrochemistry of Titanium(IV) in Basic n-Butylpyridinium Chloride-Aluminum Chloride in the Presence of Oxide" *J. Am. Chem. Soc.* **1981**, *103*, 3754-3760.
- (2) Karpinski, Z. J.; Nanjundiah, C.; Osteryoung, R. A. "Electrochemical Studies of Ferrocene and Ferrocinium Ion in Aluminum Chloride-N-1-Butylpyridinium Chloride Ionic Liquid" *Inorg. Chem.* **1984**, *23*, 3358-3364.
- (3) Sun, I. W.; Ward, E. H.; Hussey, C. L. "Reactions of Phosgene with Oxide-Containing Species in a Room-Temperature Chloroaluminate Ionic Liquid" *Inorg. Chem.* **1987**, *26*, 4309-4311.
- (4) Scheffler, T. B.; Hussey, C. L.; Seddon, K. R.; Kear, C. M.; Armitage, P. D. "Molybdenum Chloro Complexes in Room-Temperature Chloroaluminate Ionic Liquids: Stabilization of $[\text{MoCl}_6]^{2-}$ and $[\text{MoCl}_6]^{3-}$ " *Inorg. Chem.* **1983**, *22*, 2099-2100.
- (5) Sun, I. W.; Hussey, C. L. "Electrochemistry of Niobium Chloride and Oxide Chloride Complexes in Basic Aluminum Chloride-1-Methylethylimidazolium Chloride Room-Temperature Ionic Liquid" *Inorg. Chem.* **1989**, *28*, 2731-2737.

- (6) Stojek, Z.; Linga, H.; Osteryoung, R. A. "A Titration Procedure for the Determination of Oxide in Basic n-Butylpyridinium Chloride Aluminum Chloride Melts" *J. Electroanal. Chem.* **1981**, *119*, 365-370.
- (7) Zawodzinski, T. A. Jr.; Carlin, R. T.; Osteryoung, R. A. "Removal of Protons from Ambient-Temperature Chloroaluminate Ionic Liquids" *Anal. Chem.* **1987**, *59*, 2639-2640.
- (8) Zawodzinski, T. A. Jr.; Osteryoung, R. A. "Oxide and Hydroxide Species Formed on Addition of Water in Ambient-Temperature Chloroaluminate Melts: An ^{17}O NMR Study" *Inorg. Chem.* **1990**, *29*, 2842-2847.
- (9) Noël, M. A.; Trulove, P. C.; Osteryoung, R. A. "Removal of Protons from Ambient-Temperature Chloroaluminate Ionic Liquids" *Anal. Chem.* **1991**, *63*, 2892-2896.
- (10) Abdul-Sada, A. K.; Avent, A. G.; Parkington, M. J.; Ryan, T. A.; Seddon, K. R.; Welton, T. "The Removal of Oxide Impurities from Room Temperature Halogenoaluminate Ionic Liquids" *J. Chem. Soc., Chem. Commun.* **1987** 1643-1644.

- (11) Sun, I. W.; Ward, E. H.; Hussey, C. L. "Reactions of Phosgene with Oxide-Containing Species in a Room-Temperature Chloroaluminate Ionic Liquid" *Inorg. Chem.* **1987**, *26*, 4309-4311.
- (12) Ackerman, B. L.; Tsarbopoulos, A.; Allison, J. "Fast Atom Bombardment Mass Spectrometric Studies of the Aluminum Chloride/n-Butylpyridinium Chloride Molten Salt." *Anal. Chem.*, **1985**, *57*, 1766-1768.
- (13) Franzen, G.; Gilbert, B. P.; Pelzer, G.; DePauw, E. "The Anionic Structure of Room-temperature Organic Chloroaluminate Melts from Secondary Ion Mass Spectrometry" *Org. Mass Spectrom.* **1986**, *21*, 443-444.
- (14) Wicelinski, S. P.; Gale, R. J.; Pamidimukkala, K. M.; Laine, R. A. "Fast Atom Bombardment Mass Spectrometry of Low Temperature Chloroaluminate and Chlorogallate Melts" *Anal. Chem.* **1988**, *60*, 2228-2832.
- (15) Abdul-Sada, A. K.; Greenway, A. M.; Seddon, K. R.; Welton, T. "Upon the existence of $[\text{Al}_3\text{Cl}_{10}]^-$ in Room Temperature Chloroaluminate Ionic Liquids" *Org. Mass Spectrom.* **1989**, *24*, 917-918.
- (16) Abdul-Sada, A. K.; Greenway, A. M.; Seddon, K. R.; Welton, T. "A Fast Atom Bombardment Mass Spectrometric Study of Room-temperature 1-Ethyl-3-methylimidazolium Chloroaluminate(III) Ionic Liquids. Evidence for

the Existence of the Decachlorotrialuminate(III) Ion" *Org. Mass Spectrom.* **1993**, 28, 759-765.

(17) Zawodzinski, T. A. Jr.; Osteryoung, R. A. "Aspects of the Chemistry of Water in Ambient-Temperature Chloroaluminate Ionic Liquids: ^{17}O NMR Studies" *Inorg. Chem.* **1987**, 26, 2920-2922.

(18) Zawodzinski, T. A. Jr.; Osteryoung, R. A. "The Chemistry of Water in Ambient-Temperature Chloroaluminate Ionic Liquids: NMR Studies" In *Proceedings of the Joint International Symposium on Molten Salts*. Proceedings Vol 87-7, The Electrochemical Society: Penning, New Jersey, pp. 406-413.

(19) Summers, J.; Osteryoung, R. A., North Carolina State University, unpublished results.

(20) Carlin, R. T.; Crawford, W.; Bersch, M. "Nucleation and Morphology Studies of Aluminum Deposited from an Ambient-Temperature Chloroaluminate Molten Salt" *J. Electrochem. Soc.* **1992**, 139, 2720-2727.

(21) Noël, M. A. M.; Trulove, P. C.; Osteryoung, R.A. "Removal of Protons from Ambient-Temperature Chloroaluminate Ionic Liquids" *Anal. Chem.* **1991**, 63, 2892-2896.

Chapter 8

Fast Square Wave Voltammetry of Cu(I/II) in Chloroaluminate Molten Salts

8.1 Introduction

The work within this chapter was carried out for several reasons. The first reason was to verify the kinetic parameters determined in chapter six using a more modern potentiostat. Secondly, because Cu(I) is a well behaved couple in the molten salts it provided an ideal model system to test the limitations of square wave voltammetry in the melts. Third, this chapter provides an outline of the many experimental details a researcher must consider in order to obtain quality electron transfer parameters especially when one is pushing the envelope for a given technique.

8.1.1 Electrochemistry of the Cu(I)/(II) Couple

The electrochemical behavior of the Cu(I)/(II) couple in 1.5:1.0 chloroaluminate molten salts has been studied in detail and is very well behaved. The diffusion coefficient is $6.8 \times 10^{-7} \text{ cm}^2/\text{sec}$, $\beta = 0.5$, $E_{1/2} = 1.94 \text{ V}$ vs. an Al(0)/Al(III) reference, and $k_a^\circ = 0.1 \text{ cm/sec}$.¹ These factors make this couple an ideal choice to test the limits of square wave voltammetry in the

melts. For a complete discussion the reader is referred to Chapter 6 where the electron transfer kinetics are presented.

8.1.2 Square Wave Voltammetry

Square wave voltammetry is a differential pulse voltammetric technique. The theory and experiment have been thoroughly characterized and are discussed in detail in several articles including a review.²⁻⁵ The square wave voltammetric waveform combines large-amplitude square wave modulation with a staircase waveform. The resulting net current is a true differential signal and allows excellent sensitivity and rejection of background current.^{3,5} For a reversible couple using a square wave amplitude of 50 mV, 93 % of the current that would be observed in a normal pulse experiment is detected.^{3,5} The square wave voltammogram only takes a small fraction of the time it would take to conduct the normal pulse experiment. This allows for multiple scans for signal averaging to be taken in a reasonable time period.

The theory for the determination of kinetic parameters for quasi-reversible couples as well those that have CE or EC mechanisms has been published.⁴ When the couple appears reversible the net current is a symmetrical peak. If the couple is quasi-reversible and α is not 0.5 then the symmetry of the peak is destroyed. The shape and observed current using square wave voltammetry are not only a function of the electron transfer parameters, but are also a function of the experimental parameters used to obtain the voltammogram.

$$i = \left[\frac{n F A D^{1/2} C^*}{\sqrt{\pi t_p}} \right] \psi(\Delta E_s, E_{sw}) \quad (8.1)$$

In Equation 8.1, i is the measured current, F is Faraday's constant, A is the area of the electrode, D is the diffusion coefficient, C^* is the concentration of the electroactive species in solution, t_p is the pulse width, and ψ is the dimensionless current function. The dimensionless current function is a shape factor that is dependent on ΔE_s , the step height, and E_{sw} , the square wave amplitude.⁴ The variable parameters that govern the response to the square wave experiment are the step height (ΔE_s) the square wave amplitude (E_{sw}) and the pulse width (t_p). For reversible and quasi-reversible couples the optimum square wave amplitude has been established to be $50/n$ mV (n is the number of electrons transferred) and the step height has been established to be 10 mV.⁴ These parameters have been chosen to maximize current response without broadening the current peak and also to ensure adequate resolution of the current response. The pulse width (pulse time) is a function of the square wave frequency.

$$t_p = \frac{1}{\left(2 * \text{Square Wave Frequency} \right)} \quad (8.2)$$

For a quasi-reversible reaction scheme electron transfer kinetics can be specified with the dimensionless parameter $\kappa * \text{sqrt}(1/\text{square wave frequency})$. κ is the effective rate constant for charge transfer with the units $s^{-1/2}$. When $\kappa * \text{sqrt}(1/\text{square wave frequency}) \gg 1$ the reaction appears reversible; when $\kappa *$

$\sqrt{1/\text{square wave frequency}} \ll 1$ then the electron transfer appears totally irreversible.⁴ Generally kinetic data can be extracted from the range $-1 = \log(\kappa * \sqrt{1/\text{square wave frequency}})$ to $1 = \log(\kappa * \sqrt{1/\text{square wave frequency}})$.⁴ Using the experimentally determined κ of ≈ 121 for the Cu(I)/Cu(II) couple (Chapter 6), and substituting into the two limiting equations just discussed, the range of square wave frequencies of interest to determine the kinetics of electron transfer is from 0.146 kHz to 1460 kHz. The region of frequency space which would cause the largest changes in the peak height is 14.6 kHz. This is $0 = \log(\kappa * \sqrt{1/\text{square wave frequency}})$.

8.2 Specialized Experimental Procedures

8.2.1 Materials

Cu(I)Cl (99+ % Aldrich) was used without further purification. The melts used in this chapter were 1.5:1.0 mole ratio melts.

8.2.2 Equipment and Procedures

8.2.2.1 Potentiostat Frequency Response

In order to determine the frequency response of the test-bed PAR EG&G 283 potentiostat the potentiostat was hooked together with a Hewlett Packard 3312A function generator, an 1191 General Radio counter (frequency counter), and an HP 3456A Hewlett Packard digital volt meter. A 1.0 k Ω resistor was connected between the reference electrode and counter electrode leads and the working electrode and sense leads (Figure 8.1) A sinusoid function was selected on the function generator and the frequency varied for each current range on the potentiostat. At each frequency the frequency was read from the frequency counter and the root mean square voltage recorded from the digital voltmeter directly from the function generator and then from the potentiostat.

8.2.2.2 RC Time Constants

The RC time constants were measured for the tungsten microelectrodes in unadulterated 1.5:1.0 melt. The diameters of the tungsten microdisk electrodes were: 4 μm , 9 μm , 21 μm , 42.5 μm , 68 μm , and 100 μm . The Quatek analog to digital converter does not have adequate bandwidth to make these measurements. When the measurements were attempted using this analog to digital converter the entire RC decay was only described by 3 to 5 data points. In order to adequately describe the RC decay a digital oscilloscope was

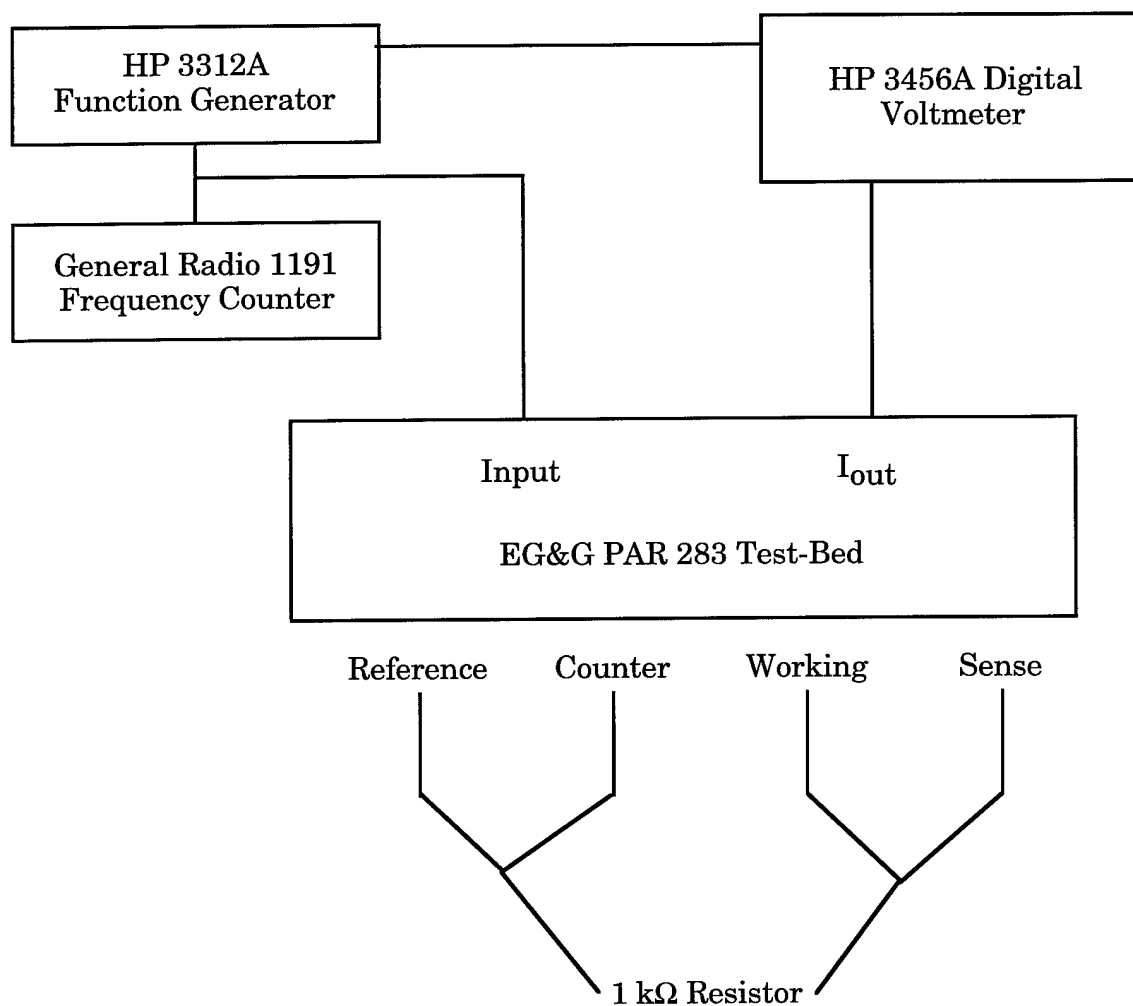


Figure 8.1 Experimental setup to determine the frequency response of the EG&G PAR 283 Test-bed potentiostat.

employed to capture the RC decay.

In these series of experiments two 486 personal computers were used. One personal computer was used to control the potentiostat while the other was used to collect data from the oscilloscope through an GPIB interface (Figure 8.2). In order to collect the data the potentiostat was used to perform a double potential step chronoamperometry experiment in which the potential was moved from 1.6 to 2.3 V vs. the aluminum reference electrode. The step served as a trigger for the oscilloscope which captured the current decay. The other computer then collected the data from the oscilloscope. This was allowed to occur 100 times and the results were signal averaged to reduce the noise. This experiment was conducted with various current ranges on the potentiostat to try and avoid bias caused by the RC time constant of the electronics in the potentiostat. In some cases as the potentiostat current range was increased the RC time constant became shorter and then was constant. In these cases the RC time constant observed for the smaller current ranges was assumed to have been biased by potentiostat RC time constant for that current range and was discarded.

Once the data had been acquired it was analyzed using FSQPLT, an in-house data-analysis program. The data were fit to a simple exponential decay.

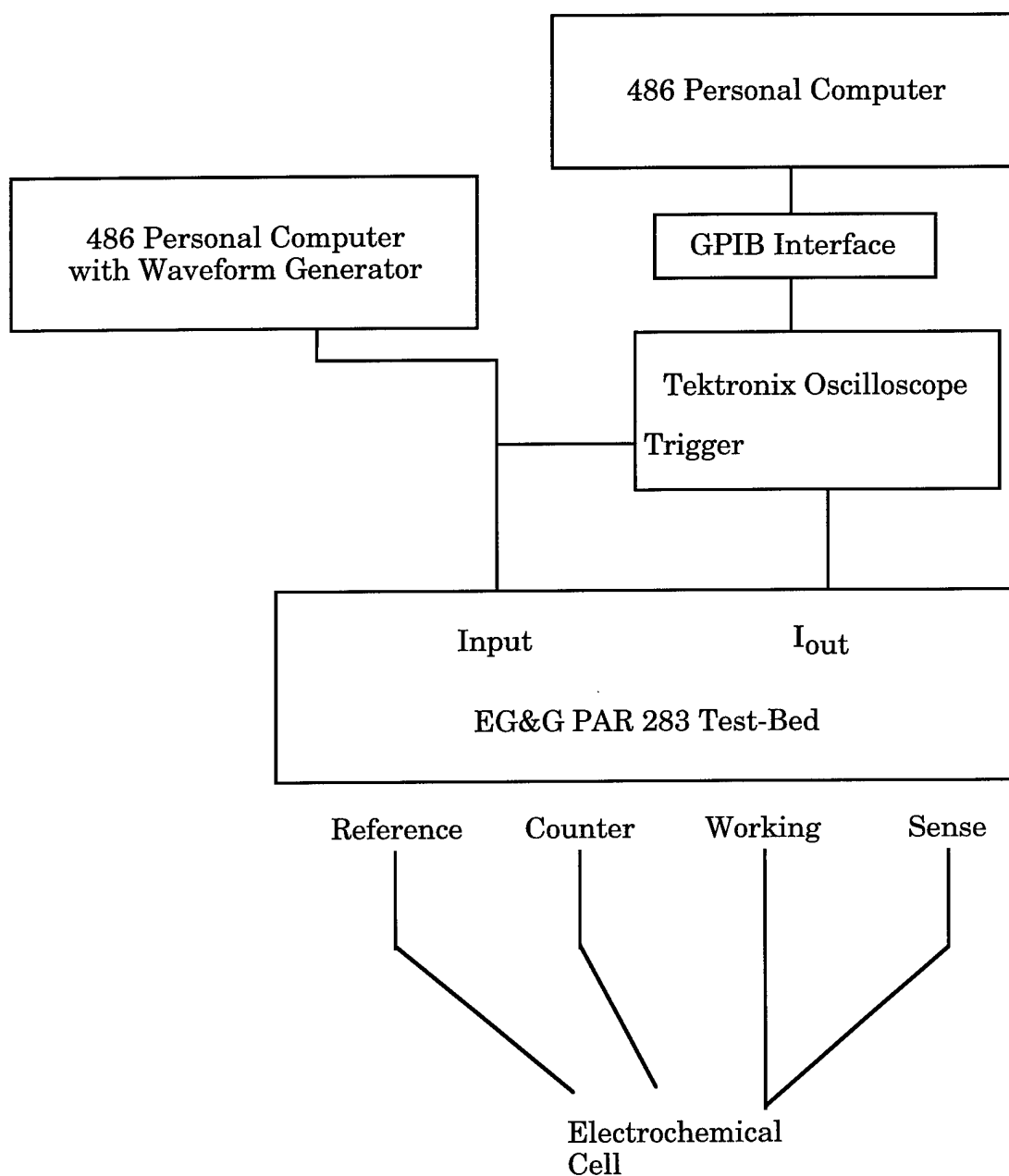


Figure 8.2 Experimental setup to determine the RC time constant of the tungsten microdisk electrodes.

8.2.2.3 Square Wave Voltammetry

Results were obtained using a test-bed PAR EG&G 283 potentiostat. The PAR 283 was coupled to a QuaTech digitizer and a waveform generator both housed within a single 486 personal computer. The PAR EG&G 283 is capable of square wave voltammetry at much higher frequencies than Mr.Coffee II, a home built potentiostat, which was limited to square wave frequencies of ≈ 80 kHz.⁶⁻⁸

Electrochemical experiments were conducted in a sealed cell constructed of an EG&G PAR 303A static mercury drop electrode glass, a Viton gasket, and a custom built cell holder (Figure 8.3). Holes were drilled through the gasket to accommodate two working electrodes, a reference electrode and a platinum counter electrode. The counter electrode consisted of a 1 mm platinum wire and the reference consisted of an aluminum wire in a 1.5:1.0 melt (Table 8.1). Several tungsten microdisk working electrodes were used in this study. The diameters of the tungsten microdisk electrodes were: 4 μm , 9 μm and 21 μm . Each working electrode was polished with a diamond suspension prior to use. The cell in Figure 8.3 is assembled in a dry box and then removed so experiments can be conducted outside the dry box. During the course of the electrochemical experiments the cell is enclosed in a Faraday cage. The temperature inside the Faraday cage was monitored. The temperature only fluctuated between 24 and 27 °C.

Prior to the acquisition of electrochemical data each working electrode

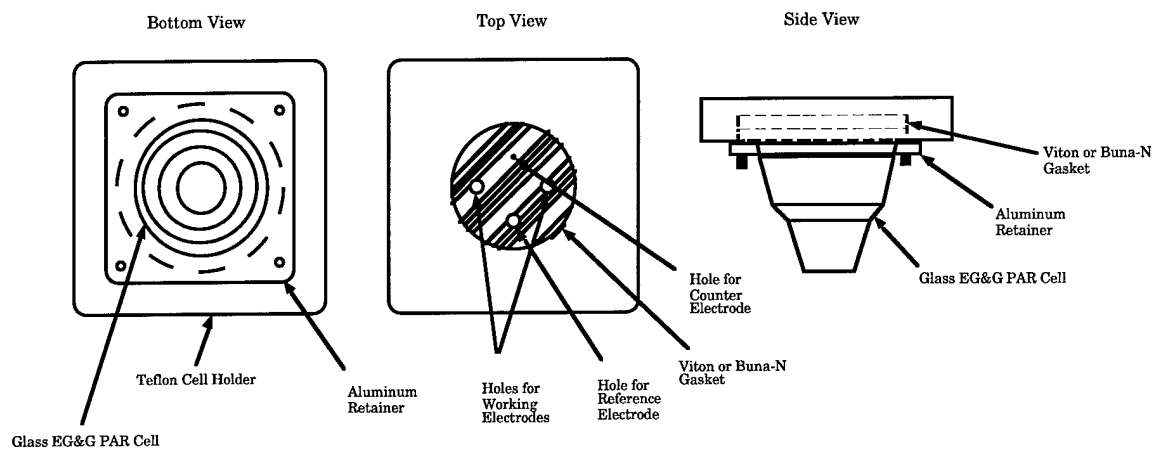


Figure 8.3 Sealed electrochemical cell used for the Cu(I)/(II) square wave measurements in a 1.5:1.0 melt.

Square Wave Experimental Parameters
20 mM Cu(I) in a 1.5:1.0 Melt
Temperature 24 to 27 °C
Voltammetry Conducted in Sealed Cell in Faraday Cage
Tungsten Microdisk Working Electrode
Aluminum Wire in 1.5:1.0 Melt Reference Electrode
Platinum Wire Loop Counter Electrode
10 mV Step Height
50 mV Square Wave Amplitude
Scanned from 1.6 to 2.3 V
Default Potential 1.6 V
1 second Delay Between Scans
100 Scans acquired for Signal Averaging

Table 8.1 Experimental Parameters used in square wave voltammetry study.

was electrochemically cleaned by cycling into the AlCl_4^- oxidation wave using cyclic staircase voltammetry. Three scans were performed with a scan rate of 500 mV / sec from 1 to 3 volts versus the $\text{Al}(0) / \text{Al}(\text{III})$ reference.⁹ After the electrochemical cleaning a test square wave voltammogram was acquired in order to monitor the performance of the system as experiments were conducted. These voltammograms were acquired with a 10 mV step, 50 mV peak to peak square wave amplitude, and a square wave frequency of 1000 Hz. During the course of a set of experiments several 'test' square wave voltammograms were obtained with the same parameters as the first. These voltammograms were then compared to check for system degradation.

A 1.5:1.0 melt was prepared and a portion was used to prepare a 20 mM solution of $\text{Cu}(\text{I})$ chloride. Experiments were conducted using WOTAN, an in-house experimental control and data-acquisition software package. Two series of square wave voltammetry experiments were run for the electrodes. The first series of experiments used melt that contained $\text{Cu}(\text{I})$ while the second identical series contained pure melt. The second series thus provided background voltammograms that had been acquired using the same experimental parameters and cell geometry.

Once the electrochemical data had been acquired it was analyzed using FSQPLT, an in-house data analysis program. This program uses the "COOL" algorithm to determine electron transfer parameters.¹⁰ The COOL algorithm is discussed more fully in Chapter 6 and the reader is referred there for additional information.

8.3 Results and Discussion

8.3.1 Potentiostat Frequency Response

The frequency data are taken as the root mean square (rms) voltage directly measured from the function generator and the rms voltage from the potentiostat. The data are then normalized by dividing the rms voltage from the potentiostat by the rms voltage from the waveform generator. This removes error caused by variations in the signal from the function generator. Next the data are scaled so that the response seen at very low values is set equal to 1. Lastly, the normalized and scaled response is converted into Decibels (Tables 8.2 to 8.6).

$$\text{Db} = 20 \log_{10}(\text{scaled response}) \quad (8.3)$$

After the data have been converted into Decibels the frequency response of each current range can be plotted as a function of frequency (Figure 8.4). Figure 8.4 is known as a Bode plot and shows in detail that each current range begins to attenuate the sinusoidal signal at different frequencies. It can also be seen that the higher current ranges do not attenuate the sinusoidal signal until higher frequencies are reached. In addition the higher current ranges, the 1 and 10 μA current ranges, show atypical frequency responses before they begin to attenuate the sinusoidal signal. This is not surprising when one considers the numbers and variety of components used to construct the detection circuits in a potentiostat.

Frequency (kHz)	Potentiostat Output	Function Generator Output	Normalized	Scaled	dB
0.035	3.160	0.001	5745.455	1.000	0.000
0.072	2.930	0.001	5232.143	0.911	-0.813
0.102	3.070	0.001	5482.143	0.954	-0.407
0.191	2.800	0.001	5000.000	0.870	-1.207
0.314	2.720	0.001	4857.143	0.845	-1.459
0.401	4.640	0.001	6270.270	1.091	0.759
0.520	2.450	0.001	4454.545	0.775	-2.210
0.618	4.090	0.001	5527.027	0.962	-0.337
0.717	2.280	0.001	4071.429	0.709	-2.992
0.908	3.470	0.001	4689.189	0.816	-1.765
1.010	2.050	0.001	3660.714	0.637	-3.915
1.041	3.280	0.001	4432.432	0.771	-2.254
3.164	1.560	0.001	2785.714	0.485	-6.288
3.254	1.950	0.001	2671.233	0.465	-6.652
10.120	1.630	0.001	2295.775	0.400	-7.968
32.303	1.600	0.001	2253.521	0.392	-8.129
100.365	1.600	0.001	2352.941	0.410	-7.754
326.189	1.550	0.001	2870.370	0.500	-6.028

Table 8.2 EG&G Par 283 Test-bed 283 potentiostat frequency response using a 1 k Ω resistor and a current range of 1 nA.

Frequency (kHz)	Potentiostat Output	Function Generator Output	Normalized	Scaled	dB
0.033	2.690	0.003	996.296	1.000	0.000
0.094	2.580	0.003	992.308	0.996	-0.035
0.097	2.609	0.003	1007.336	1.011	0.096
0.113	2.586	0.003	994.615	0.998	-0.015
0.275	2.594	0.003	1005.426	1.009	0.079
0.331	2.570	0.003	992.278	0.996	-0.035
0.411	2.568	0.003	991.506	0.995	-0.042
0.413	2.587	0.003	1006.615	1.010	0.089
0.615	2.572	0.003	1000.778	1.004	0.039
0.616	2.553	0.003	985.714	0.989	-0.093
0.800	2.561	0.003	988.803	0.992	-0.066
0.810	2.536	0.003	979.151	0.983	-0.151
0.905	2.528	0.003	976.062	0.980	-0.178
1.009	2.533	0.003	985.603	0.989	-0.094
1.035	2.512	0.003	969.884	0.973	-0.233
1.800	2.427	0.003	944.358	0.948	-0.465
1.877	2.399	0.003	929.845	0.933	-0.600
2.526	2.288	0.003	890.272	0.894	-0.977
2.540	2.299	0.003	898.164	0.902	-0.901
3.100	2.196	0.003	861.176	0.864	-1.266
3.260	2.155	0.003	841.797	0.845	-1.464
5.206	1.823	0.003	723.571	0.726	-2.778
10.206	1.188	0.002	480.850	0.483	-6.328
14.120	0.896	0.002	367.131	0.368	-8.671
18.950	0.665	0.002	275.768	0.277	-11.157
32.500	0.360	0.002	152.542	0.153	-16.300
101.700	0.168	0.002	74.444	0.075	-22.531

Table 8.3 EG&G Par 283 Test-bed 283 potentiostat frequency response using a 1 k Ω resistor and a current range of 10 nA.

Frequency (kHz)	Potentiostat Output	Function Generator Output	Normalized	Scaled	dB
0.030	2.516	0.025	99.525	1.000	0.000
0.101	2.396	0.024	99.460	0.999	-0.006
0.321	2.394	0.024	99.460	0.999	-0.006
1.003	2.390	0.024	99.376	0.999	-0.013
3.257	2.392	0.024	99.377	0.999	-0.013
10.142	2.366	0.024	98.666	0.991	-0.075
19.460	2.273	0.024	94.962	0.954	-0.408
23.737	2.195	0.024	91.824	0.923	-0.700
32.339	1.971	0.023	85.704	0.861	-1.299
51.977	1.350	0.024	57.163	0.574	-4.816
100.730	0.577	0.023	25.083	0.252	-11.971

Table 8.4 EG&G Par 283 Test-bed 283 potentiostat frequency response using a 1 k Ω resistor and a current range of 100 nA.

Frequency (kHz)	Potentiostat Output	Function Generator Output	Normalized	Scaled	dB
0.032	2.640	0.264	10.000	1.000	0.000
0.102	2.531	0.253	10.012	1.001	0.010
0.338	2.529	0.253	10.008	1.001	0.007
1.006	2.527	0.252	10.010	1.001	0.009
3.308	2.534	0.253	10.023	1.002	0.020
10.140	2.558	0.253	10.123	1.012	0.107
33.650	2.809	0.253	11.087	1.109	0.896
51.980	3.096	0.254	12.209	1.221	1.733
75.450	3.440	0.254	13.544	1.354	2.635
100.600	3.609	0.255	14.178	1.418	3.032
121.500	3.521	0.255	13.813	1.381	2.806
139.100	3.335	0.256	13.025	1.302	2.295
162.600	2.993	0.256	11.669	1.167	1.341
201.500	2.443	0.257	9.509	0.951	-0.437
213.500	2.291	0.257	8.917	0.892	-0.996
224.700	2.164	0.257	8.420	0.842	-1.494
251.300	1.894	0.257	7.366	0.737	-2.655
336.200	1.316	0.260	5.071	0.507	-5.898
1021.600	0.200	0.214	0.934	0.093	-20.596

Table 8.5 EG&G Par 283 Test-bed 283 potentiostat frequency response using a 1 k Ω resistor and a current range of 1 μ A.

Frequency (kHz)	Potentiostat Output	Function Generator Output	Normalized	Scaled	dB
0.100	2.502	2.500	1.001	1.000	0.000
0.323	2.500	2.497	1.001	1.000	0.002
1.006	2.498	2.494	1.001	1.000	0.003
3.314	2.506	2.500	1.003	1.002	0.013
10.110	2.528	2.498	1.012	1.011	0.095
33.650	2.756	2.505	1.100	1.099	0.819
101.106	3.893	2.515	1.548	1.546	3.786
201.800	6.046	2.536	2.383	2.381	7.536
257.900	5.538	2.537	2.183	2.181	6.772
343.800	4.107	2.547	1.612	1.611	4.141
416.200	3.385	2.568	1.318	1.317	2.389
496.500	2.818	2.601	1.084	1.082	0.688
539.900	2.579	2.619	0.985	0.984	-0.141
600.200	2.295	2.639	0.870	0.869	-1.223
660.500	2.045	2.640	0.775	0.774	-2.226
730.700	1.773	2.600	0.682	0.681	-3.332
805.100	1.489	2.485	0.599	0.599	-4.456
1020.000	0.930	1.726	0.539	0.538	-5.381

Table 8.6 EG&G Par 283 Test-bed 283 potentiostat frequency response using a 1 k Ω resistor and a current range of 10 μ A.

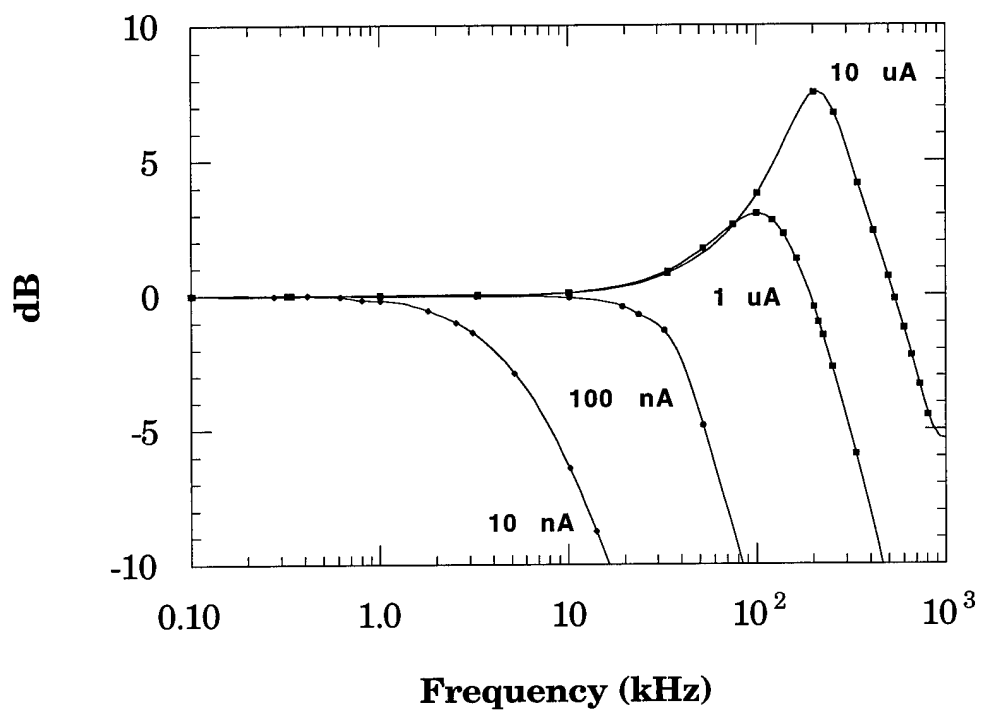


Figure 8.4 Bode plot generated from the data in Tables 8.2 to 8.6. The potentiostat being evaluated is a EG&G PAR 283 test-bed using a 1 k Ω resistor. Lines have been added simply in order to highlight the data.

Another type of plot can be generated from Tables 8.2 to 8.6 (Figure 8.5). This plot simply uses 3 dB as a cutoff. The frequency at which each current range attenuates the sinusoidal signal 3 dB is plotted as a function of frequency. This plot neglects the atypical frequency response for the 1 and 10 μA current ranges but does show that the bandwidth increases ≈ 1 decade for each decade increase in current range.

Several items should be remembered in regard to these plots. First of all, the plots were generated with data obtained using a virtual electrochemical cell consisting of a 1 $\text{k}\Omega$ resistor. The resistor has nominal capacitance and thus it does not approximate a real electrochemical cell to any degree. When a real electrochemical cell is attached to the potentiostat, the change in instrument response cannot be easily calculated. Secondly, even if a cell with nominal capacitance, one that behaved like a resistor, were attached to the potentiostat the sinusoidal response limit is not the same as the square wave response limit. For example the 1 μA current range has a 3 dB cutoff of ≈ 280 kHz for a sinusoidal signal. The square wave cutoff is approximately 1/3 to 1/5 of that, or 70 kHz. The Fourier transform of a square wave of a given frequency has significant frequency components 3 to 5 times above the square wave frequency. Using these parameters the 10 μA current range would have a square wave frequency cutoff of ≈ 180 kHz.

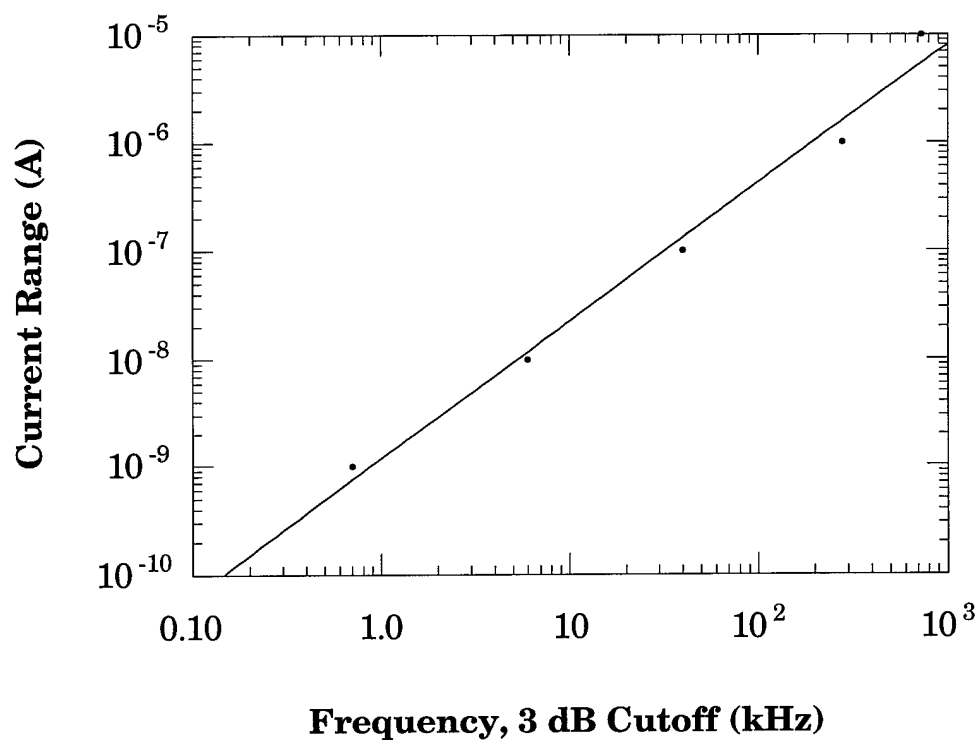


Figure 8.5 Plot of the 3 dB attenuation of a sinusoidal signal at each current range as a function of the signal frequency. The potentiostat being evaluated is a EG&G PAR 283 test-bed using a $1\text{ k}\Omega$ resistor. The line is the least squared fit to the data.

8.3.2 RC Time Constants

The RC time constants for a series of tungsten microdisk electrodes were measured (Figures 8.6 and 8.7 and Table 8.7). The plot of RC time constant vs. the diameter of the electrode is linear as expected. Also one should note that the RC time constants are very short, on the order of a few microseconds.

The RC time constant also effects the maximum square wave frequency. The time it takes for the charging current to decay to 95% of its original current is 3τ . In order to calculate the maximum square frequency that will still allow 3τ to pass before sampling the current the inverse of 3τ is calculated. This converts 3τ into frequency. This frequency must be divided by two because square wave voltammetry samples the current twice during each square wave period. So for a 9 μm diameter electrode the maximum square wave frequency based upon this criteria is 347 kHz, while that for a 21 μm diameter electrode is 166 kHz, and that for a 50 μm diameter electrode is 83 kHz. Given these limitations one must remember that square wave voltammetry is very effective at discriminating against background currents. In addition background subtraction using a blank solution can also minimize this problem.

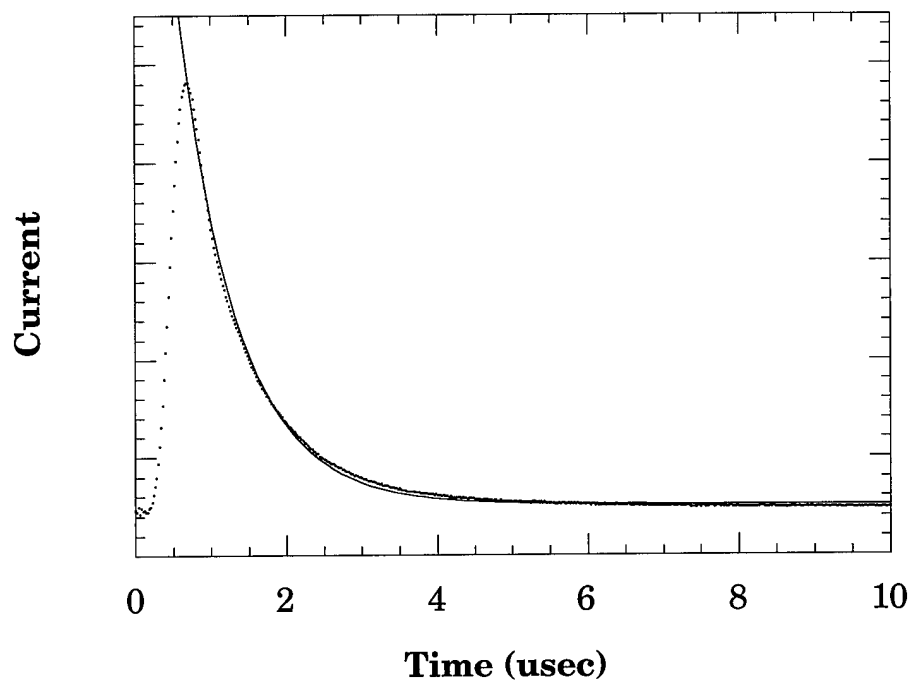


Figure 8.6 Depiction of a typical RC time constant experiment. Time zero is when the pulse is applied. The depicted data is for a 21 μm diameter tungsten electrode in 1.5:1.0 melt. The current range used on the EG&G PAR 283 test-bed potentiostat is 100 μA . The line is the best fit to the data between 0.75 and 10 μsec for an exponential decay.

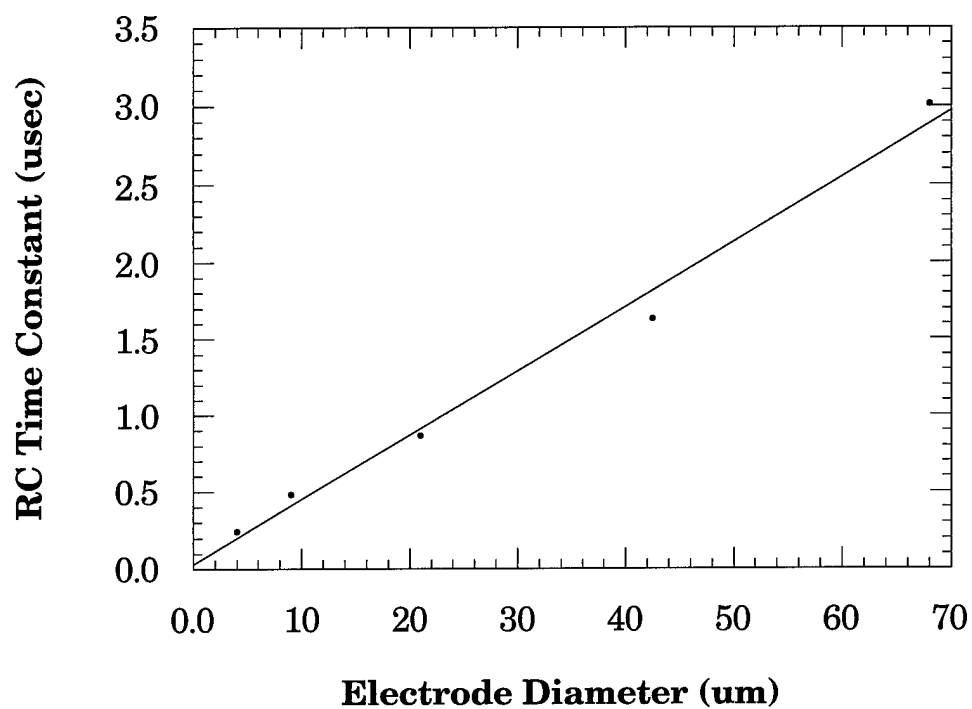


Figure 8.7 Plot of the RC time constant of a series of tungsten microdisk electrodes vs. the electrode diameter. The line is the least squared fit to the data. The RC time constants were measured in a 1.5:1.0 melt.

Electrode Diameter (μm)	RC Time Constant (μsec)
4.0	0.24
9.0	0.48
21.1	0.87
42.5	1.63
68.0	3.01

Table 8.7 Table of the RC time constants for a series of tungsten microdisk electrodes. The RC time constants were measured in a 1.5:1.0 melt.

8.3.3 Square Wave Voltammetry

This high frequency square wave voltammetry work grew directly from the electron transfer kinetics for Cu(I) discussed in Chapter 6. Initial results had been obtained using a home built potentiostat, Mr. Coffee II.^{6,7} The data obtained in Chapter 6 were limited to square wave frequencies of ≈ 80 kHz. This square wave frequency should have been adequate to obtain electron transfer parameter data. However, there was a large region of parameter space above 80 kHz that remained uninvestigated. Because the Cu(I)/(II) couple was well behaved it represented an ideal test case to measure the limits of square wave voltammetry in the melts.

In addition to the potentiostat response and the RC time constant, two other potential experimental interferences must be characterized in order to ensure the obtained square wave voltammetry data are valid. The first results from the use of microelectrodes. Although microelectrodes have advantages for the determination of kinetic parameters they do suffer from non-negligible spherical diffusion. Assuming that a microdisk electrode behaves the same as a microsphere, a crude but valid approximation of the current is given by:¹¹

$$I = \frac{nFADC^*}{r} + \frac{nFAD^{1/2}C^*}{(\pi t)^{1/2}} \quad (8.4)$$

In Equation 8.4 n is the number of electrons transferred per molecule, F is Faraday's constant (C/equiv), D is the diffusion coefficient (cm^2/sec), C^* is the bulk concentration of the electroactive species, r is the radius of the electrode (cm), and t is the time (sec). The first term of Equation 8.4 describes the

spherical component of the diffusion while the second term describes the planar diffusion. By dividing the first term of Equation 8.4 by the full equation the percentage of current due to spherical diffusion can be calculated. For Cu(I) in a 1.5:1.0 melt the spherical contribution is less than 1% for a 10 μm diameter electrode at square wave frequencies above 33 kHz. For a 25 μm diameter electrode the square wave frequency must exceed 5 kHz or spherical diffusion will contribute more than 1% of the current. This is important because the model used by the COOL algorithm does not account for spherical diffusion. If spherical diffusion is contributing significantly to the observed current this would lead to invalid electron transfer kinetic parameters.

The second potential experimental interference is due to IR drop. Although microelectrodes minimize the effects of IR drop, they do not eliminate the problem. Calculating the voltage drop across a solution simply requires the solution resistance and the observed current be known. The specific resistance (ρ) of a 1.5:1.0 melt is 64 $\Omega\text{ cm}$. The resistance = $\rho / (4\pi r_0)$. For a 10 μm diameter electrode $R = 10\text{ k}\Omega$ and for a 25 μm diameter electrode $R = 4\text{ k}\Omega$. The maximum observed current in the square wave voltammograms is $\approx 1\text{ }\mu\text{A}$. Substituting these values into $V = IR$ gives a voltage drop of 10 mV for a 10 μm diameter electrode and 4 mV for for a 20 μm diameter electrode . This IR drop should not significantly affect the observed kinetic data. However, if the observed current were greater, this effect would notably influence the calculated electron transfer parameters.

Square wave voltammetry experiments were attempted at extremely high square wave frequencies, up to 220 kHz. Because of the inability to calculate the potentiostat response in the presence of an electrochemical cell, it was impossible to predict when the electrochemical data would be perturbed by the potentiostat response. It was necessary to obtain voltammograms using the same experimental conditions but using different current ranges. Ideally if the potentiostat electronics were perturbing the observed electrochemical result at low current ranges, raising the current range would eliminate this problem and the 'real' electrochemical result would be observed. Raising the current range further would not influence the results. In reality as the current range is raised for a given signal, underdigitization and digitization noise limit the quality of the observed data.

The compromise that must be made is to use a small enough microelectrode so that the RC time constant does not interfere with the measurements of interest. At the same time a microelectrode large enough that ensure spherical diffusion does not invalidate the results must be used. A large enough microelectrode must be used so a high enough current range can be used to ensure the potentiostat bandwidth is adequate. At the same time the larger microelectrode will increase the effects of IR drop.

To further complicate these issues, the square wave voltammograms can be analyzed several different ways. There are two choices to be made when preparing to model the square wave data. The first is whether to use the net current or the forward and reverse currents. The second is whether to background subtract the voltammograms. The square wave net current helps

discriminate against charging current while the forward and reverse currents still have charging current components. If the background voltammograms can be acquired their subtraction will also discriminate against background current. Rather than attempt to present all the evaluations of the square wave data, two data sets will be presented. Each data set was acquired on a different electrode; however, the background subtracted net currents were evaluated in both cases (Figures 8.8 to 8.15 and Tables 8.8 and 8.9).

The results for both the 21 μm and 9 μm electrodes appear very reasonable with the exceptions of Figures 8.10 and 8.14. These two figures are plots of the slope vs. $1/\sqrt{t_p}$. The slope is a scaling factor that allows the peak current to be compared between voltammograms with different square wave frequencies. It is reasonable to conclude that some interference is altering the observed peak current. This is most likely due to instrumental bandwidth limitations. By raising the current range the bandwidth problem could be avoided but at the same time underdigitization may appear. A simple criterion to determine the optimal current range is to compare the signal to noise for the fitted data. The approach of raising the current range to avoid instrumental bandwidth limitations will only go so far. This limitation is easily seen in Figures 8.10 and 8.14 when the slope stops decreasing with increasing frequency. The data taken at higher frequencies reflect electron transfer combined with some instrumental response function. Obviously these data are not acceptable to determine electron transfer parameters.

Applying the signal to noise criteria and removing those data points, along with removing the data points above the cutoff frequencies from Figures

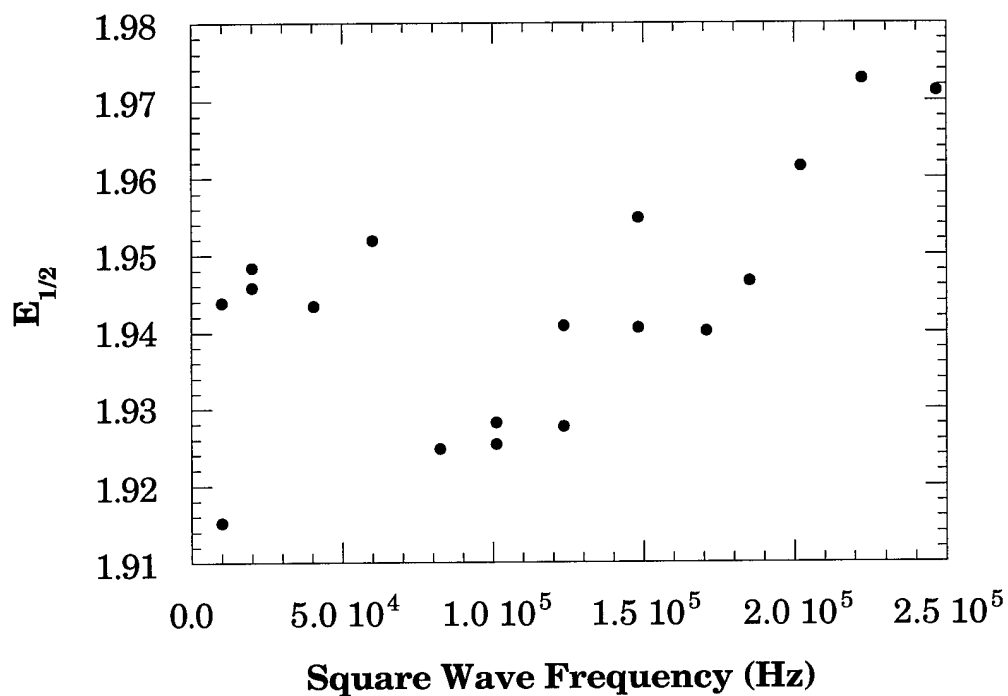


Figure 8.8 $E_{1/2}$ vs. square wave frequency from voltammograms of Cu(I)/Cu(II) in 1.5:1.0 melt using a 9 μm diameter tungsten electrode. Cu(I) concentration is 20.0 mM. Data obtained using quasi-reversible fits of the experimental data, between 1.7 to 2.2 V, from the COOL algorithm.

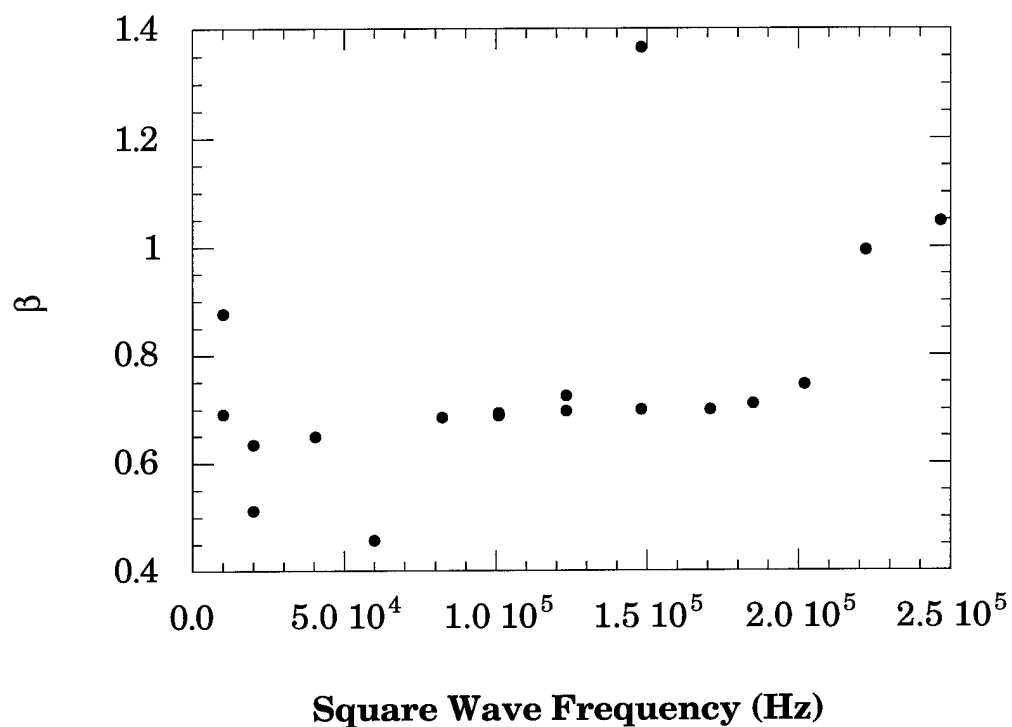


Figure 8.9 β vs. square wave frequency from voltammograms of Cu(I)/Cu(II) in 1.5:1.0 melt using a 9 μm diameter tungsten electrode. Cu(I) concentration is 20.0 mM. Data obtained using quasi-reversible fits of the experimental data, between 1.7 to 2.2 V, from the COOL algorithm.

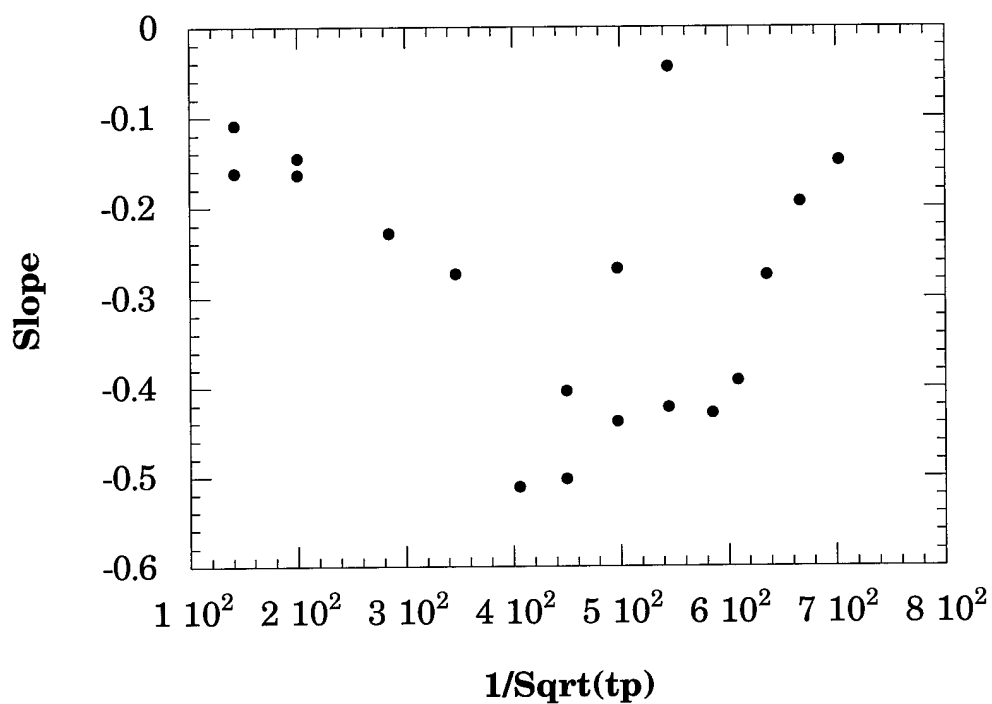


Figure 8.10 Slope vs. $1/\text{sqrt}(t_p)$ from voltammograms of Cu(I)/Cu(II) in 1.5:1.0 melt using a 9 μm diameter tungsten electrode. Cu(I) concentration is 20.0 mM. Data obtained using quasi-reversible fits of the experimental data, between 1.7 to 2.2 V, from the COOL algorithm.

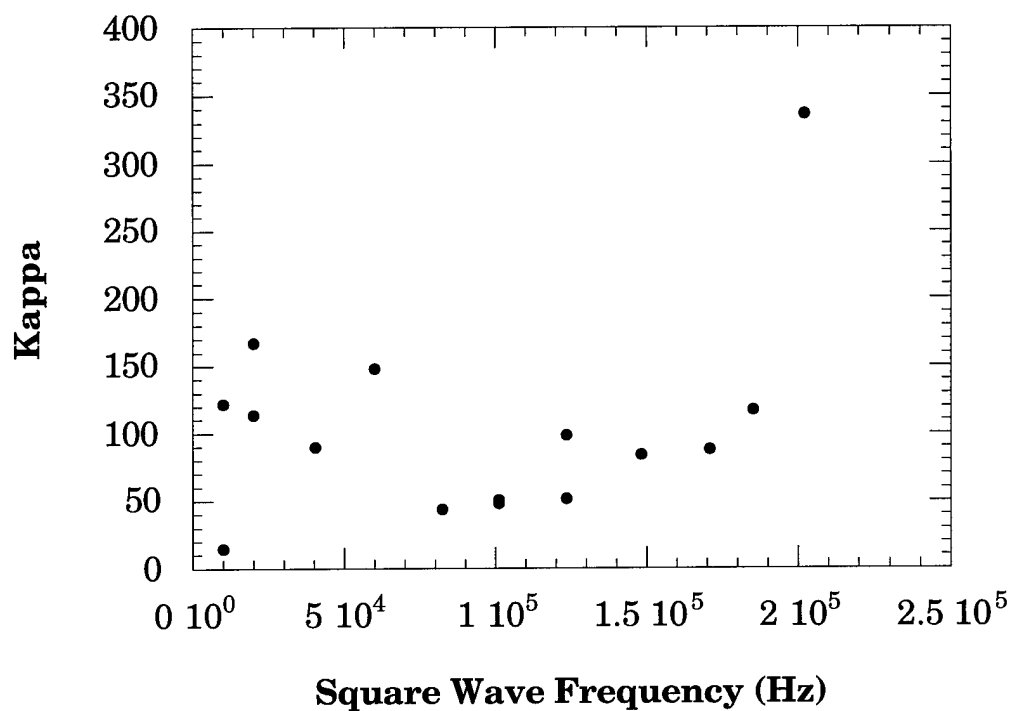


Figure 8.11 κ vs. square wave frequency from voltammograms of Cu(I)/Cu(II) in 1.5:1.0 melt using a 9 μm diameter tungsten electrode. Cu(I) concentration is 20.0 mM. Data obtained using quasi-reversible fits of the experimental data, between 1.7 to 2.2 V, from the COOL algorithm.

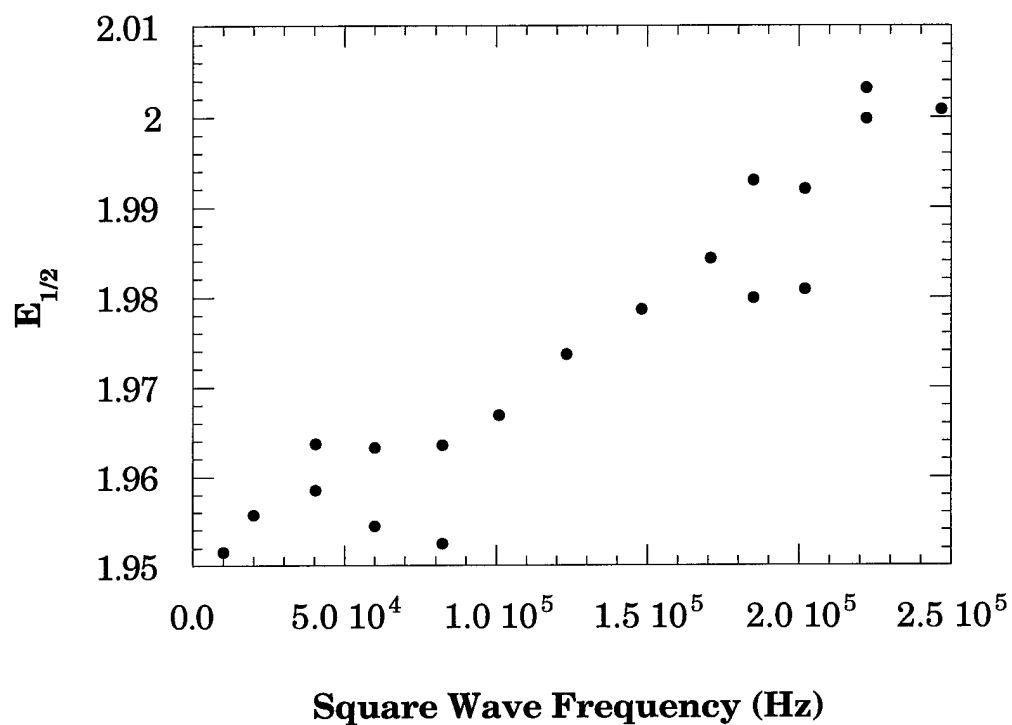


Figure 8.12 $E_{1/2}$ vs. square wave frequency from voltammograms of Cu(I)/Cu(II) in 1.5:1.0 melt using a 21 μm diameter tungsten electrode. Cu(I) concentration is 20.0 mM. Data obtained using quasi-reversible fits of the experimental data, between 1.7 to 2.2 V, from the COOL algorithm.

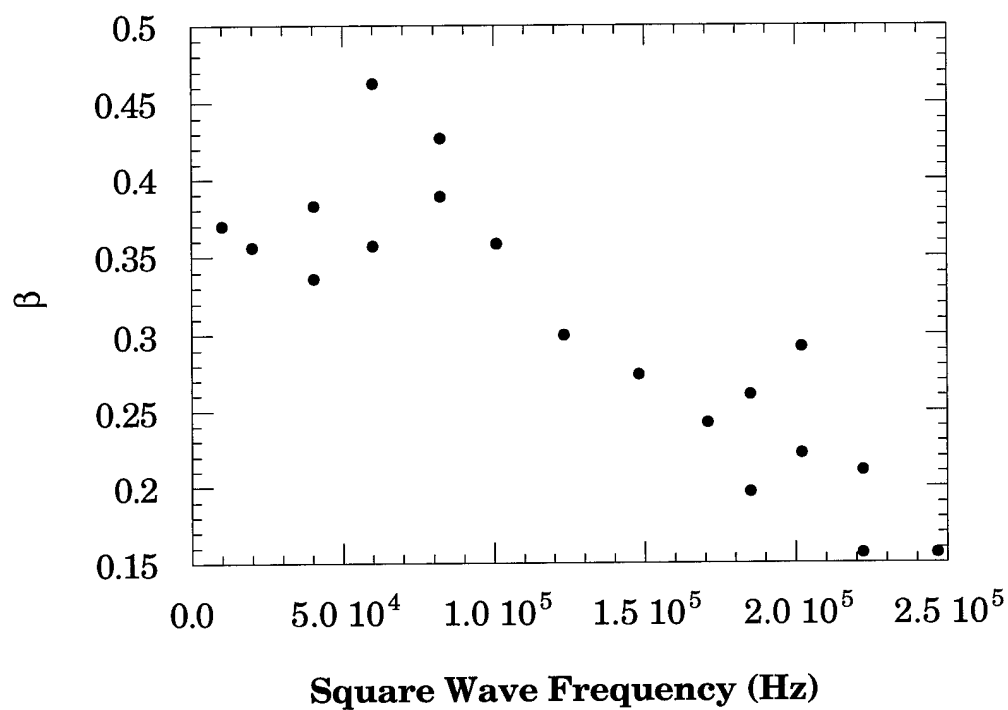


Figure 8.13 β vs. square wave frequency from voltammograms of Cu(I)/Cu(II) in 1.5:1.0 melt using a 21 μm diameter tungsten electrode. Cu(I) concentration is 20.0 mM. Data obtained using quasi-reversible fits of the experimental data, between 1.7 to 2.2 V, from the COOL algorithm.

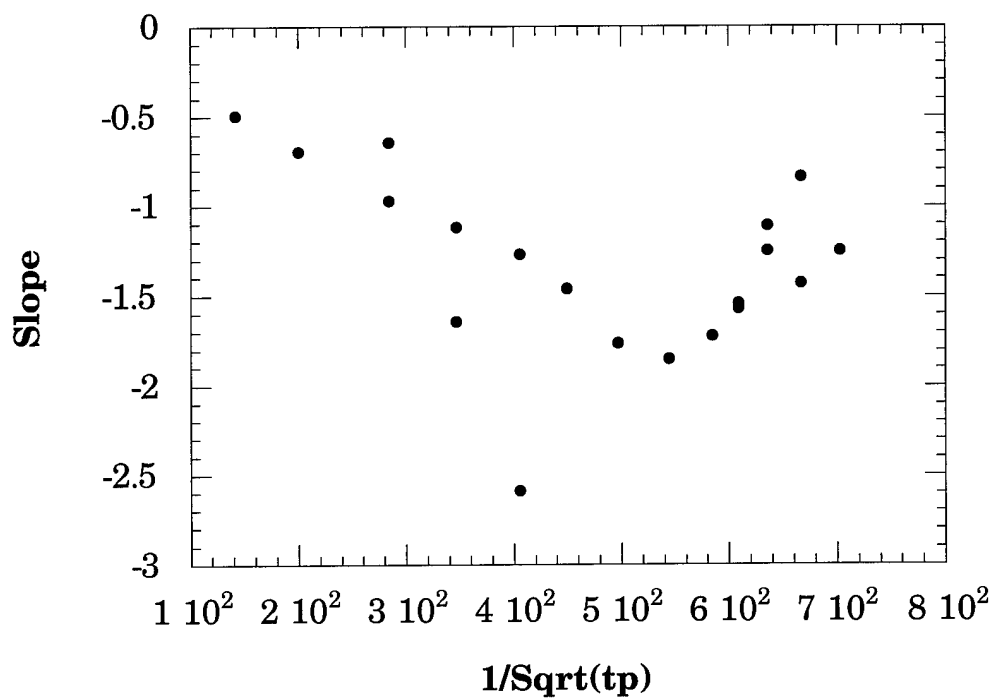


Figure 8.14 Slope vs. $1/\sqrt{t_p}$ from voltammograms of Cu(I)/Cu(II) in 1.5:1.0 melt using a 21 μm diameter tungsten electrode. Cu(I) concentration is 20.0 mM. Data obtained using quasi-reversible fits of the experimental data, between 1.7 to 2.2 V, from the COOL algorithm.

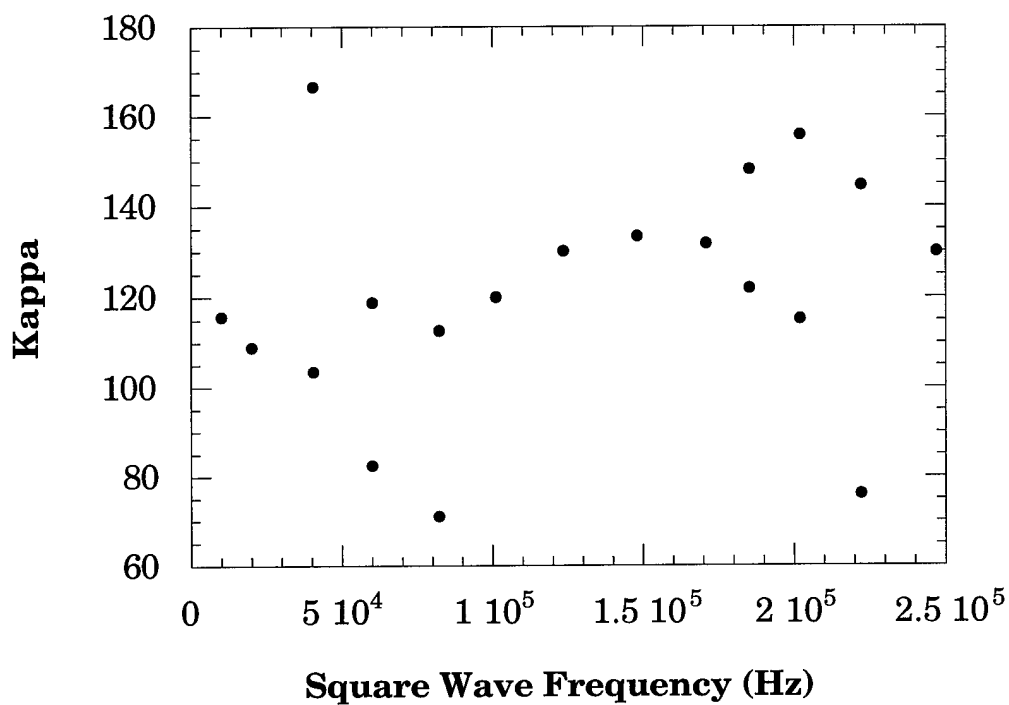


Figure 8.15 κ vs. square wave frequency from voltammograms of Cu(I)/Cu(II) in 1.5:1.0 melt using a 21 μm diameter tungsten electrode. Cu(I) concentration is 20.0 mM. Data obtained using quasi-reversible fits of the experimental data, between 1.7 to 2.2 V, from the COOL algorithm.

Current Range (μA)	Frequency (Hz)	$E_{1/2}$	Beta	Slope	Signal to Noise	$\text{sqrt}(tp)^{-1}$	Kappa
0.1	1.00E+04	1.944	0.69	-0.109	165.0	141.49	121.91
*1	1.00E+04	1.915	0.88	-0.162	89.4	141.49	14.87
0.1	2.00E+04	1.946	0.63	-0.164	195.0	200.10	113.80
*1	2.00E+04	1.948	0.51	-0.146	111.0	200.10	167.22
1	4.04E+04	1.943	0.65	-0.229	107.0	284.27	89.62
1	6.01E+04	1.952	0.46	-0.274	178.0	346.58	147.90
1	8.23E+04	1.925	0.68	-0.511	33.5	405.72	43.80
*1	1.01E+05	1.925	0.69	-0.502	14.6	449.47	48.01
10	1.01E+05	1.928	0.69	-0.404	47.5	449.47	50.23
*1	1.23E+05	1.941	0.73	-0.268	9.1	496.90	98.41
10	1.23E+05	1.928	0.70	-0.438	40.1	496.90	51.42
10	1.48E+05	1.941	0.70	-0.422	26.0	544.33	83.96
*10	1.71E+05	1.940	0.70	-0.429	18.7	584.71	87.46
*10	1.85E+05	1.947	0.71	-0.392	13.9	608.58	116.89
*10	2.02E+05	1.962	0.75	-0.275	11.3	635.64	336.22

Table 8.8 Square wave data from voltammograms of Cu(I)/Cu(II) in 1.5:1.0 melt using a 9 μm diameter tungsten electrode. Cu(I) concentration is 20.0 mM. Data obtained using quasi-reversible fits of the experimental data, between 1.7 to 2.2 V, from the COOL algorithm. Asterisks next in the number in the current range column indicates the data which was discarded using signal to noise and Figures 8.10 and 8.14.

Current Range (μA)	Frequency (Hz)	$E_{1/2}$	Beta	Slope	Signal to Noise	$\text{sqrt}(tp)^{-1}$	Kappa
1	1.00E+04	1.952	0.37	-0.494	468.0	141.49	115.62
1	2.00E+04	1.956	0.36	-0.696	282.0	200.10	108.97
1	4.04E+04	1.964	0.34	-0.643	248.0	284.27	166.62
*10	4.04E+04	1.959	0.38	-0.970	160.0	284.27	103.51
1	6.01E+04	1.954	0.46	-1.640	284.0	346.58	82.40
*10	6.01E+04	1.963	0.36	-1.120	159.0	346.58	118.75
*1	8.23E+04	1.953	0.43	-2.590	94.4	405.72	71.03
10	8.23E+04	1.964	0.39	-1.270	192.0	405.72	112.60
10	1.01E+05	1.967	0.36	-1.460	165.0	449.47	119.93
10	1.23E+05	1.974	0.30	-1.760	93.6	496.90	130.09
10	1.48E+05	1.979	0.27	-1.850	66.3	544.33	133.28
*10	1.71E+05	1.984	0.24	-1.720	43.8	584.71	131.66
*10	1.85E+05	1.993	0.20	-1.570	43.5	608.58	121.93
*100	1.85E+05	1.980	0.26	-1.540	24.8	608.58	148.03
*10	2.02E+05	1.992	0.22	-1.110	24.7	635.64	115.16
*100	2.02E+05	1.981	0.29	-1.250	19.8	635.64	155.68
*10	2.22E+05	2.000	0.21	-0.838	15.4	666.67	76.02
*100	2.22E+05	2.003	0.16	-1.430	16.9	666.67	144.53
*100	2.47E+05	2.001	0.16	-1.250	10.5	702.73	129.99

Table 8.9 Square wave data from voltammograms of Cu(I)/Cu(II) in 1.5:1.0 melt using a 21 μm diameter tungsten electrode. Cu(I) concentration is 20.0 mM. Data obtained using quasi-reversible fits of the experimental data, between 1.7 to 2.2 V, from the COOL algorithm. Asterisks next in the number in the current range column indicates the data which was discarded using signal to noise and Figures 8.10 and 8.14.

8.10 and 8.14, results in an improvement in the quality of the data (Figures 8.16 to 8.23). The data from the 9 μm diameter tungsten electrode are $E_{1/2}$ is $1.94 \pm .02$ V, β is 0.6 ± 0.1 , k_a° is 0.08 ± 0.05 cm/sec, and the diffusion coefficient is 1.7×10^{-6} cm²/sec. The data from the 21 μm diameter tungsten electrode are $E_{1/2}$ is $1.97 \pm .02$ V, β is 0.4 ± 0.1 , k_a° is 0.09 ± 0.03 cm/sec, and the diffusion coefficient is 7.5×10^{-7} cm²/sec.

These results confirm the electron transfer rates and electron transfer coefficients for Cu(I) in a 1.5:1.0 melt obtained previously but at higher frequencies. These results also demonstrate that at extremely high frequencies circuit limitations can contribute to the observed kinetics. In order to differentiate between the 'real' electron transfer kinetics and instrumental contributions, experiments were run in parallel with two tungsten microelectrodes (9 μm and 21 μm). In addition, several current levels were used at each experimental square wave frequency.

8.4 Conclusions

The diffusion coefficient and the electron transfer parameters for the Cu(I)/(II) couple in a 1.5:1.0 melt have been verified. Using the described equipment the maximum valid square wave frequency is about 150 kHz. This is an improvement factor of two over previous equipment.

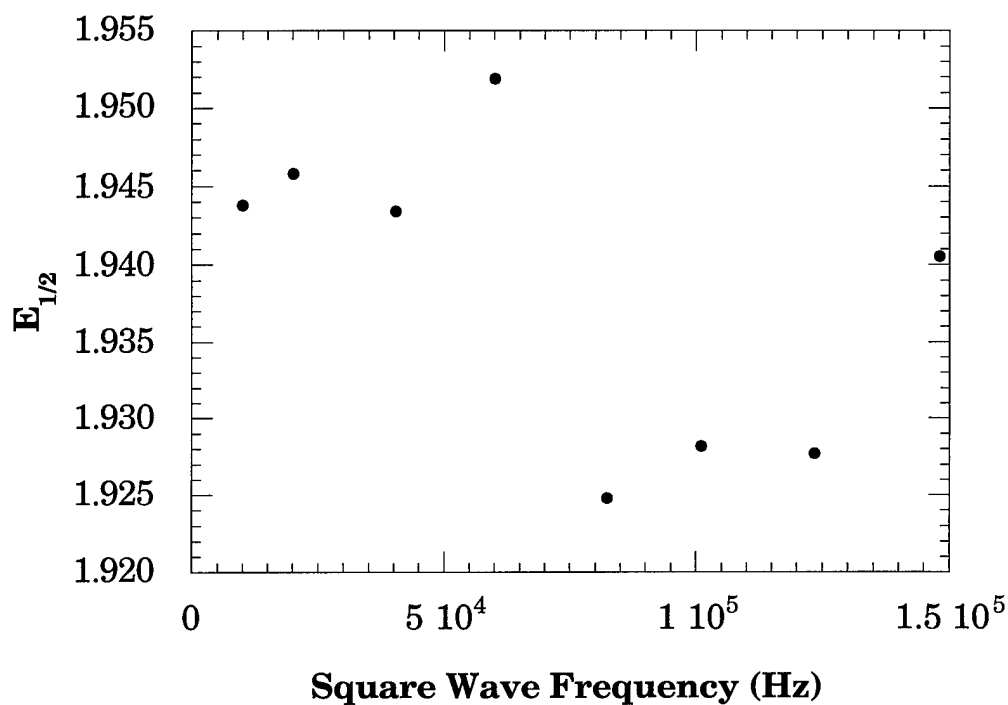


Figure 8.16 $E_{1/2}$ vs. square wave frequency from retained voltammograms of Cu(I)/Cu(II) in 1.5:1.0 melt using a 9 μm diameter tungsten electrode. Cu(I) concentration is 20.0 mM. Data obtained using quasi-reversible fits of the experimental data, between 1.7 to 2.2 V, from the COOL algorithm. Data was retained using signal to noise and Figures 8.10 and 8.14.

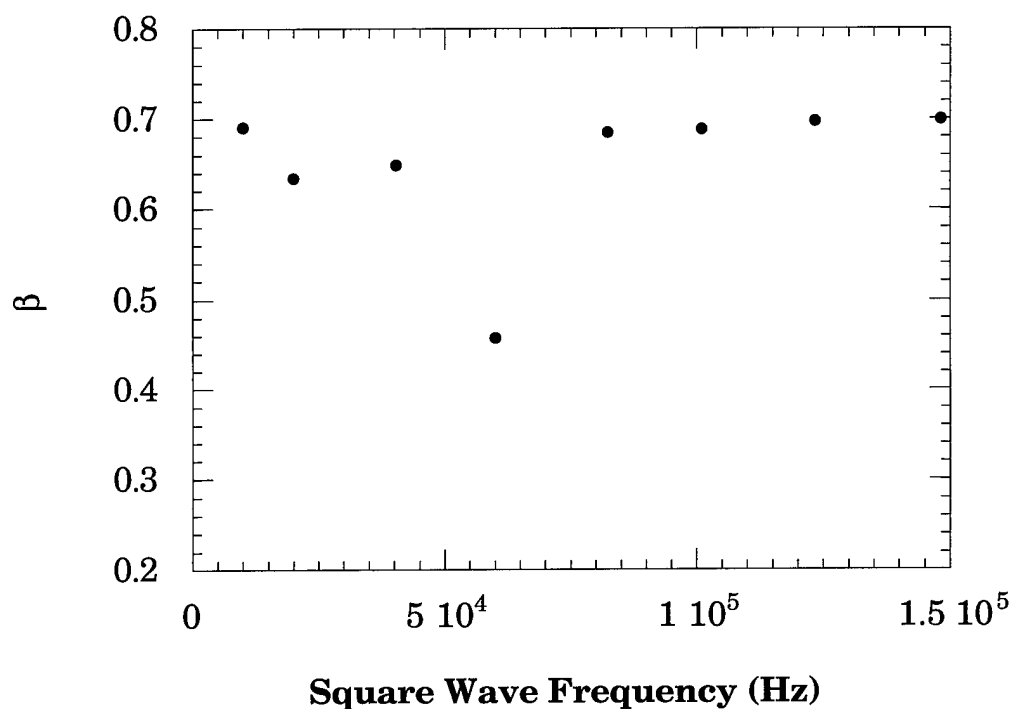


Figure 8.17 β vs. square wave frequency from retained voltammograms of Cu(I)/Cu(II) in 1.5:1.0 melt using a 9 μm diameter tungsten electrode. Cu(I) concentration is 20.0 mM. Data obtained using quasi-reversible fits of the experimental data, between 1.7 to 2.2 V, from the COOL algorithm. Data was retained using signal to noise and Figures 8.10 and 8.14.

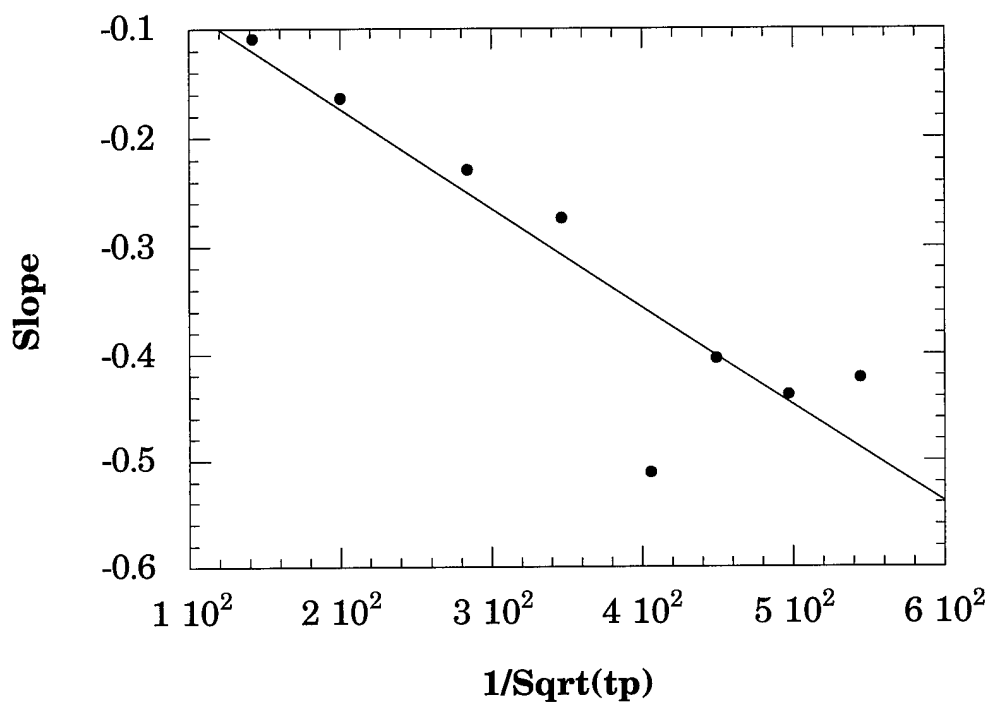


Figure 8.18 Slope vs. $1/\sqrt{t_p}$ from retained voltammograms of Cu(I)/Cu(II) in 1.5:1.0 melt using a 9 μm diameter tungsten electrode. Cu(I) concentration is 20.0 mM. Data obtained using quasi-reversible fits of the experimental data, between 1.7 to 2.2 V, from the COOL algorithm. Data was retained using signal to noise and Figures 8.10 and 8.14.

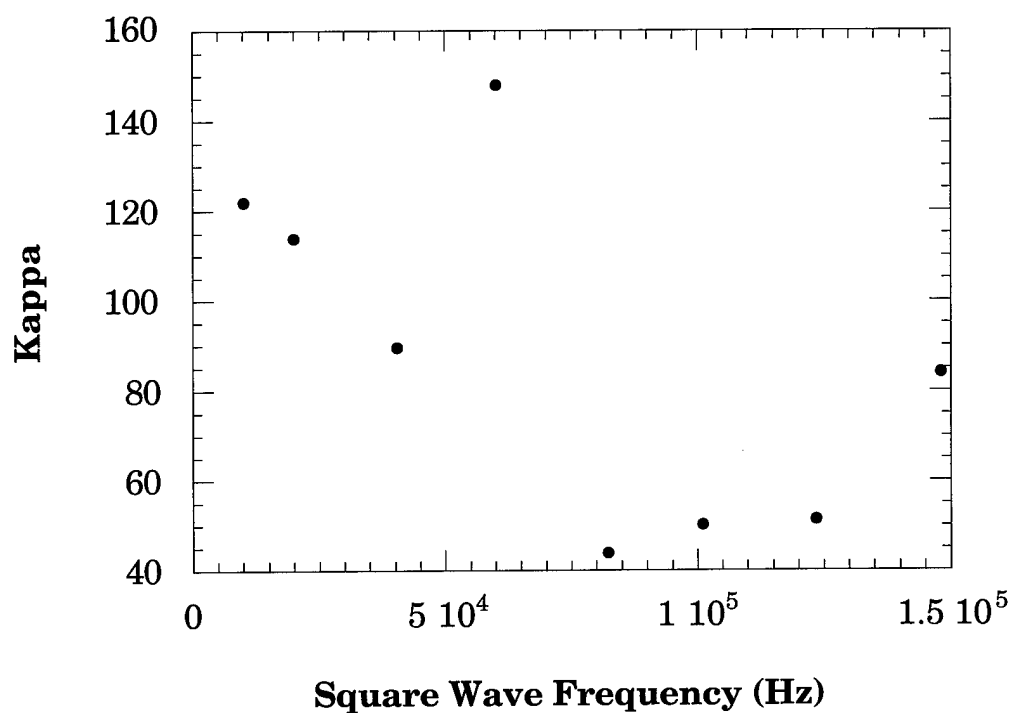


Figure 8.19 κ vs. square wave frequency from retained voltammograms of Cu(I)/Cu(II) in 1.5:1.0 melt using a 9 μm diameter tungsten electrode. Cu(I) concentration is 20.0 mM. Data obtained using quasi-reversible fits of the experimental data, between 1.7 to 2.2 V, from the COOL algorithm. Data was retained using signal to noise and Figures 8.10 and 8.14.

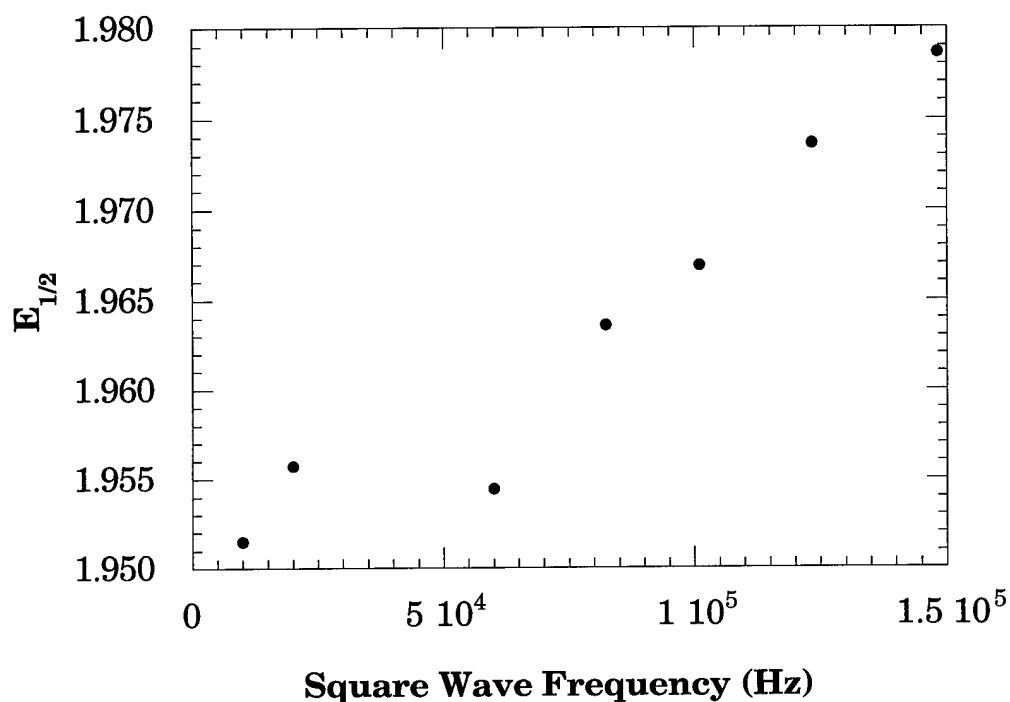


Figure 8.20 $E_{1/2}$ vs. square wave frequency from retained voltammograms of Cu(I)/Cu(II) in 1.5:1.0 melt using a 21 μm diameter tungsten electrode. Cu(I) concentration is 20.0 mM. Data obtained using quasi-reversible fits of the experimental data, between 1.7 to 2.2 V, from the COOL algorithm. Data was retained using signal to noise and Figures 8.10 and 8.14.

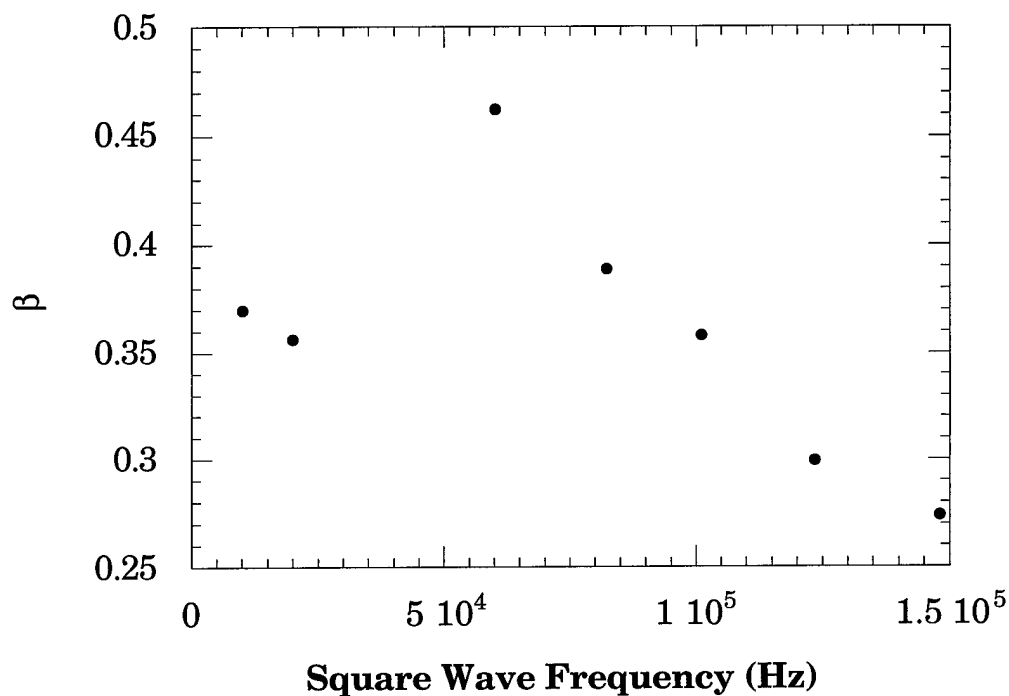


Figure 8.21 β vs. square wave frequency from retained voltammograms of Cu(I)/Cu(II) in 1.5:1.0 melt using a 21 μm diameter tungsten electrode. Cu(I) concentration is 20.0 mM. Data obtained using quasi-reversible fits of the experimental data, between 1.7 to 2.2 V, from the COOL algorithm. Data was retained using signal to noise and Figures 8.10 and 8.14.

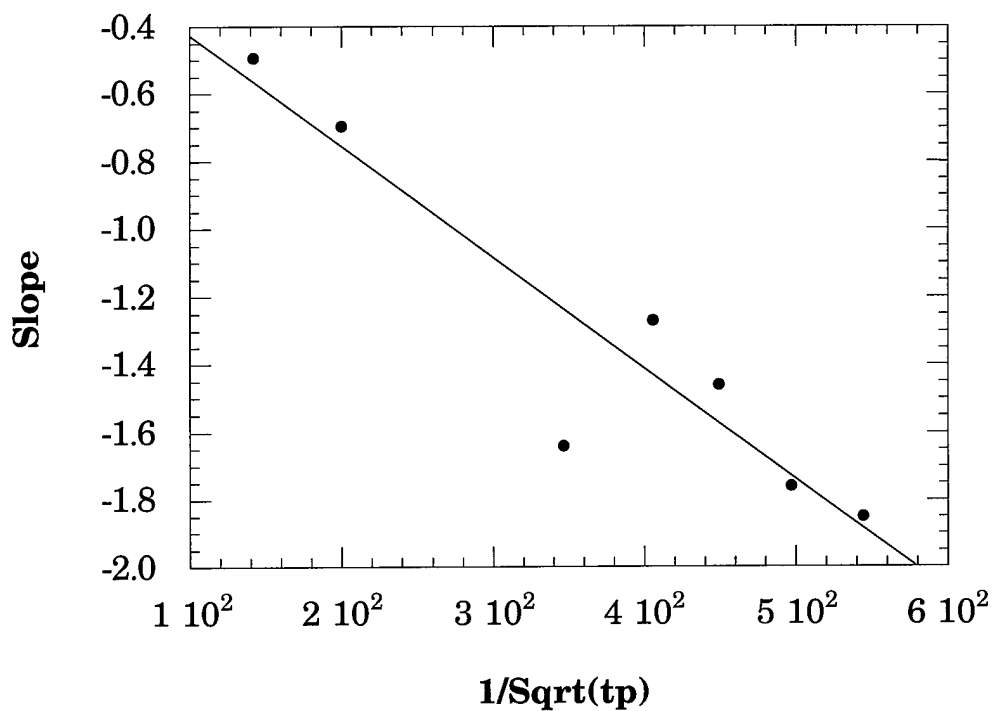


Figure 8.22 Slope vs. $1/\sqrt{t_p}$ from retained voltammograms of Cu(I)/Cu(II) in 1.5:1.0 melt using a 21 μm diameter tungsten electrode. Cu(I) concentration is 20.0 mM. Data obtained using quasi-reversible fits of the experimental data, between 1.7 to 2.2 V, from the COOL algorithm. Data was retained using signal to noise and Figures 8.10 and 8.14.

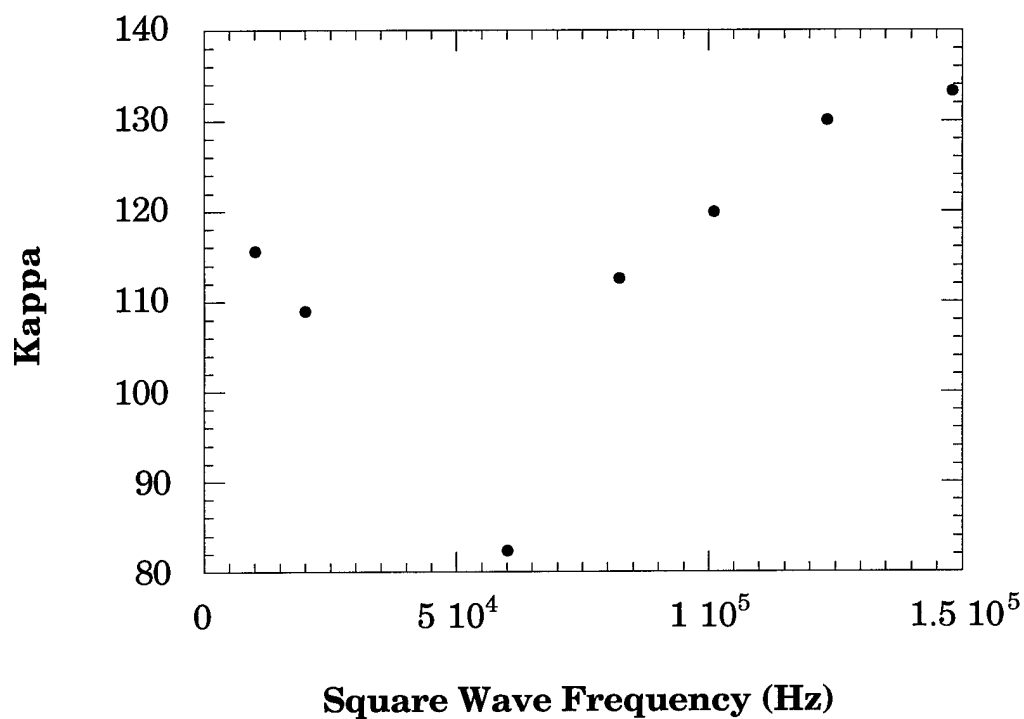


Figure 8.23 κ vs. square wave frequency from retained voltammograms of Cu(I)/Cu(II) in 1.5:1.0 melt using a 21 μm diameter tungsten electrode. Cu(I) concentration is 20.0 mM. Data obtained using quasi-reversible fits of the experimental data, between 1.7 to 2.2 V, from the COOL algorithm. Data was retained using signal to noise and Figures 8.10 and 8.14.

In order to obtain quality square wave voltammetry data at high square wave frequencies several potential experimental difficulties need to be considered. The potential experimental difficulties include: bandwidth of the potentiostat, RC time constant for the electrode, solution IR drop, under digitization of the observed current, and ensuring spherical diffusion is not contributing to the observed current. As the experimental square wave voltammetry data are being collected, identical experiments should be run at different current ranges to assess if the potentiostat is contributing to the observed kinetics. The experimental parameter that seems to be most sensitive to the introduction of instrumental artifacts is the slope. This is easily visualized when one plots the slope vs. $1/\sqrt{t_p}$.

Chapter 8 References

- (1) Carlin, R. T.; Trulove, P. C.; Mantz, R. A.; O'Dea, J. J.; Osteryoung, R. A. "Electron Transfer Kinetics for Weakly Bonded, Labile Metal-Ligand Complexes." *J. Chem. Soc., Faraday Trans.*, **1996**, 92, 3969-3973.
- (2) O'Dea, J. J.; Osteryoung, J.; Osteryoung, R. A. "Theory of Square Wave Voltammetry for Kinetic Systems" *Anal. Chem.* **1981**, 53, 695-701.
- (3) Osteryoung, J.; Osteryoung, R. A. "Square Wave Voltammetry" *Anal. Chem.* **1985**, 57, 101A-106A.
- (4) Osteryoung, J.; O'Dea, J. J. "Square Wave Voltammetry" In *Electroanalytical Chemistry: A Series of Advances*; Bard, A. J., Ed.; Marcel Dekker: New York, 1986, Vol. 14. pp. 209-308.
- (5) Go, W. S.; O'Dea, J. J.; Osteryoung, J. "Square Wave Voltammetry for the Determination of Kinetic Parameters: The Reduction of Zinc(II) at Mercury Electrodes" *J. Electroanal. Chem.* **1988**, 255, 21-44.
- (6) Noël, M. A. M.; O'Dea, J. J.; Osteryoung, R. A. "Short Time Pulse Voltammetry in Ambient Temperature Chloroaluminate Ionic Liquids." *J. Electrochem Soc.* **1992**, 139, 1231-1236.

- (7) Karpinski, Z. J.; Osteryoung, R. A. "Short Time Pulse Voltammetric Studies of Fast Heterogeneous Electron Transfer Reactions." *J. Electroanal. Chem* **1993**, *349*, 285-297.
- (8) O'Dea, J. J. Personal Communication.
- (9) Carlin, R. T.; Crawford, W.; Bersch, M. "Nucleation and Morphology Studies of Aluminum Deposited from an Ambient-Temperature Chloroaluminate Molten Salt" *J. Electrochem. Soc.* **1992**, *139*, 2720-2727.
- (10) O'Dea, J. J.; Osteryoung, J.; Lane, T. "Determining Kinetic Parameters from Pulse Voltammetric Data." *J. Phys. Chem.* **1986**, *90*, 2761-2764.
- (11) Montenegro, M. I. "Applications of Microelectrodes in Kinetics" In *Research in Chemical Kinetics*, vol 2. Compton, R. E.; Hancock, G. eds., Elsevier: The Netherlands, 1994, pp 1-80.

Appendix I

Aluminum Temperature Control Blocks

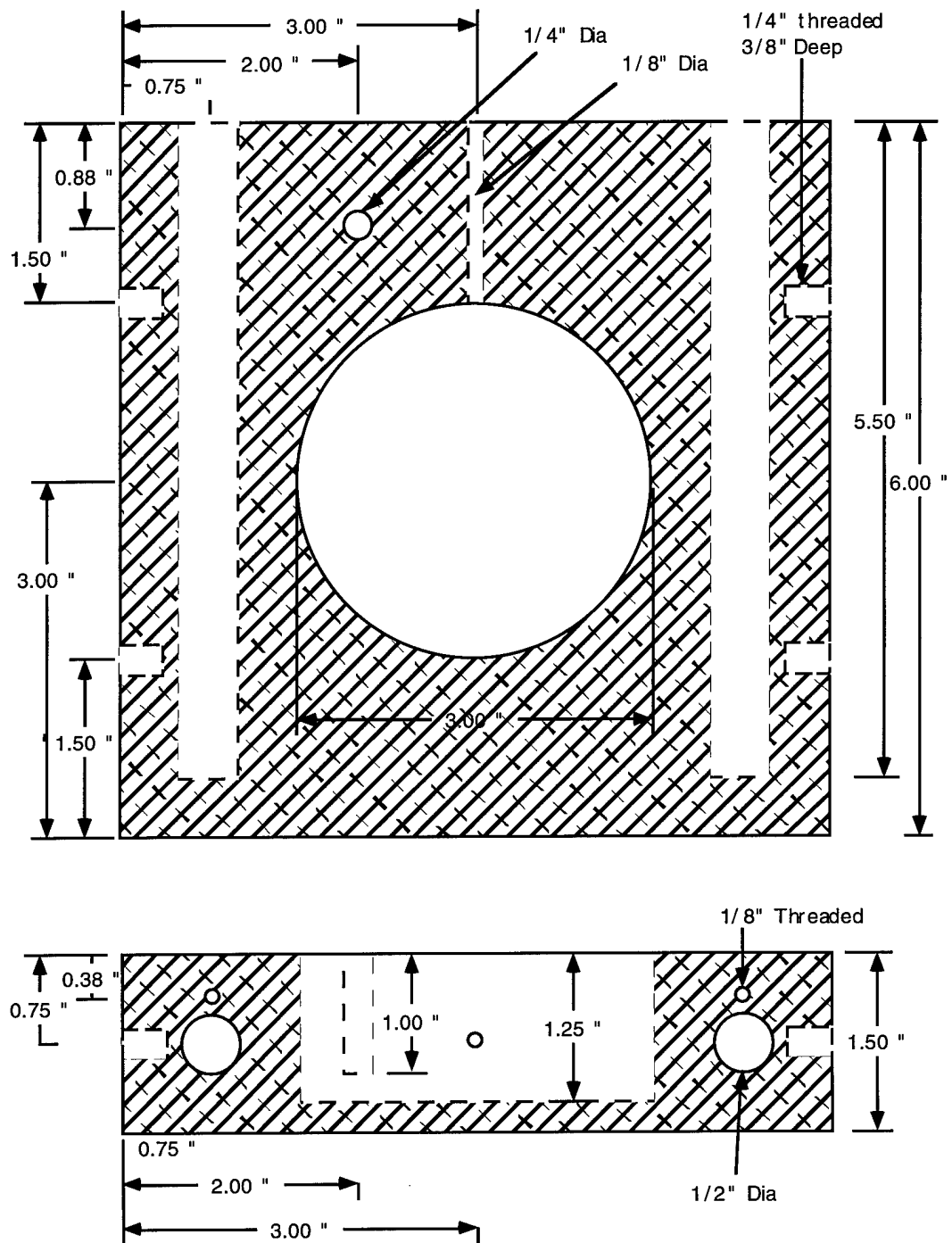


Figure AI.1. Heating Block

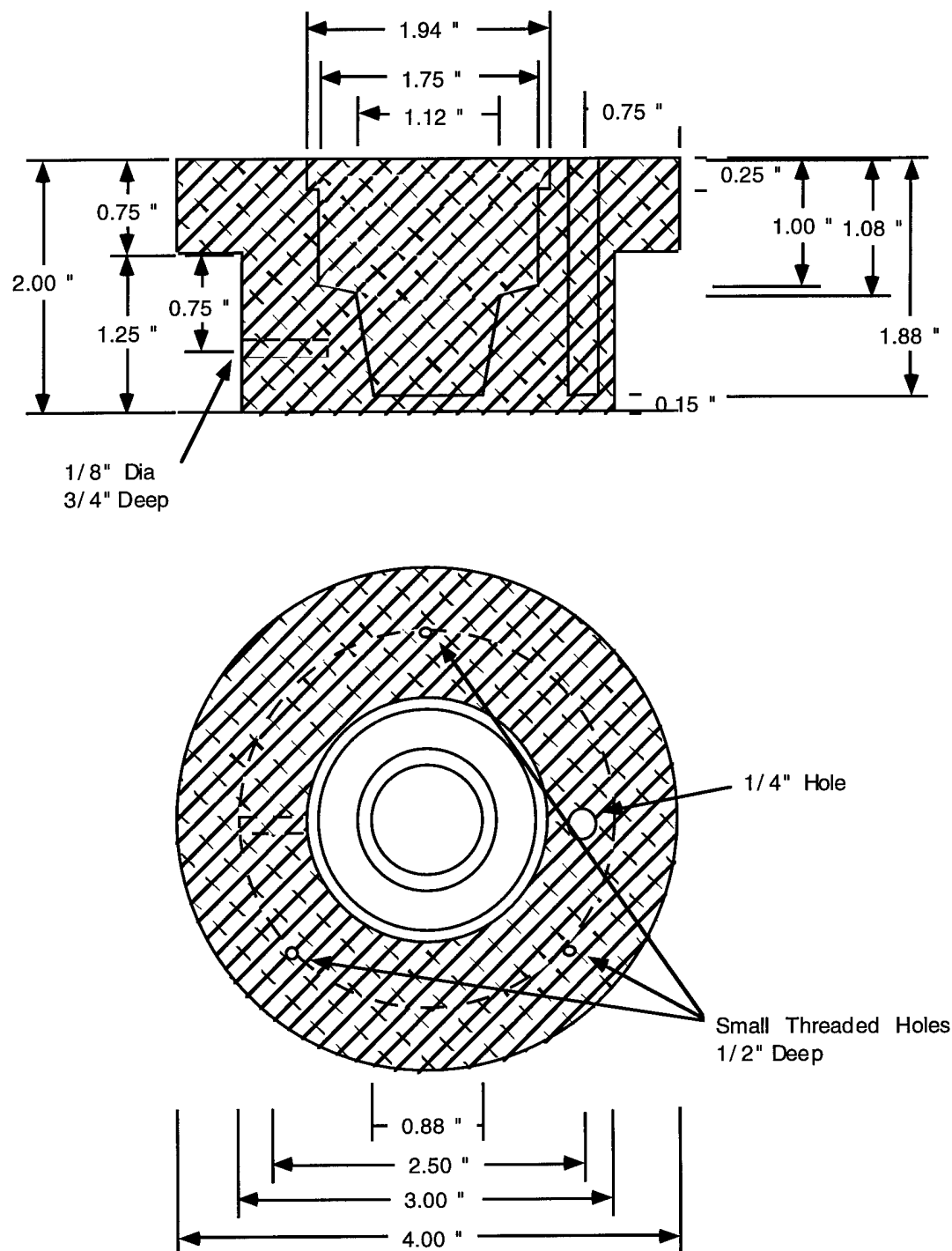


Figure AI.2. Heating block insert for use with EG&G PARC 303A cell.

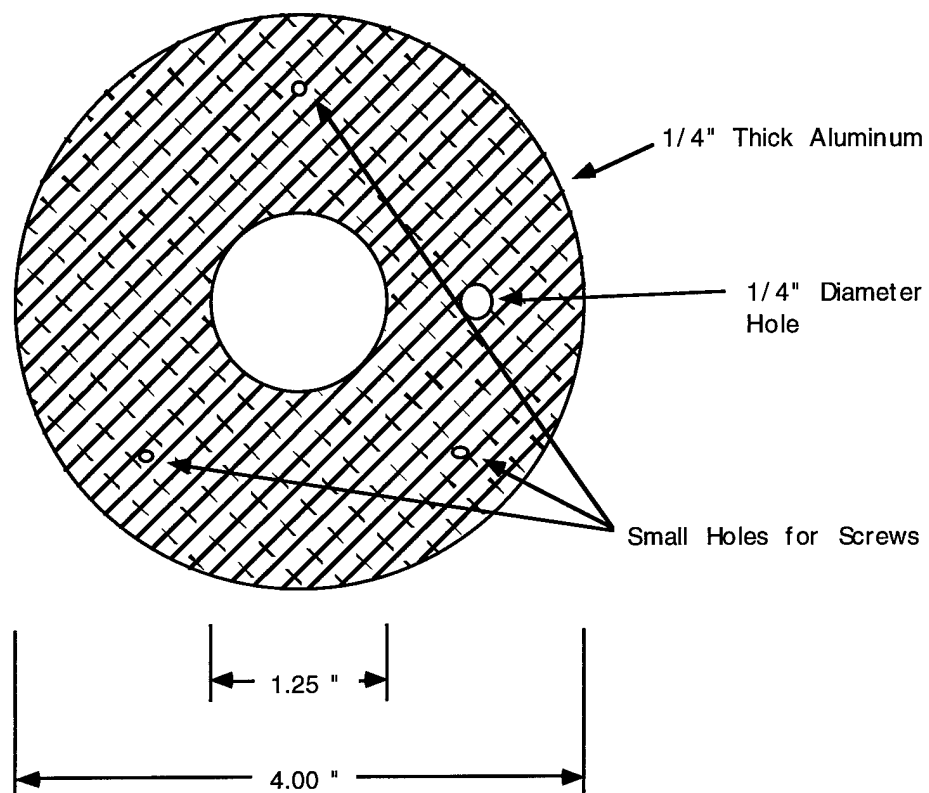


Figure AI.3. Heating block insert cover for use with EG&G PARC 303A cell.

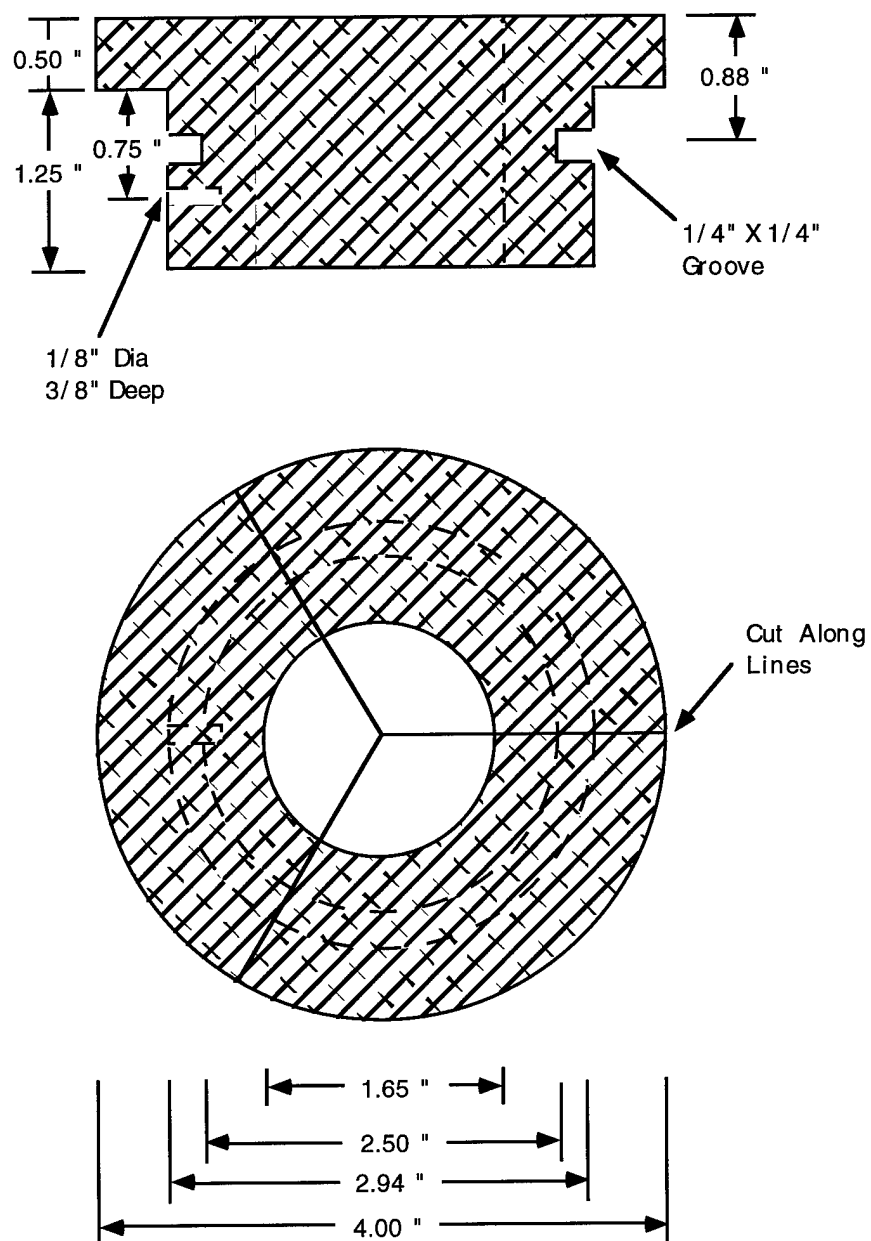


Figure AI.4. Heating block insert for use with 2 ounce Qorpak bottle.

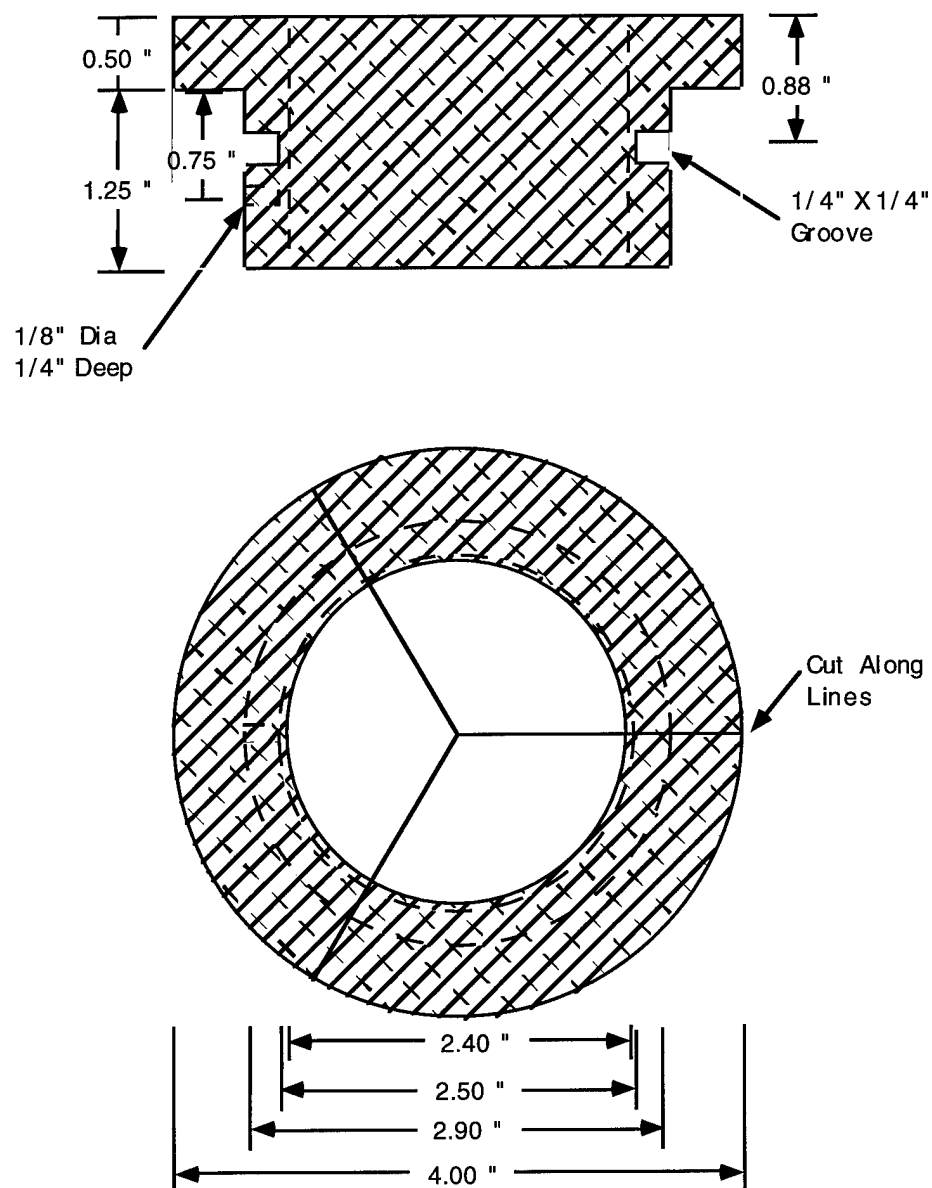


Figure AI.5. Heating block insert for use with 8 ounce Qorpak bottle.

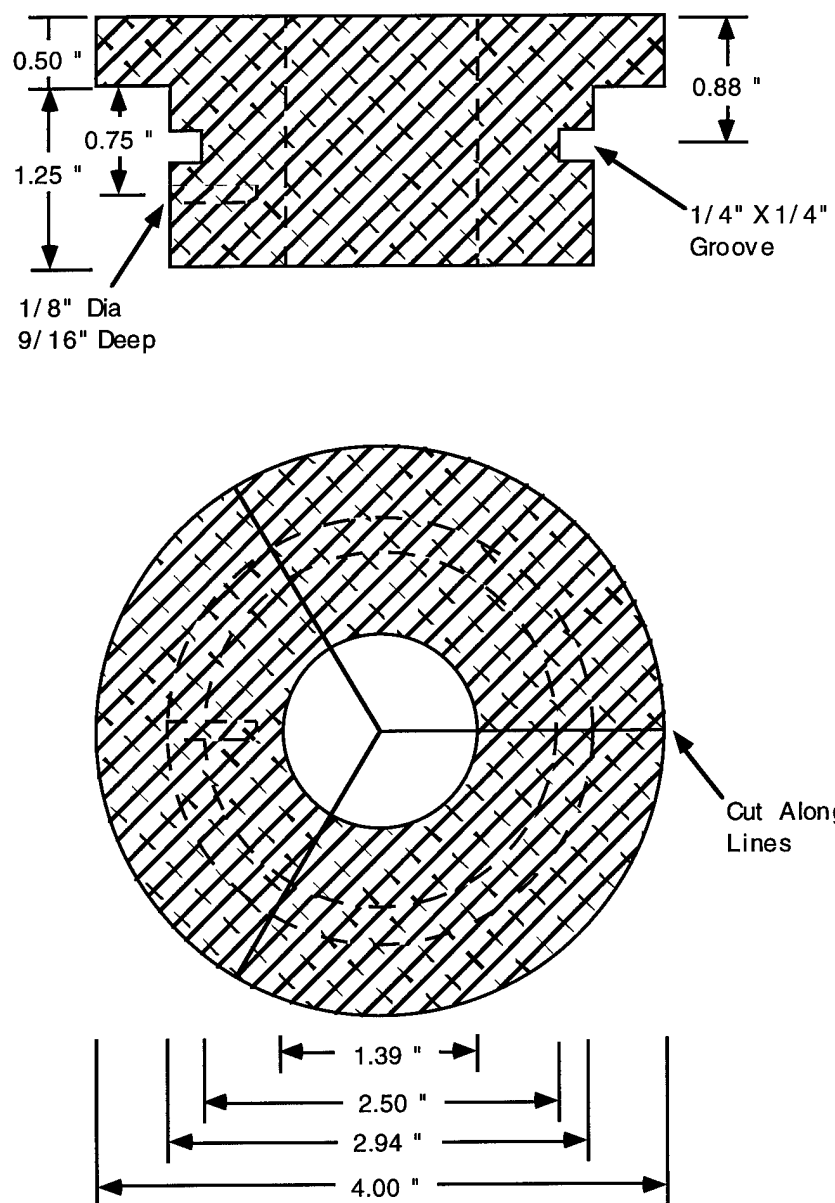


Figure AI.6. Heating block insert for use with 1.5 ounce Qorpak bottle.

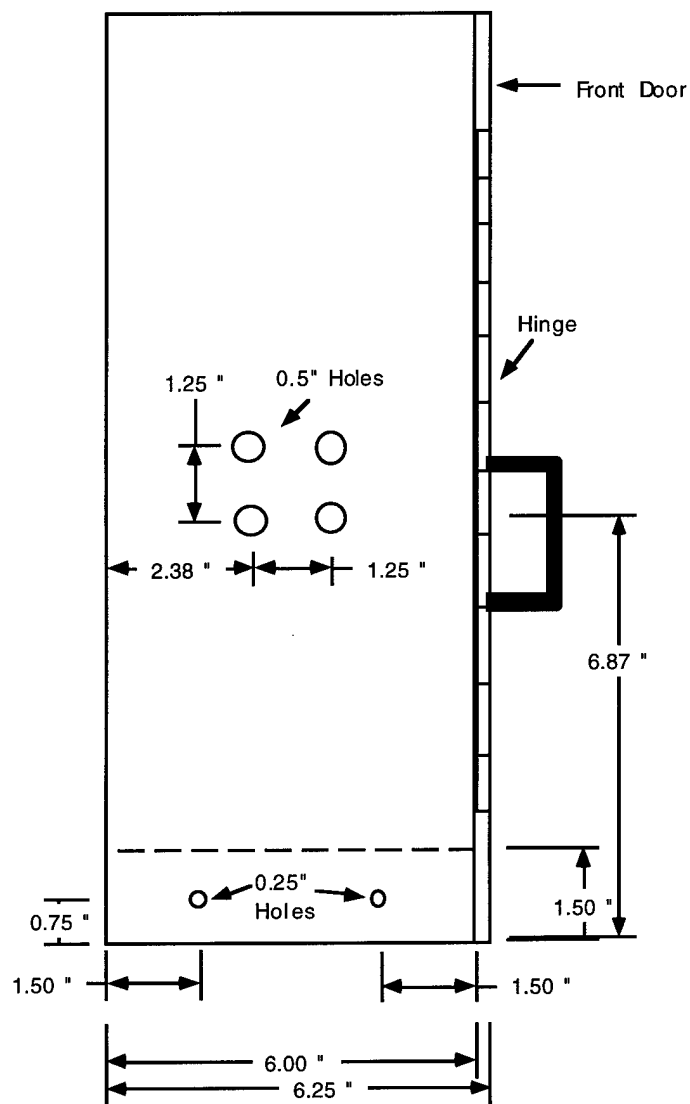


Figure AI.8. Faraday cage left side view.

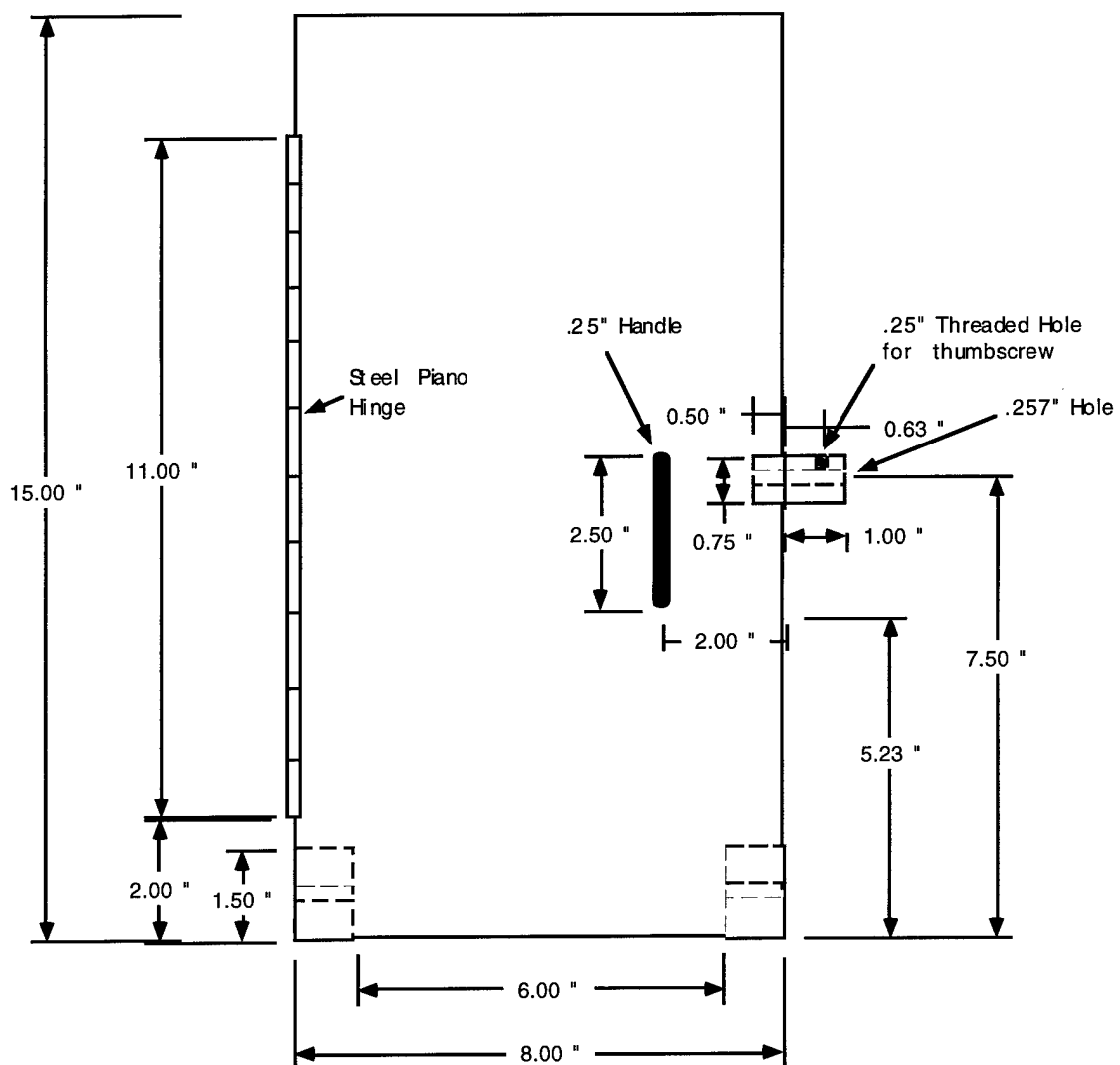


Figure AI.9. Faraday cage front view.

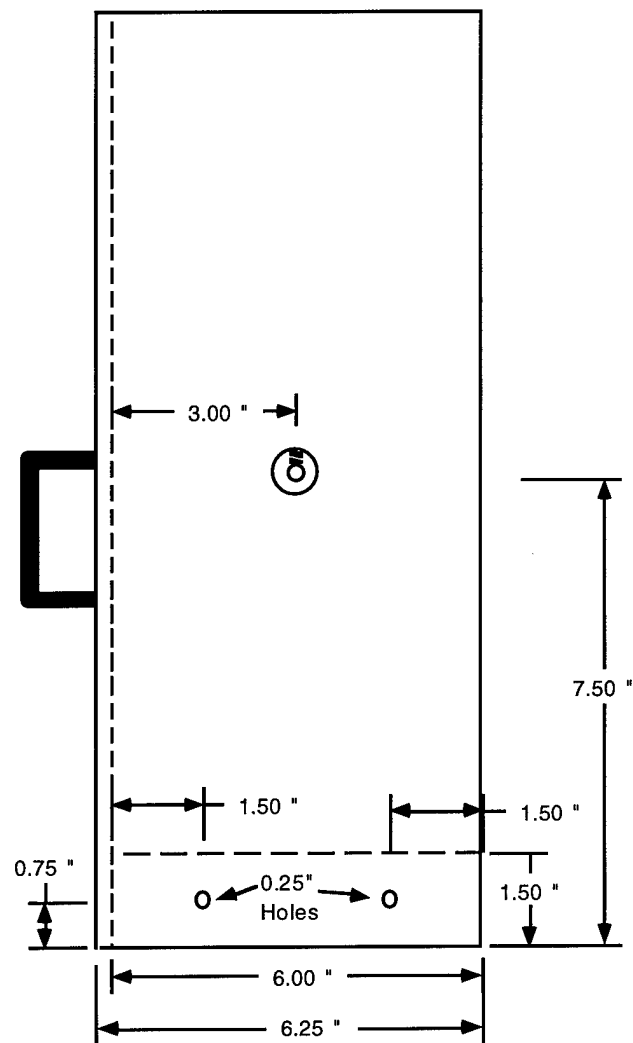


Figure AI.10. Faraday cage right side view.

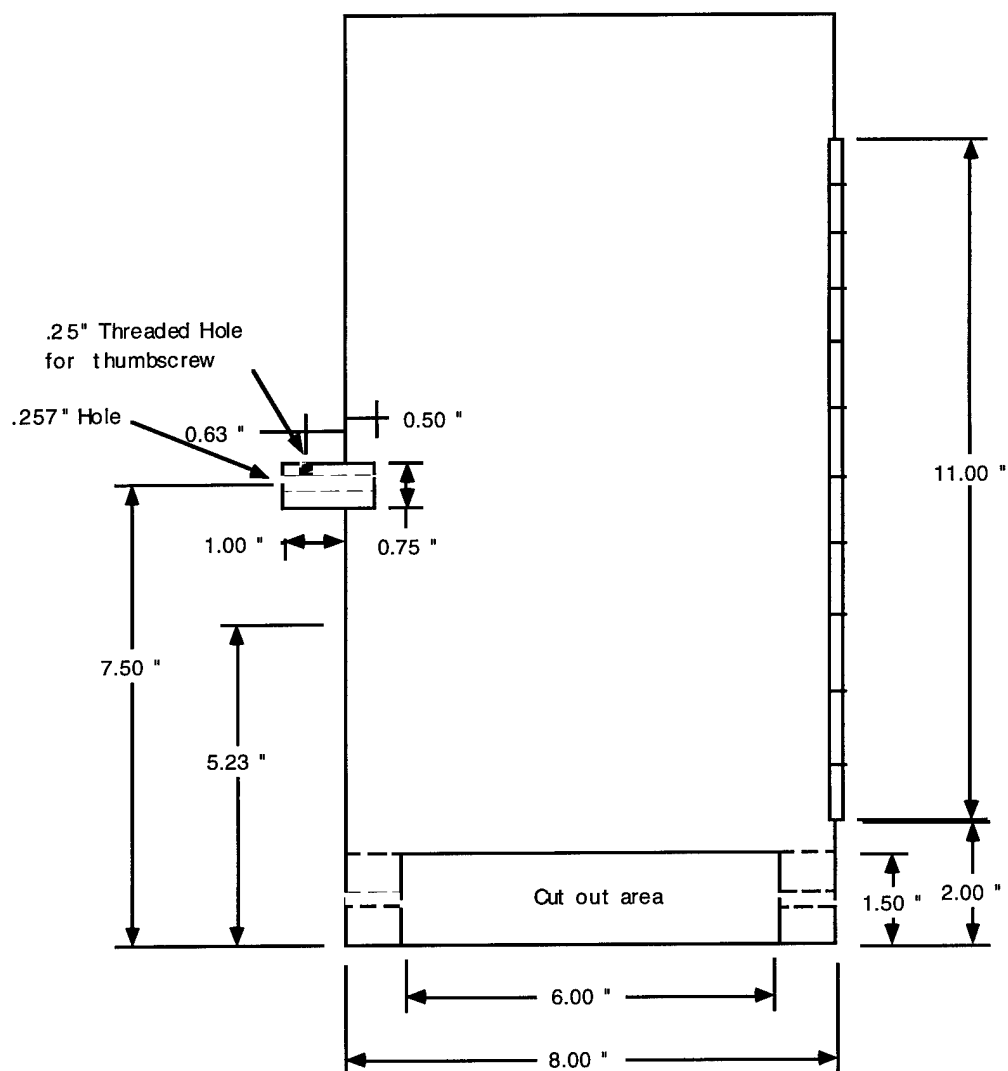


Figure AI.11. Faraday cage back view.

Appendix II

Phosgenation and Proton Removal Procedure

Procedure for the removal of oxide and proton impurities from basic melts.

The apparatus used for proton and oxide removal is pictured in Figure AII.1. All the stopcocks and valves in Figure AII.1 are numbered, and in the following procedure they will be referred to by their number and type. The apparatus is made up of several main components; these are the diffusion pump, the liquid nitrogen (LN₂) traps, the vacuum manifold, the gas manifold, the purge line, the McLeod gage, the TCD (thermal conductivity detector) gage, the gas manifold mercury bubbler, the helium line mercury bubbler, and four gas washing bottles making up the phosgene neutralizing system.

NOTE: Failure to follow these instructions is cause to have the privilege of using this piece of equipment revoked.

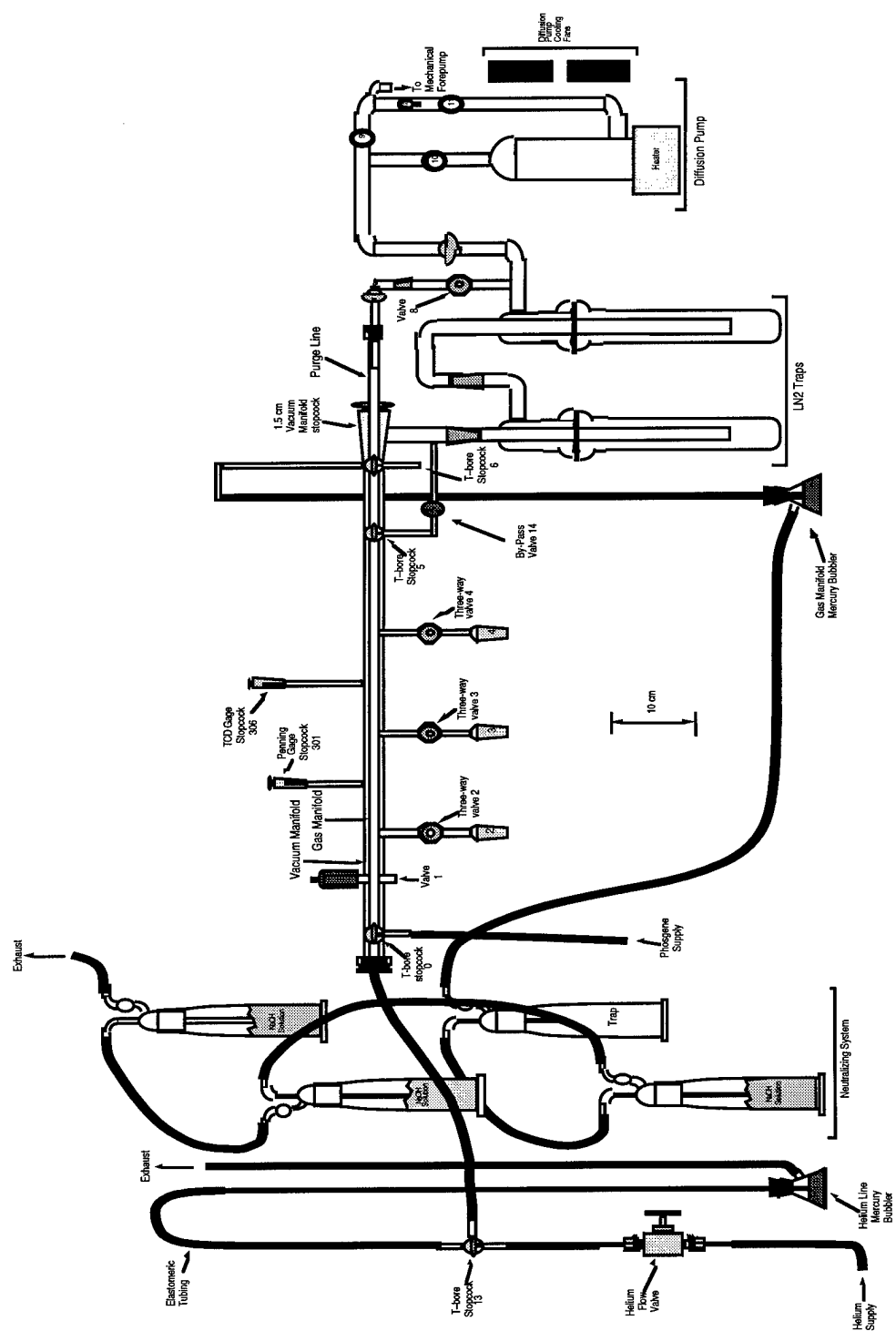


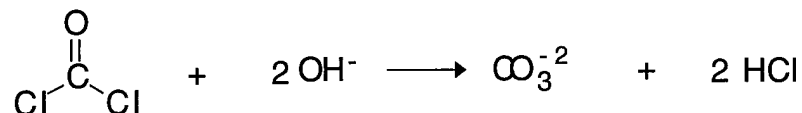
FIGURE AII.1. Diagram of the oxide and proton removal apparatus.

CAUTION: Phosgene is a highly toxic gas which has an odor resembling that of moldy hay.¹ The odor of phosgene is noticeable at levels down to 0.5 ppm in air; however, the recommended Threshold Limit Value (TLV) is only 0.1 ppm.^{2,3} Consequently, phosgene must always be handled in a operating fume hood in a well ventilated room. Furthermore, it is advisable to wear a acidic gas respirator when ever working around the apparatus when phosgene is in use.

Phosgene is soluble in both silicon and petroleum based greases and oils,³ most importantly it dissolves readily in Dow-Corning vacuum grease, Dow-Corning 705 diffusion pump oil, and mechanical vacuum pump oil. Phosgene does attack Apiezon more readily than Dow-Corning vacuum grease. The apparatus should be assembled using Dow-Corning vacuum grease. Consequently, when ever the diffusion or forepump oil is changed or vacuum grease is removed it must be done in a well ventilated hood and an acid gas respirator must be worn. As an added precaution as many doors and windows in the room should be open to provide for maximum ventilation.

Phosgene slowly penetrates most types of commercial elastomeric tubing (i.e. Tygon, neoprene, and latex). It appears that tubing manufactured out of Teflon interacts the least with phosgene (although even it is penetrated by phosgene to some extent);⁴ however, the rigidity of Teflon tubing precluded it being used for our system. Consequently, Tygon formula B-44-3 outer braid reinforced tubing was used for the connections shown in Figure A1. This tubing, which on exposure to phosgene slowly darkened, had to be replaced periodically.

Three gas washing bottles filled with 5% by weight NaOH in water are used to destroy excess phosgene by the reaction



The capacity of the neutralizing system is reached when most of the hydroxide has been consumed and is evidenced by the precipitation of Na_2CO_3 . It is important not to use greater than a 5% solution of NaOH, because higher concentrations of hydroxide will damage the frits on the gas washing bottles.

NOTE: Approximately 3 inches of mercury back-pressure should be expected due to the frits and gas washing bottles when the system has been assembled using extra coarse frits. Using less porous frits will result in greater back-pressures. In its current state the apparatus is not capable of withstanding higher back-pressures which can result in the displacement of the 1.5 cm bore high vacuum stopcock or the 4 mm high vacuum stopcock to the penning gage, and the subsequent release of phosgene into the atmosphere during the removal of phosgene from the system.

STEP-BY-STEP PROCEDURE

The following is a complete step-by-step procedure for the removal of both oxide and proton from a basic melt. If only the removal of proton is

required the segment of the procedure involving the use and removal of phosgene (Steps 57–122) is not performed; all other aspects of the two procedures are the same.

Before starting, read this procedure thoroughly and ensure that all the steps are understood. Also, check the log sheet for the apparatus and vacuum pump. The NaOH solutions must be changed after a maximum of three phosgene treatments and sooner if Na_2CO_3 precipitate is present. The vacuum pump oil should also be changed after three phosgene treatments. It is the responsibility of the person who performs the phosgene treatment after which the oil change and/or NaOH solution change is required, to perform these operations.

INITIAL APPARATUS SET-UP

Vacuum System Set-up

1. Valves 1, 8, and 14 are closed. The 1.5 cm vacuum manifold stopcock should be open.
2. Three-way valves 2, 3, and 4 are closed to both the vacuum and gas manifolds.
3. The TCD gauge and Penning gauge stopcocks, 306 and 301, are closed, and both gauges are off.

4. Valves 10, 11, and 12 are closed and valve 9 is open.
5. The diffusion pump should be off.
6. Turn on the mechanical pump.
7. The TCD and Penning stopcocks, 301 and 306, can now be opened. Allow 5 min for the vacuum to recover. If the system is performing properly the pressure should be approximately 25 millitorr. The static vacuum should be < 50 millitorr (0.050 mm Hg^o). (This is the maximum allowable fore pressure for operation of the diffusion pump).
8. If the vacuum is > 50 millitorr, check valves 1–4 and 8 to see that they are fully closed and check stopcocks 301 and 306 to see that they are well seated. Check the vacuum again; if the vacuum is still > 50 millitorr then a more thorough leak check with a Tesla coil is needed.⁵

NOTE: If the diffusion pump has just been filled or has been exposed to atmosphere since its last use, there will be a significant amount of dissolved gas present. Be careful when first applying vacuum to the diffusion pump to prevent the diffusion oil from bubbling up. The diffusion pump oil should be allowed at least 1 hour to outgas prior to heat being applied.

9. Close valve 9 and slowly open valve 11 followed by valve 10.
10. Plug in the two cooling fans for the diffusion pump, and turn on the variac, which supplies power to the diffusion pump heater, to 75% for 120 V.
11. After 5-10 minutes the diffusion pump oil will begin to boil. Close the TCD gauge, valve 306, and turn on the penning gauge.

NOTE: When the system is working properly and the trap dewars have been filled with liquid nitrogen the system pressure should be approximately $2 - 5 \times 10^{-6}$ torr.

12. Turn off the penning gauge.

Helium Purge of the Apparatus

13. T-bore stopcock 0 is opened between the gas manifold, the helium supply and closed to the phosgene supply.
14. T-bore stopcock 6 is opened between the gas manifold and the gas manifold bubbler and closed to the purge line.
15. T-bore stopcock 5 is opened between the gas manifold and the purge line and closed to the by-pass valve (14).

16. T-bore stopcock 13 is opened between the helium supply and the gas manifold and closed to the helium line bubbler.

17. Back off the helium regulator entirely. Open the valve on the helium pressure bottle.

18. Slowly open the helium flow valve 1 full turn.

19. Slowly increase the regulator pressure until gas begin to bubble through the gas manifold mercury bubbler.

NOTE: It may take up to a minute for the helium to force out the NaOH solution and begin bubbling through the neutralizing system. Do not become impatient and turn the regulator pressure up rapidly; instead increase the pressure gradually until a slow steady bubbling of helium is achieved.

20. Adjust the helium flow valve to achieve a flow rate of one bubble every couple seconds.

NOTE: The gas manifold should be maintained under a constant slow helium purge since the previous use, then steps 12 to 19 are not necessary.

USE OF APPARATUS

Attaching the Sample

The melt to be treated should be in a vacuum tight round-bottom flask with a stopcock (preferably 4 mm or larger) and a 24/40 female joint. The joint between the round-bottom flask and the stopcock should be greased with Dow-Corning vacuum grease such that only the top half of the joint is greased (Phosgene tends to dissolve in the grease and cause it to flow. If the entire joint is greased it runs into the melt.) The melt is stirred at all times with a magnetic stirrer and Teflon coated stir-bar. Ensure the stopcock is closed when removing the assembled apparatus from the drybox. When removing proton impurities, the basic melt will be incrementally raised to 70 °C. This temperature will ensure the HCl has sufficient vapor pressure to be removed. When removing oxide impurities, the basic melt should be maintained at approximately 30° C. This will allow for effective removal of oxide while limiting the reaction of phosgene with the imidazolium cation.

21. The dewars for the LN2 traps should be filled with liquid nitrogen.

NOTE: Periodically check to make sure that the LN2 dewars remain filled with liquid nitrogen. These dewars must remain filled until the trapped HCl and phosgene are removed.

22. Attach the sample to one of the three 24/40 male joints on the apparatus. Use a green poly-actal 24/40 clip to hold it in place. Make sure the 24/40 joint is uniformly greased with Dow-Corning high vacuum grease, but do not use an excessive amount. Begin stirring the sample.

NOTE: For the remainder of this procedure it will be assumed the sample is attached to 24/40 joint 3, although the procedure is exactly the same for joints 2 and 4.

23. Ensure that Helium has been flowing through the gas manifold mercury bubbler and the gas washing bottles for at least 15 minutes.

24. Open T-bore stopcock 13 to all three directions.

25. T-bore stopcock 6 is opened between the purge line and the gas manifold bubbler and closed to the gas manifold. Helium should now be bubbling only through the helium line bubbler. Increase the flow of helium through the helium line bubbler to a medium rate by adjusting the helium flow valve.

26. Turn off the variac which supplies power to the diffusion pump heater.

27. Close valves 301 and 10 followed by valve 11.

28. Open valve 9.

29. Three-way valve 3 is slowly opened to the vacuum manifold. (This evacuates the area between the sample stopcock and Three-way valve 3).

30. Very slowly open the stopcock on the sample flask. Care should be taken because bubbles of gas will begin escaping from the melt. Wait for the bubbling to slow to a few bubbles per second under full vacuum before going on to the next step (about 5 min).

31. Three-way valve 3 is closed to the vacuum manifold and then opened to the gas manifold; this vents the sample flask to the gas manifold and helium supply. When the sample flask is vented the mercury in the helium line bubbler will rise up the capillary. The mercury column will then slowly descend as helium flows into the sample flask. The sample flask is full when bubbling resumes in the helium line bubbler.

32. Three-way valve 3 is closed to the gas manifold and then opened to the vacuum manifold; this evacuates the sample flask again.

33. Vent the sample flask as described in step 31.

34. Repeat steps 32 and 33 two more times.

35. After the third evacuation and helium fill, evacuate the flask a fourth time following the procedure in step 32.

36. Close three-way valve 3 to the vacuum manifold.
37. Close valve 9 and slowly open valve 11 followed by valve 10.
38. Plug in the two cooling fans for the diffusion pump, and turn on the variac, which supplies power to the diffusion pump heater, to 75% for 120 V.
39. T-bore stopcock 6 is opened between the gas manifold and the gas manifold bubbler and closed to the purge line.
40. T-bore stopcock 13 is opened between the helium supply and the gas manifold and closed to the helium line bubbler.
41. Helium should now be flowing through the gas manifold mercury bubbler and the gas washing bottles. If the helium is not flowing go to steps 17 through 20.

Proton Removal

Before oxide impurities have been removed with phosgene proton impurities need to be removed by application of a strong vacuum. When removing proton the basic melt will be incremented up to and maintained at approximately 70 °C.

42. Place a heating mantle attached to the temperature control unit under the round-bottom flask.

43. Three-way valve 3 is slowly opened to the vacuum manifold.

44. Turn on the heating mantle to 30 °C.

45. Every 10 to 15 minutes raise the temperature control unit by 10 °C until you reach 70 °C.

NOTE: Proton removal is essentially complete when the sample flask will maintain a vacuum of $< 5 \times 10^{-6}$ torr for 10 minutes while isolated from the diffusion and fore pumps. For 50 mL of melt this can take up to 24–48 hours. Less time is required for smaller samples.

46. If only proton removal is desired then complete steps 47 through 56 otherwise go to step 57.

47. Turn off the variac and temperature control unit.

48. Close three-way valve 3 to the vacuum manifold and close the sample flask stopcock.

49. Ensure that helium has been flowing through the gas manifold mercury bubbler and the gas washing bottles for at least 15 minutes.

50. Open T-bore stopcock 13 to all three directions.

51. T-bore stopcock 6 is opened between the purge line and the gas manifold bubbler and closed to the gas manifold. Helium should now be bubbling through the helium line bubbler only. Increase the flow of helium through the helium line bubbler to a medium rate by adjusting the helium flow valve.

NOTE: For the sample flask to be safely transferred into the drybox it must be under vacuum!!

52. Three-way valve 3 is opened to the gas manifold. This vents the region between three-way valve 3 and the sample stopcock.

54. Three-way valve 3 is closed to the gas manifold.

55. Carefully remove the sample flask from the apparatus.

56. Goto step 123 to remove HCl from the traps.

Phosgene Treatment of the Basic Melt

57. Change the temperature control unit to 30° C.
58. Close three-way valve 3 to the vacuum manifold and close the sample flask stopcock.
59. Close the McLeod gage stopcock 306.
60. Turn off the variac which supplies power to the diffusion pump heater.
61. Close valve 10 followed by valve 11.
62. Open valve 9.
63. T-bore stopcock 13 is opened to all three directions.
64. T-bore stopcock 6 is opened between the purge line and the gas manifold bubbler and closed to the gas manifold. Helium should now be bubbling only through the helium line bubbler.
65. T-bore stopcock 0 is opened between the phosgene supply and the gas manifold and closed to the helium supply.

66. Valve 1 is slowly opened. Allow several minutes for the system to evacuate, then close Valve 1.

67. T-bore stopcock 0 is opened to all three directions. This vents the gas manifold and causes the mercury in the helium line bubbler to rise up the capillary. The mercury column will then descend as helium flows into the gas manifold. When bubbling resumes go to the next step.

68. Repeat steps 65-67 two more times.

CAUTION: This Stuff can Kill You!!!! Never work alone!!!! Make sure the hood is operating properly. Wear an acidic gas respirator whenever manipulating the apparatus. Have a phosgene detector kit (Matheson Toxic Gas Detector, Model 8014LA) in hand with a sampling tube in place before beginning treatment. Have some kind of timer or stopwatch available.

69. T-bore stopcock 13 is opened between the gas manifold and the helium supply and closed to the helium line bubbler.

70. T-bore stopcock 0 is opened between the helium supply and the gas manifold and closed to the phosgene supply.

71. T-bore stopcock 5 is opened between the gas manifold and the gas manifold bubbler and closed to the purge line. There should now be a flow of helium through the gas manifold bubbler and the NaOH solutions. Use the helium flow valve to adjust the flow to moderate bubbling.

72. T-bore stopcock 0 is opened to the phosgene supply and the gas manifold and closed to the helium supply.

73. Make sure the valve on the phosgene regulator is closed. Slowly open the main valve on the phosgene pressure bottle.

74. Slowly open the valve on the phosgene regulator until phosgene begins to slowly bubble through the gas manifold bubbler and the NaOH solutions. Allow approximately 30 s for the phosgene to fill the gas manifold before going to the next step.

75. Three-way valve 3 is closed to the vacuum manifold and then very slowly opened to the gas manifold. Begin timing. This opens the evacuated sample flask to the phosgene. Allow 5 min of positive phosgene pressure on the sample.

NOTE: Phosgene is very soluble in the melt, so it may take several minutes for phosgene to begin to bubble through the gas manifold bubbler and the NaOH solutions.

76. After 5 min three-way valve 3 is closed to the gas manifold. (The valve should be closed to both the gas and vacuum manifolds).

77. Close the phosgene regulator valve.

78. T-bore stopcock 0 is opened between the helium supply and the gas manifold and closed to the phosgene supply. Helium gas should now be bubbling through the gas manifold bubbler and the NaOH solutions.

79. After 5 min of additional reaction time three-way valve 3 is carefully and slowly opened to the vacuum manifold. The melt is left under full vacuum for at least 10 min before going to the next step. (After the third and final phosgene fill and evacuation go to step 82).

NOTE: When pulling a vacuum on a melt containing phosgene the melt will tend to foam, so vacuum should be applied very carefully.

80. T-bore stopcock 0 is opened to the phosgene supply and the gas manifold and closed to the helium supply.

81. Steps 74–80 are repeated two more times.

82. After the third and final phosgene fill and evacuation, the main valve on the phosgene pressure bottle is closed.

Removal of Phosgene from the Gas Manifold and the Sample Flask

83. T-bore stopcock 0 is opened to the gas manifold and the helium supply and closed to the phosgene supply.

84. Three-way valve 3 is closed to the vacuum manifold and then slowly opened to the gas manifold. This vents the sample flask to the gas manifold.

85. As soon as bubbling resumes in the gas manifold bubbler, three-way valve 3 is closed to the gas manifold and then slowly opened to the vacuum manifold. The sample flask is evacuated for approximately 5 min.

86. Steps 84 and 85 are repeated 2 more times for a total of 3 helium fills and evacuations of the sample flask. The sample flask should be under vacuum after this is completed.

87. Three-way valve 3 is closed to vacuum manifold. (The valve should now be closed to both the gas and vacuum manifolds).

88. T-bore stopcock 6 is opened between the gas manifold bubbler and the purge line and closed to the gas manifold.

89. T-bore stopcock 13 is opened to all three ways. Helium should now be bubbling through the helium line bubbler.

90. T-bore stopcock 0 is opened between the gas manifold and the phosgene supply and closed to the helium supply.

91. Valve 1 is slowly opened. This evacuates the phosgene line and the gas manifold. Allow several minutes for the vacuum to stabilize, and then close Valve 1.

92. T-bore stopcock 0 is opened to all three ways. This vents the gas manifold and the phosgene line. When bubbling resumes in the helium line bubbler go to the next step.

93. Repeat 90-92 two more times.

Removal of Phosgene from the LN2 Traps.

After treatment of the basic melt sample with phosgene, the phosgene in the LN2 traps must be carefully removed.

NOTE: If the backpressure exceeds 3" than the frits are getting clogged and need to be cleaned. In this case an alternate HCL and phosgene removal procedure can be used. This procedure does not remove phosgene and HCl from the vacuum portions of the line and the 1.5 cm vacuum manifold stopcock grease. Instead of steps 94 through 104 or

steps 123 to 137 use alternate procedure at the end of this document. Then clean the frits so they operate properly.

94. Valve 9 is closed. Valves 10, 11, and 12 should already be closed.

95. Valve 1 is carefully and slowly opened. This should cause the mercury level in the capillary of the helium line bubbler to rise 10–20 cm. The mercury level will then slowly decrease over several minutes as the vacuum manifold and LN2 traps are filled with helium.

96. When the bubbling of helium resumes turn T-bore stopcock 13 so that the stopcock is opened between the helium supply and the gas manifold and closed to the helium line bubbler.

97. Open valve 8. Adjust the helium flow valve so that gas is flowing through the gas manifold bubbler and the NaOH solutions. Allow the helium to bubble through the LN2 traps for a few minutes before going on to the next step.

NOTE: If a significant amount of oxide impurity was present in the melt being treated or if there was a large amount of melt, there will be a substantial amount of carbon dioxide in the traps. As soon as the LN2 dewars are removed this carbon dioxide will quickly vaporize and pass out the neutralizing system. Don't panic, the carbon dioxide will bubble very vigorously through the system for a few minutes before it

begins to dissipate. The phosgene, however, will take several hours before it is completely removed.

98. Remove the LN2 dewars one trap at a time. Wait for the CO₂ from the first trap to dissipate before removing the dewar from the second trap. After both dewars have been removed allow the traps to slowly warm.

NOTE: Do not try to speed up the removal of phosgene by heating the traps. This could result in a rapid boil-off of phosgene with possible catastrophic results!!!!

99. Open the ballast on the vacuum pump. This will allow any phosgene which may have gotten into the vacuum pump, to escape up the hood.

100. After all evidence of phosgene in the traps is gone (this should take several hours) valve 8 is closed.

101. The ballast on the vacuum pump is closed.

102. Valve 1 is closed.

103. T-bore stopcock 6 is opened between the gas manifold bubbler and the gas manifold and closed to the purge line. Turn down the flow of helium to the gas manifold bubbler to a slow rate by adjusting the helium flow valve.

104. Valve 9 is slowly opened to return the system to vacuum.

105. The LN2 dewars are returned to the traps.

106. Three-way valve 3 is slowly opened to the vacuum manifold.

Deprotonation after Phosgenation.

107. The TCD and Penning stopcocks, 301 and 306, can now be opened. Allow 5 min for the vacuum to recover. If the system is performing properly the pressure should be approximately 25 millitorr. The static vacuum should be < 50 millitorr (0.050 mm Hg^o). (This is the maximum allowable fore pressure for operation of the diffusion pump).

108. If the vacuum is > 50 millitorr, check valves 1, 2, 4, and 8 to see that they are fully closed and check stopcocks 301 and 306 to see that they are well seated. Check the vacuum again; if the vacuum is still > 50 millitorr then a more thorough leak check with a Tesla coil is needed.⁵

109. Close valve 9 and slowly open valve 11 followed by valve 10.

110. Plug in the two cooling fans for the diffusion pump, and turn on the variac, which supplies power to the diffusion pump heater, to 75% for 120 V.

111. After 5-10 minutes the diffusion pump oil will begin to boil. Close the TCD gauge, valve 306, and turn on the penning gauge.

NOTE: When the system is working properly and the trap dewars have been filled with liquid nitrogen the system pressure should drop below 25×10^{-3} torr once the diffusion pump begins to reflux.

112. Turn off the penning gauge and close stopcock 301.

113. Wait for at least 30 minutes for phosgene trapped in the melt to escape. If you raise the temperature before the phosgene has escaped you will chlorinate the imidazole resulting in discoloration of the melt.

114. Every 10 to 15 minutes thereafter raise the temperature control unit by 10 °C until you reach 70 °C.

NOTE: Proton removal is essentially complete when the sample flask will maintain a vacuum of $< 5 \times 10^{-6}$ torr for 10 minutes while isolated from the diffusion and fore pumps. For 50 mL of melt this can take up to 24-48 hours. Less time is required for smaller samples.

115. When proton removal is complete turn off the variac and temperature control unit.

116. Close three-way valve 3 to the vacuum manifold and close the sample flask stopcock.

117. Ensure that helium has been flowing through the gas manifold mercury bubbler and the gas washing bottles for at least 15 minutes.

118. Open T-bore stopcock 13 to all three directions.

119. T-bore stopcock 6 is opened between the purge line and the gas manifold bubbler and closed to the gas manifold. Helium should now be bubbling through the helium line bubbler only. Increase the flow of helium through the helium line bubbler to a medium rate by adjusting the helium flow valve.

NOTE: For the sample flask to be safely transferred into the drybox it must be under vacuum!!

120. Three-way valve 3 is opened to the gas manifold. This vents the region between three-way valve 3 and the sample stopcock.

121. Three-way valve 3 is closed to the gas manifold.

122. Carefully remove the sample flask from the apparatus.

Removal of HCl from the LN2 Traps.

After treatment of the basic melt sample with vacuum, the HCl in the LN2 traps must be carefully removed.

123. Turn off the Penning gage, and close the Penning gage stopcock 301.

124. Close valves 10 and 11. Valve 9 should already be closed.

125. Turn off the diffusion pump heater, but leave the cooling fans on.

126. T-bore stopcock 6 is opened between the purge line and the gas manifold bubbler and closed to the gas manifold.

127. T-bore stopcock 13 is opened to all three ways. Helium should now be bubbling through the helium line bubbler.

128. Valve 1 is carefully and slowly opened; this should cause the mercury level in the capillary of the helium line bubbler to rise 10–20 cm. The mercury level will then slowly decrease over several minutes as the vacuum manifold and LN2 traps are filled with helium.

129. When the bubbling of helium resumes turn T-bore stopcock 13 so that it is opened between the helium supply and the gas manifold and closed to the helium line bubbler.

130. Open valve 8. Adjust the helium flow valve so that gas is flowing through the gas manifold bubbler and the NaOH solutions. Allow the helium to pass through the LN2 traps for a few minutes before going on to the next step.

131. Remove the LN2 dewars one at a time, and allow the traps to slowly warm.

132. Open the ballast on the vacuum pump. This will allow any phosgene and HCl which may have gotten into the vacuum pump, to escape up the hood.

133. After all evidence of phosgene and HCl in the traps is gone (this could take up to several hours) valve 8 is closed.

134. The ballast on the vacuum pump is closed.

135. Valve 1 closed.

136. T-bore stopcock 6 is opened between the gas manifold and the gas manifold bubbler and closed to the purge line. Adjust the helium flow valve so

that a very slow flow of helium passes through the gas manifold bubbler and the NaOH solutions.

NOTE: It is best to maintain a slow flow of helium through the gas manifold while the apparatus is not in use to preclude moisture contamination and to remove any phosgene which may out-gas from the tubing.

137. Valve 9 is slowly opened to return the system to vacuum.

138. The TCD and Penning stopcocks, 301 and 306, can now be opened. Allow 5 min for the vacuum to recover. If the system is performing properly the pressure should be approximately 25 millitorr. The static vacuum should be < 50 millitorr (0.050 mm Hg^o). (This is the maximum allowable fore pressure for operation of the diffusion pump).

139. If the vacuum is > 50 millitorr, check valves 1-4 and 8 to see that they are fully closed and check stopcocks 301 and 306 to see that they are well seated. Check the vacuum again; if the vacuum is still > 50 millitorr then a more thorough leak check with a Tesla coil is needed.⁵

140. Close valve 9 and slowly open valve 11 followed by valve 10.

141. Plug in the two cooling fans for the diffusion pump, and turn on the variac, which supplies power to the diffusion pump heater, to 75% for 120 V.

142. After 5-10 minutes the diffusion pump oil will begin to boil. Close the TCD gauge, valve 306, and turn on the penning gauge.

143. Turn off the penning gauge and close stopcock 301.

144. T-bore stopcock 6 is opened between the gas manifold and the gas manifold bubbler and closed to the purge line.

145. T-bore stopcock 13 is opened between the helium supply and the gas manifold and closed to the helium line bubbler.

146. Helium should now be flowing through the gas manifold mercury bubbler and the gas washing bottles. If the helium is not flowing go to steps 17 through 20.

147. Sign the log sheets. Change the NaOH solutions if required. Change the vacuum pump oil if required.

Alternate Removal of HCl and Phosgene from the LN2 Traps.

A1. Turn off the Penning gage, and close the Penning gage stopcock 301.

- A2. Close valves 10 and 11. Valve 9 should already be closed.
- A3. Turn off the diffusion pump heater, but leave the cooling fans on.
- A4. T-bore stopcock 6 is opened between the purge line and the gas manifold bubbler and closed to the gas manifold.
- A5. T-bore stopcock 13 is opened to all three ways. Helium should now be bubbling through the helium line bubbler.
- A6. T-bore stopcock 5 is opened to all three ways.
- A7. Valve 14 is slowly opened; this should cause the mercury level in the capillary of the helium line bubbler to rise 10–20 cm. The mercury level will then slowly decrease over several minutes as the vacuum manifold and LN2 traps are filled with helium.
- A8. When the bubbling of helium resumes turn T-bore stopcock 13 so that it is opened between the helium supply and the gas manifold and closed to the helium line bubbler.
- A9. Open valve 8. Adjust the helium flow valve so that gas is flowing through the gas manifold bubbler and the NaOH solutions. Allow the helium to pass through the LN2 traps for a few minutes before going on to the next step.

NOTE: If a significant amount of oxide impurity was present in the melt being treated or if there was a large amount of melt, there will be a substantial amount of carbon dioxide in the traps. As soon as the LN2 dewars are removed this carbon dioxide will quickly vaporize and pass out the neutralizing system. Don't panic, the carbon dioxide will bubble very vigorously through the system for a few minutes before it begins to dissipate. The phosgene, however, will take several hours before it is completely removed.

A10. Remove the LN2 dewars one trap at a time. Wait for the CO₂ from the first trap to dissipate before removing the dewar from the second trap. After both dewars have been removed allow the traps to slowly warm.

NOTE: Do not try to speed up the removal of phosgene by heating the traps. This could result in a rapid boil-off of phosgene with possible catastrophic results!!!!

A11. Open the ballast on the vacuum pump. This will allow any phosgene which may have gotten into the vacuum pump, to escape up the hood.

A12. After all evidence of phosgene and/or HCl in the traps is gone (this should take several hours) valve 8 is closed.

A13. The ballast on the vacuum pump is closed.

A14. Valve 14 is closed.

A15. T-bore stopcock 5 is opened to the gas manifold and the purge line and closed to the by-pass valve (14).

A16. T-bore stopcock 6 is opened between the gas manifold and the gas manifold bubbler and closed to the purge line. Adjust the helium flow valve so that a very slow flow of helium passes through the gas manifold bubbler and the NaOH solutions.

NOTE: It is best to maintain a slow flow of helium through the gas manifold while the apparatus is not in use to preclude moisture contamination and to remove any phosgene which may out-gas from the tubing.

A17. Valve 9 is slowly opened to return the system to vacuum.

Appendix II References

- (1) *The Merck Index*; Budavari, S.; O'Neil, M. J.; Smith, A.; Heckelman, P. E., Eds.; Merck & Co.: Rahaway, NJ, 1989; 11th ed.; p 1165.
- (2) Mehlman, M. A. *Def. Sci. J.* **1987**, *37*, 269–279.
- (3) Diller, W. F.; Zante, R. *J. Toxicol. and Indust. Health* **1985**, *1*, 117–128.
- (4) Hussey, C. L., University of Mississippi, personal communication, 1991.
- (5) Moore, J. H.; Davis, C. C.; Coplan, M. A. In *Building Scientific Apparatus*; Addison–Wesley: Reading, MA, 1983; p 105.